Twinkle, twinkle, little stars: shedding light on the population of Galactic gravitational wave sources

Thesis by
Kevin Brian Burdge

In Partial Fulfillment of the Requirements for the
Degree of
Doctor of Philosophy

CALIFORNIA INSTITUTE OF TECHNOLOGY
Pasadena, California

2021
Defended May 17, 2021

© 2021

Kevin Brian Burdge
ORCID: 0000-0002-7226-836X

All rights reserved

To my wife Maiko, and my son Luke

Seht die Sterne, die da lehren
wie man soll den Meister ehren.
Jeder folgt nach Newtons Plan
Ewig schweigend seiner Bahn.

-Albert Einstein

ACKNOWLEDGEMENTS

My journey through graduate school would not have been possible were not not for many people:

Firstly, I thank my advisor, Tom Prince, who put up with my visiting his office dozens of times a day (and often came down to visit mine), which helped me thrive. I suspect that I probably communicated more with my advisor than any other graduate student in the building, and I am incredibly fortunate to have had one who was willing to devote so much time to me. Tom has not only been instrumental in developing my research career, but he has also taught me a great deal about how to be a supportive and effective mentor, and I will do my best to apply these lessons if I ever have my own graduate students and postdocs.

Shri Kulkarni, who throughout graduate school provided me with valuable advice, effectively acting as secondary advisor. Shri provided me with a broader perspective on how to approach research and life in general. I thank him for his patience, and I value his no-nonsense approach to the world. I particularly appreciate his honesty and willingness to critically discuss my weaknesses as a scientist with me, something which I wish more people were willing to do. Being aware of these weaknesses has given me focus on what to work on, and I appreciate this a great deal; I know that I will grow immensely as a scholar if I can successfully apply Shri's advice.

Jim Fuller, who also acted as a secondary advisor to me (Jim also endured many unannounced visits to his office). I appreciate the ease with which I could approach Jim about any question, and his enthusiasm in understanding the odd systems discovered in this thesis work.

Tom Marsh, who I met at the European White Dwarf workshop in 2018. I had heard about Tom prior to meeting him (and read many of his papers), but I never could have anticipated how much I would learn from him and how much I would come to value his friendship. What I value the most about working with Tom is his shared enthusiasm and excitement for every new discovery (those who know me know I am largely motivated

by my own excitement and enthusiasm, and it was a joyous experience to meet someone who shared my degree of enthusiasm for compact binaries).

David Kaplan, a role model whose rigorous and thorough approach to research I greatly admire. His remarkably dense feedback as a co-author greatly enhanced all of the publications presented in this thesis.

There are many other faculty working in the field of white dwarfs who had an incredibly positive impact on my career in the last few years, including Warren Brown, Boris Gaensicke, JJ Hermes, Mukremin Kilic, who all share my enthusiasm for double degenerates (and white dwarfs in general).

Gregg Hallinan, for renewing my enthusiasm for instrumentation, and teaching me a lot about CHIMERA.

Matthew Graham, who shared my general enthusiasm for exotic variables and fast algorithms for mining large astronomical datasets. I learned an enormous amount from conversations with Matthew over the years, and grew a lot as a data scientist as a result of his advice.

I collaborated with many excellent postdoctoral scholars during my time at Caltech, who I also wish to acknowledge:

Michael Coughlin, who has played a major role in much of my work, suffered through many nights of KPED with me, and has always been a supportive friend.

Ilaria Caiazzo, whose remarkable knowledge and enthusiasm for white dwarfs continues to amaze me, and has bolstered my enthusiasm for research.

Przemek Mroz, whose remarkable programming skills never failed to stun me, and have opened up many new scientific doors to explore.

Jan van Roestel, whose enthusiasm for white dwarfs and variable stars in general helped further fuel my own. I thank Jan in particular for all of his help with observing, and the many things he taught me about lightcurve modelling.

I also thank Marin Anderson, my office mate for several years, whose friendship made coming to the office something I always enjoyed.

I thank Kishalay De and Anna Ho, two good friends, and also colleagues within the ZTF project working on very different topics than myself, whose perspectives I always found incredibly valuable.

I thank Andrew Tisdale for his generous gift towards my research, which has enabled a significant amount of progress and contributed significantly to the discoveries presented in this thesis.

I thank the Palomar and Keck support astronomers who helped me get through many long nights, and the Caltech Optical Observatory staff, in particular Jennifer Millburn, who worked very hard over the years to help me facilitate many upgrades to instruments such as CHIMERA.

I thank Ernie and his team, whose food truck supplied a large fraction of my biomass in graduate school, and whose friendship I came to value over the many years we interacted on a daily basis (I was such a consistent patron that if I did not show up to his food truck, he would ask me the next day if everything was ok). Perhaps the saddest day in my time at Caltech was the day Ernie retired, and I enjoyed his tacos for the last time.

I thank my parents Christine and Richard for supporting me all my life, and giving me a great deal of autonomy from an early age. I also thank the rest of my family for their support, including my sister Sarina, and my grandparents. I also thank my many close friends from high school, college, and graduate school.

Finally, I thank my wife Maiko, who puts up with my eccentric personality, inspires me every day, and always gives me something to look forward to.

ABSTRACT

Time domain surveys are revolutionizing our understanding of compact binary systems containing a white dwarf and another compact object at short orbital periods. These extreme binaries are astrophysical laboratories which can probe compact object physics, the nature of Type Ia supernova progenitors, accretion physics, tidal physics, the process of binary evolution, and they will dominate the population of objects the *Laser Interferometer Space Antenna* (*LISA*) will detect. In this thesis, I present substantial advances in the discovery and characterization of compact binaries using the Zwicky Transient Facility (ZTF). This work has resulted in a ten-fold increase in the discovery rate of such binaries compared to previous work in the field, and has helped lay the groundwork for discovering and characterizing these sources using other facilities, such as the the *Transiting Exoplanet Survey Satellite* (*TESS*), the upcoming Vera Rubin Observatory (VRO) and eventually *LISA* itself.

PUBLISHED CONTENT AND CONTRIBUTIONS

Burdge, K. B., M. W. Coughlin, J. Fuller, D. L. Kaplan, et al. (2020). "An 8.8 Minute Orbital Period Eclipsing Detached Double White Dwarf Binary". In: *ApJL* 905.1, p. L7. DOI: 10.3847/2041-8213/abca91. arXiv: 2010.03555 [astro-ph.SR].

Burdge, K. B., T. A. Prince, et al. (2020). "A Systematic Search of Zwicky Transient Facility Data for Ultracompact Binary LISA-detectable Gravitational-wave Sources". In: *ApJ* 905.1, p. 32. DOI: 10.3847/1538-4357/abc261. arXiv: 2009.02567 [astro-ph.SR].

Burdge, K. B., M. W. Coughlin, J. Fuller, T. Kupfer, et al. (2019). "General relativistic orbital decay in a seven-minute-orbital-period eclipsing binary system". In: *Nature* 571.7766, pp. 528–531. DOI: 10.1038/s41586-019-1403-0. arXiv: 1907.11291 [astro-ph.SR].

Burdge, K. B., J. Fuller, et al. (2019). "Orbital Decay in a 20 Minute Orbital Period Detached Binary with a Hydrogen-poor Low-mass White Dwarf". In: *ApJL* 886.1, p. L12. DOI: 10.3847/2041-8213/ab53e5. arXiv: 1910.11389 [astro-ph.SR].

In all publications included in this thesis (Chapters 2-5):

KBB discovered all but one object presented in this thesis (the exception, ZTF J2130+4420, was discovered by Zhuyun Zhuang as she was being mentored by KBB as an undergraduate researcher). KBB conducted all of the lightcurve and spectroscopic analyses, eclipse time analyses, and was the primary author of all manuscripts. KBB also collected the majority of the data presented in this thesis, and also reduced most of it.

TABLE OF CONTENTS

Acknowledgements v
Abstract viii
Published Content and Contributions ix
Table of Contents ix
Chapter I: Introduction and summary 1
1.1 Review of previous work 1
Chapter II: Orbital Decay in a 20-minute-orbital-period detached binary with a hydrogen-poor low-mass white dwarf 5
Abstract 6
2.1 Introduction 7
2.2 Observations 8
2.3 Analysis and results 12
2.4 Discussion 23
2.5 Conclusion 30
Chapter III: General relativistic orbital decay in a seven-minute-orbital-period eclipsing binary system 32
Abstract 33
3.1 Summary of Observations 44
3.2 Period Finding 44
3.3 Lightcurve Modelling 44
3.4 Orbital Decay 45
3.5 Spectroscopic Analysis 49
3.6 Mass and Radius Analysis 52
3.7 Distance Estimate 53
3.8 Gravitational Wave Strain 54
3.9 Tidal Effects 54
3.10 Binary Models 56
3.11 Constraint on Accretion 57
3.12 Novae 59
3.13 Population Implications 61
Chapter IV: An 8.8 minute orbital period eclipsing detached double white dwarf binary 63
Abstract 64

4.1 Introduction 65
4.2 Observations 66
4.3 Discovery and analysis 72
4.4 Discussion 82
4.5 Conclusion 87
Chapter V: A systematic search of Zwicky Transient Facility data for ultracompact binary *LISA*-detectable gravitational-wave sources 91
Abstract 92
5.1 Introduction 93
5.2 Methods 94
5.3 Analysis and Results 104
5.4 Discussion of individual systems 115
5.5 Discussion 124
5.6 Conclusion 134
5.7 Appendix 138
Chapter VI: Conclusions and future prospects 147
Bibliography 150

Chapter 1

INTRODUCTION AND SUMMARY

1.1 Review of previous work

Our understanding of ultracompact binaries (defined here as having an orbital period under an hour) has evolved enormously over the past five decades, and the number of known systems has increased substantially in the past few years. Here, I give a very brief overview of the field prior to the work presented in this thesis (I will be highlighting major discoveries and advancements which occurred from 1972-2018, which give context to the work presented in the remainder of this thesis). For an excellent review on the topic, please see Postnov and Yungelson, 2014. These extreme binaries are astrophysical laboratories which can be used to probe compact object physics, the nature of Type Ia supernova progenitors, accretion physics, tidal physics, the process of binary evolution, and they will dominate the population of objects detected by the *Laser Interferometer Space Antenna* (*LISA*).

AM CVns

The first class of ultracompact binaries discovered are the known as AM Canum Venaticorum stars, named after the prototype, AM CVn, an 18-minute orbital-period binary in which a carbon-oxygen core white dwarf is actively and stably accreting helium-rich matter from a degenerate donor. It is not surprising that these objects were discovered before their detached counterparts, as they are mass-transferring, and at short orbital periods (under 20 minutes) have a luminosity budget dominated by a permanently high-state helium-rich accretion disk, which vastly outshines either degenerate component, making them orders of magnitude brighter than detached systems at similar distances. The prototype, AM CVn, has an apparent magnitude of ~ 14 in Gaia G, making it the brightest ultracompact binary system known, as seen from Earth. AM CVn was first recognized as a photometrically periodic variable in 1967 (Smak, 1967), and Faulkner et al., 1972 was the first to correctly interpret this variability as an orbital period.

Since the recognition of AM CVn as an accreting double-degnerate binary by Faulkner et al., 1972, over 53 additional such objects were identified through 2018 (of which 43 had confirmed orbital periods under an hour), and their properties are excellently summarized in the review by Ramsay, Green, et al., 2018. One of the most important results of these additional discoveries, was the recognition that AM CVns appear to undergo a transition, with short period systems (orbital periods under $\sim$ 20 minutes) existing in a permanent high-state, in which they often exhibit optical periodicity, but do not exhibit outbursts, and longer period systems (orbital periods over $\sim$ 20 minutes), which spend much of their time with low-state accretion disks, undergo transient outbursts in which the disk transitions into a high-state. Many of the 53 AM CVns discovered between 1972 and 2018 (over two-thirds) are longer period systems which undergo outbursts, and do not exist in a permanent high-state. Selection bias is partially responsible for the over-abundance of such systems, as many were discovered as a result of searches for their outbursts (Levitan et al., 2015) or in spectroscopic campaigns (Ramsay, Green, et al., 2018), rather than searches based on photometric periodicity.

Direct impact accretors

There are two known accreting double-degenerate binaries in which matter is thought to directly impact on the surface of the accretor, rather than forming an accretion disk. The systems, HM Cancri ($P_b \approx 5.4$ min) and V407 Vulpeculae ($P_b \approx 9.5$ min), were both discovered as ROSAT X-ray sources, exhibiting strong periodicity in their X-ray emission on their orbital periods (Israel et al., 1999). The objects were originally mis-interpreted as intermediate polars (Haberl and Motch, 1995; Burwitz and Reinsch, 1999), and then as double degenerate polars (Cropper et al., 1998; Reinsch et al., 2000). Finally, their nature was correctly recognized by Marsh and Steeghs, 2002, and their mass transfer characteristics (and possible connection to AM CVn type binaries) was further explored in Marsh, Nelemans, et al., 2004. The conclusion of this work is that stably mass-transferring AM CVns may originate from double white dwarfs with sufficiently large mass ratios; however, recent work such as that presented in Shen, 2015 suggests that double white dwarfs may not at all be a progenitor channel for AM CVns, and that systems like HM Cnc and V407 Vul will ultimately merge (in the other two channels

they are thought to originate from hot subwarfs and evolved CV donors; for further discussion see Ramsay, Green, et al., 2018).

Detached double degnerates

Detached double degenerate systems have undergone a much more rapid evolution than their AM CVn counterparts. It was not until 1995 that a double white dwarf binary which would merge within a Hubble time was reported by Marsh, 1995, with an orbital period of 3.47 hours (prior to that, the only two close double degenerate binaries known had orbital periods of 1.56 and 1.18 days, as reported in Saffer et al., 1988; Bragaglia et al., 1990). Very quickly after the result of Marsh, 1995, Marsh, Dhillon, et al., 1995 reported several new systems that were discovered after the realization that He-Core WDs can only form via binary evolution. This success ultimately paved the way to the Extremely Low Mass White Dwarf (ELM) survey conducted in the 2010s (Brown, Kilic, Allende Prieto, and Kenyon, 2010; Kilic, Brown, Allende Prieto, Agüeros, et al., 2011; Brown, Kilic, Allende Prieto, and Kenyon, 2012; Kilic, Brown, Allende Prieto, Kenyon, et al., 2012; Brown, Kilic, Allende Prieto, Gianninas, et al., 2013; Gianninas, Kilic, et al., 2015; Brown, Gianninas, et al., 2016; Brown, Kilic, Allende Prieto, and Kenyon, 2012), which resulted in the discovery of 98 new detached double degenerate systems. This spectroscopic survey discovered over half of all known double degenerates, and the majority of the known systems which will interact within a Hubble time. Of the sample of systems reported by the ELM survey, only eight have orbital periods shorter than an hour, meaning that the vast majority have orbital frequencies too small for *LISA* to detect as gravitational wave sources.

Summary of the state of affairs circa 2018

In summary, as of 2018 the population of binary systems under an hour orbital period was dominated by AM CVn type systems, of which 43 were identified between 1972 and 2018. A more rare class of accreting double degenerate binary, direct impact accretors, manifested itself in the ROSAT era, with two systems identified in the late 1990s, whose nature was recognized in the early 2000s. No new direct impact accretor has been identified in the two decades since these discoveries. Finally, seven detached double degenerate binaries were known with orbital periods under an hour as of 2018, all

products of the ELM survey (with one additional one reported more recently in Brown, Kilic, Bédard, et al., 2020). Unfortunately, because of the low donor mass in the AM CVn systems, the majority of these systems lack the chirp mass needed to produce sufficient gravitational wave strain for a *LISA* detection, with only the most nearby systems (like the prototype AM CVn) reaching the needed strain threshold. Of the 43 AM CVns, 7 detached double degenerates, and 2 direct impact accretors with orbital periods under an hour, only 11 systems were predicted to be *LISA* detectable with an signal-to-noise ratio (SNR) greater than 20, with 2 additional systems having an SNR greater than 5, as reported in Kupfer, Korol, et al., 2018.

Then, in March 2018, the Zwicky Transient Facility began to operate, and the state of affairs evolved rapidly.

The contents of this thesis

This thesis documents the rapid progress in identifying new sub-hour orbital period binary systems using the Zwicky Transient Facility. As just discussed, prior to 2018, 52 such binary systems were known in total, of which the majority (43) were AM CVn type systems. Using ZTF, I have discovered twenty new binary systems with orbital periods under an hour in the span of 3 years, of which nine will be detectable by *LISA* with an SNR greater than 5. The selection method used in my work, which is based on searching for photometric periodicity, yielded no outbursting AM CVn systems (only high-state systems), a remarkable departure from the demographics of the AM CVn population reported in Ramsay, Green, et al., 2018. The detached double-degenerate systems consist in about equal parts double helium-core white dwarfs and carbon-oxygen core and helium core white dwarf pairs, in strong contrast to the population observed in the ELM survey (which only encompassed a single double helium-core white dwarf in a sample of 99 objects!). As discussed in Chapter 5, these departures from the populations observed in previous work can easily be accounted for in selection biases associated with photometric selections. The remainder of this thesis consists of four publications of work conducted between 2018-2020, including three noteworthy individual systems, and a paper documenting the full sample of objects as of mid-2020. In the conclusion, we mention the implications of several unpublished more recent discoveries.

Chapter 2

ORBITAL DECAY IN A 20-MINUTE-ORBITAL-PERIOD DETACHED BINARY WITH A HYDROGEN-POOR LOW-MASS WHITE DWARF

Burdge, K. B. et al. (2019). "Orbital Decay in a 20 Minute Orbital Period Detached Binary with a Hydrogen-poor Low-mass White Dwarf". In: *ApJL* 886.1, p. L12. DOI: 10.3847/2041-8213/ab53e5. arXiv: 1910.11389 [astro-ph.SR].

Kevin. B. Burdge[1], Jim Fuller[1], E. Sterl Phinney[1], Jan van Roestel[1], Antonio Claret[2,3], Elena Cukanovaite[4], Nicola Pietro Gentile Fusillo[4], Michael W. Coughlin[1], David L. Kaplan[5], Thomas Kupfer[6], Pier-Emmanuel Tremblay[4], Richard G. Dekany[7], Dmitry A. Duev[1], Michael Feeney[7], Reed Riddle[7], S. R. Kulkarni[1], Thomas A. Prince[1]

[1]Division of Physics, Mathematics and Astronomy, California Institute of Technology, Pasadena, CA 91125, USA
[2]Instituto de Astrofísica de Andalucía, CSIC, Apartado 3004, 18080 Granada, Spain
[3]Dept. Física Teórica y del Cosmos, Universidad de Granada, Campus de Fuentenueva s/n, 10871, Granada, Spain
[4]Department of Physics, University of Warwick, Coventry, CV4 7AL, UK
[5]Department of Physics, University of Wisconsin-Milwaukee, Milwaukee, WI, USA
[6]Kavli Institute for Theoretical Physics, University of California Santa-Barbara, Santa Barbara, CA, USA
[7]Caltech Optical Observatories, California Institute of Technology, Pasadena, CA, USA

ABSTRACT

We report the discovery of a detached double white dwarf binary with an orbital period of $\approx$ 20.6 minutes, PTF J053332.05+020911.6. The visible object in this binary, PTF J0533+0209B, is a $\approx 0.17\,M_{\odot}$ mass white dwarf with a helium-dominated atmosphere containing traces of hydrogen (DBA). This object exhibits ellipsoidal variations due to tidal deformation, and is the visible component in a single-lined spectroscopic binary with a velocity semi-amplitude of $K_B = 618.7 \pm 6.9\,km\,s^{-1}$. We have detected significant orbital decay due to the emission of gravitational radiation, and we expect that the *Laser Interferometer Space Antenna* (*LISA*) (Amaro-Seoane et al., 2017) will detect this system with a signal to noise of $8.4^{+4.2}_{-3.0}$ after four years of operation. Because this system already has a well determined orbital period, radial velocity semi-amplitude, temperature, atmospheric composition, surface gravity, and orbital decay rate, a *LISA* signal will help fully constrain the properties of this system by providing a direct measurement of its inclination. Thus, this binary demonstrates the synergy between electromagnetic and gravitational radiation for constraining the physical properties of an astrophysical object.

2.1 Introduction

After expanding into red giants at the end of their lives, most stars leave behind dense white dwarf remnants. Stars in binary systems can engulf their companions during this process and leave behind compact binaries with orbital periods of hours to days, and when this process occurs twice, it can produce double white dwarf binaries with orbital periods less than an hour (Ivanova et al., 2013). According to general relativity (Einstein, 1905), these binary systems emit gravitational radiation at twice their orbital frequency. Although few such gravitational wave sources are currently known (Kupfer, Korol, et al., 2018), the *Laser Interferometer Space Antenna* (*LISA*) should detect tens of thousands of systems within the galaxy (Nissanke et al., 2012, e.g.). This emission of gravitational radiation causes the orbits of these systems to decay, and can result in orbital periods as short as a few minutes.

The few known binary systems emitting gravitational radiation with sufficient strain for *LISA* to detect have been referred to as *LISA* “verification" binaries, as they will serve as tests that the detector is operating as expected; however, these binaries are rich probes of astrophysics which provide insight into binary evolution, the population of Type Ia progenitors, white dwarf physics, tidal physics, accretion physics, and are not simply sources which will “verify" *LISA*'s functionality. Most of the known *LISA* detectable binaries are mass transferring AM CVn systems (Kupfer, Korol, et al., 2018). These are strong *LISA* gravitational wave sources due to their short orbital periods; however, constraining their physical parameters is complicated by the accretion they undergo, which dominates their optical luminosity and determines their period evolution, thereby preventing the measurement of a chirp mass due to decay induced by gravitational wave emission. Detached eclipsing double white dwarf binaries, such as ZTF J153932.16+502738.8 (Burdge, Coughlin, et al., 2019) and SDSS J065133.338+284423.37 (Brown, Kilic, Hermes, et al., 2011) are the best characterized *LISA* gravitational-wave sources known, with precisely measured system parameters; however, currently only these two systems have been characterized with such precision.

We report the discovery of PTF J053332.05+020911.6 (hereafter referred to as PTF J0533+0209), a detached double white dwarf binary system with an orbital period of $1233.97298 \pm 0.00017\,s$. In this binary, there is only one visible component in the

optical spectrum, and thus, this system is a single-lined spectroscopic binary. The system exhibits relativistic Doppler beaming, ellipsoidal modulation, and orbital decay due to the emission of gravitational radiation. We will refer to the unseen massive companion in this binary as PTF J0533+0209A, and the lower mass, tidally deformed, visible component of this binary as PTF J0533+0209B. In this paper, we report our measurements of the observable quantities of this system and present the physical parameters we infer from these (Table 1). We conclude by discussing the future study of detached, non-eclipsing systems like PTF J0533+0209 in the era of *LISA*.

2.2 Observations

Table 2.1: Table of observed parameters

Gaia	RA	$83.383588013\,deg \pm 0.34\,mas$
Gaia	Dec	$+2.153208645\,deg \pm 0.33\,mas$
Gaia	Parallax	$0.47 \pm 0.48\,mas$
Gaia	pm RA	$1.43 \pm 0.74\,mas\,yr^{-1}$
Gaia	pm Dec	$2.56 \pm 0.91\,mas\,yr^{-1}$
GALEX	NUV	$20.38 \pm 0.28\,m_{AB}$
Pan-STARRS	g	$19.00 \pm 0.02\,m_{AB}$
Pan-STARRS	r	$19.15 \pm 0.01\,m_{AB}$
Pan-STARRS	i	$19.40 \pm 0.01\,m_{AB}$
Pan-STARRS	z	$19.60 \pm 0.03\,m_{AB}$
Pan-STARRS	y	$19.61 \pm 0.06\,m_{AB}$

Photometric color selection

We discovered PTF J0533+0209 during a broad search for post-common envelope binaries (Ivanova et al., 2013). In order to target hot young remnants of the common envelope phase, we used the Pan-STARRS DR1 (Chambers et al., 2016) photometric survey to target blue objects, selecting all objects with a color satisfying the condition $(g - r) < 0$ (see Table 1–note that the values in the table are observed apparent magnitudes, and have not been de-reddened).

PTF photometry

After imposing the photometric color cut, we cross-matched the resulting sample with the archival Palomar Transient Factory (PTF) (Law et al., 2009) photometric database. The Palomar Transient Factory (and the Intermediate Palomar Transient Factory) was a northern-sky synoptic survey using the 48-inch Samuel Oschin Telescope at Palomar Observatory. The survey was conducted in PTF r and g bands with a typical exposure time of $60\,s$, resulting in limiting magnitudes of approximately 21 and 20, respectively. We restricted ourselves to a search in r band because it is the most heavily sampled of the PTF bands. Additionally, we required a minimum of 20 epochs in the lightcurves. This cross match yielded $\approx 180,000$ sources. We discovered PTF J0533+0209 via a period search. We detected the object with high significance because it falls in the most heavily sampled field in all of PTF, located inside the constellation of Orion, which was observed over 5000 times, primarily in the first two years of PTF. This field did not use the typical PTF exposure time of $60\,s$, but instead used $30\,s$ exposures. These observations were taken in two brief intervals, one consisting of ≈ 3000 observations in Dec 2009-Jan 2010, and another in Dec 2010 with ≈ 2000 observations (Table 5.7).

High-speed photometry

We used the high-speed photometer on 200-inch Hale telescope at Palomar Observatory, CHIMERA (Harding et al., 2016), to obtain a well-sampled follow-up lightcurve of the object. The instrument consists of a pair of electron-multiplying charge-coupled devices (EM CCDs), and has a dichroic and dual channels, allowing us to obtain simultaneous observations in g' and i'. We used $10\,s$ exposures for all observations operating with the conventional amplifier, and these lightcurves served as the basis for our analysis of the ellipsoidal modulation and relativistic Doppler beaming exhibited by the visible component in the system (Figure 2.1).

Additionally, we used the Kitt Peak Electron Multiplying CCD demonstrator (KPED) (Coughlin, Dekany, et al., 2019), a high-speed EM CCD photometer mounted on Kitt Peak National Observatory's 84-inch telescope, to obtain additional observations to use as timing epochs (in order to measure the orbital decay). We obtained observations in g'. Unlike our CHIMERA observations, we operated KPED with electron multiplying

gain enabled, effectively eliminating read noise. The detector acquired images at a rate of 8 Hz, which we then stacked to 10 s coadditions in order to match the exposure time used with CHIMERA. Table 5.7 gives a summary of these observations.

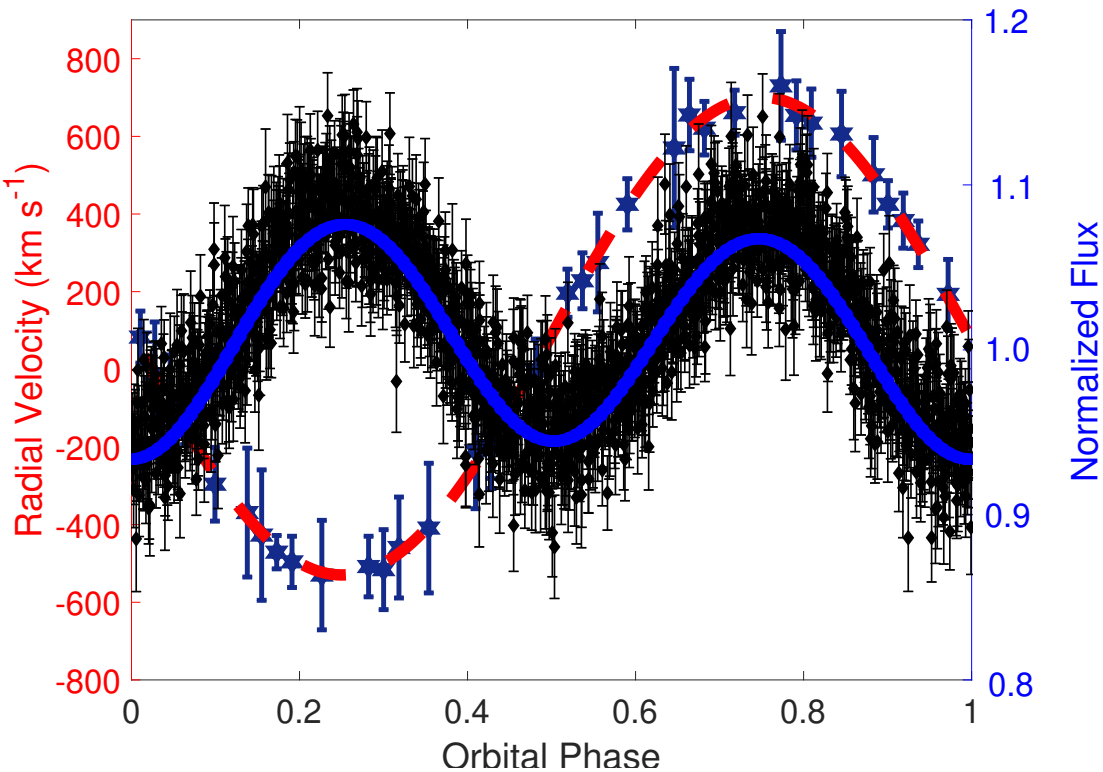

Figure 2.1: Light curve model (solid blue line) overplotted with g' phase folded CHIMERA lightcurve, and radial velocity curve derived from LRIS spectra (dashed red line). The CHIMERA lightcurve exhibits ellipsoidal modulation, a geometric effect in which the brightness of the binary is modulated at twice the orbital frequency due to the tidal deformation of one object. The CHIMERA lightcurve also exhibits relativistic Doppler beaming manifested in the maximum at the phase of highest blueshift (Orbital Phase 0.25) being a few percent higher in relative flux than the phase of maximum redshift (Orbital Phase 0.75). A sinusoidal fit to the radial velocity curve yields a semi-amplitude of $K = 618.7 \pm 6.9\, km\, s^{-1}$.

All photometric data were reduced using a custom pipeline.

Table 2.2: Table of observations

Table 2.3:

Instrument	Filter	Date	# of Exposures	Exposure Time
PTF	PTF r	Dec 4 2009-Jan 15 2010	3020	30s
PTF	PTF r	Dec 9-15 2010	1775	30s
CHIMERA	g'	Dec 14 2017	1600	10s
CHIMERA	i'	Dec 14 2017	1600	10s
CHIMERA	g'	Dec 15 2017	1000	10s
CHIMERA	i'	Dec 15 2017	1000	10s
CHIMERA	g'	Sept 17 2018	700	10s
CHIMERA	i'	Sept 17 2018	700	10s
CHIMERA	g'	Sept 18 2018	700	10s
CHIMERA	i'	Sept 18 2018	700	10s
CHIMERA	g'	Dec 31 2018	719	10s
CHIMERA	i'	Dec 31 2018	719	10s
KPED	g'	Sept 8 2018	716 (stacked)	10s (stacked)
KPED	g'	Sept 9 2018	804 (stacked)	10s (stacked)
KPED	g'	Sept 10 2018	737 (stacked)	10s (stacked)
KPED	g'	Sept 11 2018	206 (stacked)	10s (stacked)
KPED	g'	Sept 16 2018	707 (stacked)	10s (stacked)
KPED	g'	Sept 17 2018	759 (stacked)	10s (stacked)
KPED	g'	Dec 9 2018	1546 (stacked)	10s (stacked)
KPED	g'	Dec 10 2018	236 (stacked)	10s (stacked)
KPED	g'	Feb 26 2019	706 (stacked)	10s (stacked)
KPED	g'	Mar 23 2019	668 (stacked)	10s (stacked)
KPED	g'	Mar 29 2019	490 (stacked)	10s (stacked)
KPED	g'	Mar 31 2019	344 (stacked)	10s (stacked)
KPED	g'	Apr 2 2019	204 (stacked)	10s (stacked)
LRIS	Blue Arm	Nov 15 2017	18	120s
LRIS	Blue Arm	Mar 19 2018	40	120s

Spectroscopy

On October 25, 2017, we observed the object on the Hale Telescope with four consecutive 5-minute exposures using the Double Spectrograph (Oke and Gunn, 1982). While these spectra have low signal to noise (SNR), they nonetheless reveal the presence of large Doppler shifts on the order of several hundred km s^{-1}. We reduced this data using the pyraf-dbsp reduction pipeline (Bellm and Sesar, 2016).

We then obtained an additional fifty-eight 2-minute exposures using the Low Resolution Imaging Spectrometer (LRIS) (Oke, Cohen, et al., 1995) on the 10-m W. M. Keck I Telescope on Mauna Kea, with the 400/8500 grism and a 2x2 binning on the blue arm. Eighteen of these exposures were obtained on Nov 15, 2017 and the remaining forty on March 19th, 2018. These exposures were sufficiently short to allow us to create a time resolved radial velocity curve (Figure 2.1) and also assemble a co-added spectrum for atmospheric fitting with minimal broadening of the features from the Doppler shifts (Figure 2.2). In individual exposures, we averaged an SNR of 4-5, with a wavelength coverage from 3400-5600 angstroms, and a resolution of approximately $\frac{\lambda}{\Delta\lambda} = 700$. In order to ensure wavelength stability, we took a HeNeArCdZn arc at the telescope position of the object. For both nights, we used five consecutive dome flats and five bias frames to perform calibrations, and reduced the data using the lpipe pipeline (Perley, 2019).

2.3 Analysis and results

Discovery

We discovered the PTF J0533+0209 by applying the multi-harmonic analysis of variance (MHAOV) period finding routine to the sample of color-selected lightcurves (Schwarzenberg-Czerny, 1996), searching periods from 7.2 minutes to 1000 days. PTF J0533+0209 exhibits strong ellipsoidal modulation in its PTF lightcurve (Figure 2.4), and thus exhibits significant power at half the orbital period in its power spectrum (Figure 4.2). We used MHAOV because of its superior sensitivity to sharp non-sinusoidal periodic features such as eclipses while still remaining sensitive to sinusoidal lightcurves such as that of PTF J0533+0209. We used the implementation of MHAOV available in the Vartools package (Hartman and Bakos, 2016). In the initial search for periodic objects, we use heliocentric Julian dates as timestamps. However, all timestamps in this

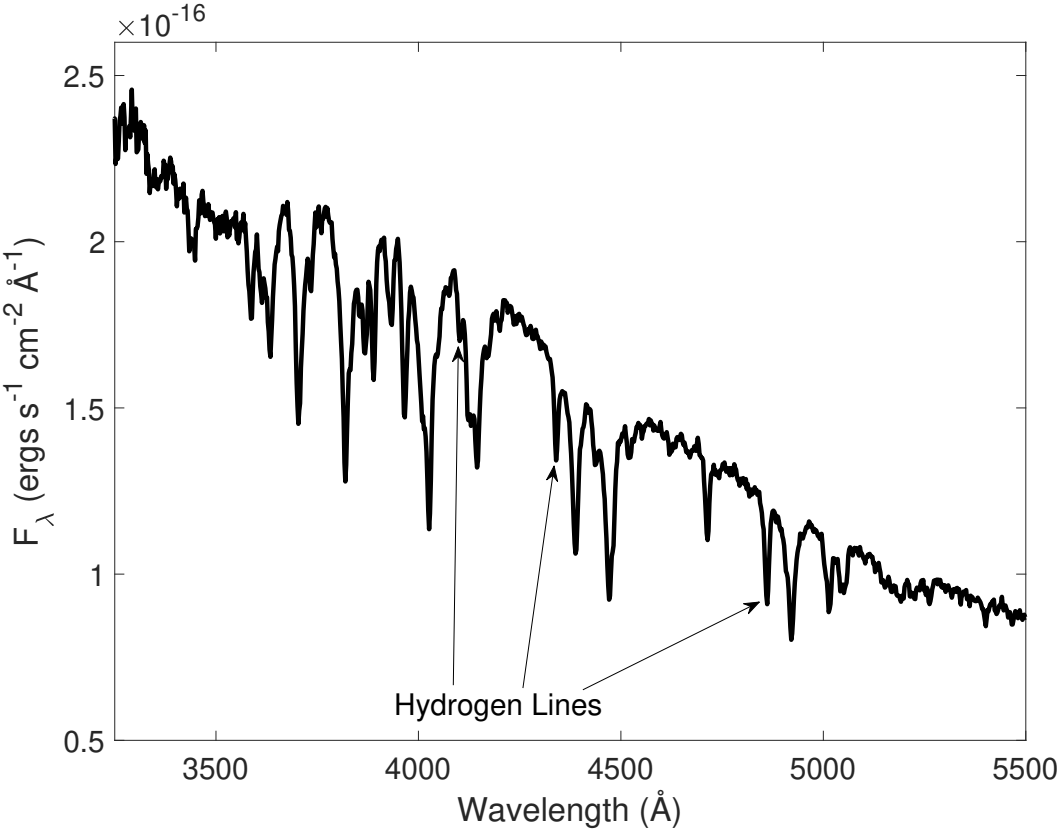

Figure 2.2: The coadded LRIS spectrum of the PTF J0533+0209B. We have labelled the hydrogen absorption lines. All other prominent absorption features are He I lines.

publication have been corrected to mid-exposure barycentric Julian dates.

Orbital dynamics

We measured the Doppler shift of the absorption lines in each time-resolved spectrum by fitting the centroids of the Hydrogen Balmer lines of H_β and H_γ, as well as the neutral helium lines at wavelengths of 4471, 4713, and 4921 Å. All of these lines belong to PTF J0533+0209B. We derived the velocity semi-amplitude of PTF J0533+0209B, K_B, by performing a weighted least squares fit of a sinusoid to the combined RV data, with a fixed ω corresponding to the orbital period derived from the PTF data. We

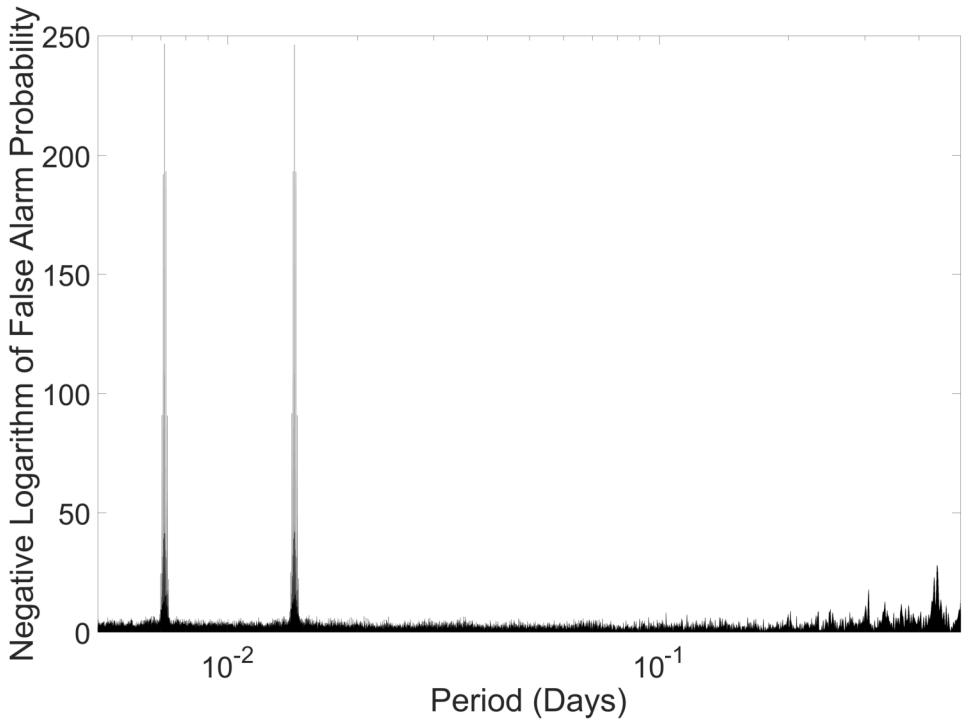

Figure 2.3: A power spectrum of PTF J0533+0209 generated using a multiharmonic analysis of variance routine. The spectrum clearly illustrates two strong signals, one corresponding to half of the orbital period (due to the ellipsoidal modulation), and another strong feature at the orbital period, due to Doppler beaming and gravity darkening. Note that the Y axis is in units of the negative logarithm of the formal false alarm probability reported by the algorithm, which is defined as the probability of a signal with no periodic component at this frequency, producing a feature of this amplitude in the power spectrum (VanderPlas, 2018). The feature seen at long periods occurs near 0.5 days, and is likely due to the sidereal day.

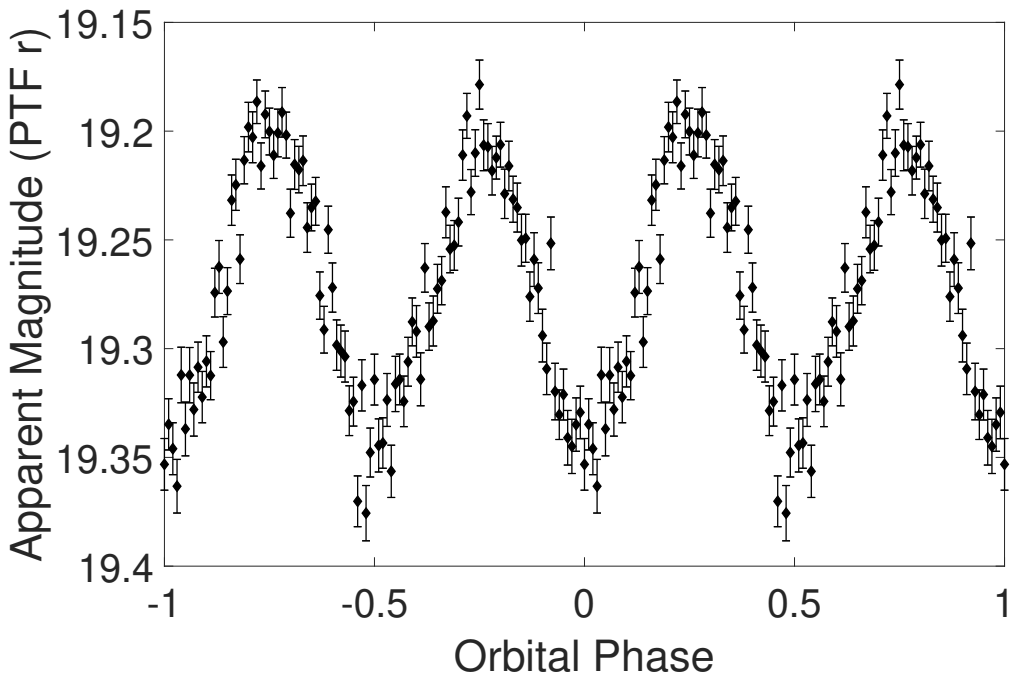

Figure 2.4: The phase-folded binned PTF r band lightcurve of PTF J0533+0209, illustrating the strong ellipsoidal modulation which enabled the detection of the source via its optical periodicity.

derive a velocity semi-amplitude of $K_B = 618.7 \pm 6.9$ km s^{-1} and a systemic velocity of $\gamma = 76.0 \pm 4.3$km s^{-1}, where we have obtained the 1 sigma error bars from the covariance matrix of the least squared fit to the time-resolved radial velocity measurements. The mass function of PTF J0533+0209A is given by:

$$\frac{M_A^3 \sin^3(i)}{(M_A + M_B)^2} = \frac{PK_B^3}{2\pi G}, \tag{2.1}$$

where M_A is the mass of PTF J0533+0209A, M_B is the mass of PTF J0533+0209B, i is the orbital inclination, and G is the gravitational constant.

Thus, using Equation 5.2, we can constrain the relationship between the physical parameters of interest in the left hand side of the equation with the measured P and K_B.

Atmospheric Fitting

We calculated a grid of DBA (helium-dominated with traces of hydrogen) white dwarf atmosphere models to fit the spectra of PTF J0533+0209B (we found no evidence of any spectroscopic features associated with PTF J0533+0209A). The grid spans the effective temperature range of $11\,000 \leq T_{eff} \leq 30\,000$ K in steps of 1 000 K, the surface gravity range of $5.5 \leq \log g \leq 9.0$ in steps of 0.5 dex and the hydrogen-to-helium number density ratio of $-1.0 \leq \log H/He \leq -10.0$ in steps of 0.5 dex. A detailed description of the model atmosphere code can be found in Bergeron et al., 2011.

Analogous to the well-established spectroscopic method used for DA white dwarfs, we compared the absorption line profiles of the continuum-normalized spectrum of PTF J0533+0209B with our newly computed models. In our fit we included a E(B-V) reddening of 0.13 and assumed an extinction constant $A_V = 3.1$ (Green, Schlafly, et al., 2019).

The best-fit model solution corresponds to $T_{eff} = 20\,000 \pm 800$ K, $\log g = 6.3 \pm 0.1$, and $\log H/He = -2.7 \pm 0.1$ (Figure 2.5). For limb- and gravity-darkening coefficients, an additional grid of atmosphere models was computed for $\log H/He = -2.56$, $19\,250 \leq T_{eff} \leq 20\,500$ K in steps of 250K and $5.4 \leq \log g \leq 7.2$ in steps of 0.6 dex. For each model we calculated the specific intensity at 20 different angles.

Lightcurve Modelling

Because this binary exhibits significant ellipsoidal modulation, we can impose constraints on the system parameters by modelling its lightcurve. We see ellipsoidal variations in the lightcurve because PTF J0533+0209B is being tidally deformed, and over the course of the orbit, we see different geometric cross sections of the object. Equation 5.1 gives the fractional flux variation due to ellipsoidal modulation:

$$\frac{\Delta F_{ellipsoidal}}{F} = 0.15 \frac{(15+u)(1+\tau)}{3-u} \left(\frac{R}{a}\right)^3 q \sin^2 i, \tag{2.2}$$

where the fractional flux variation due to ellipsoidal variations, $\frac{\Delta F_{ellipsoidal}}{F}$ depends on the ratio of the radius of the tidally deformed object to the semi-major axis, R/a, the

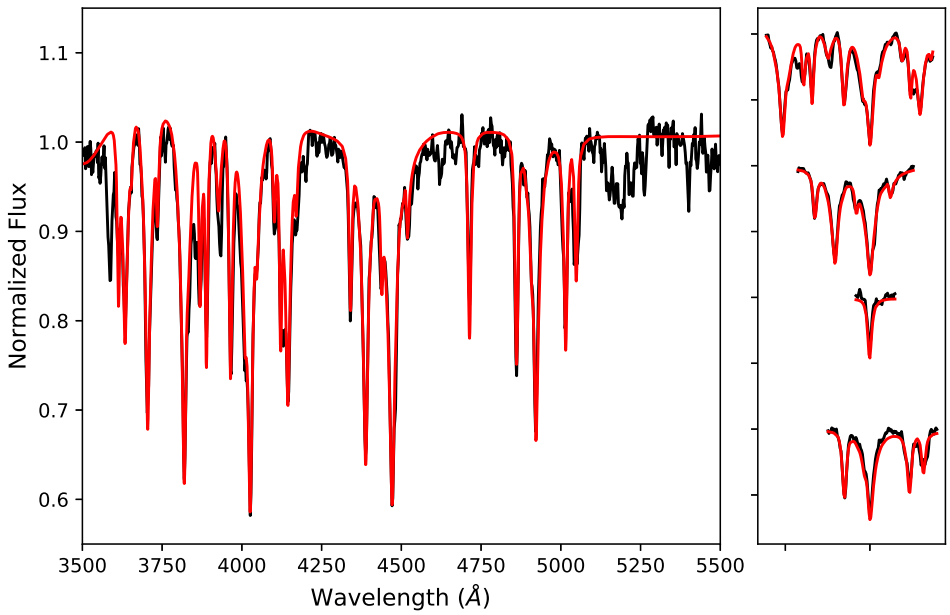

Figure 2.5: The normalized coadded LRIS spectrum of the object is shown in black. In red, we have overlplotted the best-fit DBA atmospheric model. The four right-hand panels illustrate zoomed-in plots of the atmospheric fit to the absorption lines.

tidally deformed component's linear limb darkening coefficient u, its gravity darkening coefficient τ, the mass ratio of the binary q, and the inclination i (Bloemen et al., 2012).

Because this object is strongly deformed, we must also account for an additional effect known as gravity darkening, which visibly manifests itself as an asymmetry in the two flux minima of the ellipsoidal modulation. This is a result of the flux emitted on the surface of the deformed object near the first Langrange point (L1) being less than that emitted from the surface near the L2 point. Von Zeipel's theorem (von Zeipel, 1924) states that the flux emitted off of the surface element of a star is proportional to the local gravitational field. Although the material at the surface of a tidally deformed star falls on a gravitational equipotential surface $\phi = const$, the gradient of the gravitational potential along this surface is not necessarily constant or symmetric, i.e., $-\nabla\phi = g \neq const$, and

this is manifested by an asymmetry between the flux emitted by surface elements at L1 and L2.

We used the ellc package to model the lightcurve (Maxted, 2016). We modelled both the g' and i' lightcurves, adopting a linear limb darkening model, and fixing the linear limb darkening coefficient of the secondary u_2 to a value of 0.25 for the g' lightcurve, and to 0.18 for the i' lightcurve. We also fixed the passband dependent gravity darkening coefficient of the secondary, τ_2, to 0.25 for the g' lightcurve, and 0.19 for the i' lightcurve. These coefficients were computed using the procedure outlined in Claret, 2017, adjusted for DBA atmospheres (Claret, Cukanovaite & Burdge 2019, in preparation). We computed and fixed the Doppler beaming factors of PTF J0533+0209B to 1.94 for g' and 1.54 for i' (Loeb and Gaudi, 2003) using the atmospherically derived temperature of $T_{eff} = 20000\,K$. The free parameters in the model were the ratio of the radii to the semi-major axis for the two components, R_A/a and R_B/a, the inclination i, the time of minimum light t_0, the semi-major axis a, and the mass ratio $q = M_B/M_A$. Although we see no sign of luminosity from PTF J0533+0209A in the spectrum or the spectral energy distribution, as an initial test, we conducted an iteration of modelling with the surface brightness ratio, J, and albedo of PTF J0533+0209B, $heat_B$, as free parameters to investigate whether PTF J0533+0209B might be irradiated by its unseen companion. We found the solution did not converge to any particular value of these parameters for the g' or i' lightcurves, and that the parameters exhibited no co-variance with any other parameters. We performed the same exercise considering the possibility of PTF J0533+0209A being irradiated by PTF J0533+0209B, and found a similar result. Based on this, for the final iteration of modelling, we assumed no luminosity contribution from PTF J0533+0209A, and omitted accounting for any kind of irradiation effect. The faint GALEX NUV apparent magnitude (see Table 2.1) also suggests it is unlikely that there is an unseen hot companion.

Orbital Period Decay

Because of the short orbital period and non-interacting nature of this system, we expect a possible measurable orbital decay due to the emission of gravitational radiation (Taylor, Fowler, et al., 1979). One can determine the orbital frequency derivative, $\dot{f}$, by measuring

a change in the phase of the lightcurve over time, $\Delta t_{ellipsoidal}$, as illustrated in Equation 3.1:

$$\Delta t_{ellipsoidal}(t - t_0) = \left(\frac{1}{2}\dot{f}(t_0)(t - t_0)^2 + ...\right)P(t_0), \tag{2.3}$$

where t_0 is the reference epoch, $t - t_0$ is the time since the reference epoch, $f(t_0)$, $\dot{f}(t_0)$, etc, are the orbital frequency and its derivatives at the reference epoch, and $P(t_0) = \frac{1}{f(t_0)}$ is the orbital period at the reference epoch.

In order to extract the timing epochs from PTF, KPED, and CHIMERA data, we used a least squares fit of a sinusoid to the data and measured the phase of this sinusoid. We then used a least squares fit of a quadratic to these time stamps as a function of epoch (Figure 4.6) to measure the orbital decay rate, $\dot{P}$. We report the derived ephemeris in Table 4.3.

If purely due to general relativity, the decay should be governed by the expression given in Equation 5.4:

$$\dot{f}_{GW} = \frac{96}{5}\pi^{\frac{8}{3}}\left(\frac{GM_c}{c^3}\right)^{\frac{5}{3}} f_{GW}^{\frac{11}{3}}, \tag{2.4}$$

where $M_c = \frac{(M_1 M_2)^{\frac{3}{5}}}{(M_1+M_2)^{\frac{1}{5}}}$ is the chirp mass, c is the speed of light, and $f_{GW} = \frac{2}{P}$ is the gravitational wave frequency. Thus, we can use the measured decay rate to constrain the chirp mass of the system. Such decay has been observed in several known detached double degenerate systems, including ZTF J1539+5027 (Burdge, Coughlin, et al., 2019) and SDSS J0651+2824 (Brown, Kilic, Hermes, et al., 2011), as well as some accreting systems such as HM Cancri (Strohmayer, 2005).

Tidal Contribution to Orbital Decay

Equation 2.5 gives an estimate for tidal contribution to the measured orbital decay:

$$\frac{\dot{P}_{tide}}{\dot{P}_{GW}} \simeq \frac{3(M_A + M_B)}{M_A M_B}\left[\kappa_A M_A\left(\frac{R_A}{a}\right)^2 + \kappa_A M_2\left(\frac{R_B}{a}\right)^2\right], \tag{2.5}$$

where $\dot{P}_{tide}$ is the tidal contribution to the orbital decay, expressed as a fraction of the contribution to orbital decay from the emission of gravitational radiation, $\dot{P}_{GW}$, which is a function of the ratio of the radii to the semi-major axis of the two components, the

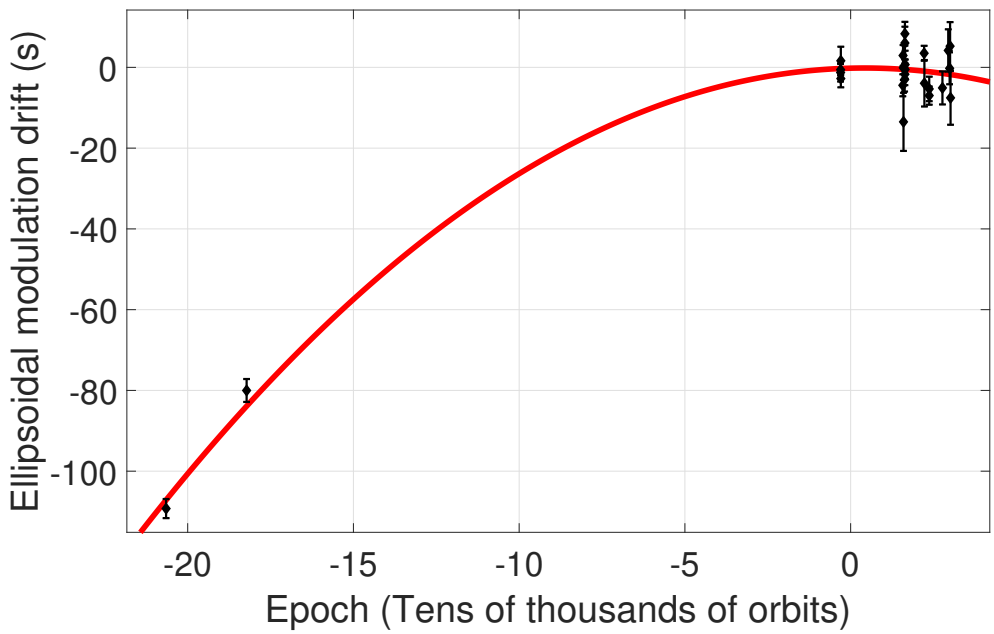

Figure 2.6: The measured drift of the ellipsoidal modulation of PTF J0533+0209 over time. The two initial points, both originating from Palomar Transient Factory data acquired nearly a decade before the other epochs, illustrates that this signal has shifted in phase by over $100s$ since these observations, consistent with the expectations of orbital decay via gravitational radiation.

component masses, and also κ_a and κ_b, dimensionless constants reflecting the internal structure of the white dwarf (Burdge, Coughlin, et al., 2019).

Using the masses derived from the combined analysis, as well as $\kappa_a = 0.14$ and $\kappa_b = 0.066$ based on white dwarf models, we estimate a tidal contribution of $\frac{\dot{P}_{tide}}{\dot{P}_{GW}} \simeq 0.02$. We correct the chirp mass inferred from $\dot{P}$ by accounting for this tidal contribution, though it does not significantly alter the solution, as it is less than a sixth of the measurement uncertainty on $\dot{P}$. As the measurement of $\dot{P}$ improves with time, the tidal contribution will become large compared to the measurement uncertainty, and will become the dominant source of uncertainty on the chirp mass.

Parameter Estimation

In order to estimate the physical parameters of the system, we combined the measurements of orbital kinematics and orbital period decay with the lightcurve models fit to the CHIMERA g' and i' data taken on December 14-15 of 2017. The atmospheric fit parameters only entered this modelling as a basis for deriving the limb and gravity darkening coefficients used in the lightcurve modelling. The free parameters of this analysis were the masses M_A and M_B, the inclination i, the radius R_B, and the time of minimum light t_0. We used the multinest algorithm (Feroz et al., 2009) to sample over these free parameters, and present the corner plots of the resulting analysis in Figure 4.5. The inferred parameters from this analysis, as well as the atmospheric analysis and timing analysis, are listed in Table 4.3.

Table 4: Table of physical parameters

M_A	$0.652^{+0.037}_{-0.040}\,M_\odot$
M_B	$0.167^{+0.030}_{-0.030}\,M_\odot$
i	$72.8^{+0.8}_{-1.4}\,degrees$
R_B	$0.057^{+0.004}_{-0.004}\,R_\odot$
T_B	$20000^{+800}_{-800}\,K$
$log(g)_B$	$6.3^{+0.1}_{-0.1}$
$\log H/He_B$	$-2.7^{+0.1}_{-0.1}$
T_0	$2458145.096848^{+0.000046}_{-0.000046}\,BJD_{TDB}$
$P(T_0)$	$1233.97298^{+0.00017}_{-0.00017}\,s$
$\dot{P}(T_0)$	$(-3.94 \pm 0.80) \times 10^{-12}\,s\,s^{-1}$

Distance Estimate

PTF J0533+0209 has a corresponding entry in the Gaia DR2 catalog (Gaia Collaboration, 2018), with a measured parallax of $\bar{\omega} = 0.4741$ and uncertainty $\sigma_{\bar{\omega}} = 0.4786$. Since we are in a regime where $\sigma_{\bar{\omega}} > \bar{\omega}$, we cannot simply infer the distance as the reciprocal of the parallax. We adopt an exponentially decreasing space density prior (Bailer-Jones et al., 2018), with an assumed characteristic length scale of 400 pc (Kupfer, Korol, et al., 2018). Using this technique, we infer a distance of $D = 1.5^{+0.7}_{-0.5}\,kpc$, and we adopt this distance for our estimate of the *LISA* gravitational wave strain of the system. If we assume a length scale of 200 pc, the solution becomes $D = 1.05^{+0.4}_{-0.3}\,kpc$, and for a

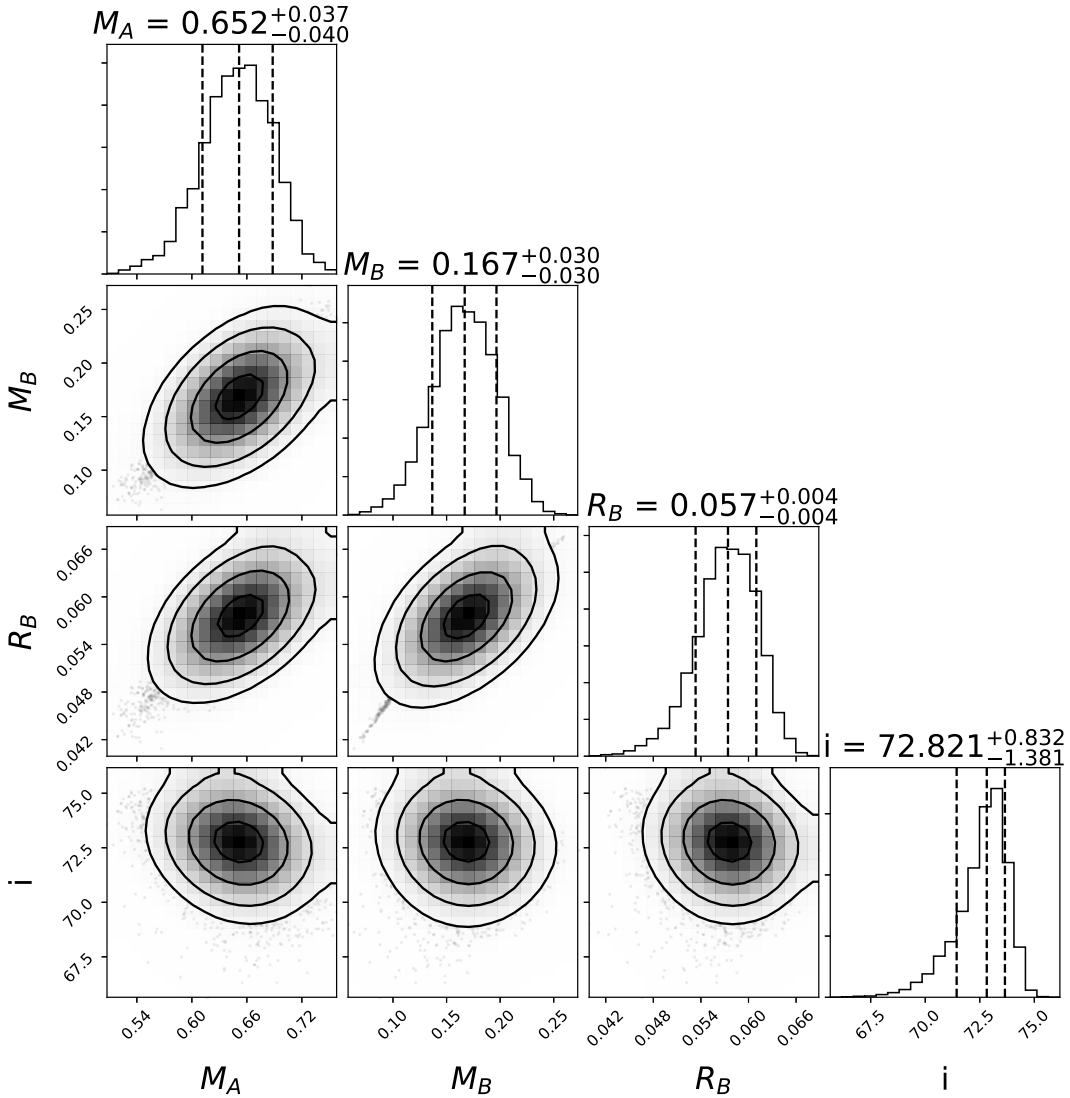

Figure 2.7: Corner plots of the physical parameters inferred as a result of the analysis combining the lightcurve modelling with radial velocity and chirp mass constraints.

length scale of 800 pc, $D = 2.3^{+1.4}_{-0.9}\,kpc$. We would like to note that using our inferred radius and temperature, we estimate a distance of $D = 2.7^{+0.2}_{-0.2}\,kpc$, farther than any of these estimates.

Gravitational Wave Strain

To calculate the characteristic strain (Korol, Rossi, Groot, et al., 2017), S_c, we use the expression in Equation 5.5, where c is the speed of light, and T_{obs} is the operation time of the *LISA* mission.

$$S_c = \frac{2(GM_c)^{5/3}(\pi f)^{2/3}}{c^4 D}\sqrt{fT_{obs}}, \tag{2.6}$$

When computing the characteristic strain, we marginalized over the posterior distributions for the masses derived from our combined analysis, and the distance estimated using the parallax measurement and the assumption of a 400 pc length scale. The point and uncertainties corresponding to PTF J0533+0209 in Figure 5.9 reflects the posterior distribution of the characteristic strain of this object.

However, in order to compute the estimated SNR of the source in *LISA*, we must account for instrument response, as well as the source position in the sky, and the source inclination. Thus, to compute the SNR, we calculate the amplitude of the signal at the detector, $A = \sqrt{|F_+|^2|h_+|^2 + |F_\times|^2|h_\times|^2}$, which depends on the two gravitational wave polarizations, h_+ and $h_\times$, and *LISA*'s response patterns in coupling to these polarizations, F_+ and $F_\times$ (Korol, Rossi, Groot, et al., 2017).

2.4 Discussion

LISA gravitational wave source

Based on its component masses, inclination, and distance of $D = 1.5^{+0.7}_{-0.5}\,kpc$ based on the parallax measurement and 400 pc length scale, we estimate that *LISA* will detect PTF J0533+0209 with a signal to noise ratio of $8.4^{+4.2}_{-3.0}$ at the end of the nominal four-year mission lifetime (Figure 5.9). If we instead use the distance of $D = 2.7^{+0.2}_{-0.2}\,kpc$ inferred from the radius, temperature, and apparent magnitude of the object, the estimated signal to noise after four years is $4.7^{+0.9}_{-0.9}$. By the launch of *LISA* in 2034, we estimate that the orbital decay of PTF J0533+0209 will have caused the ellipsoidal modulation to have drifted by $> 900s$ in phase since the initial PTF epochs, allowing for a precise

constraint on the chirp mass with regular monitoring over this time period. With the chirp mass constrained, the strain measured by *LISA* will enable a direct probe of the distance to the object, helping verify the estimates of radius and surface temperature in this analysis . Perhaps the best example of *LISA*'s utility is that it will be able to provide an independent measurement of the inclination angle of the system (Shah, van der Sluys, et al., 2012). This is because the gravitational wave signal can be decomposed into two polarization components, h_+ and $h_\times$, and the strain amplitudes of these components include factors of $\left(1 + \cos^2(i)\right)$ and $2\cos(i)$, respectively (Thorne, 1987). Combined with the measurements of K_B, and $\dot{P}$, this will provide a constraint on both component masses independent of the model-dependent fit of the ellipsoidal modulation.

Binary Formation Models

PTF J0533+0209 provides interesting constraints on compact binary formation physics. In particular, the combination of the extremely low-mass white dwarf (ELM WD), high surface temperature, and low surface hydrogen (H) abundance is difficult to understand, since most ELM WDs are H-rich (DA) WDs due to helium (He) sedimentation. H-deficient CO WDs, such as DB WDs, are thought to originate from AGB stars undergoing a late He-burning shell flash during the early WD cooling phase. The shell flash induces convection that subsumes the H-envelope, mixing H deep into the star where it is quickly burnt (Althaus, Serenelli, et al., 2005). However, the He-core ELM WD in PTF J0533+0209 could not have undergone such a He-burning pulse, so the H could not be destroyed in the same way that it is for DB WDs. Nor is it likely the H has been totally stripped due to mass transfer like in AM CVn systems, because there is no reason to think that mass transfer has yet begun in this system. Several H-poor proto-ELM WDs have been discovered (see e.g., Kaplan, Bhalerao, et al. 2013; Gianninas, Curd, et al. 2016), though these have higher H-abundances and low surface gravities, and can likely be explained by weaker gravitational settling opposed by rotational mixing Istrate et al., 2016.

To understand the formation of PTF J0533+0209, we constructed models of binary stars using the MESA stellar evolution code (Paxton, Bildsten, et al., 2011; Paxton, Cantiello, et al., 2013; Paxton, Marchant, et al., 2015). First, we evolve a $1.2\,M_\odot$ star up the red

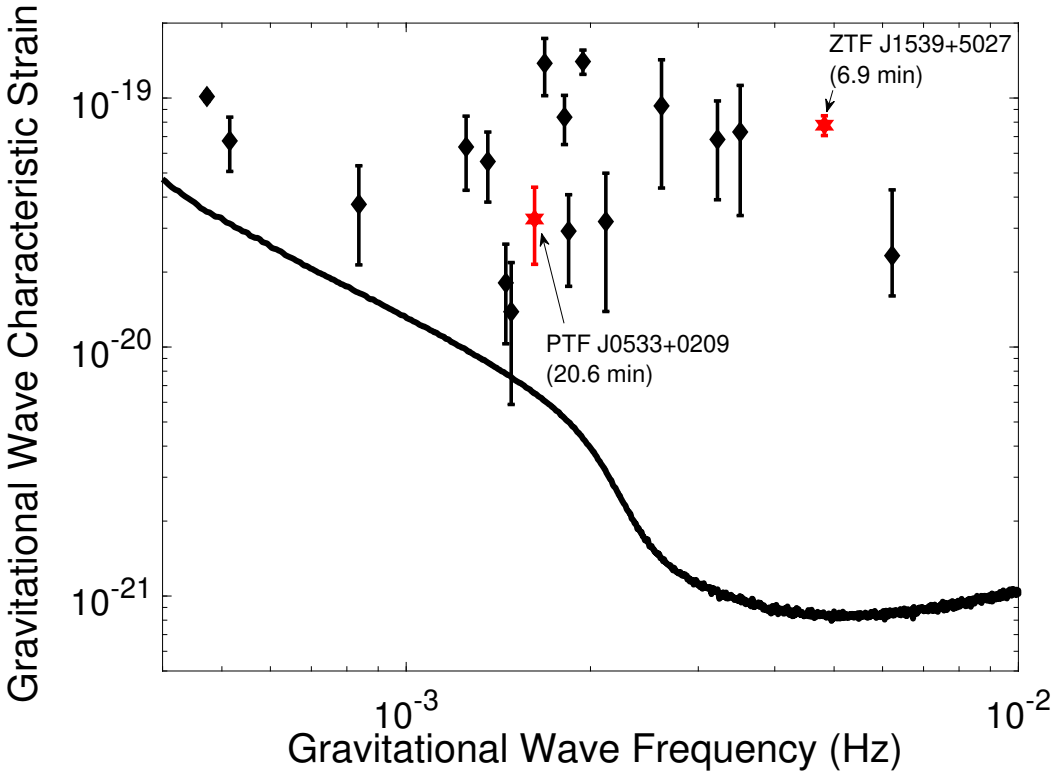

Figure 2.8: A plot of the characteristic gravitational wave strains of the known *LISA* detectable binaries after 4 years of integration and the *LISA* sensitivity curve (shown as the smooth black curve). The black diamonds are sources reported in Kupfer, Korol, et al., 2018, whose errors have been estimated using Gaia parallaxes, with the exception of HM Cancri, which we assigned a uniform prior in distance of 4.2-20 kpc. The red stars indicate the two *LISA* gravitational wave sources discovered in the recent survey for *LISA* sources using PTF/ZTF (Burdge, Coughlin, et al., 2019).

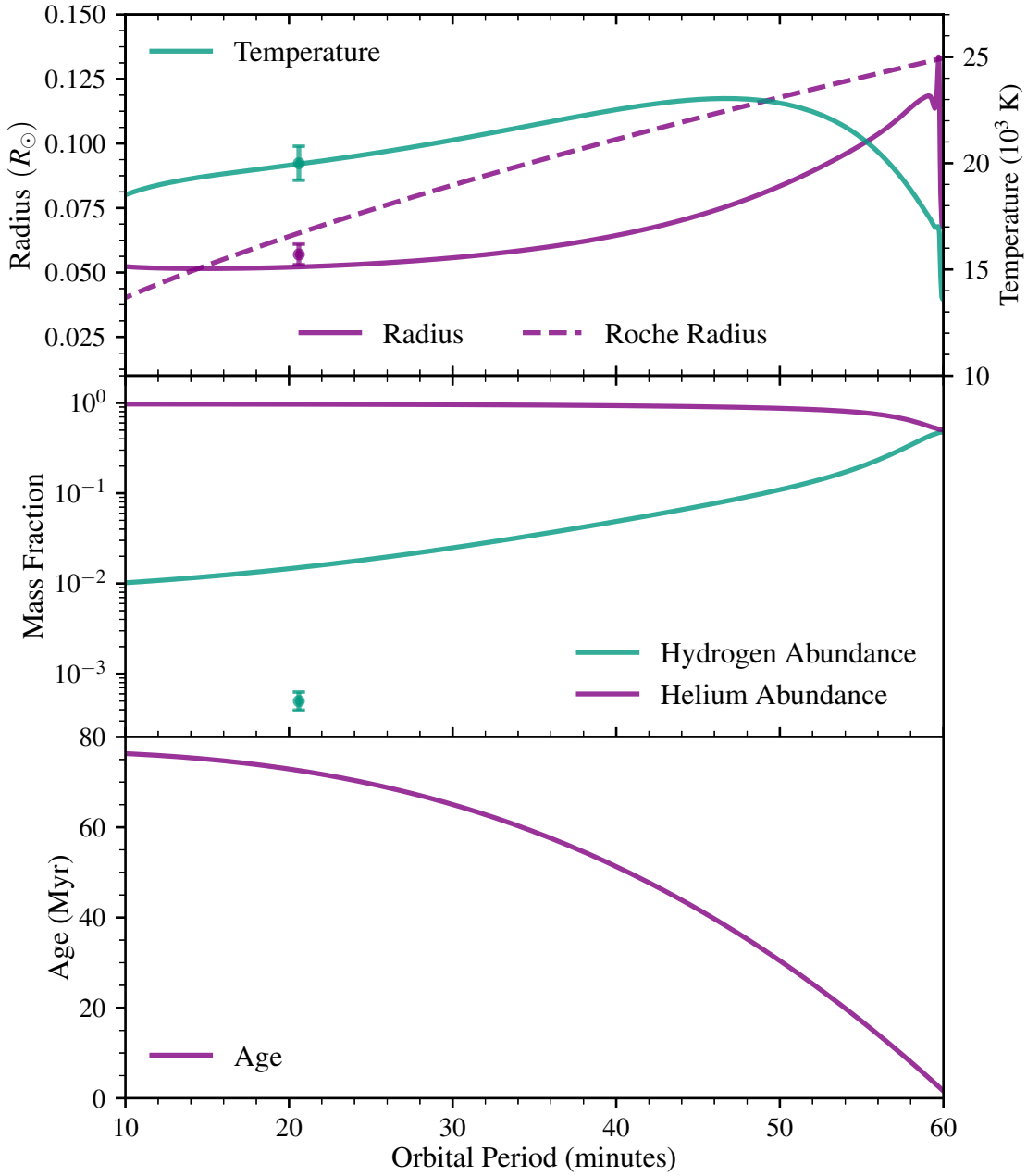

Figure 2.9: Binary Evolution Model of PTF J0533+0209, beginning with a 0.19 $M_\odot$ ELM WD and a 0.66 $M_\odot$ CO WD in a one-hour orbit. The ELM WD cools and contracts, and at an orbital period of 20 minutes it has nearly the same surface temperature and radius as the ELM WD in PTF J0533+0209, whose properties are denoted by colored points with error bars. The surface hydrogen abundance decreases due to extra mixing in the model (see text), though it remains larger than our spectroscopic measurements.

giant branch until its core helium mass is $0.187\,M_\odot$. We then strip the outer layers until the star has a mass of $0.19\,M_\odot$, leaving it with $10^{-3}\,M_\odot$ of hydrogen, and place it in a binary with a $0.66\,M_\odot$ companion in a 1 hour orbit. This mimics a common envelope (CE) event that births a compact binary system with masses consistent with our measurements for PTF J0533+0209. We evolve this system using MESA's binary module, allowing for orbital decay via gravitational radiation, while simultaneously evolving the structure of the ELM WD. We enforce tidal synchronization at all times, as short-period binary WDs are expected to be nearly tidally synchronized (Fuller and Lai, 2012). Rotational mixing is included via MESA's implementation of Eddington-Sweet circulation with `am_D_mix_factor = 1` and `D_ES_factor = 1`. We note that this amount of rotational mixing is very optimistic, as it is a factor of 30 larger than expected (Heger et al., 2000), yet we shall see below that even this excessive estimate of rotational mixing cannot explain the observed hydrogen depletion.

Figure 2.9 shows the evolution of the system described above. As the system ages, the WD contracts, and the model radius is $R \simeq 0.05\,R_\odot$ at a 20 minute orbital period. Because of extra mixing in our model (see below), the temperature initially increases as H is mixed into the interior and burned, but the temperature then decreases as H is depleted. The mass, temperature, and radius of our model at 20 minutes are all approximately consistent with PTF J0533+0209. If the post-CE period is substantially longer than one hour, the ELM WD cools to temperatures lower than observed. So, the system can only be explained by the CE formation channel if the ELM WD is born at a fairly short orbital period.

While the match with observations above is encouraging, it is difficult to explain the low H abundance from this model, which initially has a roughly equal surface mass fraction of H and He after the CE event. The Eddington-Sweet mixing keeps the outermost layers of the WD well-mixed due to the tidally enforced rapid rotation of the ELM WD, but it does not mix H into the deep interior. In the limited number of models we have explored, rotational mixing is not enough to mix H down into the He core where it can be burned, allowing the surface H to be depleted. In order to greatly deplete the surface H abundance, we have added an ad-hoc mixing diffusivity of $D_{mix} = 2.5 \times 10^3\,cm^2/s$, which causes H to mix deep enough to burn. Figure 2.9 shows that the surface mass

fraction of H is depleted by a factor of 50 down to $\sim 10^{-2}$ in this model, though it is still much larger than our measurements indicate. Without the extra mixing, the surface mass fraction remains nearly constant. Our models do not include gravitational settling and diffusion, which would cause the surface mass fraction of H to *i*ncrease as He gravitationally settles. The burning of H in our model keeps it warmer compared to a model without mixing, so our model cools slower than a normal WD of the same mass.

This model is not meant to be a “fit" to the observed properties, and some other combination of mass, initial orbital period, extra mixing, etc., can likely provide a better match to the data. Our main claim is that some sort of extra mixing or other method of removing H from the ELM WD must be at play. Since PTF J0533+0209 is in a very short-period binary compared to other H-rich ELMs, we suspect the extra mixing may be related to rotational or tidal effects that are much stronger in tight binaries. Also, if PTF J0533+0209 evolved from the CE channel, the system was likely born at an orbital period less than a couple hours in order for the ELM WD to be so hot. Based on the findings of Fuller and Lai, 2013, we find that tidal heating is unlikely to heat up the ELM WD to the observed temperature at an orbital period of 20 minutes. From equation 10 of Burdge, Coughlin, et al., 2019, the “tidal" temperature to which the ELM WD can be heated is only $\sim 7000\,K$, much below the observed temperature. A tidally induced nova (Fuller and Lai, 2012) could heat up the ELM WD, but these events are not expected to occur at such long orbital periods.

It may be possible that H-burning flashes contribute to the depletion of H near the surface, as such flashes in a compact binary will cause the ELM to overflow its Roche lobe and lose much of its expanding H envelope. The model described above had a small enough initial H mass that it did not encounter such flashes, but we have attempted to simulate flashing models with a larger initial H mass. For numerical reasons, we have not been able to simulate the flash-induced mass loss in a compact binary, however, the models indicate that the H at the base of the envelope would not overflow the Roche lobe during these events and would likely be retained. Hence, we believe H flashes may have contributed to the depletion of H, but some extra mixing (e.g., rotational mixing, or mixing induced via tidally excited gravity waves) is likely required to further deplete the remaining H to the observed level. One possibility is that the H-burning flashes

induce more mixing below the convective H-burning shell than predicted by our models, a phenomenon also thought to occur during classical novae (e.g., Alexakis et al. 2004; Denissenkov et al. 2013). This could mix H downward where it is burnt and dilute the H shell with dredged up He, potentially reducing the observed H-abundance to the level observed.

We have also attempted to create a system like PTF J0533+0209 from a stable mass transfer scenario like that described in Sun and Arras, 2018; Tauris, 2018; Li et al., 2019. We evolve systems near the orbital period bifurcation (Podsiadlowski et al., 2003) such that the donor is evolved (and hence H-poor) and the binary shrinks to sub-hour orbital periods via magnetic braking and gravitational radiation. This channel typically forms low-mass ELM WDs with masses in the range $0.15\,M_\odot \lesssim M \lesssim 0.2\,M_\odot$ that detach at very short orbital periods, so it can certainly produce systems similar to PTF J0533+0209. However, the donor in these models is usually lower surface temperature and higher H abundance than observed in PTF J0533+0209. Hence, while it might be possible to form a system like PTF J0533+0209 through stable mass transfer, we consider the CE channel to be more likely.

Evolutionary fate

Based on its measured orbital decay rate, PTF J0533+0209 has a characteristic decay timescale of $\tau_c = \frac{3}{8}\frac{P}{|\dot{P}|} \approx 3,700,000$ years. However, in a fraction of this time, PTF J0533+0209B will overflow its Roche lobe and initiate mass transfer onto PTF J0533+0209A, which occurs at an orbital period of ≈ 14 minutes in Figure 2.9, though precisely when this occurs depends on the rate at which PTF J0533+0209B cools and shrinks compared to its merger timescale. The binary will continue to evolve to shorter orbital periods due to the emission of gravitational radiation and eventually mass transfer will begin to remove mass from the degenerate helium core of PTF J0533+0209B (Kaplan, Bildsten, et al., 2012), which will expand in response to this mass loss, consequentially increasing the mass transfer rate and producing a feedback loop. Given the mass ratio of the binary, this means that PTF J0533+0209 will likely evolve into an AM CVn system at longer orbital periods (Marsh, Nelemans, et al., 2004), or alternatively, could result in a merger producing an R Coronae Borealis type star (Paczyński, 1971).

2.5 Conclusion

We have discovered PTF J0533+0209, a detached double white dwarf binary with a 20 minute orbital period using purely its ellipsoidal modulation. This more luminous component of this system exhibits a DBA atmosphere, unlike most of its double white dwarf counterparts, which is not easy to explain from standard binary formation and stellar evolution models. We have detected orbital decay in this system using archival time domain data, and estimated that the gravitational waves which the system emits should be detectable by *LISA*.

Modern synoptic time domain surveys are not only becoming wider and deeper, but crucially, increasingly well-sampled as a consequence of their large fields of view and roboticized observing capabilities. Thus, before *LISA* begins to decode the gravitational-wave signal from tens of thousands of galactic binaries in the Milky Way, these surveys hold the key to uncovering a large population of these systems. Some of these binaries, like ZTF J1539+5027 (Burdge, Coughlin, et al., 2019), will be extremely well calibrated via their optical behavior because of eclipses and/or a double-lined spectroscopic nature. However, systems like PTF J0533+0209, which exhibit a handful of very well-defined observables like a single radial velocity amplitude, ellipsoidal modulation, orbital decay rate, etc., will be far more numerous than their eclipsing, double-lined counterparts. Objects like PTF J0533+0209 demonstrate the scientific promise of the *LISA* era of astrophysics because *LISA* will transform such systems from being constrained by highly model-dependent assumptions to over-constrained systems which will instead test the fidelity of physical models.

Acknowledgments

K.B.B thanks the National Aeronautics and Space Administration and the Heising Simons Foundation for supporting his research. JF acknowledges support from an Innovator Grant from The Rose Hills Foundation and the Sloan Foundation through grant FG-2018-10515.

Based on observations obtained with the Samuel Oschin Telescope at the Palomar Observatory as part of the Palomar Transient Factory project, a scientific collaboration between the California Institute of Technology, Columbia University, Las Cumbres

Observatory, the Lawrence Berkeley National Laboratory, the National Energy Research Scientific Computing Center, the University of Oxford, and the Weizmann Institute of Science.

The KPED team thanks the National Science Foundation and the National Optical Astronomical Observatory for making the Kitt Peak 2.1-m telescope available. The KPED team thanks the National Science Foundation, the National Optical Astronomical Observatory and the Murty family for support in the building and operation of KPED. In addition, they thank the CHIMERA project for use of the Electron Multiplying CCD (EMCCD).

Some of the data presented herein were obtained at the W.M. Keck Observatory, which is operated as a scientific partnership among the California Institute of Technology, the University of California, and the National Aeronautics and Space Administration. The Observatory was made possible by the generous financial support of the W.M. Keck Foundation. The authors wish to recognize and acknowledge the very significant cultural role and reverence that the summit of Mauna Kea has always had within the indigenous Hawaiian community. We are most fortunate to have the opportunity to conduct observations from this mountain.

The research leading to these results has received funding from the European Research Council under the European Union's Horizon 2020 research and innovation programme n.677706 (WD3D)

This research benefited from interactions at the ZTF Theory Network Meeting that were funded by the Gordon and Betty Moore Foundation through Grant GBMF5076 and support from the National Science Foundation through PHY-1748958.

Chapter 3

GENERAL RELATIVISTIC ORBITAL DECAY IN A SEVEN-MINUTE-ORBITAL-PERIOD ECLIPSING BINARY SYSTEM

Burdge, K. B. et al. (2019). "General relativistic orbital decay in a seven-minute-orbital-period eclipsing binary system". In: *Nature* 571.7766, pp. 528–531. DOI: 10.1038/s41586-019-1403-0. arXiv: 1907.11291 [astro-ph.SR].

Kevin. B. Burdge[1], Michael W. Coughlin[1], Jim Fuller[1], Thomas Kupfer[2], Eric C. Bellm[3], Lars Bilsten[2,4], Matthew J. Graham[1], David L. Kaplan[5], Jan van Roestel[1], Richard G. Dekany[6], Dmitry A. Duev[1], Michael Feeney[6], Matteo Giomi[7], George Helou[8], Stephen Kaye[6], Russ R. Laher[8], Ashish A. Mahabal[1], Frank J. Masci[8], Reed Riddle[6], David L. Shupe[8], Maayane T. Soumagnac[9], Roger M. Smith[6], Paula Szkody[3], Richard Walters[6], S. R. Kulkarni[1], Thomas A. Prince[1]

[1]Division of Physics, Mathematics and Astronomy, California Institute of Technology, Pasadena, CA, USA [2]Kavli Institute for Theoretical Physics, University of California Santa-Barbara, Santa Barbara, CA, USA
[3]Department of Astronomy, University of Washington, Seattle, WA, USA
[4]Department of Physics, University of California, Santa Barbara, CA, USA
[5]Department of Physics, University of Wisconsin-Milwaukee, Milwaukee, WI, USA
[6]Caltech Optical Observatories, California Institute of Technology, Pasadena, CA, USA
[7]Humboldt-Universität zu Berlin, Berlin, Germany
[8]IPAC, California Institute of Technology, Pasadena, CA, USA
[9]Benoziyo Center for Astrophysics, Weizmann Institute of Science, Rehovot, Israel

ABSTRACT

General relativity (Einstein, 1905) predicts that short orbital period binaries emit significant gravitational radiation, and the upcoming Laser Interferometer Space Antenna (*LISA*) (Amaro-Seoane et al., 2017) is expected to detect tens of thousands of such systems (Nissanke et al., 2012); however, few have been identified (Kupfer, Korol, et al., 2018), and only one is eclipsing–the double white dwarf binary SDSS J065133.338+284423.37(Brown, Kilic, Hermes, et al., 2011), which has an orbital period of 12.75 minutes. Here, we report the discovery of an eclipsing double white dwarf binary system with an orbital period of only 6.91 minutes, ZTF J153932.16+502738.8. This system has an orbital period close to half that of SDSS J065133.338+284423.37, and an orbit so compact that the entire binary could fit within the diameter of the planet Saturn. The system exhibits a deep eclipse, and a double-lined spectroscopic nature. We observe rapid orbital decay, consistent with that expected from general relativity. ZTF J153932.16+502738.8 is a significant source of gravitational radiation close to the peak of *LISA*'s sensitivity(Amaro-Seoane et al., 2017), and should be detected within the first week of *LISA* observations.

The Zwicky Transient Facility (ZTF) (Bellm, Kulkarni, Graham, et al., 2019; Graham, Kulkarni, et al., 2019) is a northern-sky synoptic survey using the 48-inch Samuel Oschin Telescope at Palomar Observatory. In June 2018, we undertook an initial search for periodic sources among all of the 20 million ZTF lightcurves available at that time. The analysis identified ZTF J153932.16+502738.8 (henceforth referred to as ZTF J1539+5027), as a candidate binary system with a short orbital period. On the same night as identifying the candidate, an observation with the Kitt Peak 84-Inch Electron Multiplying Demonstrator (KPED) (Coughlin, Dekany, et al., 2019) confirmed the discovery, and revealed a remarkably deep eclipse occurring precisely every 6.91 minutes. Next, we used the high-speed imaging photometer CHIMERA (Harding et al., 2016) on the 200-inch Hale telescope at Palomar Observatory to observe the system (Figure 1), confirming the deep primary eclipse, and revealing a shallow secondary eclipse.

The short orbital period means that the two components must be dense objects–white dwarfs. Because the primary eclipse is significantly deeper than the secondary eclipse, we can infer that one white dwarf (the primary) is hotter and more luminous than its companion (the secondary), as the detected flux is almost completely attenuated when the cooler object occults the hotter. By modelling the lightcurve (Methods), we can estimate the orbital inclination, i, the radius of the primary, R_1, and the secondary, R_2, relative to the semi-major axis of the orbit, a (Methods).

Because of ZTF J1539+5027's extremely short orbital period, general relativity predicts that it will undergo rapid orbital decay due to the emission of gravitational radiation (Taylor, Fowler, et al., 1979). With CHIMERA and KPED, we can precisely measure the time of eclipse, and use these eclipse times to measure a changing orbital period. If a system has a constant orbital period derivative, we expect the deviation of eclipse times, $\Delta t_{eclipse}$, (compared to those of a system with constant orbital period) to grow quadratically in time. Equation 3.1

$$\Delta t_{eclipse}(t - t_0) = \left(\frac{1}{2}\dot{f}(t_0)(t - t_0)^2 + \frac{1}{6}\ddot{f}(t_0)(t - t_0)^3 + ...\right)P(t_0) \tag{3.1}$$

illustrates this, where t_0 is the reference epoch, $P(t_0)$ is the orbital period at the reference epoch, $f(t_0)$, $\dot{f}(t_0)$, etc, are the orbital frequency and its time derivatives at the reference

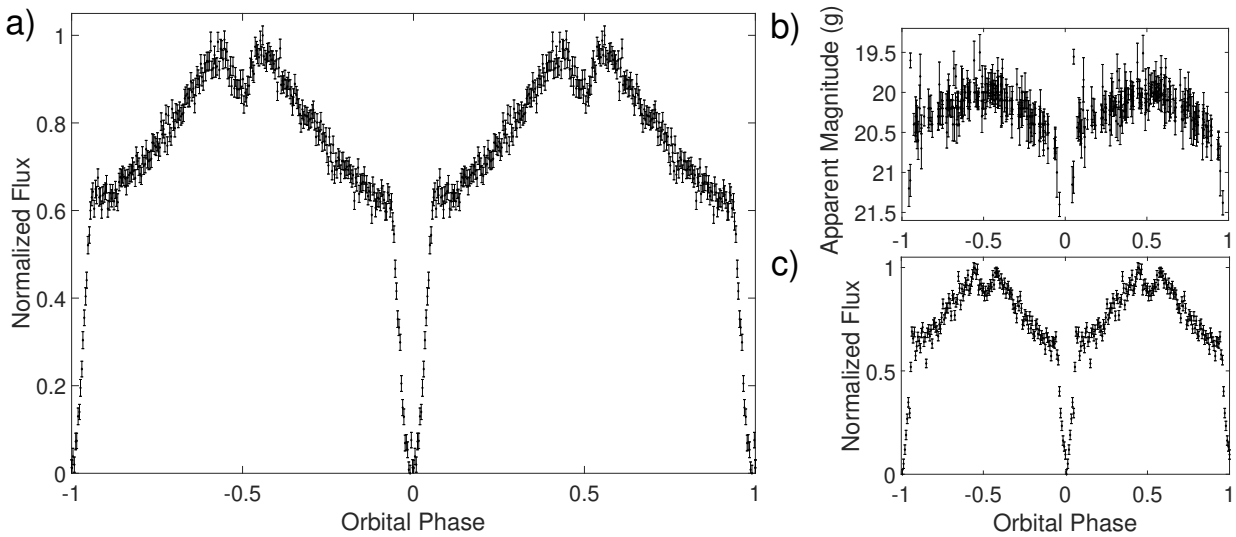

Figure 3.1: **Lightcurve of ZTF J1539+5027 a)** The binned CHIMERA g' lightcurve of ZTF J1539+5027, phase-folded on the 6.91 minute orbital period. At phase 0, the lightcurve exhibits a deep primary eclipse, indicating that the hot primary star is producing most of the observed light. Outside of eclipse, there is a quasi-sinusoidal modulation because the primary star heavily irradiates one side of its companion. At phases ±0.5, the secondary eclipse occurs as the hot primary transits the irradiated face of its companion. **b)** The phase-folded ZTF g-band lightcurve of the object. We were able to discover the object because of its periodic behavior. **c)** A binned g' lightcurve obtained with KPED, phase-folded on the orbital period. Error bars are 1σ intervals.

epoch, and $t - t_0$ is the time since the reference epoch.

We also used IRSA/IPAC (Masci, Laher, Rebbapragada, et al., 2017) to retrieve photometry from archival Palomar Transient Factory (PTF/iPTF) data (Law et al., 2009) spanning 2009, 2010, 2011, and 2016. Figure 2 shows a fit of all of the timing epochs with a second order polynomial, which resulted in a highly significant detection of the orbital decay, corresponding to an orbital period derivative of $\dot{P} = (-2.373 \pm 0.005) \times 10^{-11}\,\mathrm{s\,s^{-1}}$ (Table 1). The corresponding characteristic orbital decay timescale is: $\tau_c = \frac{3}{8}\frac{P}{|\dot{P}|} \approx 210,000$ years.

To measure the orbital velocities of the white dwarfs in the binary, we obtained phase-resolved spectroscopy using the Low Resolution Imaging Spectrometer (LRIS) (McCarthy et al., 1998) on the 10-m W. M. Keck I Telescope on Mauna Kea. These

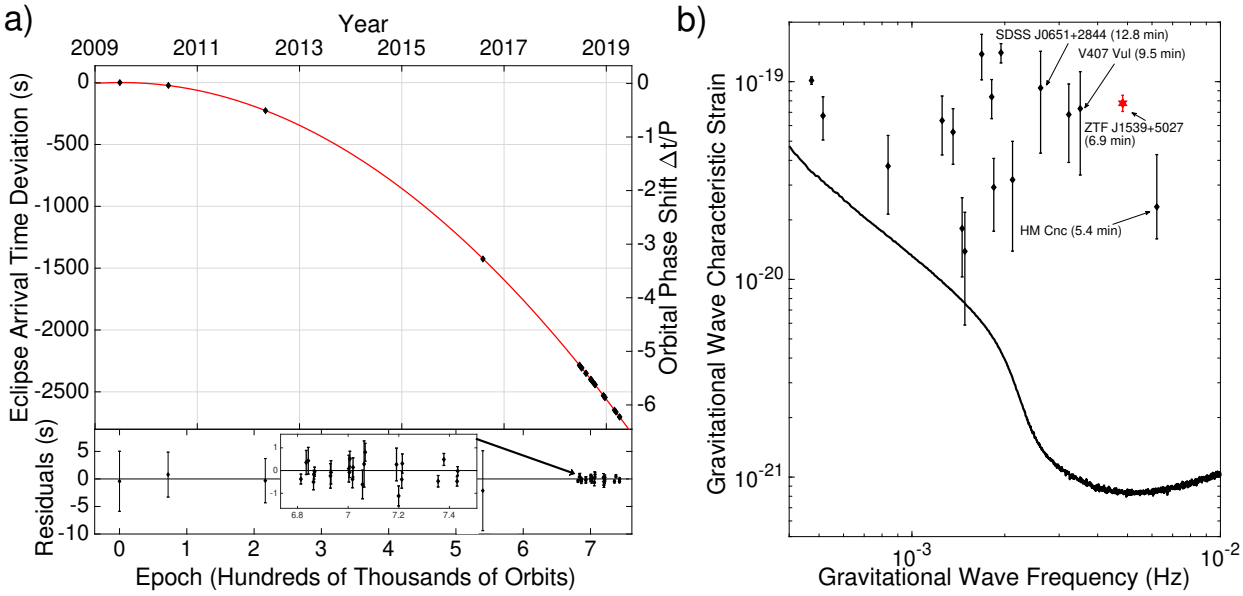

Figure 3.2: **Orbital decay and gravitational wave strain of ZTF J1539+5027 a)** A 2nd order polynomial fit to the deviation of the measured eclipse times as a function of time, compared to a system with constant orbital period. The consistency with a quadratic deviation demonstrates that the orbital period decreases with time. The orbital decay inferred is consistent with that expected from gravitational wave emission. The initial four timing epochs come from PTF/iPTF photometry, and the remainder were obtained with CHIMERA and KPED. **b)** The characteristic gravitational wave strain and frequency for ZTF J1539+5027 (red star in the plot). See Table 1 for masses and the distance. The black diamonds are other known *LISA* sources, all of which are compact binaries (Kupfer, Korol, et al., 2018). The smooth black curve is the expected sensitivity threshold of *LISA* after 4 years of integration (Amaro-Seoane et al., 2017). For HM Cancri (right-most point) we have assumed a uniform prior in distance from 4.2-20 kpc (Roelofs et al., 2010; Bildsten et al., 2006). Error bars on panel **a)** are 1σ. Errors on panel **b)** are taken fromKupfer, Korol, et al., 2018 for all points except ZTF J1539 and HM Cnc, which are 68% CIs.

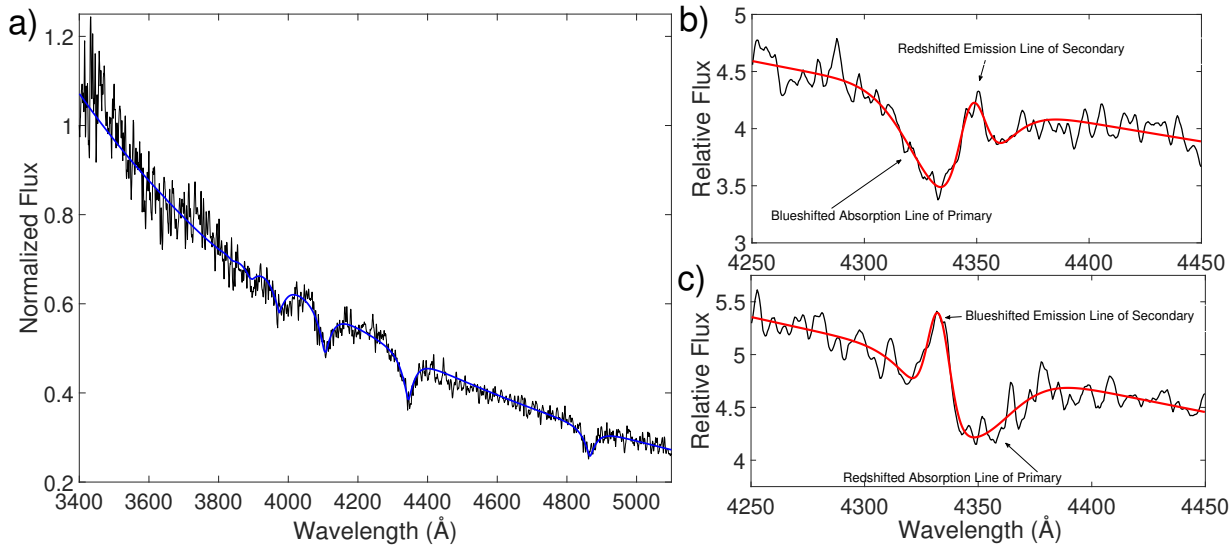

Figure 3.3: **Optical spectrum of ZTF J1539+5027 a)** The LRIS spectrum of ZTF J1539+5027 immediately after the primary eclipse. This is an ideal phase to isolate the photosphere of the hot primary, because it minimizes flux contributed by the irradiated face of the secondary. The smooth blue line is a fit of a white dwarf atmospheric model to this spectrum, yielding an effective photospheric temperature of $T_{eff,1} = 48,900 \pm 900\,K$ and a logarithm of surface gravity $\log(g)_1 = 7.75 \pm 0.06\ \log(cm\,s^{-2})$ for the hot primary. **b)** and **c)** Two phase-resolved spectra of the hydrogen $n = 5$ to $n = 2$ transition at ≈ 4340. The smooth red line is a double Gaussian fit to the absorption and emission line used to measure the Doppler shifts of these features **b)** illustrates a phase in which the emission line associated with the cooler secondary is redshifted, while the absorption line associated with the primary is blueshifted. **c)** exhibits the opposing phase.

observations (Figure 3) revealed broad and shallow hydrogen absorption lines characteristic of a hot hydrogen-rich (DA) white dwarf associated with the bright primary, and within these absorption lines, narrower hydrogen emission lines apparently arising from the cooler secondary. The emission lines move out of phase with the absorption lines, making this a double-lined spectroscopic binary. There are also weak neutral helium absorption and emission lines that exhibit similar behavior. The Doppler shifts of the emission lines in the spectra track the cool secondary, suggesting that the emission lines are not associated with accretion onto the hot and compact primary, but instead arise from the irradiated surface of the secondary.

Using the spectroscopic observations, lightcurve modelling, and the orbital decay, we can constrain the masses of the white dwarfs in several ways: **(1):** With a mass-radius relation for the hot primary and constraints from lightcurve modelling, although this depends on parameters of white dwarf models, and only weakly constrains the mass of the secondary; **(2):** Using the spectroscopically measured radial velocity semi-amplitudes; however, this is challenging due to the blended absorption/emission lines, the latter depending on modelling irradiation effects and a substantial center of light correction; **(3):** With the chirp mass inferred from the measured orbital decay; however, this approach must account for potential tidal contributions.

Because each of these methods rely on different model dependent assumptions, we chose to estimate physical parameters by combining these constraints (Figure 4). We present the physical parameters resulting from this analysis in Table 1, alongside those of SDSS J0651+2844 (Brown, Kilic, Hermes, et al., 2011; Hermes, Kilic, et al., 2012; Kupfer, Korol, et al., 2018). We conclude that the hot primary is a $\approx 0.6\,M_\odot$ (likely carbon-oxygen) white dwarf, while the cool secondary is a $\approx 0.2\,M_\odot$ (likely helium-core) white dwarf.

Because of their remarkably short orbital period, the white dwarfs experience significant tidal distortion. Tidal energy dissipation may heat and spin up the white dwarfs, in addition to increasing the orbital decay rate. Based on theoretical predictions (Fuller and Lai, 2013), tidal torques likely cause the spin periods of the white dwarfs to synchronize with the orbital period. We expect that tidal energy dissipation may increase the orbital decay rate by $\approx 7\%$ relative to gravitational wave emission alone (Methods), though we cannot currently measure this due to uncertainty in the white dwarf masses. Future detection of the second derivative of the orbital decay rate, $\ddot{f}$, will enable a direct measurement of the tidal contribution to the orbital decay.

When *LISA* (Amaro-Seoane et al., 2017) first begins to operate (circa 2034), we estimate that it will detect ZTF J1539+5027 within a week. At the end of *LISA*'s 4-year mission, we estimate the SNR will be 143^{+13}_{-13} (Methods). Not only does the source radiate high-strain gravitational waves, but *LISA*'s sensitivity peaks at about 5 mHz, close to the 4.8 mHz gravitational wave frequency of this source, resulting in an exceptionally large

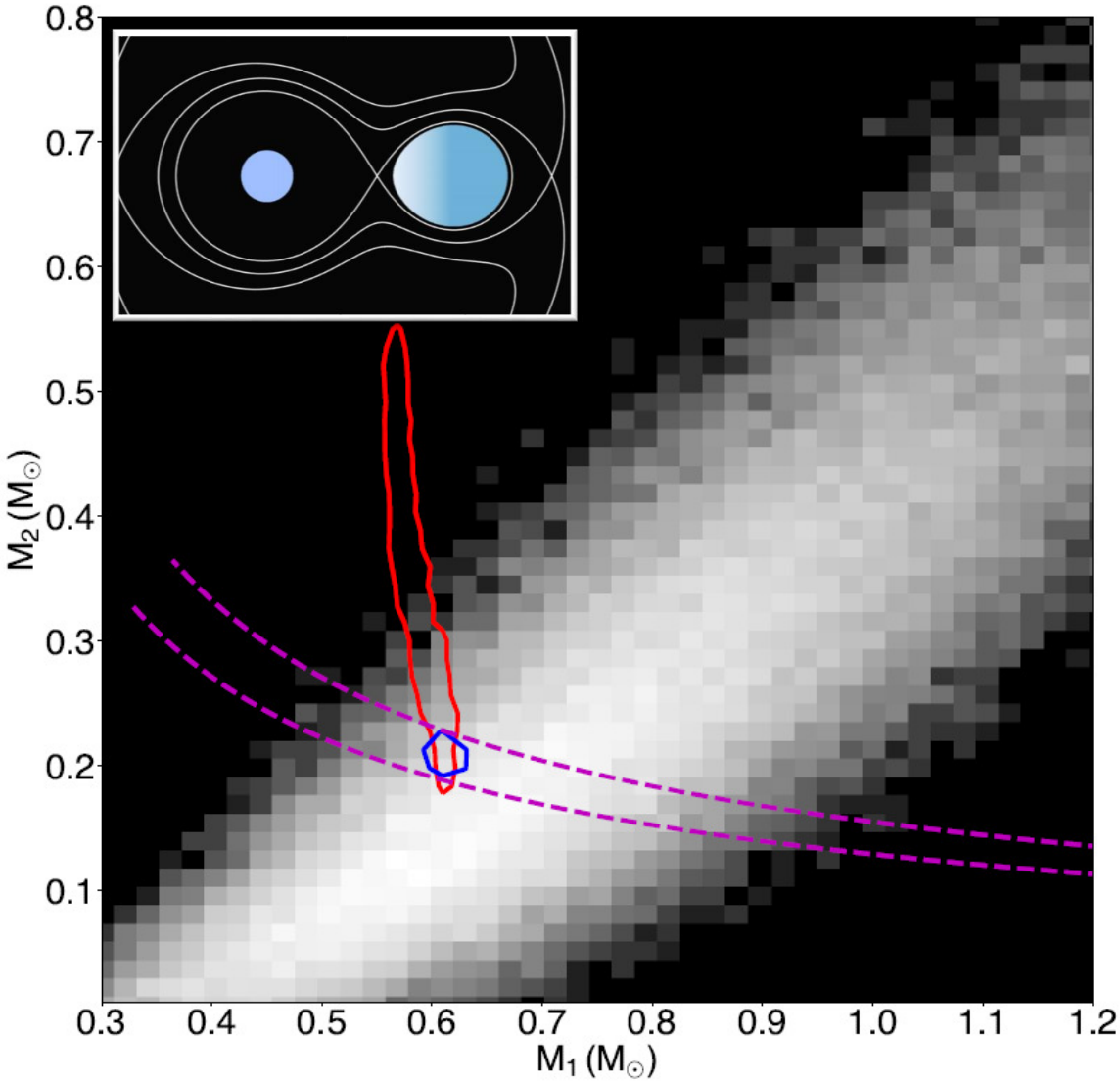

Figure 3.4: **Constraints on component masses in ZTFJ1539+5027** A graphical representation of the analysis used to derive final values for the masses of the two white dwarfs, with an inset illustrating the two components of the binary drawn to scale based on these parameters together with Roche potentials. The background white bins represent the spectroscopic constraint. The red line is a 50% contour level of the constraint inferred from applying a mass-radius relation to the hot primary white dwarf (Althaus, Camisassa, et al., 2015), and combining it with the ratio of the primary's radius to the semi-major axis, $\frac{R_1}{a}$, inferred from lightcurve modelling. The magenta dashed lines are constraints imposed by the measured chirp mass; the upper dashed line assumes orbital decay purely due to general relativity, whereas the lower dashed line includes a 10 percent tidal contribution. The blue line is a 50% contour level representing a combination of all of these constraints (Table 1).

SNR. This system will serve as a crucial "verification source" for *LISA* (Amaro-Seoane et al., 2017), because its well-constrained inclination predicts the relative amplitude of the signal in the two gravitational wave polarizations (Shah, Nelemans, et al., 2013), and the precisely measured orbital decay already tightly constrains its chirp mass.

ZTF J1539+5027 poses challenges for models of binary evolution and the physics of accretion. The spectroscopically measured temperature of the hot primary is $T_{eff,1} = 48,900 \pm 900\,K$. The cooling age of such a hot white dwarf is $\approx$ 2.5 million years (Holberg and Bergeron, 2006), significantly shorter than the > 200 million year cooling age of the secondary (Istrate et al., 2016). Thus, some recent heating must have occurred. Tidal heating could increase the surface temperature of the primary to nearly $50,000\,K$, though more realistic calculations (Methods) suggest temperatures closer to half this value. A more plausible explanation is that the heating is due to recent accretion, especially since the radius of the secondary indicates it is on the brink of Roche lobe overflow. Such accretion could heat the primary to its observed temperature for accretion rates of $\dot{M} \gtrsim 10^{-9} M_{\odot}\,yr^{-1}$ (Methods).

However, we see no evidence for active accretion. The only other known binary systems with orbital periods shorter than 10 minutes, V407 Vul ($P \approx 9.5$ minutes) (Ramsay, Cropper, et al., 2000) and HM Cancri ($P \approx 5.4$ minutes) (Roelofs et al., 2010), were discovered because of periodic X-ray emission, thought to arise from a hot spot formed by direct impact accretion (Marsh, Nelemans, et al., 2004). Unlike the other two sub-10-minute binaries, ZTF J1539+5027 exhibits no detectable X-ray flux. Based on an upper limits from observations by the XRT X-ray telescope on the Neil Gehrels Swift Observatory (Gehrels et al., 2004), the EPIC-pn instrument on the XMM Newton Observatory (Jansen et al., 2001), and optical constraints, we have estimated an upper limit of $\dot{M} < 2\times10^{-8} M_{\odot}\,yr^{-1}$, contributing 10% of its energy to a hot spot. Reaching this upper limit requires fine-tuning the accretion hot spot temperature (Methods). Active accretion could still be occurring if the accretion energy is channeled primarily into heating the optically thick atmosphere of the accretor, and is then radiated at the $50,000\,K$ observed.

It is also possible that the accretion proceeds intermittently. One way of temporarily

halting accretion could be a recent nova eruption on the surface of the primary. We expect that a $0.6\,M_\odot$ white dwarf accreting from a companion at a rate of $\dot{M} \sim 10^{-9} M_\odot\, yr^{-1}$ should experience (Wolf et al., 2013) recurrent novae on timescales of $\sim 10^5\, yr$. However, while mass transfer may temporarily cease after each nova, calculations suggest that it is unlikely to catch the system in this short-lived phase (Methods). We conclude that the most likely scenarios are intermittent accretion with a mechanism allowing for phases of little-to-no mass transfer, or active accretion in which the accretion energy is radiated almost entirely in the ultraviolet and optical.

The orbit of ZTF J1539+5027 will continue to decay for $\approx 130,000$ years until it reaches a period of $\approx$5 minutes at which point the degenerate core of the secondary will begin to expand in response to mass loss, dramatically increasing the rate of mass transfer (Kaplan, Bildsten, et al., 2012). If the mass transfer is stable, which is likely based on the mass ratio (Marsh, Nelemans, et al., 2004) of $q \sim 1/3$, the binary will evolve into an AM CVn system and the orbital period will increase. Alternatively, unstable mass transfer would result in a merger that could produce an R Cor Bor star (Paczyński, 1971), or, less likely, a detonation of accreted helium on the primary could lead to a double-detonation that disrupts the primary Shen, Kasen, et al., 2018.

KBB thanks the National Aeronautics and Space Administration and the Heising Simons Foundation for supporting his research.

Based on observations obtained with the Samuel Oschin Telescope 48-inch and the 60-inch Telescope at the Palomar Observatory as part of the Zwicky Transient Facility project. ZTF is supported by the National Science Foundation under Grant No. AST-1440341 and a collaboration including Caltech, IPAC, the Weizmann Institute for Science, the Oskar Klein Center at Stockholm University, the University of Maryland, the University of Washington (UW), Deutsches Elektronen-Synchrotron and Humboldt University, Los Alamos National Laboratories, the TANGO Consortium of Taiwan, the University of Wisconsin at Milwaukee, and Lawrence Berkeley National Laboratories. Operations are conducted by Caltech Optical Observatories, IPAC, and UW.

The KPED team thanks the National Science Foundation and the National Optical Astronomical Observatory for making the Kitt Peak 2.1-m telescope available. The

Table 3.1: Table of Parameters

M_1	$0.610^{+0.017}_{-0.022}\,M_\odot$	$0.49^{+0.02}_{-0.02}\,M_\odot$
M_2	$0.210^{+0.014}_{-0.015}\,M_\odot$	$0.247^{+0.015}_{-0.015}\,M_\odot$
R_1	$1.562^{+0.038}_{-0.038} \times 10^{-2}\,R_\odot$	$1.42^{+0.1}_{-0.1} \times 10^{-2}\,R_\odot$
R_2	$3.140^{+0.054}_{-0.052} \times 10^{-2}\,R_\odot$	$3.71^{+0.12}_{-0.12} \times 10^{-2}\,R_\odot$
a	$11.218^{+0.080}_{-0.082} \times 10^{-2}\,R_\odot$	$16.48^{+0.39}_{-0.43} \times 10^{-2}\,R_\odot$
i	$84.15^{+0.64}_{-0.57}\,degrees$	$86.9^{+1.6}_{-1.0}\,degrees$
T_0	$2458305.6827886 \pm 0.0000012\,BJD_{TDB}$	$2455652.5980910 \pm 0.0000084\,BJD_{TDB}$
P	$414.7915404 \pm 0.0000029\,s$	$765.206543 \pm 0.000055\,s$
$\dot{P}$	$(-2.373 \pm 0.005) \times 10^{-11}\,s\,s^{-1}$	$(-0.98 \pm 0.28) \times 10^{-11}\,s\,s^{-1}$
d	$2.34 \pm 0.14\,kpc\,(spec.)$	$1.0 \pm 0.1\,kpc\,(spec.)\ 0.9 \pm 0.5\,kpc\,(parallax)$
$T_{eff,1}$	$48,900 \pm 900\,K$	$8,700 \pm 500\,K$
$T_{eff,2}$	$< 10,000\,K$	$16,530 \pm 200\,K$
$\log(g)_1$	$7.75 \pm 0.06\ \log(cm\,s^{-2})$	
$\log(g)_2$		$6.76 \pm 0.04\ \log(cm\,s^{-2})$
K_1	$292^{+254}_{-283}\,km\,s^{-1}$	
K_2	$961^{+178}_{-139}\,km\,s^{-1}$	$616.9^{+5.0}_{-5.0}\,km\,s^{-1}$
$4\,Yr\,LISA\,SNR$	143^{+14}_{-13}	$94^{+12}_{-10}\,(using\,spec.\,distance)$

KPED team thanks the National Science Foundation, the National Optical Astronomical Observatory and the Murty family for support in the building and operation of KPED. In addition, they thank the CHIMERA project for use of the Electron Multiplying CCD (EMCCD).

Some of the data presented herein were obtained at the W.M. Keck Observatory, which is operated as a scientific partnership among the California Institute of Technology, the University of California and the National Aeronautics and Space Administration. The Observatory was made possible by the generous financial support of the W.M. Keck Foundation. The authors wish to recognize and acknowledge the very significant cultural role and reverence that the summit of Mauna Kea has always had within the indigenous Hawaiian community. We are most fortunate to have the opportunity to conduct observations from this mountain.

This research benefited from interactions at the ZTF Theory Network Meeting that were funded by the Gordon and Betty Moore Foundation through Grant GBMF5076 and support from the National Science Foundation through PHY-1748958

We thank John Hoffman, the creator of `cuvarbase`. We thank Thomas Marsh, Sterl Phinney, and Valeryia Korol for valuable discussions. We thank Gregg Hallinan and Christoffer Fremling for helping observe the object.

Competing Interests: The authors declare that they have no competing financial interests.
Contributions: KBB discovered the object, conducted the lightcurve analysis, eclipse time analysis, and was the primary author of the manuscript. KBB and MWC conducted the spectroscopic analysis. KBB, MWC, and TAP conducted the combined mass-radius analysis. KBB and MWC reduced the optical data. KBB, MWC, and DLK reduced and analysed the X-ray observations. JF conducted the theoretical analysis, including that on tides, and MESA evolutionary models. KBB, MWC, TK, SRK, JvR, and TAP all contributed to collecting data on the object. KBB, MWC, JF, TK, ECB, LB, MJG, DLK, JvR, SRK, and TAP contributed to the physical interpretation of the object. TK, ECB, RGD, MF, MG, SK, RRL, AAM, FJM, RR, DLS, MTS, RMS, PS and RW contributed to the implementation of ZTF; MJG is the project scientist, TAP and GH are Co-PIs, and SRK is PI of ZTF. RGD, DAD, MF, RR contributed to the implementation of

KPED; MWC is project scientist, and SRK is PI of KPED. TAP is KBB's PhD advisor. Correspondence: Correspondence and requests for materials should be addressed to KBB (email: kburdge@caltech.edu)

3.1 Summary of Observations

Extended Data Table 1 provides a summary of all observations used in our analysis.

3.2 Period Finding

We identified ZTF J1539+5027 by using the conditional entropy (Graham, Drake, et al., 2013) period finding algorithm on 20 million available ZTF lightcurves containing more than 50 epochs as of June 5, 2018, which originated exclusively from the ZTF collaboration's extragalactic high cadence survey (Bellm, Kulkarni, Barlow, et al., 2019). These lightcurves correspond to approximately 10 million sources, each with a ZTF-g and ZTF-r lightcurve.

ZTF J1539+5027 exhibited the most significant signal of all the objects whose strongest (lowest entropy) period fell in the 6–7 minute range. We used a Graphics Processing Unit (GPU) implementation of the conditional entropy algorithm included in the `pycuda` based `cuvarbase` package (available on GitHub). The algorithm was executed on a pair of NVIDIA GTX 1080 Ti GPUs.

3.3 Lightcurve Modelling

To model the lightcurve, we used data from three nights of CHIMERA g' observations (July 5-7 2018), with a total of $12,999$ individual 3-s exposures.

To fit the CHIMERA data, we used the `ellc` package (Maxted, 2016) to model the lightcurve and fit for the ratio of the radii to the semi-major axis, $r_1 = R_1/a$, $r_2 = R_2/a$, inclination, i, mass ratio, $q = \frac{M_2}{M_1}$, surface brightness ratio, J, of the unheated face of the secondary compared to the hot primary, and the mid-eclipse time of the primary eclipse, t_0. We adopted a linear limb darkening model, with limb darkening coefficients for the primary (ldc_1) and secondary (ldc_2). We treated the primary as a spherical object, but invoked a Roche approximation for the secondary. We also included a gravity darkening coefficient for the secondary (gdc_2) and a single free heating parameter ($heat_2$) to attempt

to fit the sinusoidal variation due to the irradiation of the secondary, which acts as an albedo of the secondary, but in this system must be larger than 1 to achieve a good fit because a significant amount of incident ultraviolet light is reprocessed into optical wavelengths.

We allowed the limb and gravity darkening coefficients to vary as free parameters in the fit, using uniform priors for each with values of $ldc_1 = 0.15 \pm 0.15$, $ldc_2 = 0.4 \pm 0.2$, and $gdc_2 = 0.6 \pm 0.1$, based on extrapolations of existing models (Gianninas, Strickland, et al., 2013; Claret and Bloemen, 2011).

We performed the final fit using the period derived from the quadratic fit to the timing epochs (Table 1). We left r_1, r_2, i, J, q, t_0, ldc_1, ldc_2, gdc_2, and $heat_2$ as free parameters. Extended Data Figure 1 illustrates the corner plots from this fit, but excludes t_0, which did not exhibit significant covariance with any other parameter. We fixed the eccentricity to 0, because measuring this quantity depends on the shape of the secondary eclipse, which in turn depends on the poorly understood irradiation of the secondary. We ruled out the possibility of significant eccentricity, because we failed to detect any sign of apsidal precession in the eclipse time measurements, and furthermore, we tried fitting for this using the lightcurve modelling, and found a value consistent with 0. Because we lack a good physical model for the irradiation of the secondary, we also do not account for Doppler beaming, which we expect to alter the shape of the lightcurve at the few percent level, peaking at phases between the eclipses, where the irradiation dominates the behavior of the lightcurve.

3.4 Orbital Decay

To measure the orbital decay, we independently fit each night of KPED and CHIMERA data for mid-eclipse times using the lightcurve modelling performed with `ellc`. We convert all timestamps to Barycentric Julian Dates (BJD) in Barycentric Dynamical Time (TDB) to achieve the required timing precision. Because the eclipse time is not strongly covariant with model dependent parameters such as gravity and limb darkening, we omitted these from the fits to reduce complexity (but still fitting for all other parameters described in the previous section). We also extracted photometry from archival PTF/iPTF data, and because of significant smearing due to the exposure time of 60-s (particularly

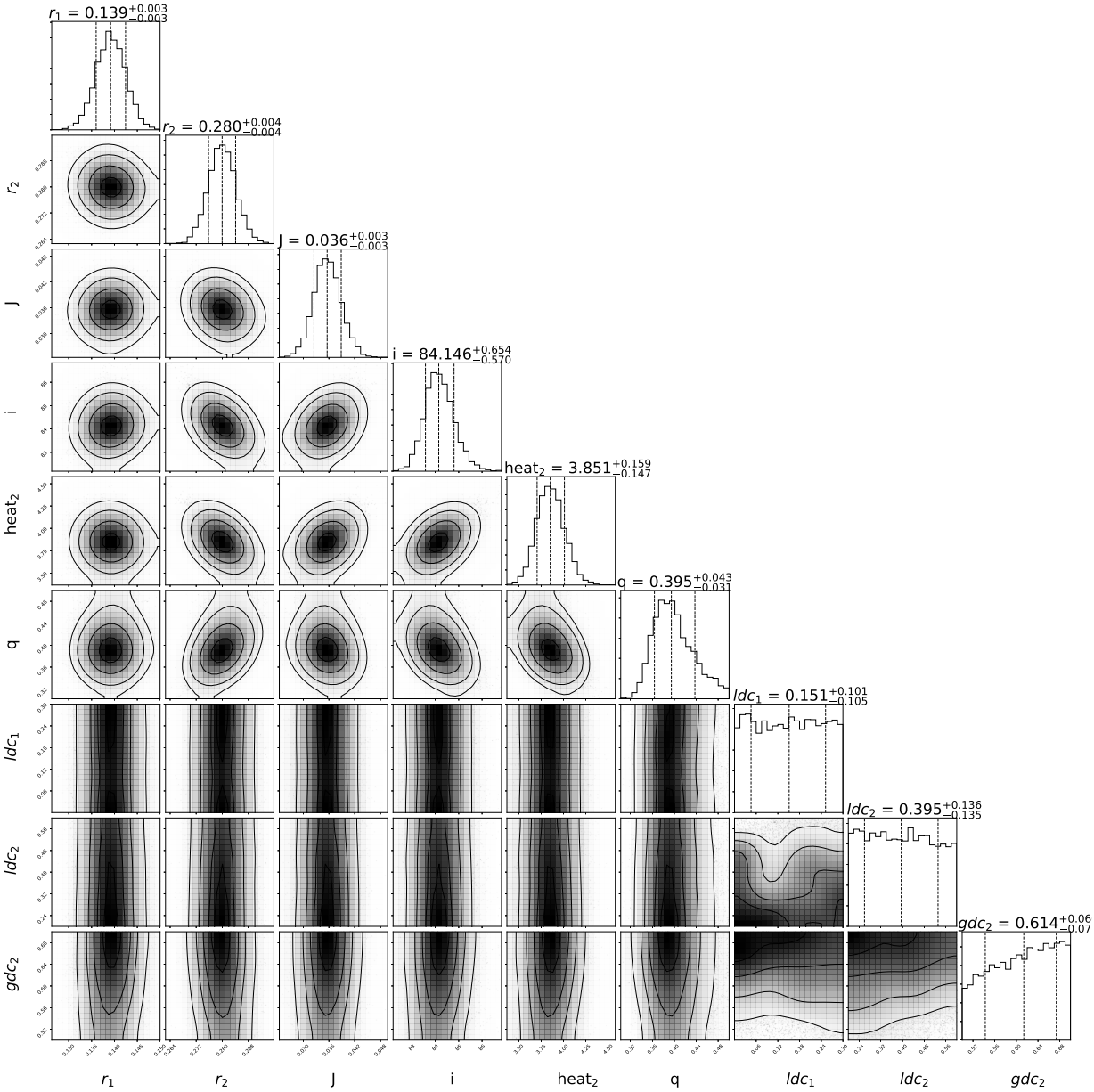

Figure 3.5: **Extended Data Figure 1: Corner plots of lightcurve modelling** The corner plots of the lightcurve fit to $12,999$ g' epochs taken with CHIMERA on July 5, 6, and 7 2018. Please note that the two limb darkening coefficients, as well as gravity darkening of the secondary (bottom three panels), were allowed to vary to ensure that assumptions regarding them were not strongly covariant with the other physical quantities of interest.

for the primary eclipse), we extracted timing epochs by performing a least squares fit of a sinusoid to this data (Extended Data Figure 2).

After obtaining the timing epochs, we measured the deviation of each eclipse time since the start of observations relative to a model with a constant orbital period (Figure 2). This was non-trivial, because the eclipse time had drifted by multiple orbits since the PTF epochs. However, upon allowing for an integer number of orbits to have passed, only one solution yielded a significant fit when using a quadratic model (corresponding to 5 orbits since the initial epoch). A linear model failed in all cases, and a cubic model produced a cubic coefficient consistent with 0, so for the final emphemeris, we chose to use a least squares fit of a quadratic to the these mid-eclipse times to estimate $\dot{P}$ (this fit is the red curve down in (Figure 3a), which resulted in an adjusted $R^2 = 0.999995$. This quadratic fit is independent of any model assumptions about decay due to tidal contribution, general relativity, or any other mechanism; it only indicates that the orbital period is decreasing with with an approximately constant rate as a function of time over the course of the observations.

In addition to extracting $\dot{P}$, we verified our measurement by fitting a quadratic to only mid-eclipse times extracted from CHIMERA and KPED data (Extended Data Figure 3), and obtained a value of $\dot{P} = (-2.487 \pm 0.19) \times 10^{-11}\,\mathrm{s\,s^{-1}}$, consistent with the $\dot{P} = (-2.373 \pm 0.005) \times 10^{-11}\,\mathrm{s\,s^{-1}}$ value obtained when including PTF/iPTF data. Moreover, these values are both consistent with the value of $\dot{P} = (-2.378 \pm 0.049) \times 10^{-11}\,\mathrm{s\,s^{-1}}$ obtained by fitting only the four PTF/iPTF epochs and excluding all CHIMERA and KPED data.

With $\dot{P}$ measured, we assessed how much contribution there was due to "secular acceleration" (Shklovskii, 1970) and differential Galactic acceleration (Lorimer and Kramer, 2012). For the former we used the proper motion as measured from the second data release of Gaia (Gaia Collaboration, 2018), $\mu = 5.1 \pm 2.2\,mas\,yr^{-1}$. This caused an apparent excess $\dot{P}_{Shk}$ of $(8.3 \pm 3.6) \times 10^{-7} (d/1\,kpc)\,ms\,yr^{-1}$ where d is the distance. This term must be subtracted from the measured value to obtain the intrinsic $\dot{P}$. Similarly, differential Galactic acceleration leads to an apparent $\dot{P}_{DGR}$ of $-3.5 \times 10^{-7}\,ms\,yr^{-1}$ at a distance of 2.4 kpc, computed using the `MWPotential2014` potential (Bovy, 2015).

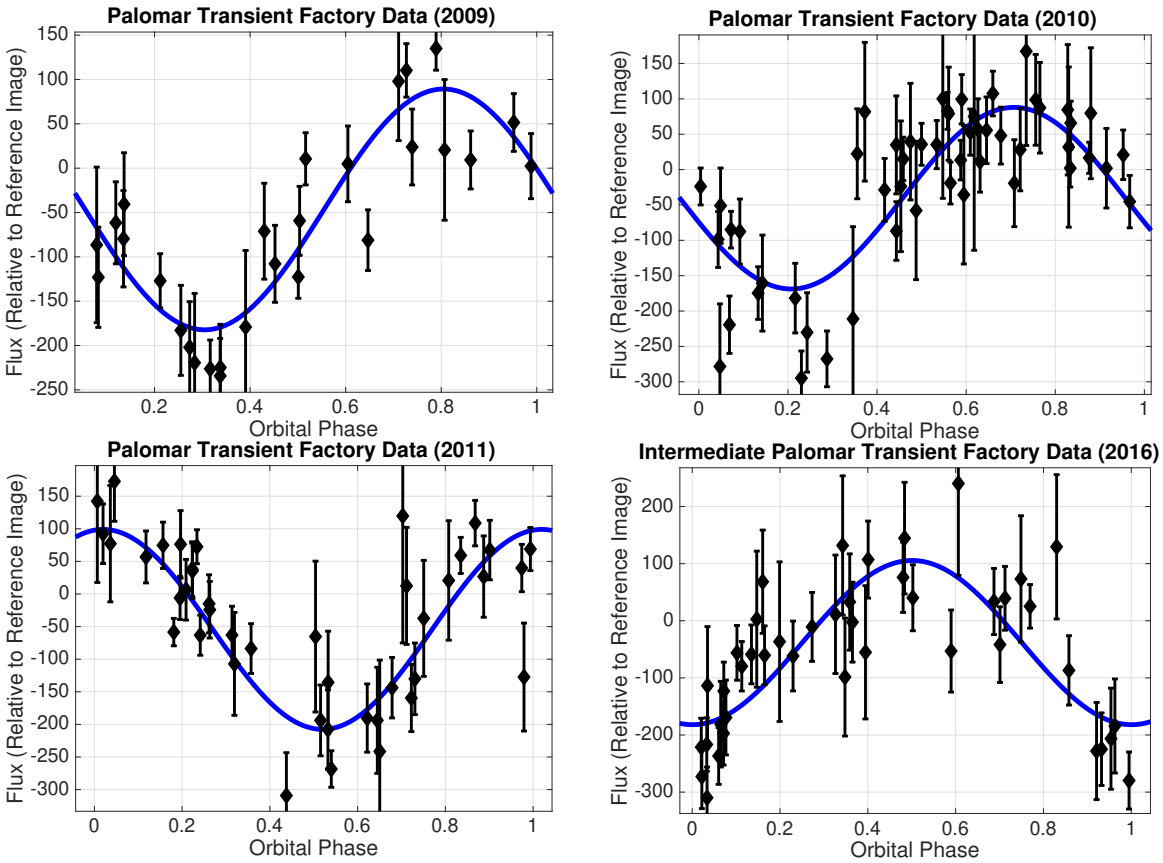

Figure 3.6: **Extended Data Figure 2: Fits to archival Palomar Transient Factory Data** Least squares fits of single harmonic sinusoids (smooth blue lines) to archival Palomar Transient Factory and Intermediate Palomar Transient Factory data used to determine the orbital decay rate. This archival data was extracted by using forced photometry on difference images. Because this is a least squares fit of a sinusoid to the data, this timing technique uses the reflection effect in the system as its primary clock, rather than the mid-eclipse time. All error bars are 1 sigma. To determine the time of the epoch, we take the mean of all epochs used, and then calculate the phase of eclipse nearest to this mean time.

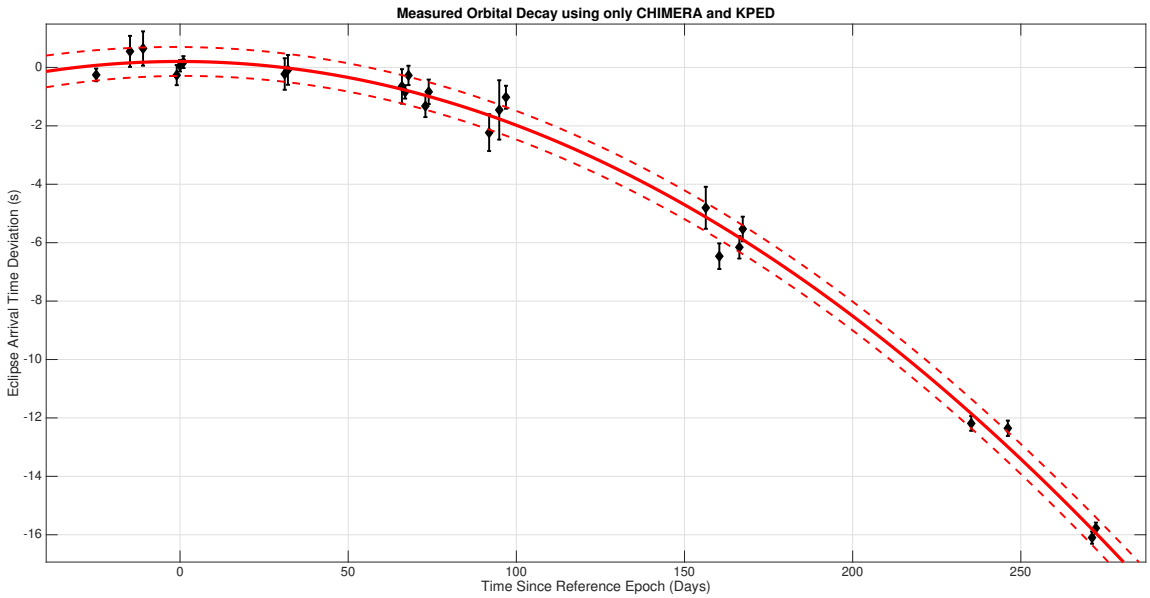

Figure 3.7: **Extended Data Figure 3: Orbital decay measured with CHIMERA and KPED** A quadratic fit (smooth red curve) to timing epochs exclusively originating from CHIMERA and KPED data (with the 68 percent confidence interval shown by the red dashed lines). This solution yielded a $\dot{P}$ consistent with the much more precise solution derived by including PTF/iPTF data. All error bars on the timing epochs are 1 sigma.

Both of these contributions are significantly smaller than the measured $\dot{P}$ and are therefore negligible compared to the uncertainties from tidal contributions (Section 9).

3.5 Spectroscopic Analysis

To perform the spectroscopic analysis, first we coadded 317 individual spectra (all taken with a 52 s exposure) into 12 phase-bins, using the emphemeris for the mid-eclipse time of the primary eclipse to define phase 0. We then fit stellar atmospheric models (Levenhagen et al., 2017) and obtained measurements of the logarithm of the surface gravity of the primary, $\log(g)_1$, and its effective photospheric temperature, $T_{eff,1}$, using the spectrum immediately after the phase of the primary eclipse (phase 0.0833), to minimize the flux contributed by the irradiated face of the secondary (Figure 3a).

In order to measure radial-velocity semi-amplitudes of the objects, K_1 and K_2, we used a double Gaussian model to fit the line associated with the hydrogen $n = 5$ to $n = 2$

transition in each phase-binned spectrum to extract the Doppler shifts of the emission and absorption lines.

To derive overall radial velocities, we adopted an out-of-phase sine wave model for the absorption and emission features,

$$v_1(j) = K_{1measured} \sin\left(\frac{2\pi j}{12}\right) + A, \quad v_2(j) = K_{2measured} \sin\left(\frac{2\pi j}{12} + \pi\right) + B, \tag{3.2}$$

where j encodes the index of the phase-bin and A and B are the systemic velocities of each white dwarf, $K_{1measured}$ and $K_{2measured}$ are the observed velocity semi-amplitudes, and $v_1(j)$ and $v_2(j)$ are the Doppler shifted velocities associated with each phase-bin (Extended Data Figure 4). We required the two systemic velocities to satisfy $A > B$ when sampling, because the gravitational redshift of the primary should exceed that of the secondary because of the primary's larger surface gravity. We used a Kernel Density Estimator (KDE) applied to the posterior distributions for the measured velocity semi-amplitudes $K_{1measured}$ and $K_{2measured}$ to assign the probabilities when sampling.

In order to derive masses from these spectroscopic fits, we applied corrections to the measured velocity semi-amplitudes. First, we applied a smearing correction of 20% to both $K_{1measured}$ and $K_{2measured}$, due to our phase-binned spectra each being co-additions of spectra taken over a third of the orbital phase (though each individual spectrum was taken over only an eighth of the orbital phase, broader coadditions were necessary to reach sufficient SNR for measuring radial velocities). We used a prior of $C = 0.68 \pm 0.04$ for the center of light correction term, based on the mass ratio estimate (Horne and Schneider, 1989). This modified the velocity amplitude of the secondary by:

$$K_2 = \frac{K_{2measured}}{1 - C\frac{R_2}{a}(1+q)}, \tag{3.3}$$

where R_2/a was taken from the lightcurve fitting, and the mass ratio was defined as $q = K_1/K_2$ (thus requiring us to solve this expression to isolate K_2). We applied the center-of-light correction to the secondary, because one face of it is heavily irradiated (meaning that the emission lines arise from a location different than the center of mass).

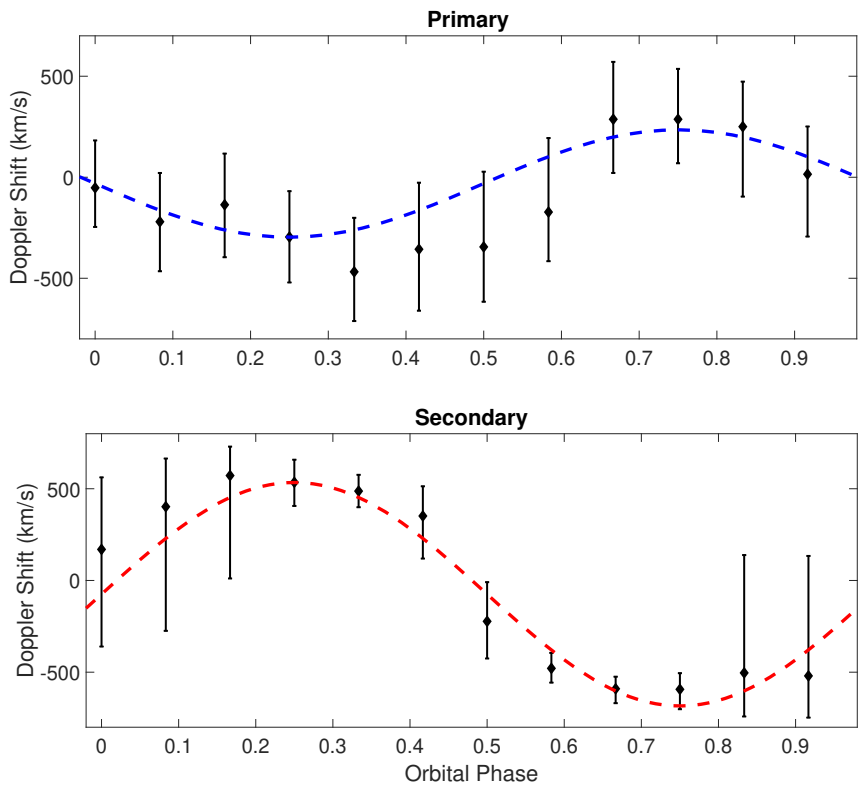

Figure 3.8: **Extended Data Figure 4: Radial velocity measurements of ZTFJ1539+5027** A plot of the measured Doppler shifts vs. orbital phase for the primary and secondary. The primary eclipse occurs at orbital phase 0. In the top panel, we plot measured Doppler shifts of the more massive primary, extracted from 12 phase bins of coadded spectra. The dashed blue line illustrates the fit of a sinusoid to this data (adjusted $R^2 = 0.7118$). The lower panel shows the Doppler shift measurements of the secondary, and also the best-fit sinusoid to this data (adjusted $R^2 = 0.9757$). Because of the low SNR of the spectra, these fits have large uncertainties (especially in the case of the primary, with its shallow and broad absorption lines). This is reflected in the broad distribution of possible masses associated with the spectroscopic constraint illustrated in Figure 3.4. All error bars are 68% CIs.

3.6 Mass and Radius Analysis

There are three main constraints that contribute to the overall mass and radius estimates.

6.1 Spectroscopic Constraint:

Using Kepler's law and Classical Mechanics, we can relate the velocity semi-amplitude, inclination, and period of a binary to the masses with a binary mass function:

$$\frac{M_2^3 \sin^3(i)}{(M_1 + M_2)^2} = \frac{PK_1^3}{2\pi G}, \tag{3.4}$$

where G is the gravitational constant. Because we have measured both K_1 and K_2, as well as P and i, we can write two such equations, and derive constraints on the two masses (Figure 4).

6.2 White Dwarf Model Constraint:

We used a mass-radius relation from models for a carbon-oxygen white dwarf (Althaus, Camisassa, et al., 2015), which depends on mass, metallicity, hydrogen fractional mass in the atmosphere, and radius, together with the spectroscopic measurements of $T_{eff,1}$ and $\log(g)_1$, to derive constraints on these properties. In these fits, we marginalized over metalicity and hydrogen mass fraction. We used the measured ratio of the radius of the primary to the semi-major axis $\frac{R_1}{a}$ (from the lightcurve modelling), and combined this with Kepler's law, and the white dwarf model constraints (Althaus, Camisassa, et al., 2015), to constrain the system parameters. This also weakly constrains the mass of the secondary, which enters into Kepler's law as contributing to the total mass of the system.

6.3 Chirp Mass Fit:

We used the measured $\dot{f}$ to infer the chirp mass, $M_c = \frac{(M_1 M_2)^{\frac{3}{5}}}{(M_1+M_2)^{\frac{1}{5}}}$, which is be related to the orbital decay rate by Equation 5:

$$\dot{f} = \frac{96}{5}\pi^{\frac{8}{3}} \left(\frac{GM_c}{c^3}\right)^{\frac{5}{3}} f^{\frac{11}{3}}, \tag{3.5}$$

where c is the speed of light. Because the chirp mass inferred from $\dot{f}$ assumes the decay is caused purely by general relativity, we also computed a chirp mass assuming a 10

percent tidal contribution to $\dot{f}$ as a lower bound on M_c.

6.4 Combined Fit:

To combine all of the constraints described above, we created a KDE based on the M_1 and M_2 estimates from the spectroscopic, white dwarf model, and chirp mass constraints. The posterior distribution of this combined analysis yielded the values for the masses reported in Table 1. The radii were computed using r_1 and r_2 from the lightcurve modelling, and the semi-major axis a determined with the masses and the orbital period.

3.7 Distance Estimate

Because no reliable parallax measurement exists for ZTF J1539+5027, we instead used its bolometric luminosity to estimate the distance. First, we measured the apparent magnitude of the hot primary without contribution from the irradiated face of the secondary by performing a least squares fit of a sinusoid to the ZTF-g lightcurve, omitting data from the eclipse, and measuring the minimum of this sinusoid. This yields an apparent ZTF-g band apparent magnitude of 20.38 ± 0.05.

Next, we used the atmospherically determined temperature of the primary, $T_{eff,1} \approx 48,900\,K$, to infer the absolute g' luminosity of the $0.6\,M_\odot$ DA white dwarf (Holberg and Bergeron, 2006). The spectroscopic temperature puts ZTF J1539+5027 approximately between two temperatures in the models–one corresponding to $T_{eff,1} = 45,000\,K$ and the other to $T_{eff,1} = 55,000\,K$. These corresponded to g' absolute magnitudes of 8.71 and 8.35, respectively, and we adopted these values as the lower and upper bounds on the object's absolute luminosity, and assume a uniform distribution of possible absolute luminosities between these values. Using this to solve for the distance of the object, we estimated a distance of $d = 2.34 \pm 0.14\,kpc$, though we emphasize that the error bars derived using atmospherically determined quantities tend to be underestimated. We also incorporated a uniform distribution of $E(B-V)$ in the range of 0 to 0.04 to account for the effects of extinction at these coordinates (Green, Hermes, et al., 2018).

3.8 Gravitational Wave Strain

The expression for the characteristic strain (Korol, Rossi, Groot, et al., 2017) used in Figure 2b (including the value plotted for ZTF J1539+5027) is:

$$S_c = \frac{2(GM_c)^{5/3}(\pi f)^{2/3}}{c^4 d}\sqrt{fT_{obs}}, \tag{3.6}$$

where d is the distance to the object, T_{obs} is the integrated observation time of the *LISA* mission. Though it is the conventional quantity used to construct such diagrams, the characteristic strain does not capture any information about source inclination, detector response, etc.

In order to compute the signal to noise (Korol, Rossi, Groot, et al., 2017) for *LISA*, we directly invoked the signal amplitude at the detector $A = \sqrt{|F_+|^2|h_+|^2 + |F_\times|^2|h_\times|^2}$, where h_+ and $h_\times$ are the two gravitational wave polarization amplitudes, and F_+ and $F_\times$ are the *LISA* detector response patterns corresponding to these polarizations. The h_+ polarization amplitude includes a factor of $(1 + \cos^2(i))$ and the $h_\times$ polarization a factor of $2\cos(i)$, meaning that systems like ZTF J1539+5027 with an inclination close to 90 degrees exhibit a gravitational wave signal up to a factor of $\sqrt{8}$ smaller than an equivalent face-on system with an inclination close to 0 degrees in situations where $F_+ \approx F_\times$. In Table 1, we include an estimate for both the SNR of ZTF J1539+5027, and SDSS J0651+2844 computed using the same technique.

3.9 Tidal Effects

Tidal Contribution to Orbital Decay

Tidal dissipation can transfer orbital energy into rotational and thermal energy within the stars. The former effect can cause the orbit to decay slightly faster than gravitational radiation alone, while the latter effect can increase the surface temperatures of the stars. Studies of tidal synchronization and heating predict that tidal energy dissipation scales more strongly with orbital period than gravitational radiation (Fuller and Lai, 2012; Fuller and Lai, 2013). As the orbit decays and the white dwarfs draw nearer to each other, tides begin to act on a shorter timescale than orbital decay, spinning up the stars toward synchronous rotation. The “critical" orbital period, P_c, below which tidal spin-up can occur faster than orbital decay, lies in the range $P_c \sim 45 - 130$ minutes (Fuller and

Lai, 2012), depending on the white dwarf mass and age. In any case, at an orbital period of only 6.91 minutes, we expect the stars in ZTF J1539+5027 to be spinning synchronously with the orbit. In this regime, the rate of tidal energy transfer from the orbit to the stellar interiors is

$$\dot{E}_{tide} \simeq 4\pi^2 I \frac{\dot{P}_{GW}}{P^3}\,, \tag{3.7}$$

where $I = I_1 + I_2$ is the combined moment of inertia of the two stars, and $\dot{P}_{GW}$ is the orbital period decay caused by gravitational waves.

Comparing Equation 3.7 with the orbital energy lost to gravitational wave emission, the tidal contribution $\dot{P}_{tide}$ to the total orbital decay rate $\dot{P}$ is given by

$$\frac{\dot{P}_{tide}}{\dot{P}_{GW}} \simeq \frac{12\pi^2 I a}{G M_1 M_2 P^2}\,. \tag{3.8}$$

The moment of inertia of star 1 is $I_1 = \kappa_1 M_1 R_1^2$ (and similarly for star 2), where κ_1 is a dimensionless constant determined by the internal structure of the white dwarf. Equation 3.8 can also be written as

$$\frac{\dot{P}_{tide}}{\dot{P}_{GW}} \simeq \frac{3(M_1+M_2)^2}{M_1 M_2}\left[\kappa_1 \frac{M_1}{M_1+M_2}\left(\frac{R_1}{a}\right)^2 + \kappa_2 \frac{M_2}{M_1+M_2}\left(\frac{R_2}{a}\right)^2\right]. \tag{3.9}$$

From the white dwarf models (Section 3.10), we find $\kappa_1 \simeq 0.14$ and $\kappa_2 \simeq 0.11$. Using $M_1 \simeq 0.61 M_\odot$, $M_2 \simeq 0.21 M_\odot$, $R_1/a \simeq 0.14$, $R_2/a \simeq 0.28$, we find $\dot{P}_{tide}/\dot{P}_{GW} \simeq 0.067$. Thus, we expect the orbit to decay several percent faster than gravitational radiation alone, provided that the stars are tidally locked. There is an additional effect of orbital decay caused by orbital energy used to raise a tidal bulge in each star (Benacquista, 2011; Shah, Nelemans, et al., 2013), but we find it to be more than an order of magnitude smaller than Equation 3.9.

Tidal Heating

The tidal energy dissipation within the white dwarfs is partitioned between kinetic energy used to spin up the white dwarfs and heat that can diffuse out and increase their surface temperatures. For an aligned, sub-synchronous and rigidly rotating white dwarf, the ratio of tidal heating to tidal energy dissipation is $\dot{E}_{heat}/\dot{E}_{tide} = 1 - P/P_{spin}$, where P_{spin} is the spin period of the white dwarf (Fuller and Lai, 2012). At orbital periods

below the critical value P_c, the spin period, P_{spin}, decreases to approach the orbital period. Calculations suggest that the tidal heating rate in this regime is expected to be $\dot{E}_{heat} \sim \dot{E}_{tide}(P/P_c)$ (Fuller and Lai, 2013), such that the tidal heating rate is much smaller than the energy dissipation rate, because most of the energy is converted to rotational energy.

To estimate an upper limit on the surface temperature of each white dwarf that can be obtained from tidal heating alone, we assume $\dot{E}_{heat} \sim \dot{E}_{tide} \approx 6\pi^2 I/(P^2 t_{GW})$, where $t_{GW} = \frac{3}{2}\frac{P}{|\dot{P}|}$ is the gravitational wave timescale. If the tidal heat is instantaneously reradiated, this corresponds to a surface temperature

$$\begin{aligned} T_{tide} &= \left(\frac{\dot{E}_{heat}}{4\pi\sigma_B R^2}\right)^{1/4} \\ &= \left(\frac{3\pi\kappa M}{2\sigma_B P^2 t_{GW}}\right)^{1/4}, \end{aligned} \tag{3.10}$$

where σ_B is the Stefan-Boltzmann constant, and M is the mass of the white dwarf. Note that this temperature depends only weakly on the white dwarf mass and moment of inertia, and is independent of the white dwarf radius. Using the same values as above and the measured value $t_{GW} \approx 830,000\,yr$, we find an upper limit of $T_{tide} \approx 44,000\,K$ for the primary white dwarf. However, accounting for the suppression factor $P/P_c \sim 6.9/60$, such that $\dot{E}_{heat} \sim \dot{E}_{tide}(P/P_c)$, yields a more realistic temperature $T_{tide} \approx 25,000\,K$. Hence, while tidal heating may be able to heat the primary to temperatures near that observed, our best estimate suggests substantially lower temperatures. Applying Equation 3.10 to the secondary white dwarf predicts an upper limit due to tidal heating of $T_{tide} \approx 33,000\,K$, but our best estimate is $T_{tide} \approx 19,000\,K$. A measured nightside temperature near this value would be consistent with tidal heat powering the nightside flux of the secondary. However, the value of the surface brightness ratio in g' suggests a secondary temperature of $T_{eff,2} < 10,000\,K$.

3.10 Binary Models

To understand the evolutionary state of ZTF J1539+5027, we have constructed several binary models using the MESA stellar evolution code (Paxton, Marchant, et al., 2015). The models contain a helium white dwarf of 0.2 or 0.25 $M_\odot$ with a point mass companion

of 0.6 or 0.55 $M_\odot$. The mass of the hydrogen envelope of the helium white dwarf is then reduced to the values shown in Extended Data Figure 5. We initialize these runs at orbital periods of 1 hour to mimic the end of a common envelope event that formed the tight binary. The helium white dwarf is evolved simultaneously with the orbit, with angular momentum losses due to gravitational waves and fully non-conservative mass transfer.

Extended Data Figure 5 shows a plot of the mass loss rate from the secondary as function of orbital period. The secondary overflows its Roche lobe and begins mass transfer at orbital periods ranging from $P \sim 6.5 - 13$ minutes, and the expected mass loss rates at $P = 7$ minutes are typically $\dot{M} \sim 3 \times 10^{-9}\, M_\odot\, yr^{-1}$ (ranging from 0 up to $10^{-8}\, M_\odot\, yr^{-1}$, depending on the white dwarf masses and hydrogen envelope mass). During the initial phase of slow mass transfer, the secondary loses its non-degenerate hydrogen envelope as the Roche lobe contracts inward. The mass accreting onto the primary can greatly heat it as gravitational potential energy is converted to heat. The energy released by accretion is $\dot{E}_{accrete} \sim GM_1\dot{M}/R_1$, with order unity corrections due to its non-zero kinetic and gravitational energy when it is lost from the secondary. We do not evolve the primary (accretor), but we may crudely estimate its temperature by assuming that the accretion energy is uniformly radiated as a blackbody over its surface. The corresponding accretion temperature (assuming 100% efficiency) is

$$T_{accretion} = \left(\frac{GM_1\dot{M}}{4\pi\sigma_B R^3}\right)^{1/4}. \tag{3.11}$$

The bottom panel of Extended Data Figure 5 shows that once mass transfer begins, it can easily increase the primary's temperature to $T_1 \gtrsim 50,000\, K$.

3.11 Constraint on Accretion

Although accretion could explain the high temperature of the primary, we have not detected any evidence of ongoing mass-transfer. We have constrained the possibility of active accretion contributing luminosity to an accretion hot spot using both optical and X-ray data. The upper limit we inferred is $\dot{M} < 2 \times 10^{-8} M_\odot\, yr^{-1}$, and this is only possible in a very narrow hot spot temperature range (Extended Data Figure 6). For both the optical and X-ray constraint we have assumed that only 10% of accretion energy

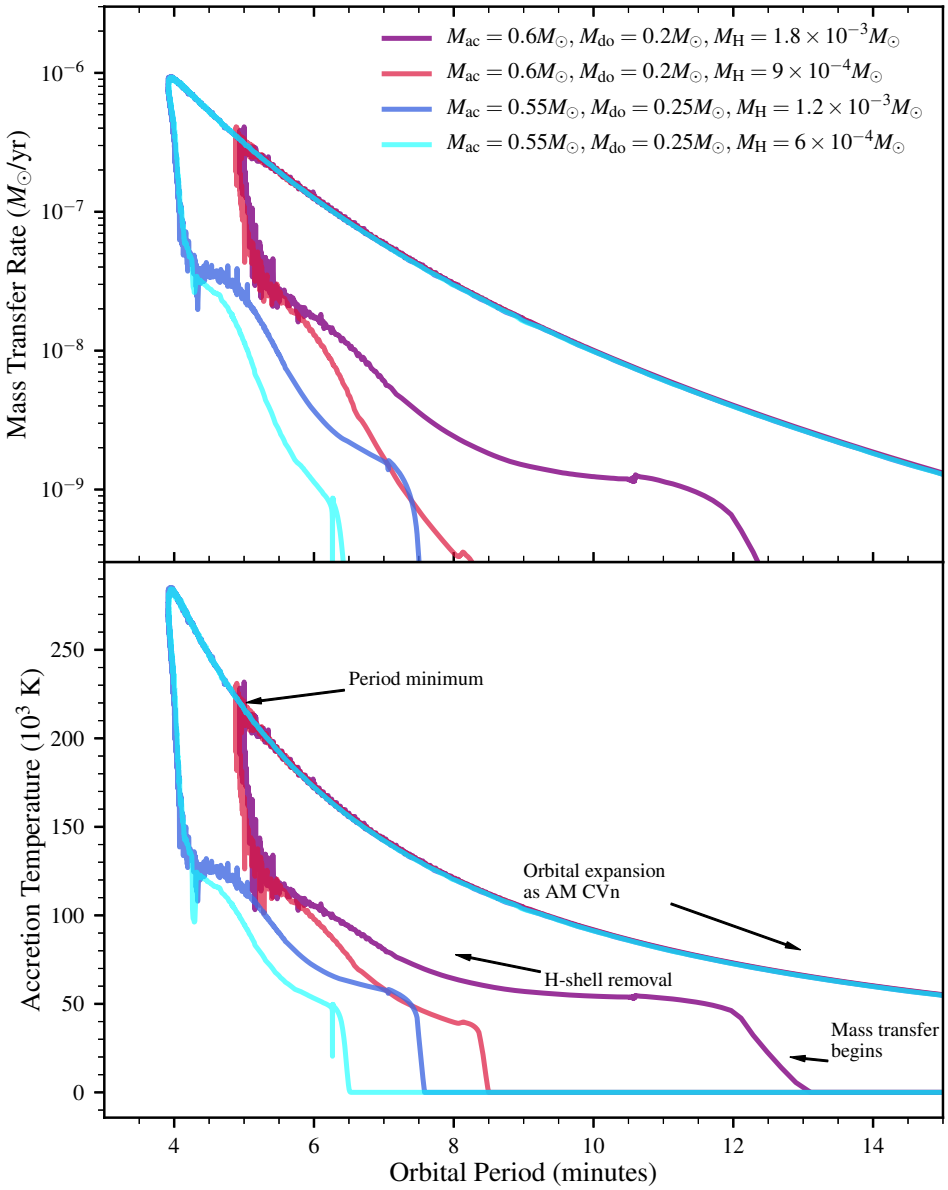

Figure 3.9: **Extended Data Figure 5: Binary evolution models** Binary stellar evolution models for systems similar to ZTF J1539+5027. **Top:** Mass transfer rate as a function of orbital period. Systems begin at large orbital period and move towards smaller period due to gravitational radiation, and in some cases they move back out due to stable mass transfer. Except for high-mass donors with thin hydrogen envelopes, mass transfer is expected to begin at orbital periods longer than 7 minutes. **Bottom:** Corresponding accretion temperature from Equation 3.11.

is being converted to the luminosity of the hot spot. This is based on a model where we assume 90% of the accretion energy is being deposited into heating the optically thick photosphere of the white dwarf, while only 10% is contributing to luminosity immediatly re-radiated in the form of a hot spot. We estimated the upper limit by computing the X-ray flux using NASA's WebPIMMS mission count rate simulator, using a 3-sigma upper limit on the background count rate determined from the X-ray images. We assumed a hydrogen column density (Kalberla et al., 2005) of $nH = 1.5 \times 10^{20}\, cm^{-2}$. We used the distance of $d = 2.4\, kpc$ to convert the upper limit on the unabsorbed X-ray flux to an X-ray luminosity. For the optical constraint, we computed an upper limit on the optical luminosity of the hot spot as 10% the luminosity of the photosphere of the hot primary, based on an absence of emission lines in our coadded spectra, which have an SNR of approximately 10. We calculated the upper limit on $\dot{M}$ at various temperatures by integrating a Planck function at the corresponding temperature over the instrument passbands, and then computed the maximum bolometric luminosity, $L_{accretion}$, an emitting region at this temperature could have and still be consistent with the non-detections in these passbands. We then determined the corresponding upper limit on $\dot{M}$ by equating $L_{accretion} = 0.1 G M_1 \dot{M} / R_1$. We obtained the XMM EPIC-pn data from the public XMM-Newton science archive (observation ID: 0800971501 PI: Pratt, Gabriel). The SWIFT observation was obtained with our own program (observation ID: 00010787001, 00010787002 PI: Kulkarni).

3.12 Novae

The high temperature of the primary may plausibly be explained if the white dwarf is cooling after having recently undergone a nova outburst, caused by accretion of hydrogen from the secondary or a tidally induced nova (Fuller and Lai, 2012). The nova likely ejects an amount of mass comparable to the hydrogen shell mass which must be accreted, which for a $0.6 M_\odot$ white dwarf is $M_H \sim 10^{-4}\, M_\odot$ (Wolf et al., 2013). Following the nova, the orbit widens slightly, and the system is brought out of contact such that mass transfer from the secondary ceases. The change in semi-major axis following the loss of the nova shell is $\Delta a / a \sim M_H / (M_1 + M_2)$. The length of time the binary is detached

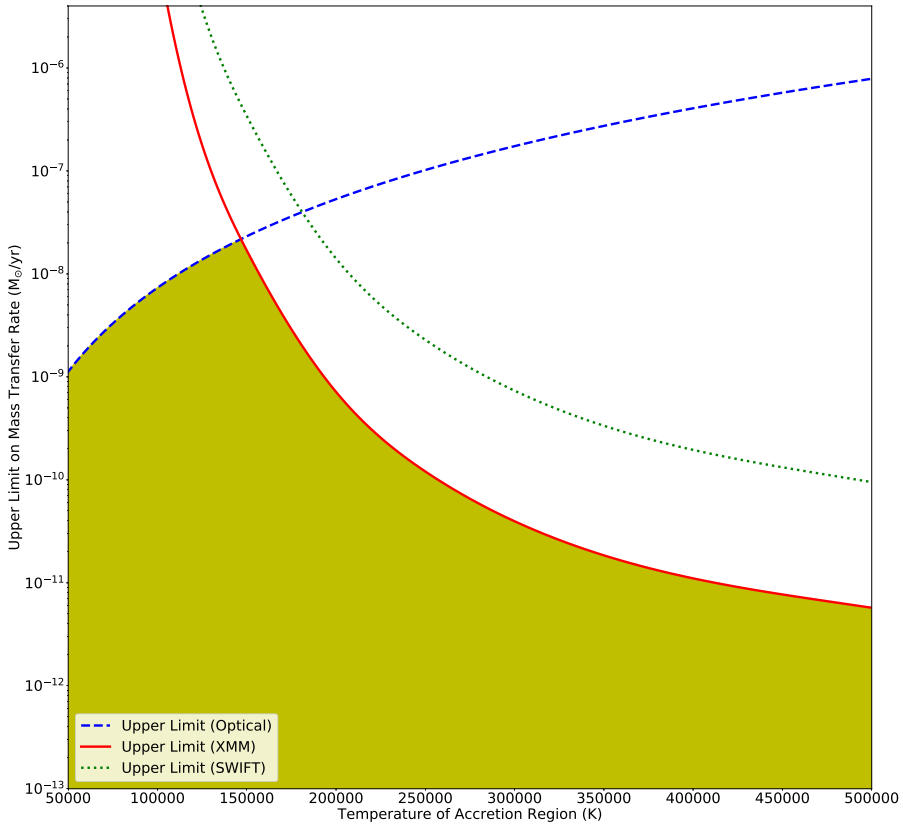

Figure 3.10: **Extended Data Figure 6: X-ray and optical constraints on accretion in ZTFJ1539+5027** The constraints on mass transfer resulting from the non-detection of any signatures of accretion in both the optical and X-ray bands. The upper limits are expressed in terms of the mass accretion rate contributing to the accretion luminosity of a hypothetical hot spot. The solid red curve illustrates the constraint imposed by the XMM EPIC-pn X-ray non-detection, which rules out significant mass transfer contributing to a hot spot with temperatures greater than $\approx 150,000\,K$, while the green dotted line illustrates a weaker upper limit imposed by the non-detection in a SWIFT XRT observation. We constructed the dashed blue curve, which represents the optical constraint, by requiring that any accretion luminosity originating from a hot spot should contribute $< 10\%$ to the luminosity in the band ranging from 320 to 540 nm, as we know from the optical spectrum (Figure 3.3) that this light is dominated by the $\approx 50,000\,K$ photosphere of the hot primary, and also see no signature of a hot spot in the CHIMERA lightcurve (Figure 3.1). We chose the threshold of $< 10\%$, because given the SNR of the spectra, we expect we should be able to detect optically thin emission with an amplitude at the 10% level. Other white dwarfs with such a hot spot (such as HM Cancri) exhibit such emission, particularly in lines associated with ionized helium.

before gravitational wave emission brings the system back into contact is

$$t_{detach} = t_{GW}\frac{\Delta a}{a} \sim t_{GW}\frac{M_H}{M_1 + M_2}\,. \tag{3.12}$$

Using $M_H = 10^{-4}\,M_\odot$, we estimate $t_{detach} \sim 100$ yr. This can be compared to the time spent accreting mass between subsequent novae.

$$t_{accrete} = \frac{M_H}{\dot{M}}\,. \tag{3.13}$$

As the non-degenerate hydrogen envelope of the low-mass secondary is stripped off (see discussion in (Kaplan, Bildsten, et al., 2012)), the approximate mass transfer rate is expected to be $\dot{M} \lesssim 10^{-8} M_\odot\, yr^{-1}$ (Extended Data Figure 5). The time between novae outbursts is thus $t_{accrete} \gtrsim 10^4$ years. Then the ratio of time spent in a detached state relative to an accreting state is $t_{detach}/t_{accrete} < 10^{-2}$. Hence, while it is possible that the system is in a detached state following a nova caused by mass transfer, the chances of catching the system in this state are small. To help rule out the possibility, we used the WASP instrument on the Hale telescope to obtain a deep H-α image of the field and found no evidence for a remnant nova shell; however, this analysis was limited by the lack of an off-band image.

3.13 Population Implications

From (Brown, Kilic, Kenyon, et al., 2016), the merger rate of He+CO WDs in the Milky Way is roughly 0.003 yr^{-1}. This number is reached from both observational and population synthesis arguments. The number of systems with decay time equal or less than the ~210 kyr decay time of ZTF J1539+5027 is thus ~630. Out to the distance of 2.3 kpc, given a local surface density of 68 $M_\odot\, pc^{-2}$ from (Bovy and Rix, 2013), the stellar mass is $\sim 10^9\, M_\odot$, roughly 2% of the total disk mass of $\sim 5 \times 10^9\, M_\odot$. We thus expect to find ~13 binaries with a similar distance and merging timescale as ZTF J1539+5027. The fraction of eclipsing systems is roughly $R/a \sim 0.25$ for our measured parameters, hence we may expect ~3 eclipsing systems like ZTF J1539+5027. ZTF can detect such systems in most of the volume out to its distance, as long as they are as bright as this system. We may be missing slightly longer period systems that are dimmer because they have not yet started mass transfer. We comment that the estimate

from (Brown, Kilic, Kenyon, et al., 2016) found that many double WDs must be born at short orbital periods in order to explain the abundance of short period systems relative to longer period systems, and ZTF J1539+5027 may support that conclusion.

Chapter 4

AN 8.8 MINUTE ORBITAL PERIOD ECLIPSING DETACHED DOUBLE WHITE DWARF BINARY

Burdge, K. B. et al. (2020). "An 8.8 Minute Orbital Period Eclipsing Detached Double White Dwarf Binary". In: *ApJL* 905.1, p. L7. DOI: 10.3847/2041-8213/abca91. arXiv: 2010.03555 [astro-ph.SR].

Kevin. B. Burdge[1], Michael W. Coughlin[2], Jim Fuller[1], David L. Kaplan[3], S. R. Kulkarni[1], Thomas R. Marsh[4], Eric C. Bellm[5], Richard G. Dekany[6], Dmitry A. Duev[1], Matthew J. Graham[1], Ashish A. Mahabal[1], Frank J. Masci[7], Russ R. Laher[7], Reed Riddle[6], Maayane T. Soumagnac[8], Thomas A. Prince[1]

[1]Division of Physics, Mathematics and Astronomy, California Institute of Technology, Pasadena, CA 91125, USA
[2]School of Physics and Astronomy, University of Minnesota, Minneapolis, Minnesota 55455, USA
[3]Department of Physics, University of Wisconsin-Milwaukee, Milwaukee, WI 53211, USA
[4]Department of Physics, University of Warwick, Coventry CV4 7AL, UK
[5]DIRAC Institute, Department of Astronomy, University of Washington, 3910 15th Avenue NE, Seattle, WA 98195, USA
[6]Caltech Optical Observatories, California Institute of Technology, Pasadena, CA, USA
[7]IPAC, California Institute of Technology, 1200 E. California Blvd, Pasadena, CA 91125, USA
[8]Lawrence Berkeley National Laboratory, 1 Cyclotron Road, Berkeley, CA 94720, USA
[9]Benoziyo Center for Astrophysics, Weizmann Institute of Science, 76100 Rehovot, Israel
[10]Infrared Processing and Analysis Center, California Institute of Technology, 1200 E. California Blvd, Pasadena, CA 91125, USA

ABSTRACT

We report the discovery of ZTF J2243+5242, an eclipsing double white dwarf binary with an orbital period of just 8.8 minutes, the second known eclipsing binary with an orbital period less than ten minutes. The system likely consists of two low-mass white dwarfs, and will merge in approximately 400,000 years to form either an isolated hot subdwarf or an R Coronae Borealis star. Like its 6.91 *min* counterpart, ZTF J1539+5027, ZTF J2243+5242 will be among the strongest gravitational wave sources detectable by the space-based gravitational-wave detector *The Laser Space Interferometer Antenna* (*LISA*) because its gravitational-wave frequency falls near the peak of *LISA*'s sensitivity. Based on its estimated distance of $d = 2425^{+108}_{-114}\,pc$, *LISA* should detect the source within its first few months of operation, and should achieve a signal-to-noise ratio of 63 ± 7 after four years. We find component masses of $M_A = 0.323^{+0.065}_{-0.047}\,M_\odot$ and $M_B = 0.335^{+0.052}_{-0.054}\,M_\odot$, radii of $R_A = 0.0298^{+0.0013}_{-0.0012}\,R_\odot$ and $R_B = 0.0275^{+0.0012}_{-0.0013}\,R_\odot$, and effective temperatures of $T_A = 26300^{+1700}_{-900}\,K$ and $T_B = 19200^{+1500}_{-900}\,K$. We determined all of these properties, and the distance to this system, using only photometric measurements, demonstrating a feasible way to estimate parameters for the large population of optically faint ($r > 21\,m_{AB}$) gravitational-wave sources which the Vera Rubin Observatory (VRO) and *LISA* should identify.

4.1 Introduction

The population of known double white dwarfs (DWDs) which will merge within a Hubble time (orbital periods $\lesssim 12\,hrs$) has increased substantially over the last decade, in large part due to efforts such as the extremely low mass white dwarf (ELM) survey (Brown, Kilic, Allende Prieto, and Kenyon, 2010; Kilic, Brown, Allende Prieto, Agüeros, et al., 2011; Brown, Kilic, Allende Prieto, and Kenyon, 2012; Kilic, Brown, Allende Prieto, Kenyon, et al., 2012; Brown, Kilic, Allende Prieto, Gianninas, et al., 2013; Gianninas, Kilic, et al., 2015; Brown, Gianninas, et al., 2016; Brown, Kilic, Kosakowski, Andrews, et al., 2020) and the Supernova Type Ia Progenitor (SPY) survey (Napiwotzki, Christlieb, et al., 2003; Napiwotzki, Karl, et al., 2020), several of which emit gravitational waves detectable with the *The Laser Space Interferometer Antenna* (*LISA*) (Amaro-Seoane et al., 2017). Over the past two years, through massive expansions in densely sampled time-domain photometric measurements, the Zwicky Transient Facility (ZTF) has facilitated a rapid growth in the population of known DWDs with orbital periods under an hour (Burdge, Prince, et al., 2020). Two of the sources discovered by ZTF so far, the eclipsing DWD binaries ZTF J1539+5027 ($P_b \approx 6.91\,min$) (Burdge, Coughlin, et al., 2019) and ZTF J0538+1953 ($P_b \approx 14.44\,min$) (Burdge, Prince, et al., 2020), should be detected by *LISA* with a high signal-to-noise ratio, enabling precise parameter estimation using gravitational waves (Littenberg and Cornish, 2019). Thus, using the gravitational wave signal from such a system combined with electromagentic constraints, we will be able to probe novel white dwarf (WD) physics such as the efficiency of tides in these objects (Piro, 2019).

Here, we report the discovery of ZTF J2243+5242, a DWD binary with an orbital period of just $8.8\,min$, the second shortest eclipsing binary system known at the time of discovery. ZTF J2243+5242 is a high signal-to-noise (SNR) *LISA*-detectable gravitational-wave source which should be detected within the first month of *LISA*'s operation and reach an SNR of 63 ± 7 four years into the mission. Unique among the binary systems known at $P_b < 10\,min$, this system likely consists of a pair of helium-core white dwarfs (He WDs) or hybrid (helium/CO core) WDs with a mass ratio near unity, suggesting that it will result in a merger (Marsh, Nelemans, et al., 2004). This binary is also unique among known $P_b < 10\,min$ systems because neither object is near to filling its

Roche lobe (our inferred parameters suggest $\frac{R}{R_L} \approx \frac{2}{3}$ for both objects, where R is the volume-averaged WD radius, and R_L is the radius of the Roche lobe), indicating that the system is well detached. Here, we discuss the properties of this system, its past and future evolutionary history, and prospects for the discovery of more such sources in the eras of *LISA*) and the Vera Rubin Observatory (VRO) (Ivezić et al., 2019).

4.2 Observations

Before we discuss the discovery and analysis of this object (Section 4.3), we briefly discuss the different data-sets and observations that we used.

ZTF Observations

ZTF is a northern sky synoptic survey based on observations with the 48-inch Samuel Oschin Schmidt telescope at Palomar Observatory (Bellm, Kulkarni, Graham, et al., 2019; Masci, Laher, Rusholme, et al., 2019; Graham, Kulkarni, et al., 2019; Dekany et al., 2020). The camera has a 47 deg^2 field of view, and reaches a 5σ limiting apparent magnitude of approximately 20.8 in g-band, 20.6 in r-band, and 20.2 in i-band, with standard 30 s exposures.

ZTF J2243+5242 had 218 r-band and 382 g-band good quality photometric detections in its ZTF archival lightcurves at the time of this writing. As illustrated by Figure 4.1, the discovery was enabled primarily by the g-band lightcurve, probably because the object is approximately 30% brighter in g-band than it is in r-band, and because ZTF is also more sensitive in g-band than in r-band (Masci, Laher, Rusholme, et al., 2019). Note that the ZTF archive only contains 5σ detections in science images, but in order to model the ZTF lightcurve, after discovery, we extracted forced photometry from ZTF difference images to obtain the best quality lightcurve possible (Yao et al., 2019). Using difference images helped improve the photometry significantly due to nearby bright star to the north west, as seen in the Pan-STARRS1 image cutout shown in Figure 4.2. The ZTF lightcurves extracted using forced photometry contained 1384 r-band and 827 g-band observations. The ZTF forced photometry lightcurves contain substantially more epochs than the archival lightcurves, as the archival lightcurves only include 5σ detections of the source in science images. Additionally, the ZTF archival lightcurves are constructed

by cross matching 5σ detections in individual science exposures with a seed catalog generated by the ZTF reference image constructed from a co-add of ZTF images in each field. In the case of ZTF J2243+5242, this seed catalog generated from the reference image missed the source entirely in one field, meaning that all of the several hundred epochs of photometry in that field are completely absent in the ZTF archive, even ones where the source was clearly detected at the 5σ level in individual exposures. It is possible that in ZTF Phase II, the data archive could be enhanced to include forced photometry, and a more robust seed catalog based on Pan-STARRS1 or *Gaia*.

High-speed photometry

We obtained high speed photometric follow-up of the system using the dual-channel high speed photometer CHIMERA (Harding et al., 2016) on the 200-inch Hale telescope at Palomar observatory. We conducted a campaign of observations over several nights, using g' as the blue channel filter, and alternating between r' and i' on the red channel. The phase-folded and binned lightcurves from these observations can be seen in Figure 4.3. We used a combination of $3\,s$ and $5\,s$ exposure times, due to variable conditions across our nights of observing. All CHIMERA data were reduced using a publicly available pipeline[1], with a newly implemented PSF photometry mode to accommodate reductions for this object, which has a bright neighboring star. Because we were not read-noise limited, we operated the CCD in frame transfer mode using the conventional (as opposed to the electron multiplying) 1 MHz amplifier. On nights of poor seeing ($> 1''$), we binned the readout 2x2 in order to reduce the read-noise. For further details, please see Table 5.7.

Spectroscopic follow-up

Using the Low-Resolution Imaging Spectrometer (LRIS) on the 10-m W. M. Keck I Telescope on Mauna Kea (Oke, Cohen, et al., 1995), we conducted phase-resolved spectroscopy on the object. We used an exposure time of $66\,s$, about one eighth of the orbital period, in order to avoid significant Doppler smearing over the course of an exposure. A co-added spectrum of one phase bin is illutrated in Figure 4.4. Due to issues with the red channel, we only analyzed data from the blue channel, which covered

[1] `https://github.com/mcoughlin/kp84`

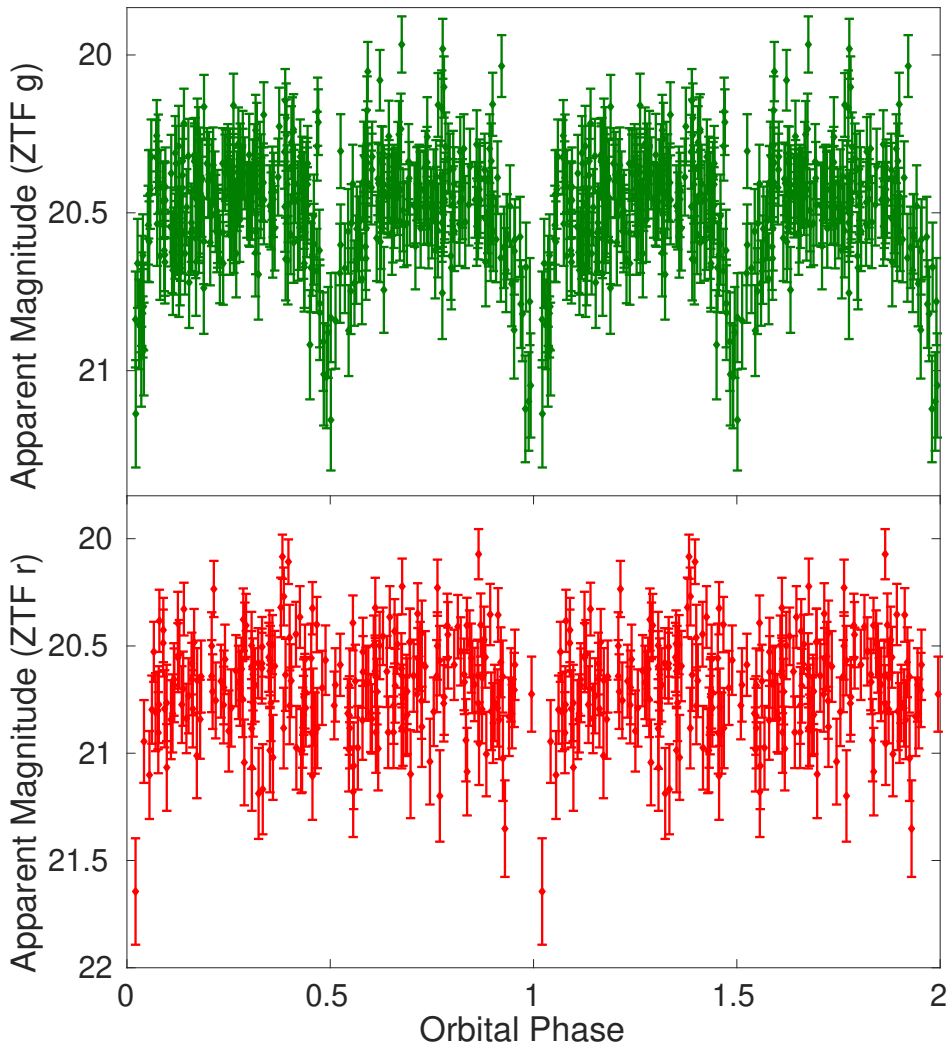

Figure 4.1: Archival ZTF g-band (top) and r-band (bottom) lightcurves of the system folded at a period of 527.934814 ± 0.000021 s. Because the system is 30 percent brighter in g-band than in r-band, and ZTF also slightly more sensitive in g-band, the discovery was enabled primarily by the g-band data.

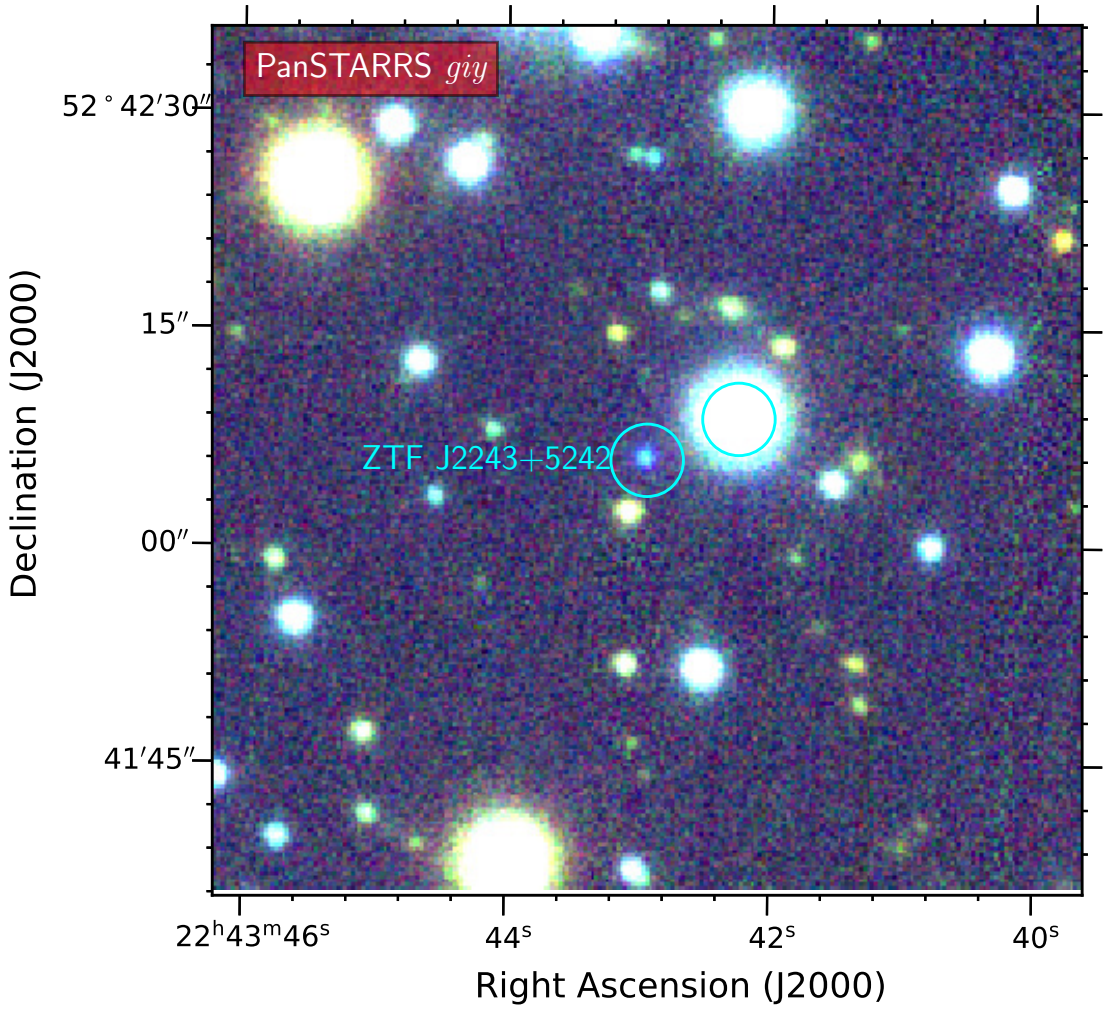

Figure 4.2: A 60″ × 60″ Pan-STARRS1 color giy-bands image of ZTF J2243+5242, which is the blue object in the center of the image. We illustrate 2.″5 apertures around the source and a nearby bright star in cyan. Due to the source's proximity to the bright star to the north west (*Gaia* $G \approx 14.5\, m_V$), we extracted forced difference image photometry for the ZTF lightcurve we used when modelling the source, PSF photometry for the CHIMERA high speed photometry, and used a 2.″5 aperture for extracting Swift UVOT photometry rather than the default 5″ radius.

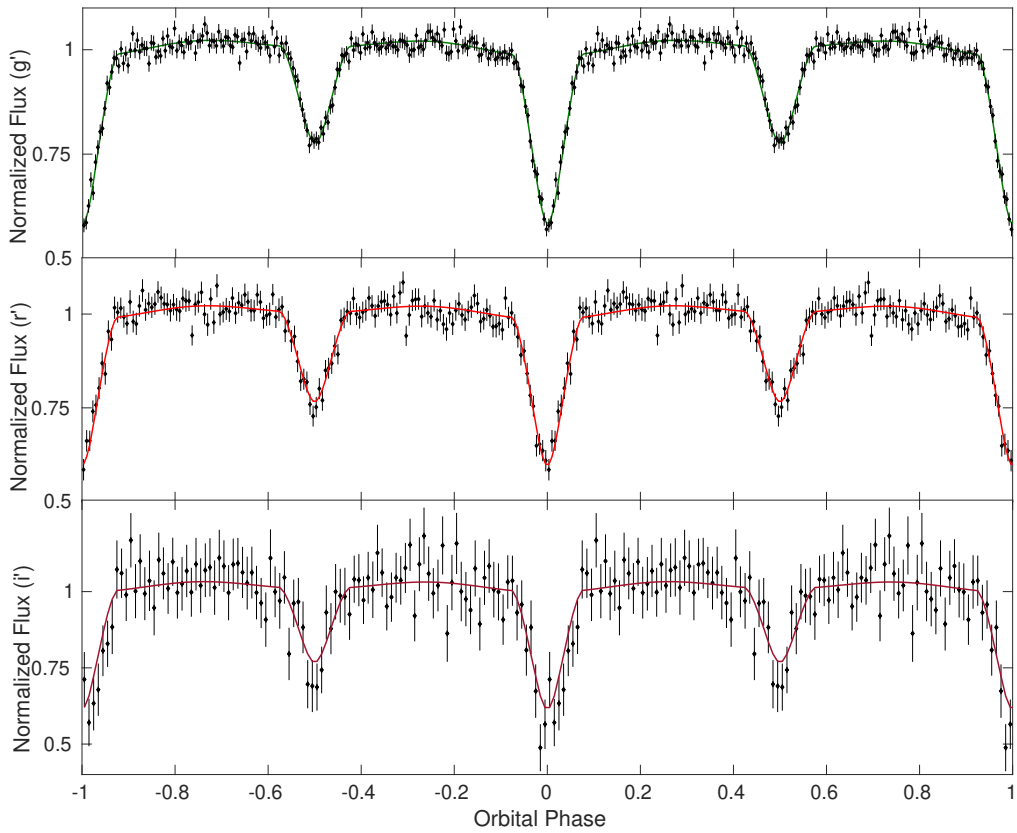

Figure 4.3: The binned, phase-folded CHIMERA g' (top), r' (middle), and i' (bottom) lightcurves of the system, with the best fit LCURVE (Copperwheat et al., 2010) model overplotted.

a wavelength range of approximately 3200 to 5500. We used the 600/4000 grism as the dispersive element, and binned the readout 4x4 in order to decrease the readout time to 30 s. We obtained a total of 312 exposures (see Table 5.7). We reduced the data with the publically available lpipe pipeline (Perley, 2019), and in order to construct our phase-binned spectra, we divided the orbital phase into 12 bins, and co-added all spectra with a mid-exposure time falling within each bin.

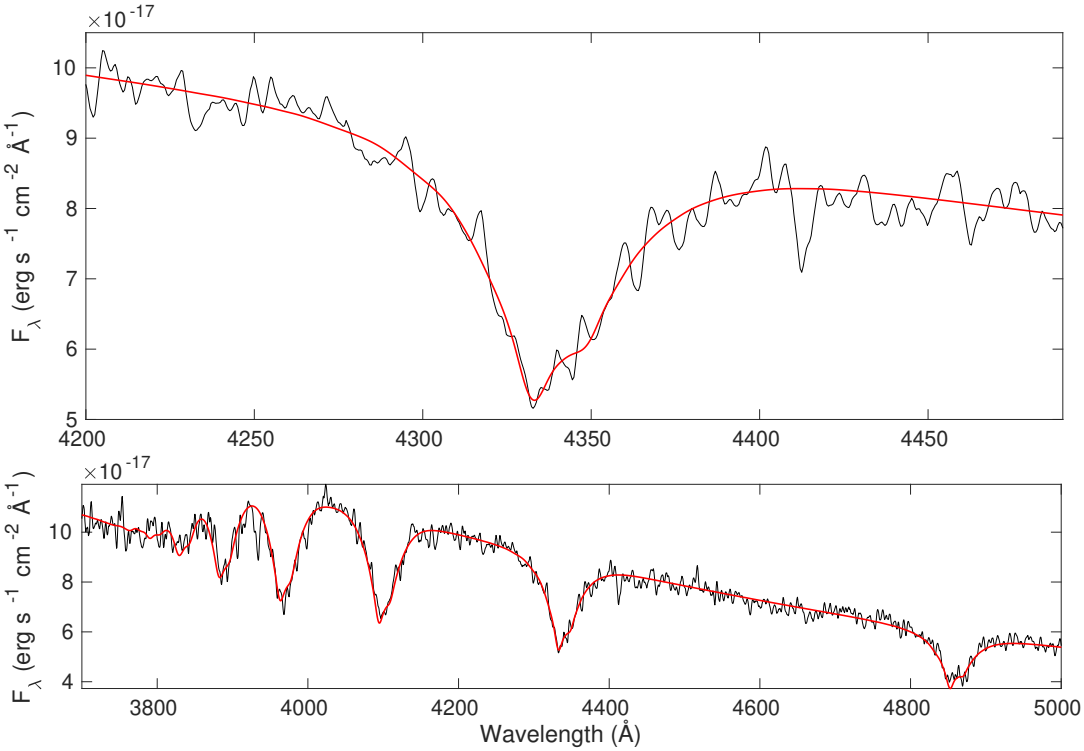

Figure 4.4: An example of a spectroscopic model fit to a phase-binned spectrum of ZTF J2243+5242. Such fits were performed on 12 phase-binned spectra, and used a composite spectrum of two WD models with relative luminosity contributions and effective surface temperatures fixed by lightcurve modelling. The splitting seen in the line cores is indicative that the system is double-lined. We did not measure radial-velocities from these spectra due to the low signal-to-noise ratio.

Swift observations

We targeted the binary system with a 5075 *s* observation from the *Neil Gehrels Swift Observatory* on 2020 April 02 in order to obtain ultraviolet photometry for the source using the UVOT instrument (see Table 4.2), as well as an observation with the X-ray telescope (XRT) (Observation ID: 00013301001) (Gehrels et al., 2004). The UVOT observation used 4 exposures with lengths 448 s–1708 s, all with the UVM2 filter (centered at 2246 Å).

Table 4.1: Table of observations

Telescope	Instrument	Filter/Mode	Date (UTC)	# of Exposures	Exposure Time (s)
Palomar 48-inch	ZTF	ZTF g	Apr 24 2018–Sep 05 2020	827	30
Palomar 48-inch	ZTF	ZTF r	Apr 09 2018–Sep 04 2020	1384	30
Palomar 200-inch	CHIMERA	g'	July 15 2020	1500	5
Palomar 200-inch	CHIMERA	g'	Jul 21 2020	4100	5
Palomar 200-inch	CHIMERA	r'	Jul 21 2020	4100	5
Palomar 200-inch	CHIMERA	g'	Jul 23 2020	5000	3
Palomar 200-inch	CHIMERA	i'	Jul 23 2020	2100	5
Palomar 200-inch	CHIMERA	g'	Aug 19 2020	6800	3
Palomar 200-inch	CHIMERA	r'	Aug 19 2020	4100	5
Palomar 200-inch	CHIMERA	g'	Oct 16 2020	2000	3
Keck I	LRIS	Blue Arm	Jul 18 2020	165	66
Keck I	LRIS	Blue Arm	Sept 16 2020	147	66
Swift	UVOT	UVM2	Apr 02 2020	4	5075
Swift	XRT	PC	Apr 02 2020	1	5075

4.3 Discovery and analysis

Photometric selection

Like the systems described in Burdge, Prince, et al. (2020), ZTF J2243+5242 was selected using a broad color cut using Pan-STARRS (Chambers et al., 2016) which encompassed all objects with $g - r < 0.2$ and $r - i < 0.2$ (see Burdge, Prince, et al. 2020 for further details). As seen by the apparent magnitudes listed in Table 4.2, the object's temperature is large enough that it has a color of $g - r \approx -0.21$, and thus could have been targeted with a more restrictive selection. Currently, it is feasible to systematically search a broad selection, but in the VRO era, more restrictive selections may prove valuable in reducing the number of candidates. It is worth noting that the only two binary systems with even shorter orbital periods, HM Cnc (Ramsay, Hakala, et al., 2002) and ZTF J1539+5027 (Burdge, Coughlin, et al., 2019), also both exhibit exceptionally blue Pan-STARRS1 colors, of $g - r \approx -0.28$ and $g - r \approx -0.39$, respectively. Unlike HM Cnc and ZTF J1539+5027, which are both substantially brighter in the ultraviolet than in the optical, ZTF J2243+5242 is fainter in these bands, due to modest extinction resulting from its location in the Galactic plane ($b \approx -5.5$).

Table 4.2: Photometric apparent magnitudes and astrometry

Survey	Filter/Quantity	Measured Value
Swift UVOT	$UVM2$	$20.73 \pm 0.15\, m_{AB}$
Pan-STARRS1	g	$20.359 \pm 0.029\, m_{AB}$
Pan-STARRS1	r	$20.571 \pm 0.027\, m_{AB}$
Pan-STARRS1	i	$20.733 \pm 0.024\, m_{AB}$
Pan-STARRS1	z	$20.92 \pm 0.12\, m_{AB}$
Gaia	G	$20.635 \pm 0.016\, m_V$
Gaia	RA	$340.929043146\, deg \pm 1.05\, mas$
Gaia	Dec	$+52.701660186\, deg \pm 0.85\, mas$
Gaia	Parallax	$-1.57 \pm 1.05\, mas$
Gaia	pm RA	$+0.48 \pm 2.29\, mas\, yr^{-1}$
Gaia	pm Dec	$-5.12 \pm 2.10\, mas\, yr^{-1}$
	E(g−r)	$0.16 \pm 0.02\, m_{AB}$

Reddenning estimated using distance reported in Table 4.3, with extinction maps of Green, Schlafly, et al. (2019).

Period finding

ZTF J2243+5242 was discovered using a graphics processing unit (GPU) based implementation of the conditional entropy algorithm (Graham, Drake, et al., 2013) in the cuvarbase package[2], executed on four Nvidia 2080 Ti GPUs. Notably, because the system exhibits two similar depth eclipses, it was detected at half its period (at $\approx 4.4\, min$), and until we obtained follow-up photometry, it was unclear whether the object had a $4.4\, min$ or $8.8\, min$ orbital period.

Swift UVOT and XRT Results

In the *Swift* UVOT data, we could see ZTF J2243+5242 in the images, but there was a brigher source about 7.″5 to the north west that complicated photometry. Rather than use the default aperture of 5″ radius (where the point spread functions overlap) we measured photometry for ZTF J2243+5242 using a 2.″5 radius. We first summed the individual exposures using `uvotimsum` and then performed aperture photometry with a 2.″5 radius using `uvotsource`, with a nearby region with radius 40″ used to define the background. We find a source magnitude of $20.73 \pm 0.10\, m_{AB}$ for ZTF J2243+5242, which has been

[2] `https://github.com/johnh2o2/cuvarbase`

corrected to 5″ radius using the default point spread function present in the *Swift* `CALDB`. We include a systematic uncertainty of 0.05 mag to account for standard *Swift* processing as well as our non-standard aperture choice.

For the *Swift* XRT data, there was no obvious emission present at the position of ZTF J2243+5242. There is 1 event within a circle with radius 9″ (the half-power point of the XRT) centered on ZTF J2243+5242. This was entirely consistent with background emission, where we find a mean of 0.58 counts in similar circles randomly distributed across the image. Therefore we can set a 3-σ upper limit of 3 counts in 5044 s, or a rate limit of $< 0.6 \times 10^{-3}\, count\, s^{-1}$.

Lightcurve+SED modelling and parameter estimation

We modelled ZTF J2243+5242 by fitting the CHIMERA lightcurve with a model generated using LCURVE (Copperwheat et al., 2010), while simultaneously fitting the Pan-STARRS1 and *Swift* photometry listed in Table 4.2. Here, we describe this modelling procedure in detail.

Our overall modelling procedure sampled over 14 free parameters: the component masses M_A and M_B, temperatures T_A and T_B, volume averaged radii R_A and R_B, orbital inclination i, time of superior conjuction T_0, period P_b, period derivative $\dot{P}_b$, distance to the system d, and three absorption parameters α_g, α_r, α_i which describe the reprocessing of radiation which occurs when the stars irradiate each other. We fixed the gravity and and limb darkening coefficients using the work described in Claret, Cukanovaite, et al. (2020b), using a 4-parameter limb-darkening law (Claret, 2000). We estimate the Doppler beaming coefficients for the system based on Claret, Cukanovaite, et al. (2020a). In order to reduce the model dependence of the analysis, we did not invoke white dwarf mass-radius relations as was done in (Burdge, Prince, et al., 2020), but instead rejected any samples in which the smaller mass component in the system was also the hotter and smaller in radius, as these solutions would be physically inconsistent with a white dwarf equation of state.

After constructing a likelihood function based on these free parameters, we performed our sampling using the nested sampling package, Multinest (Feroz et al., 2009). We used an evidence tolerance of 0.5, with 1000 live points. A final model fit to the CHIMERA

g', r', and i' data using the parameters reported in Table 4.3 is illustrated in Figure 4.3. Corner plots from this comprehensive analysis, showing the covariance between parameters, are illustrated in Figure 4.5. Note that for ease of reading, we have omitted some free parameters such as T_0, P_b, $\dot{P}_b$, and the absorption coefficients. The final parameters we derived from the analysis are reported in Table 4.3. The remainder of this section discusses how we constructed our likelihood function and other details of our sampling procedure.

Lightcurve fit: We simultaneously fit the CHIMERA g', r', and i', as well as ZTF r-band and g-band lightcurves from all nights, allowing each pass-band a free parameter representing the absorption coefficient (to model the reprocessing of radiation that arises from the stars irradiating the other, which is generally wavelength dependent). All other free parameters were the same for the lightcurve models of the three bands. Although the ZTF data has much lower SNR than the CHIMERA data, it was fit alongside the CHIMERA data because it strongly constrains the orbital period and its derivative due to its temporal baseline.

SED Fit: We also use the parameters we sample over to generate a synthetic SED by computing a synthetic WD model atmosphere using Tremblay, Bergeron, and Gianninas (2011), with Stark broadening from Tremblay and Bergeron (2009), and use these synthetic spectra to compute photometry for our passbands. Because we sample over the masses and radii of the components, for each iteration, we can compute the surface gravity of both objects, and by using these in combination with the temperatures of both objects (which we also sample over), and the radii and distances to the objects, we have all the degrees of freedom needed to compute synthetic photometry for these objects. We compute the reddening for each iteration, by querying the extinction maps of (Green, Schlafly, et al., 2019), supplying the distance of each sample to estimate the reddening for that particular iteration (which we then use to redden our synthetic photometry in order to correctly fit the SED).

Ephemeris constraint: We fit for the time of superior conjunction, T_0, which is well-constrained by the deep primary eclipse in the CHIMERA data (whose sharp ingress and egress allow for a precise measurement of the mid-eclipse time). We also fit for

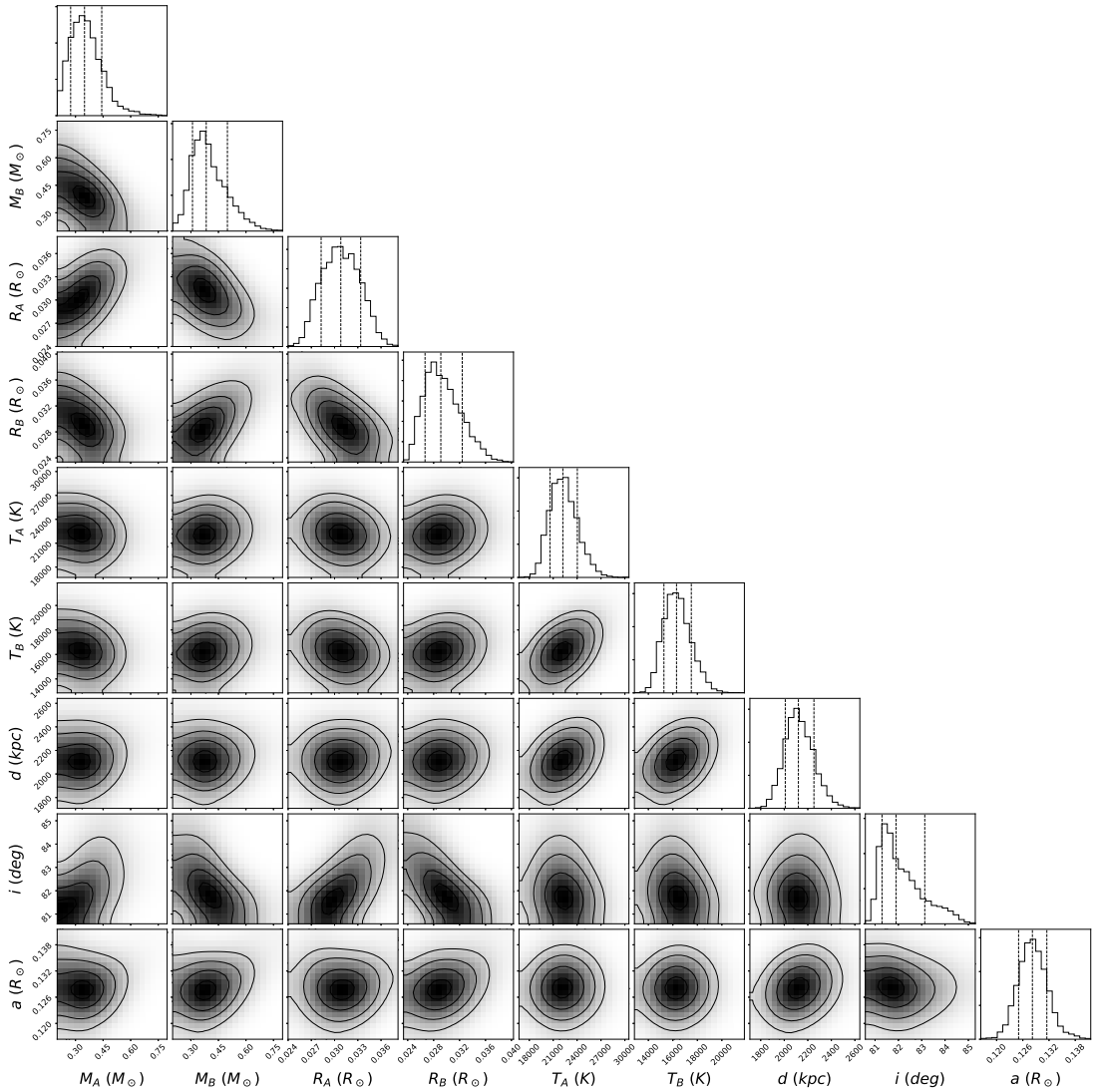

Figure 4.5: Corner plots illustrating the covariances of quantities estimated during our combined analysis. Note that for readability, we have omitted some parameters including the time of superior conjunction, T_0, the orbital period, P_b, it's derivative, $\dot{P}_b$, and the absorption coefficients.

the orbital period P_b, and its derivative, $\dot{P}_b$. The latter two parameters are primarily constrained by ZTF forced photometry (Yao et al., 2019), with its two year baseline. We should be able to measure these parameters more precisely with continued monitoring of the system using high speed photometers like CHIMERA, but at present, the baseline of the CHIMERA observations is short enough that ZTF provides a far better constraint. We would like to note that unlike Burdge, Coughlin, et al. (2019) and Burdge, Fuller, et al. (2019), we measured $\dot{P}_b$ for this system by fitting for the parameter in our lightcurve model, rather than constructing a diagram like the one shown in Figure 4.6 and fitting a quadratic to it. The reason for this is because there is a significant amount of ZTF data distributed throughout the last two years which contains information about the orbit between the period when the CHIMERA data was obtained and the two densely sampled ZTF nights, and thus we decided to model all the data coherently.

Mass constraints: In sampling over masses for the two WDs, we used a uniform prior of $0.15 - 0.7\ M_\odot$ in order to speed up sampling. Our final mass estimates converged within these boundaries, indicating that we did not need to widen this prior to consider lower or higher mass solutions. The masses are primarily constrained by ellipsoidal modulation in the lightcurve, and the orbital decay of the system.

Because we fit the ZTF lightcurves (with their long baseline) in combination with our CHIMERA data, we are able to place tight constraints on the orbital period P_b, and the orbital period derivative, $\dot{P}_b$. This allows us to constrain masses by assuming that the orbit is evolving according to energy loss due to gravitational-wave emission,

$$\dot{f}_{GW} = \frac{96}{5}\pi^{\frac{8}{3}}\left(\frac{G\mathcal{M}}{c^3}\right)^{\frac{5}{3}} f_{GW}^{\frac{11}{3}}, \tag{4.1}$$

(Taylor and Weisberg, 1989), where the chirp mass is given by $\mathcal{M} = \frac{(M_A M_B)^{\frac{3}{5}}}{(M_A+M_B)^{\frac{1}{5}}}$, and the gravitational wave frequency is twice the orbital frequency, $f_{GW} = \frac{2}{P_b}$.

We use the assumption that the orbital decay is due to general relativity to place an upper bound on $\mathcal{M}$; however, it is predicted that tidal effects could significantly contribute to the evolution of a binary at these short orbital periods, and thus we estimate an additional fractional tidal contribution of approximately 7.5 percent based on Equation

9 of Burdge, Coughlin, et al. (2019), where we have taken $\kappa_A = 0.12$ and $\kappa_B = 0.12$, which are constants determined by the internal structure of each WD. We estimated these values based on simulations performed in Burdge, Coughlin, et al. (2019), which estimated $\kappa \approx 0.11$ for the lower mass He WD in ZTF J1539+5027, and $\kappa \approx 0.14$ for the CO WD in the system (in our case, the two WDs fall between these two, and likely have a structure more similar to the He WD in ZTF J1539+5027). In any case, this approximation leads to an estimated tidal contribution of up to 7.5 percent, and we use this constraint to place a lower bound on the chirp mass. Thus, when we sample, we sample over $\dot{P}_b$ which is fit by the lightcurves, and we also estimate a purely relativistic $\dot{P}_{b_{GW}}$ based on our masses M_A and M_B for that sample, and reject any solutions falling outside the range $\dot{P}_b < \dot{P}_{b_{GW}} < 0.925 \times \dot{P}_b$ to allow for solutions to the masses which accommodate up to a 7.5 percent tidal contribution to the orbital evolution.

In addition to the chirp mass constraint discussed above, these masses are also constrained by the fractional amplitude of ellipsoidal variations in the lightcurve, which are given by

$$\frac{\Delta F_{ellipsoidal}}{F} = 0.15 \frac{(15+u)(1+\tau)}{3-u} \left(\frac{R}{a}\right)^3 q \sin^2(i), \tag{4.2}$$

(Morris, 1985), where u is the linear limb-darkening coefficient, and τ is the gravity darkening coefficient in the system and $q = \frac{M_B}{M_A}$ is the mass ratio of the system. In ZTF J2243+5242, the ellipsoidal variations exhibit a semi-amplitude of approximately 1.5 percent, which is quite small compared to systems like ZTF J1539+5027. This helps constrain the masses by driving the mass ratio q towards unity.

Inclination and radius constraints: In addition to constraining the mass ratio q and the $T0$, modelling the CHIMERA lightcurve allows us to precisely estimate the inclination, i, and the ratio of the component radii, R_A and R_B, with respect to the semi-major axis a. These constraints arise primarily from the total duration of the eclipses, and the duration of ingress/egress. Because we also sample over masses, we are able to directly constrain the semi-major axis because we know the total mass of the system, $M_A + M_B$. There is an asymmetry in the posterior distribution of the inclination, likely due to this system being on the edge of a grazing/total eclipse (it is unclear from our data whether it is flat-bottomed or not).

Temperature constraints: The temperatures of the two white dwarfs are constrained by an interplay of modelling the lightcurves and fitting the Pan-STARRS1 and Swift UVM2 photometry. This is because the ratio of eclipse depths in the lightcurve places stringent constraints on the surface brightness ratio and therefore the temperature ratio, whereas the SED sets the overall temperature scale. We wish to note that because of the high temperature of the objects $T > 15000\,K$, most of their flux is found in the ultraviolet, and thus the Swift UVM2 photometric measurement dominates this estimate, and is highly sensitive to the assumed reddening. Our solution for the temperatures is lower than that inferred from the spectroscopic modelling by about 2σ, likely due to the uncertainties in reddening. In any case, we wish to emphasize that the spectroscopic and SED temperature estimates differ by < 20 percent, and both estimates still give a similar physical picture of the system and its evolutionary history.

Distance constraints: The distance is primarily constrained by the fit to the SED, since the overall flux contribution of each WD to the SED photometry depends only on $\frac{R}{d}$. The lightcurve fit is not directly sensitive to the distance, but it does constrain the ratio of the radii and temperature of the two WDs used in computing the synthetic photometery, as discussed above. The distance we estimate to the system, $d = 2425^{+109}_{-115}$, is consistent with that of the nearby bright star to the northwest seen in Figure 4.2, which has a *Gaia* parallax of $\bar{\omega} = 0.479 \pm 0.024$ mas; however, uncertainties in the astrometric solution are currently too large to establish an association (if associated, the objects would be separated by ~ 15000 AU).

Spectroscopic modelling

The phase-resolved spectra revealed that ZTF J2243+5242 is a double-lined spectroscopic binary which consists of two hydrogen rich (DA) white dwarfs (see Figure 4.4). Due to the limited signal-to-noise ratio of the phase-binned spectra we acquired, our radial velocity estimates from these data are more uncertain than the lightcurve modelling, and rather sensitive to parameters such as the assumed surface gravity and redenning. The low SNRs of the spectra are a consequence of the faint nature of the object, the short exposure time needed to preserve temporal resolution, and large readout duty cycle of the observations.

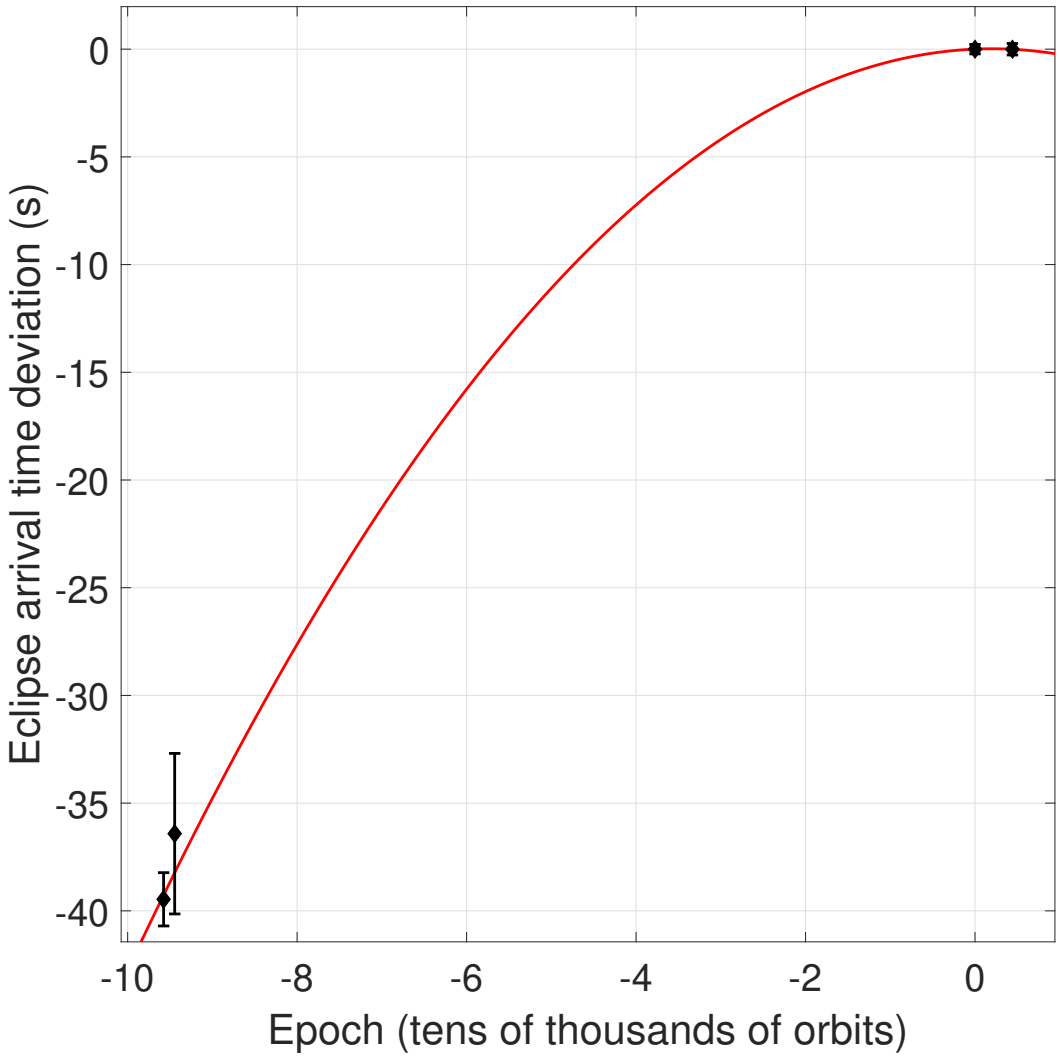

Figure 4.6: Eclipse timing of ZTF J2243+5242, demonstrating its orbital decay. The two black diamonds on the right (with small error bars) illustrate eclipse times derived from CHIMERA data, whereas the two points at much earlier times are derived from two nights of ZTF data, each of which contains over 3 hours of continuous observations of the source. The overplotted red parabola illustrates the predicted orbital evolution based on our derived $\dot{P}_b$.

We fit the spectra in order to estimate the effective temperatures of the WDs in the system. We use the synthetic DA NLTE white dwarf atmospheric models described in Tremblay, Bergeron, and Gianninas (2011), with stark broadening from Tremblay and Bergeron (2009). We generate a composite WD spectrum by using the ratio of the radii of the two components inferred from lightcurve modelling to weight each component's flux appropriately, and also fix the ratio of the temperatures of the two components based on lightcurve modelling (as the relative depth of the eclipses constrains this quite well). We also fixed the surface gravities of both objects based on masses and radii inferred from lightcurve modelling. We use the masses estimated from the lightcurve analysis to appropriately Doppler shift the spectral components of each WD based on the phase of each spectrum.

By fitting the spectra with these model atmospheres, we estimate temperatures of $T_A = 26520 \pm 130\,K$ and $T_B = 19670 \pm 100\,K$. These estimates are more precise than those estimated from the SED alone, and we report them here as a point of reference to compare the estimates from our combined analysis (see Table 4.3), which are based on the spectral energy distribution (SED) alone. We take both approaches to illustrate the feasibility of estimating temperature from just the SED, as this will be far more practical for the large number of faint WDs discovered by VRO and *LISA* than attempting spectroscopic follow-up of these systems. An example of a fit of the spectrum of the object is illustrated in Figure 4.4. Note that such an estimate is mainly feasible for eclipsing systems, in which the relative luminosity and radii of the two components can be constrained.

We estimated the masses of the two components by summing all spectra with phases near quadrature where the Doppler shift of each object as viewed from Earth is at a maximum. These stacked spectra at quadrature were constructed from taking a weighted sum of spectra with mid-exposure phases falling between $0.2 - 0.3$ and the other stack using spectra with mid-exposures between phases $0.7 - 0.8$. We then analyzied each of the two stacks at quadrature using a boostrapping technique, where we resampled the flux at each wavelength according to the corresponding error bar, and we performed 1000 iterations of this to estimate the uncertainty in our mass estimates. We performed 1000 iterations on both the co-addition at phases $0.2 - 0.3$, and $0.7 - 0.8$, and estimated the uncertainties by combining all of the results of this boostrapping exercise. The results of this analysis

are that $M_A = 0.308^{+0.074}_{-0.074}\,M_\odot$, and $M_B = 0.274^{+0.047}_{-0.047}\,M_\odot$, which are consistent with the masses estimated using the photometric analysis. The estimated masses were sensitive to how we treated the estimated surface gravity of each object (the estimates we report fixed the quantity based on estimates from the lightcurve modelling, but if instead we computed it based on the fit mass and fixed radius, our estimates shifted). Additionally, because we fit the entire flux calibrated spectrum (from 3700−5000) without introducing any additional normalization of the continuum, we found that the estimated masses were sensitive to factors such as assumed reddening. Because the mass estimates should depend only on the Doppler shift of the Balmer lines and not a factor such as reddening, we repeated the fit locally around each Balmer line, and also conducted a global fit where we introduced the reddening as a free parameter rather than fixing it (effectively allowing the fit to best match the full spectral model across the entire wavelength range). We found that the analysis locally around the Balmer lines agreed with our full fit of the lines+continuum well in the case where reddening was allowed to be a free parameter; however, the best fit model estimated a reddening of E(g−r)= $0.27 \pm 0.03\,m_{AB}$, noticeably larger than that reported by (Green, Schlafly, et al., 2019). With this value of reddening, which best fits the full spectrum, we estimate a temperature of $T_A = 28400 \pm 560\,K$ and $T_B = 20700 \pm 400\,K$ for the hotter WD, indicating that it is possible the temperatures may be slightly higher than those reported in Table 4.3 if the reddening of (Green, Schlafly, et al., 2019) is indeed an underestimate (it is also possible the flux calibration is imperfect, and that this discrepancy in reddening arises from this).

4.4 Discussion

Evolutionary history

Given the masses reported in Table 4.3, it is likely that the system consists of a pair of He WDs, though the uncertainties do allow for masses potentially consistent with either carbon-oxygen (CO) WDs, or hybrid WDs (Perets et al., 2019). If the system is indeed a pair of He WDs, one evolutionary channel from which ZTF J2243+5242 could have formed is via an episode of stable mass transfer, followed by a common envelope event. There is a tight relation between the radius of a star ascending the red giant branch, and its He core mass, and thus a close relationship between the mass of a He WD and the

Table 4.3: Physical parameters

Quantity:	Measured value
M_A	$0.323^{+0.065}_{-0.047}\,M_\odot$ (LC) $0.317^{+0.074}_{-0.074}\,M_\odot$ (Spect)
M_B	$0.335^{+0.052}_{-0.054}\,M_\odot$ (LC) $0.274^{+0.047}_{-0.047}\,M_\odot$ (Spect)
R_A	$0.0298^{+0.0013}_{-0.0012}\,R_\odot$
R_B	$0.0275^{+0.0012}_{-0.0013}\,R_\odot$
T_A	$26300^{+1700}_{-900}\,K$ (SED) $26520^{+130}_{-130}\,K$ (Spect)
T_B	$19200^{+1500}_{-900}\,K$ (SED) $19670^{+100}_{-100}\,K$ (Spect)
i	$82.12^{+0.51}_{-0.38}\,deg$
a	$0.1227^{+0.0025}_{-0.0024}\,R_\odot$
K_A	$455^{+66}_{-66}\,km\,s^{-1}$
K_B	$521^{+84}_{-84}\,km\,s^{-1}$
γ	$6^{+62}_{-62}\,km\,s^{-1}$
T_0	$59053.3448647^{+0.0000021}_{-0.0000022}\,MBJD_{TDB}$
P_b	$527.934890^{+0.000032}_{-0.000033}\,s$
$\dot{P}_b$	$1.37^{+0.12}_{-0.14} \times 10^{-11}\,s\,s^{-1}$
d	$2425^{+108}_{-114}\,pc$

Measured component and orbital parameters for ZTF J2243+5242. All parameters are derived from a combined analysis of the spectral energy distribution and CHIMERA lightcurves, with the exception of T_A and T_B, for which we also report estimates based on the optical spectrum of the system. The component parameters given here are the masses, M_A and M_B, radii, R_A and R_B, surface temperatures, T_A and T_B. We also report the distance to the system d, and orbital parameters including the semi-major axis, a, inclination i, radial velocity semi-amplitudes K_A and K_B. systemic velocity γ, the time of superior conjunction T_0, the orbital period, P_b, and its derivative, $\dot{P}_b$. For the temperature estimates, T_A and T_B, we give estimates both based on a spectroscopic fit (Spect), and based purely on the spectral energy distribution (SED).

orbital period at which its progenitor star underwent a mass transfer event, stripping it of its envelope (Rappaport et al., 1995). Rappaport et al. (1995) estimated the relation as

$$P_{orb} = 1.3 \times 10^5 M_{WD}^{6.25}/(1 + 4M_{WD}^4)^{1.5}\, days, \tag{4.3}$$

where P_{orb} is the orbital period at the start of the mass transfer event which forms the He WD, and M_{WD} is the mass of the remnant He WD in solar masses. This suggests that the progenitor of ZTF J2243+5242 underwent a common envelope event at an orbital period of $\approx 160\, days$, with an initial orbital period somewhat shorter due to the orbital widening that occurred during the preceding stable mass-transfer phase.

For a detached compact binary which has a measured $\dot{P}_b$, if one assumes that the system is undergoing orbital decay due to general relativity and can determine a cooling age, one can estimate the orbital period that the system exited common envelope by extrapolating the orbital evolution back in time.

In order to estimate the orbital period at which the system might have exited common envelope, we modeled the evolution of the primary WD with MESA using its pre-computed WD model with $M = 0.35\, M_\odot$. Using this model, we estimate that the system is roughly 17 million years old, and exited the common envelope phase with an orbital period of 36 minutes, which is consistent with the observation from the ELM survey that most close He-Core WD binaries emerge from the common envelope phase at orbital periods under an hour (Brown, Kilic, Kenyon, et al., 2016). The actual age and initial orbital period could be slightly longer if diffusion and/or rotational mixing processes allow for more extended hydrogen burning or hydrogen shell-flashes (Althaus, Miller Bertolami, et al., 2013). Based on the models of Istrate et al. (2016), these processes last less than 10 Myr in a WD of this mass, so the system is very likely younger than 30 Myr and was born at an orbital period less than an hour.

A caveat to this calculation is that tidal heating may contribute significantly to the luminosity of the WDs in ZTF J2243+5242, and thus may impact our age estimates. From Burdge, Coughlin, et al., 2019, the upper limit to the surface temperature produced by tidal heating is $T_{tide} = (\pi\kappa M\dot{P}/2\sigma_B P^3)^{1/4} \approx 30,000\, K$ for each of the WDs in ZTF J2243+5242. In a more realistic estimate for tidal heating, which accounts for the

expected near spin-orbit synchronism, the tidal heating rate is reduced by roughly an order of magnitude, so that the tidal temperature would be closer to $T_{tide} \sim 18,000\,K$. Hence, it is quite possible that the luminosity of the secondary is dominated by tidal heat. While tidal heating may contribute to the luminosity of the primary, its significantly higher temperature (despite a similar mass and radius) suggests its luminosity is dominated by normal white dwarf cooling, validating the young age estimate above. Hence, these rapidly merging systems may spend only a tiny fraction of their lives as DWDs.

Future evolution

ZTF J2243+5242 is undergoing rapid orbital decay. The system is currently clearly detached, with $\frac{R}{R_L} \approx \frac{2}{3}$ for both components; however, the two components will start interacting in approximately 320, 000 years, likely evolving into a direct impact accretor and bright source of X-rays like HM Cnc and V407 Vul. Based on the mass ratio of the system, mass transfer will likely be unstable (Marsh, Nelemans, et al., 2004), and the system will merge in $< 400,000$ years. After merger, the system is likely to form either an isolated hot subdwarf star, or an R Coronae Borealis star. In any case, the remnant of this merger will eventually cool to form a $\sim 0.5 - 0.7\,M_\odot$ CO WD on the white dwarf cooling track, which may be rapidly rotating. Merging pairs of He WDs like ZTF J2243+5242 demonstrate that some “normal-mass" CO WDs with $M \sim 0.6\,M_\odot$ likely form from merger events.

Implications for *LISA* and the VRO

As demonstrated in this work, using just photometric measurements, we were able to estimate component parameters for ZTF J2243+5242, including masses, temperatures, and radii, as well as orbital parameters such as inclination, period, orbital period decay rate, time of superior conjunction, and semi-major axis. This has major implications for the eras of the VRO (Ivezić et al., 2019), and *LISA* (Amaro-Seoane et al., 2017), which we discuss here.

LISA and the VRO are both expected to significantly increase the number of known short period DWDs. The VRO is an upcoming optical southern sky synoptic survey using the Simonyi Survey Telescope, which has an effective aperture of 6.5-m, and the instrument

has a field of view of 9.6 square degrees, about a quarter of ZTF's (Ivezić et al., 2019). The survey is expected to reach a 5-sigma depth of approximately 24.5 in r in a 30 s exposure, about 4 magnitudes fainter than ZTF.

The VRO, with its smaller field of view, will acquire about a quarter the number of samples of ZTF in an equivalent survey time, and thus will not perform as well in recovering periodic objects at the same signal-to-noise ratio. By the time the survey does reach a comparable number of samples to ZTF after two and a half years, which should take the VRO about a decade or so, the frequency evolution of these objects will make it impossible to recover them without acceleration searches (Katz et al., 2020). The VRO could partially compensate for this by adopting two 15 s exposures rather than a single 30 s one, as this not only doubles the numbers epochs for such sources, but actually provides a crucial ingredient—high time resolution. Such exposures would be consecutive, effectively measuring both the flux and its derivative at a given time (which, for points in eclipse, is very valuable). Eclipsing DWDs such as ZTF J2243+5242 and ZTF J1539+5027 can significantly change their brightness in $< 15\,s$ during the ingress and egress of their primary eclipse, so such a measurement would be highly sensitive to this kind of rapid photometric variability, greatly enhancing the facility's discovery capabilities in ultra-fast timescale optical variability. The other fundamental challenge is that the VRO will divide its exposures into many filters, complicating period finding (an important element in preparing for this survey will be to adapt a wide range of algorithms to cope with this technical challenge) (VanderPlas, 2018).

The VRO should contribute significantly to the discovery of low and moderate amplitude sources like ZTF J2243+5242 at < 23.0 in r, where improved photometric precision can partially compensate for lack of temporal resolution compared to more densely sampled surveys such as ZTF. These binaries will be so faint that obtaining phase-resolved spectroscopy for more than a handful will be impossible without substantial time on an extremely large telescope (ELT). Our analysis of ZTF J2243+5242 gives hope that it will be feasible to characterize the photometrically variable systems among these without depending on spectroscopic follow-up. As discussed above, we were able to constrain many parameters in this system using just photometric measurements; this means that the large number of faint eclipsing binaries discoverable by the VRO (and eventually *LISA*)

could be characterized simply by obtaining a single high signal-to-noise lightcurve on a high speed photometer, and combining modelling of this lightcurve with a measurement of $\dot{P}_b$ using the longer baseline VRO data, or in some cases, such modelling could be possible using just the VRO lightcurves alone. Such analyses open up the possibility of characterizing a large population of such systems, and identifying properties such as masses/core compositions, which have implications for both the binary evolutionary processes which form these systems, and also the outcomes of the interactions/mergers.

In the era of *LISA*, short orbital period systems like ZTF J2243+5242 and ZTF J1539+5027 will be particularly valuable astrophysical laboratories. Because these systems fall near the peak of *LISA*'s sensitivity (see Figure 5.9), they are detectable at large distances (ZTF J2243+5242 reaches an SNR of 7 in *LISA* at $\approx 20\,kpc$, and ZTF J1539+5027 at $\approx 30\,kpc$). *LISA*, which will be unhindered by Galactic extinction, should easily detect most of these kinds of objects in the Milky Way.

One way to prepare for *LISA* is by developing ground and space-based instrumentation optimized to best characterize the optically detectable portion of its source population in an efficient manner. We hope that in this work and Burdge, Coughlin, et al. (2019), Burdge, Fuller, et al. (2019), Burdge, Prince, et al. (2020), and Coughlin, Burdge, et al. (2020), we have demonstrated that high speed photometers, which can obtain densely sampled high signal-to-noise lightcurves with high temporal resolution will be one of the most powerful tools for such characterization. Such instruments on 10-m and 30-m class telescopes could be used to characterize binaries like ZTF J2243+5242 and ZTF J1539+5027 to 10-30 kpc–distances well matched to *LISA*'s sensitivity threshold.

4.5 Conclusion

Here, we described the discovery and characterization of ZTF J2243+5242, the second eclipsing binary known with an orbital period under 10 minutes. The system is a DWD with an orbital period of just 8.8 minutes, and will be a strong *LISA* gravitational-wave source. We performed a comprehensive analysis of the system using just photometric measurements, demonstrating the considerable value of photometry not just as a tool for discovering such extreme systems, but also one which can be used to precisely characterize these objects at great distances and faint apparent magnitudes. We were

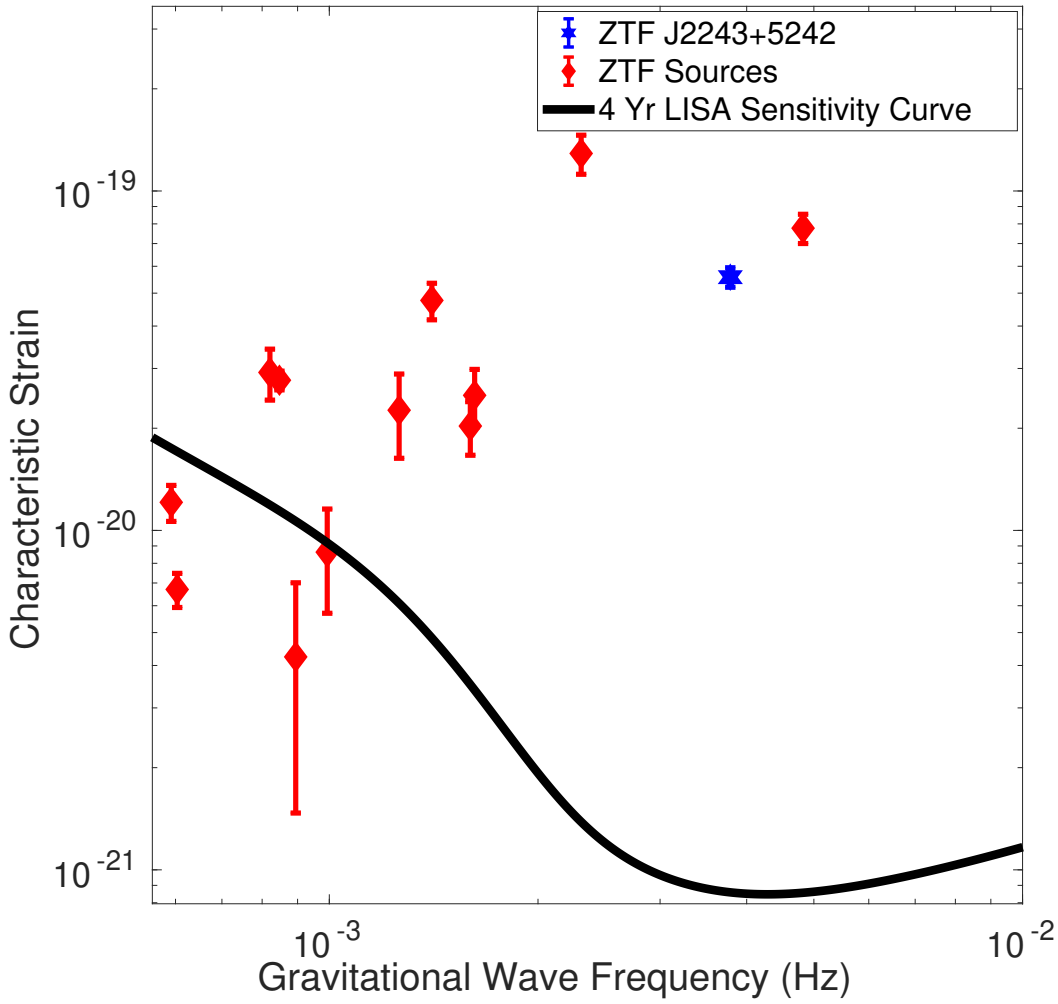

Figure 4.7: The current ZTF sample of ultracompact binary sources reported in Burdge, Prince, et al. (2020) (red diamonds). ZTF J2243+5242 is indicated as the blue six point star, the second shortest period system shown here. Because the power spectral density of *LISA*'s sensitivity curve is expected to increase substantially at a frequency corresponding to around 15 *min*, sources below this period, like ZTF J0538+1953, ZTF J2243+5242, and ZTF J1539+5027 should all be detected by *LISA* with high signal-to-noise (SNR), enabling precise parameter estimation using GWs. It is worth noting that these high-SNR sources are all eclipsing binaries, making them particularly valuable astrophysical laboratories.

able to determine that ZTF J2243+5242 likely consists of two He WDs which will merge in approximately 400,000 years, with component masses of $M_A = 0.323^{+0.065}_{-0.047}\,M_\odot$ and $M_B = 0.335^{+0.052}_{-0.054}\,M_\odot$.

ZTF has already significantly altered the landscape of extremely short orbital period binary systems known in the Galaxy, and will continue to do so as it acquires more epochs during ZTF phase II, and receives improvements to its archival photometry. The current discoveries mark the beginning of a golden era for discovering these objects, a sample which will profoundly alter our understanding of compact binary evolution as we continue to discover more of them and understand both the processes which lead to their creation, and their eventual fates upon merger.

K.B.B thanks the National Aeronautics and Space Administration and the Heising Simons Foundation for supporting his research. M.W.C. acknowledges support from the National Science Foundation with grant number PHY-2010970. JF acknowledges support from an Innovator Grant from The Rose Hills Foundation, and the Sloan Foundation through grant FG-2018-10515. TRM was supported by the UK's Science and Technology Facilities Council through grant ST/T000406/1.

Based on observations obtained with the Samuel Oschin Telescope 48-inch and the 60-inch Telescope at the Palomar Observatory as part of the Zwicky Transient Facility project. ZTF is supported by the National Science Foundation under Grant No. AST-1440341 and a collaboration including Caltech, IPAC, the Weizmann Institute for Science, the Oskar Klein Center at Stockholm University, the University of Maryland, the University of Washington, Deutsches Elektronen-Synchrotron and Humboldt University, Los Alamos National Laboratories, the TANGO Consortium of Taiwan, the University of Wisconsin at Milwaukee, and Lawrence Berkeley National Laboratories. Operations are conducted by COO, IPAC, and UW.

Some of the data presented herein were obtained at the W.M. Keck Observatory, which is operated as a scientific partnership among the California Institute of Technology, the University of California and the National Aeronautics and Space Administration. The Observatory was made possible by the generous financial support of the W.M. Keck Foundation. The authors wish to recognize and acknowledge the very significant

cultural role and reverence that the summit of Mauna Kea has always had within the indigenous Hawaiian community. We are most fortunate to have the opportunity to conduct observations from this mountain.

Chapter 5

A SYSTEMATIC SEARCH OF ZWICKY TRANSIENT FACILITY DATA FOR ULTRACOMPACT BINARY *LISA*-DETECTABLE GRAVITATIONAL-WAVE SOURCES

Burdge, K. B. et al. (2020). "A Systematic Search of Zwicky Transient Facility Data for Ultracompact Binary LISA-detectable Gravitational-wave Sources". In: *ApJ* 905.1, p. 32. DOI: 10.3847/1538-4357/abc261. arXiv: 2009.02567 [astro-ph.SR].

Kevin. B. Burdge[1], Thomas A. Prince[1], Jim Fuller[1], David L. Kaplan[2], Thomas R. Marsh[3], Pier-Emmanuel Tremblay[3], Zhuyun Zhuang[1], Eric C. Bellm[4], Ilaria Caiazzo[1], Michael W. Coughlin[5], Vik S. Dhillon[6], Boris Gaensicke[3], Pablo Rodriguez-Gil[7,8], Matthew J. Graham[1], JJ Hermes[9], Thomas Kupfer[10], S. P. Littlefair[6], Przemek Mroz[1], E. S. Phinney[1], Jan van Roestel[1], Yuhan Yao[1], Richard G. Dekany[11], Andrew J. Drake[1], Dmitry A. Duev[1], David Hale[11], Michael Feeney[11], George Helou[12], Stephen Kaye[11], Ashish A. Mahabal[1], Frank J. Masci[12], Reed Riddle[11], Roger Smith[11], Maayane T. Soumagnac[13,14], S. R. Kulkarni[1]

[1]Division of Physics, Mathematics and Astronomy, California Institute of Technology, Pasadena, CA 91125, USA
[2]Department of Physics, University of Wisconsin-Milwaukee, Milwaukee, WI, USA
[3]Department of Physics, University of Warwick, Coventry CV4 7AL, UK
[4]DIRAC Institute, Department of Astronomy, University of Washington, 3910 15th Avenue NE, Seattle, WA 98195, USA
[5]School of Physics and Astronomy, University of Minnesota, Minneapolis, Minnesota 55455, USA
[6]Department of Physics & Astronomy, University of Sheffield, Sheffield S3 7RH, UK
[7]Instituto de Astrofísica de Canarias, Vía Láctea s/n, La Laguna, E-38205 Tenerife, Spain
[8]Departamento de Astrofísica, Universidad de La Laguna, E-38206 La Laguna, Tenerife, Spain
[9]Department of Astronomy, Boston University, 725 Commonwealth Ave., Boston, MA 02215, USA
[10]Kavli Institute for Theoretical Physics, University of California, Santa Barbara, CA 93106, USA
[11]Caltech Optical Observatories, California Institute of Technology, Pasadena, CA, USA
[12]IPAC, California Institute of Technology, 1200 E. California Blvd, Pasadena, CA 91125, USA
[13]Lawrence Berkeley National Laboratory, 1 Cyclotron Road, Berkeley, CA 94720, USA
[14]Department of Particle Physics and Astrophysics, Weizmann Institute of Science, Rehovot 76100, Israel

ABSTRACT

Using photometry collected with the Zwicky Transient Facility (ZTF), we are conducting an ongoing survey for binary systems with short orbital periods ($P_b < 1\,hr$) with the goal of identifying new gravitational-wave sources detectable by the upcoming *Laser Interferometer Space Antenna* (*LISA*). Here, we present a sample of fifteen binary systems discovered thus far, with orbital periods ranging from $6.91\,min$ to $56.35\,min$. Of the fifteen systems, seven are eclipsing systems which do not show signs of significant mass transfer. Additionally, we have discovered two AM Canum Venaticorum (AM CVn) systems and six systems exhibiting primarily ellipsoidal variations in their light curves. We present follow-up spectroscopy and high-speed photometry confirming the nature of these systems, estimates of their *LISA* signal-to-noise ratios (SNR), and a discussion of their physical characteristics.

5.1 Introduction

The upcoming *Laser Interferometer Space Antenna* (*LISA*; Amaro-Seoane et al. (2017)) will be a space-based millihertz-frequency gravitational-wave detector. Astrophysical sources of gravitational radiation in this frequency band include merging supermassive black hole binaries, extreme mass ratio inspirals, and Galactic binaries with short orbital periods. With an anticipated number of more than ten thousand detectable sources in the Milky Way (Nissanke et al., 2012), close double-degenerate binaries are by far the largest population of detectable gravitational-wave sources, but only a few have been discovered to date (Kupfer, Korol, et al., 2018). This population of sources presents a unique opportunity to use the synergy of information carried by electromagnetic and gravitational radiation to understand processes such as binary evolution, the population of Type Ia supernova and R Coronae Borealis (R CrB) progenitors (Webbink, 1984), tidal physics in degenerate objects (Fuller and Lai, 2012), and Galactic structure (Korol, Rossi, and Barausse, 2019); however, because these sources are so numerous, they will also present a technical challenge by acting as a formidable background for *LISA* (Nelemans et al., 2001).

Since the beginning of science operations in March 2018, Zwicky Transient Facility (ZTF) (Bellm, Kulkarni, Graham, et al., 2019; Dekany et al., 2020; Graham, Kulkarni, et al., 2019; Masci, Laher, Rusholme, et al., 2019) has accumulated hundreds of epochs across the northern sky, with more than a thousand in some regions. Here, we present results from a new survey using ZTF data with the goal of discovering *LISA* sources in the optical time domain. The survey identifies objects which undergo periodic flux variations on short timescales. We conduct additional spectroscopic and photometric follow-up of objects which exhibit a strong periodic signal with a period shorter than 30 min. By targeting objects in this manner in an all-sky survey, we can search millions of candidates, in contrast to the narrower selection criteria used in surveys such as the highly successful Extremely Low Mass (ELM) survey. The ELM survey spectroscopically followed up all candidates in a narrow parameter space, resulting in the discovery of 98 detached double-white dwarfs (DWDs), over half of the known double-degenerate population (Brown, Kilic, Allende Prieto, and Kenyon, 2010; Kilic, Brown, Allende Prieto, Agüeros, et al., 2011; Brown, Kilic, Allende Prieto, and Kenyon, 2012; Kilic,

Brown, Allende Prieto, Kenyon, et al., 2012; Brown, Kilic, Allende Prieto, Gianninas, et al., 2013; Gianninas, Kilic, et al., 2015; Brown, Gianninas, et al., 2016; Brown, Kilic, Kosakowski, Andrews, et al., 2020), including several systems which are strong candidate *LISA*-detectable gravitational-wave sources (Brown, Kilic, Hermes, et al., 2011; Kilic, Brown, Gianninas, et al., 2014; Brown, Kilic, Bédard, et al., 2020). Until recently, there were only two known detached eclipsing binaries under an hour orbital period, both discoveries made by the ELM survey (Brown, Kilic, Hermes, et al., 2011; Brown, Kilic, Kosakowski, and Gianninas, 2017).

In June 2019, using ZTF's first internal data release, we discovered the shortest orbital period eclipsing binary system known, ZTF J1539+5027, with an orbital period of just 6.91 *min* (Burdge, Coughlin, et al., 2019). We originally tested the viability of a photometric selection strategy using archival Palomar Transient Factory (PTF) data (Law et al., 2009), and discovered PTF J0533+0209, a $\approx$ 20.6 minute orbital period detached DBA WD binary (Burdge, Fuller, et al., 2019). Since these two discoveries, we have confirmed 13 additional short period binary systems either spectroscopically via radial velocity shifts, or photometrically if they exhibit eclipses (an unambiguous indicator of binarity). These systems are diverse, and include detached DWDs, accreting AM Canum Venaticorum (AM CVn) objects (Ramsay, Green, et al., 2018), and accreting systems involving helium stars/hot sub-luminous subdwarfs (sdBs/sdOs) (Heber, 2016). Even among just the detached DWD population, there exists a rich phase space of possible combinations of core compositions involving helium-core white dwarfs (He WD) and carbon-oxygen core WDs (CO WD), each of which originate from distinct evolutionary scenarios. Thus, in this work, we devote some discussion to describing the unique characteristics of each system. As a point of reference to guide the reader, we have included Table 5.1 below to highlight essential characteristics of the fifteen systems discussed in this work.

5.2 Methods

Sample Selection

We used the Pan-STARRS1 (PS1) source catalog (Chambers et al., 2016) to select our sample of objects to period search. Focusing on "blue" objects, we imposed a

Table 5.1: ZTF/PTF Short period binaries

Name	Right Ascension (h:m:s)	Declination (d:m:s)	Orbital period (min)	Nature of photometric variability	Spectroscopic characteristics
ZTF J1539+5027[1]	15:39:32.16	+50:27:38.72	6.91	Eclipsing+irradiation	DA, double-lined
ZTF J0538+1953	05:38:02.73	+19:53:02.89	14.44	Eclipsing+irradiation	DA, double-lined
ZTF J1905+3134	19:05:11.34	+31:34:32.37	17.20	Eclipsing High State AM CVn	Double-peaked He 2 emission
PTF J0533+0209[2]	05:33:32.06	+02:09:11.51	20.57	Ellipsoidal	DBA single-lined
ZTF J2029+1534	20:29:22.31	+15:34:30.97	20.87	Eclipsing	DA, double-lined
ZTF J0722−1839	07:22:21.49	-18:39:30.57	23.70	Eclipsing	DA, double-lined
ZTF J1749+0924	17:49:55.30	+09:24:32.40	26.43	Eclipsing	DA, double-lined
ZTF J2228+4949	22:28:27.07	+49:49:16.44	28.56	High State AM CVn	Double-peaked He 2 emission
ZTF J1946+3203	19:46:03.89	+32:03:13.13	33.56	Eclipsing+Ellipsoidal	DAB/sdB, single-lined
ZTF J0643+0318	06:43:36.77	+03:18:27.45	36.91	Accreting He star	He 1 absorption/He 2 emission
ZTF J0640+1738	06:40:18.69	+17:38:45.01	37.27	Ellipsoidal	sdB, single-lined
ZTF J2130+4420[3]	21:30:56.71	+44:20:46.42	39.34	Ellipsoidal	sdB, single-lined
ZTF J1901+5309[4]	19:01:25.42	+53:09:29.27	40.60	Eclipsing	DA, double-lined
ZTF J2320+3750	23:20:20.43	+37:50:30.84	55.25	Ellipsoidal	DA, single-lined
ZTF J2055+4651[5]	20:55:15.98	+46:51:06.45	56.35	Eclipsing+Ellipsoidal	sdB, single-lined

The coordinates and basic photometric and spectroscopic characteristics of the fifteen short period binaries discovered so far using PTF/ZTF data. Coordinates are taken from *Gaia* and are in J2000.0. For apparent magnitudes, see Table 5.2. More precise orbital periods and uncertainties are reported in Table 5.3. Burdge, Coughlin, et al. (2019)[1], Burdge, Fuller, et al. (2019)[2], Kupfer, Bauer, Marsh, et al. (2020)[3], Coughlin, Dekany, et al. (2019)[4], Kupfer, Bauer, Burdge, van Roestel, et al. (2020)[5]

photometric color selection of $(g - r) < 0.2$ and additionally $(r - i) < 0.2$ (see Table 5.2). We selected blue objects, because we expected that close binary WDs, especially those at orbital periods sufficiently short to be strong *LISA* sources, should have elevated temperatures due to tidal heating (Fuller and Lai, 2013).

ZTF Photometry

We used ZTF photometry to identify all of our sources (with the exception of PTF J0533+0209). ZTF is a northern sky synoptic survey based on the 48-inch Samuel Oschin Schmidt telescope at Palomar Observatory, surveying the sky in ZTF g-, r-, and i-bands down to a declination of $-28°$ with 30 s exposures. ZTF has a 47 deg^2 field of view and a median 5σ limiting magnitude of 20.8 in g-band, 20.6 in r-band, and 20.2 in i-band. The instrument's large field of view allows it to rapidly accumulate a large number of epochs across the sky, and the resulting dense sampling serves as a crucial element in identifying sources.

period-finding

Because the fidelity of period-finding depends strongly on the number of samples in a lightcurve (especially at short periods where there are large numbers of trial frequencies), rather than impose a cutoff on apparent magnitude, we instead required a minimum of 50 total photometric 5σ detections in archival ZTF data. This selection produced approximately 10 million candidates to search. We combined data from multiple filters by computing the median magnitude in each filter, and shifting g- and i-band so that their median magnitude matched the r-band data. We do this in order to maximize the number of epochs available in each lightcurve. We used a graphics processing unit (GPU) implementation of the conditional entropy period-finding algorithm (Graham, Drake, et al., 2013) and later the Box Least Squares (BLS) algorithm (Kovács et al., 2002). Although BLS is optimized for identifying eclipsing systems, conditional entropy is computationally less costly, and was responsible for the discovery of 12 of the 15 systems in the sample. The only system discovered in a later BLS search was ZTF J1749+0924. We originally discovered ZTF J2130+4420, which is the brightest object in the sample, using the analysis of variance algorithm (Schwarzenberg-Czerny, 1996) in a search of bright sources between the WD track and the main sequence. It was later

Table 5.2: Optical and ultraviolet apparent magnitudes of the sample

Survey:	GALEX	GALEX	Pan-STARRS1	Pan-STARRS1	Pan-STARRS1	*Gaia*
Filter:	FUV	NUV	g	r	i	G
	(m_{AB})	(m_{AB})	(m_{AB})	(m_{AB})	(m_{AB})	(m_V)
ZTF J1539+5027	18.754 ± 0.084	19.334 ± 0.073	20.134 ± 0.041	20.521 ± 0.069	20.805 ± 0.049	20.491 ± 0.017
ZTF J0538+1953		19.59 ± 0.16	18.777 ± 0.015	18.881 ± 0.011	19.1049 ± 0.0060	18.8346 ± 0.0061
ZTF J1905+3134			20.778 ± 0.046	21.15 ± 0.28	21.19 ± 0.13	20.900 ± 0.030
PTF J0533+0209		20.38 ± 0.28	18.995 ± 0.015	19.150 ± 0.013	19.405 ± 0.014	19.1030 ± 0.0075
ZTF J2029+1534	20.12 ± 0.23	20.49 ± 0.20	20.380 ± 0.024	20.662 ± 0.047	20.962 ± 0.093	20.5745 ± 0.0118
ZTF J0722−1839			18.976 ± 0.012	19.194 ± 0.016	19.4888 ± 0.0095	19.1040 ± 0.0061
ZTF J1749+0924	20.19 ± 0.26		20.357 ± 0.022	20.474 ± 0.014	20.666 ± 0.029	20.538 ± 0.013
ZTF J2228+4949		19.43 ± 0.12	19.317 ± 0.028	19.390 ± 0.034	19.571 ± 0.022	19.2758 ± 0.0060
ZTF J1946+3203			19.400 ± 0.035	19.266 ± 0.020	19.240 ± 0.025	19.1905 ± 0.0059
ZTF J0643+0318		21.68 ± 0.48	18.384 ± 0.012	18.269 ± 0.058	18.306 ± 0.037	18.271 ± 0.019
ZTF J0640+1738			19.222 ± 0.017	19.409 ± 0.024	19.486 ± 0.016	19.2521 ± 0.0062
ZTF J2130+4420		15.727 ± 0.012	15.3269 ± 0.0049	15.6412 ± 0.0078	15.806 ± 0.028	15.4611 ± 0.0061
ZTF J1901+5309		17.331 ± 0.041	17.8909 ± 0.0055	18.2512 ± 0.0031	18.5764 ± 0.0055	18.0686 ± 0.0023
ZTF J2320+3750		21.39 ± 0.28	19.411 ± 0.024	19.394 ± 0.025	19.536 ± 0.028	19.3997 ± 0.0070
ZTF J2055+4651			17.720 ± 0.042	17.652 ± 0.023	17.647 ± 0.015	17.6539 ± 0.0093

recovered by both the conditional entropy algorithm, and as part of a search of the hot subdwarf catalog (Geier et al., 2017) as discussed in Kupfer, Bauer, Marsh, et al. (2020) (PTF J0533+0209 was also discovered with the AOV algorithm–see Burdge, Fuller, et al. (2019)). The BLS algorithm is able to recover all systems as well, but with greater than an order of magnitude longer run-time relative to conditional entropy. The conditional entropy algorithm phase-folds lightcurves on a grid of trial frequencies, partitions the lightcurve into magnitude and phase bins, and computes the conditional entropy of the partitioned phase-folded lightcurve corresponding to each frequency. For further details on the sensitivity of this algorithm, please see the Appendix.

We determine the best period of the object by selecting the trial frequency which minimizes the conditional entropy. We visually inspect the most significant phase-folded lightcurves (all with significance greater than 8), where significance is simply defined as the minimum entropy value divided by the standard deviation of entropy values across the full periodogram, and from this we select the most promising candidates for follow-up. We performed this visual inspection on 24635 lightcurves with a minimum entropy corresponding to a period below 30 minutes, and determined that 337 of these were likely real periodic signals based on the appearance of their lightcurves. We then began to systematically follow-up systems which exhibited photometric behavior suggestive of binarity (eclipses, or asymmetric minima in ellipsoidal variables). Follow-up of objects in this sample is ongoing.

One challenge of searching for periodic variables in a sample of millions of objects over a large frequency grid (for further details see the Appendix) is the increase in opportunity for objects to exhibit significant random fluctuations in their power spectra. This means that many of the lower-amplitude periodic variables recovered actually show a smaller "significance" than some non-periodic objects, hence the value in visually inspecting a moderate number of objects at low significance, rather than only the most significant sources. Note that targeting objects with "best" periods under 30 mins yielded many discoveries with orbital periods between 30 and 60 minutes, as systems which exhibit ellipsoidal variations and eclipsing systems in which there is a prominent secondary eclipse exhibit significant power at twice their orbital frequency.

The ZTF phase-folded lightcurves of all short period binary systems discovered from this sample are illustrated in Figure 5.1.

In order to determine the uncertainties in the orbital period reported in Table 5.3, we used a bootstrapping technique in which we sub-sampled each ZTF lightcurve 1000 times, using 90 percent of the points in each sub-sample, with replacement, and computed the standard deviation of the best periods of the 1000 trials. For ellipsoidal systems, we used Lomb-Scargle (Lomb, 1976; Scargle, 1982) for this bootstrapping exercise, and for eclipsing systems, we used BLS. For ZTF J1539+5027 and PTF J0533+0209, which have well-measured orbital evolution, we instead used the linear component of the quadratic fit to the timing residuals to determine the uncertainty in the period (for further details, see Burdge, Coughlin, et al. (2019)).

Of the short period candidates recovered by conditional entropy, we immediately identified two as ellipsoidal variables with periods between 30 and 60 minutes (ZTF J2130+4420 and ZTF J2055+4651) because they clearly exhibited significant power at twice their orbital frequency, distinguishing them from the large number of δ Scuti stars in this period range (Breger, 2000). Spectroscopic characterization later revealed additional ellipsoidal variables with orbital periods between 30 and 60 minutes. Some candidates exhibiting a dominant period below 30 min failed to show indications of binarity in follow-up characterization. Some of these were identified as likely belonging to other classes of short period variables including pulsating WDs such as GW Vir, V777 Her, and ZZ Ceti stars (Fontaine and Brassard, 2008), hot subdwarf p-mode pulsators (Charpinet et al., 1996), blue large amplitude pulsators (Pietrukowicz et al., 2017), He WD radial mode pulsators (Kupfer, Bauer, Burdge, Bellm, et al., 2019), rapidly rotating magnetic WDs (Brinkworth et al., 2013; Reding et al., 2020). One significant source of interlopers in the sample originates from intermediate polars (Patterson, 1994), which contain magnetic WDs which have been spun up to a short spin period, and exhibit periodicity on the timescale of minutes. These objects often have blue color, emit X-rays, and can show strong photometric periodicity on minute timescales due to flux variations on the WD spin period (Ramsay, Wheatley, et al., 2008). The crucial diagnostic we use to rule out a minutes-timescale orbital period in these systems is phase-resolved spectroscopy, as they do not exhibit radial velocity shifts on the WD spin period.

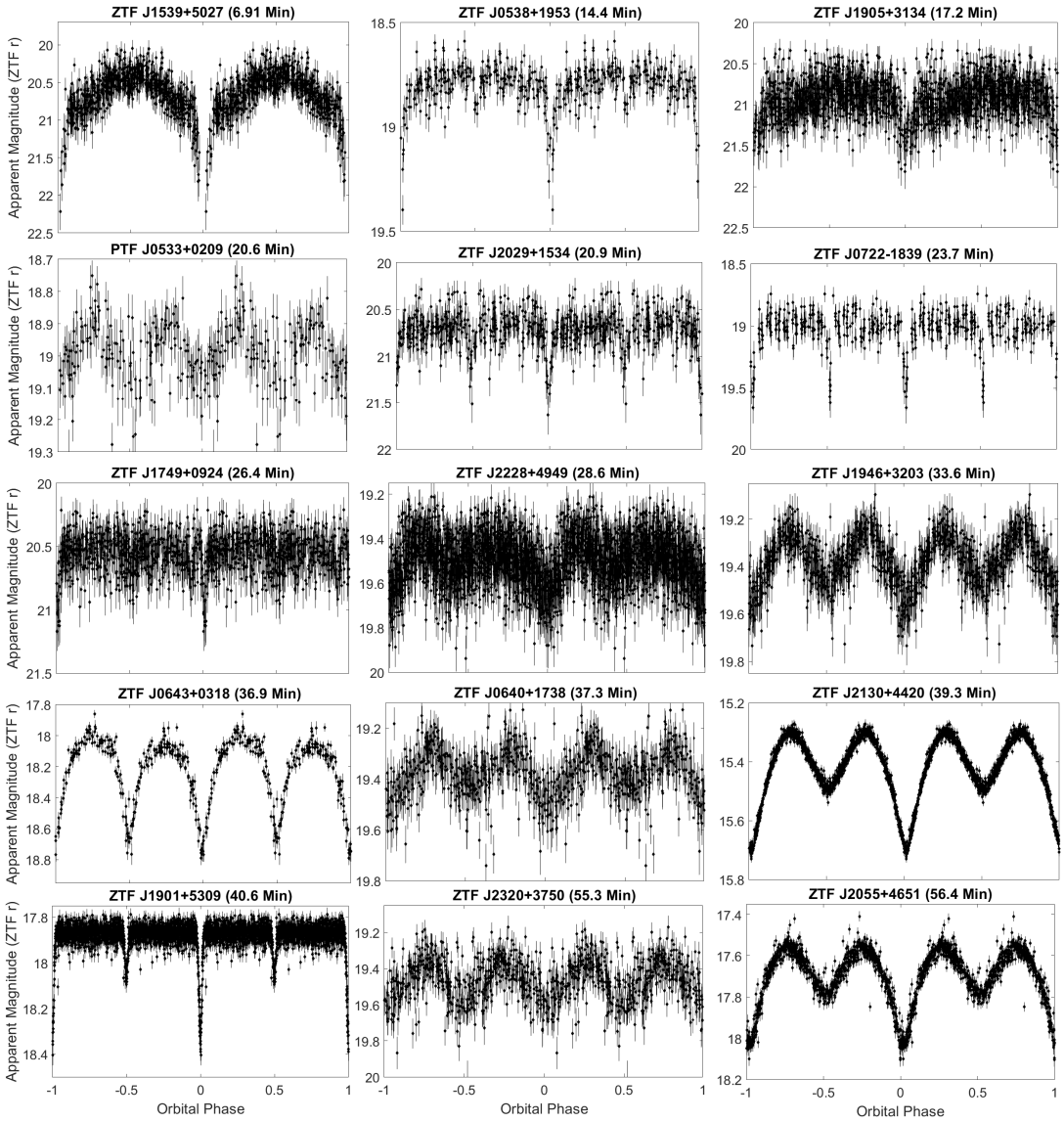

Figure 5.1: The phase-folded ZTF lightcurves of the sample (all filters combined), at periods as recovered by the algorithm described in Section 2.3.

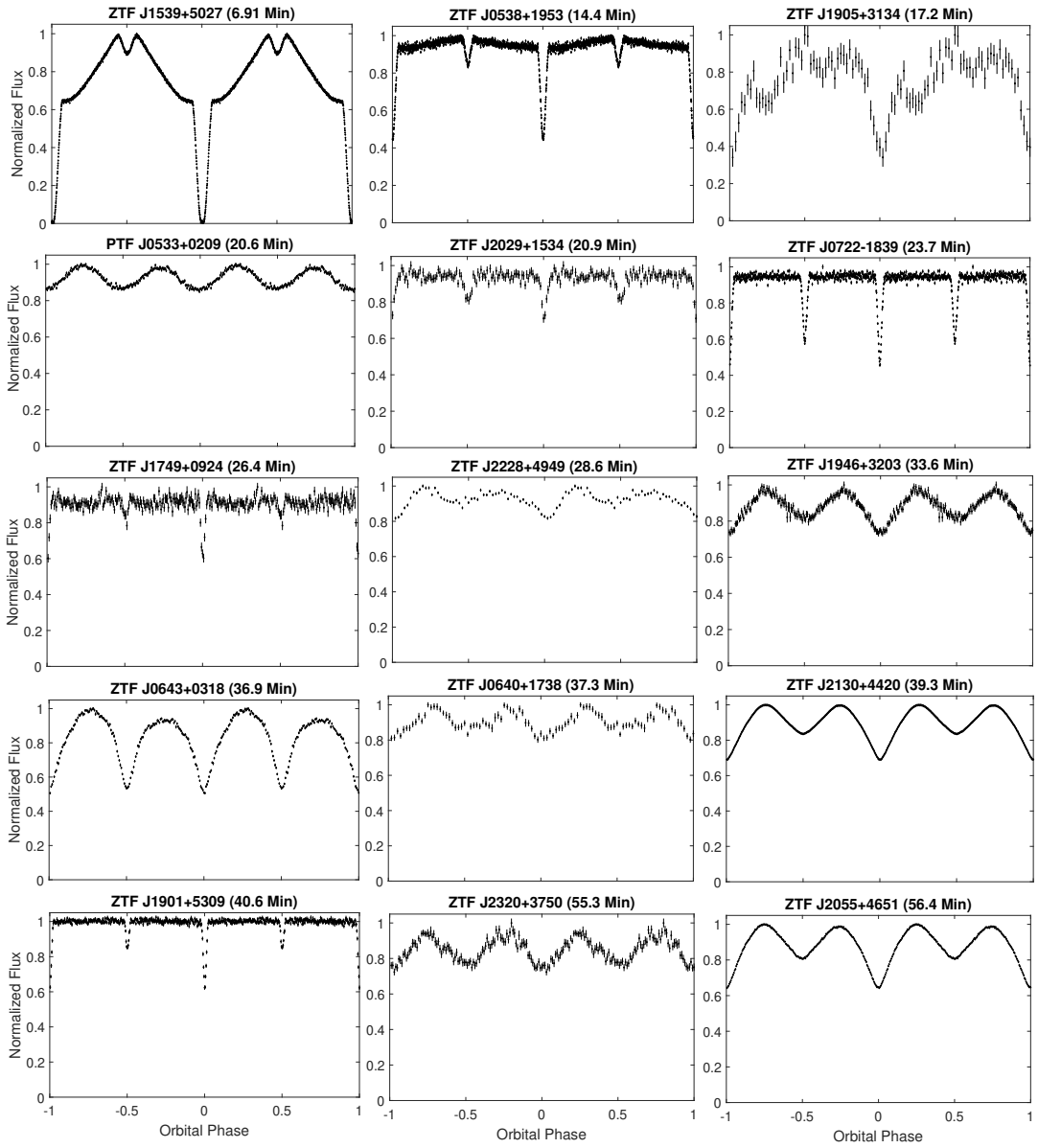

Figure 5.2: The best available lightcurves for our sample, phase-binned at the orbital periods. See Table 5.7 for further details on which instruments were used to obtain each lightcurve. J2228+4949 and J0640+1738 have only ZTF lightcurves, and thus we plot the binned versions of those here. All of these systems were confirmed as binaries via spectroscopic follow-up.

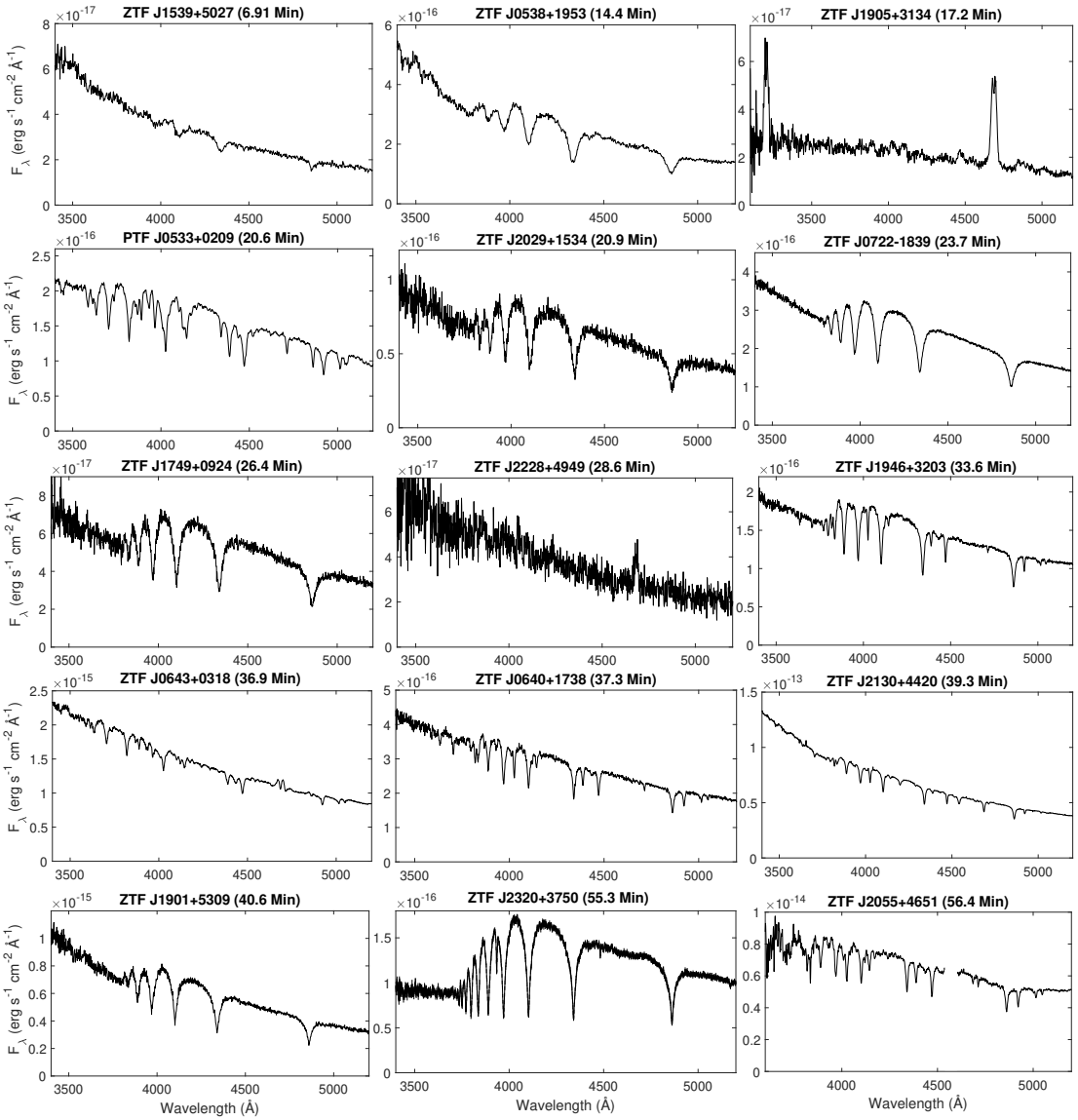

Figure 5.3: The best available spectra for our sample, coadded in the rest frame of absorption lines. By fitting these spectra, we were able to obtain radial velocity semi-amplitudes for seven systems (see Figure 5.4), and fit objects for an effective temperature and surface gravity using spectroscopic WD models. We used these spectroscopically derived parameters in combination with lightcurve modelling to derive the physical parameters reported in Table 5.5. See the Appendix for further details on which instruments were used to obtain each spectrum. ZTF J1539+5027, J0538+1953, J2029+1534, J0722−1839, J1749+0924, J1901+5309, and J2320+3750 show hydrogen-rich atmospheres, while J0533+0209, J1946+3203, J0640+1738, J2130+4420, and J2055+4651 exhibit mixed H/He atmospheres, and the three mass transferring systems, J1905+3134, J2228+4949, and J0643+0318 have only helium lines in their spectra.

High Speed Photometry

High-speed photometric follow-up proved a crucial element in characterizing candidates from our period searches, as such observations can confirm the presence of eclipses and more subtle photometric effects such as Doppler beaming and gravity darkening. In this work, we present data collected from four different high-speed photometers: the Caltech HIgh-speed Multi-color camERA (CHIMERA) on the 5.1-meter Hale telescope at Palomar Observatory (Harding et al., 2016), the Kitt Peak Electron Multiplying CCD Demonstrator (KPED) on the 2.1-meter telescope at Kitt Peak National Observatory (Coughlin, Dekany, et al., 2019), HiPERCAM on the 10.4-meter Gran Telescopio Canarias (Dhillon, Dixon, et al. 2018, Dhillon et al. in prep), and ULTRACAM on the 3.5-meter New Technology Telescope at La Silla Observatory (Dhillon, Marsh, et al., 2007). In all cases, the instruments were run in frame transfer mode, effectively eliminating readout time overheads. We reduced the CHIMERA, KPED, HiPERCAM and ULTRACAM data with publically available pipelines [1,2,3]. Lightcurves obtained with these instruments are illustrated in Figure 5.2. For further details on these observations, please see the Appendix.

Spectroscopic follow-up

We conducted most of our spectroscopy using the Low Resolution Imaging Spectrometer (LRIS) (Oke, Cohen, et al., 1995) on the 10-meter W. M. Keck I Telescope on Mauna Kea. Exposure times varied from object to object, but were restricted to be no more than an eighth of the orbital period in order to minimize Doppler smearing. We reduced all data with the lpipe pipeline (Perley, 2019). For all sequences of exposures, we took a HeNeArCdZn arc at the telescope position of the object at the completion of the sequence in order to ensure stable wavelength calibration (which can depend strongly on instrument flexure). For any sequences of observations exceeding an hour, we obtained an arc at the start and finish of observations, or if longer than two hours, an arc once every two hours. For further details on instrument configuration, and other spectrographs used, please see the Appendix. The spectra we obtained are presented in Figure 5.3.

[1] `https://github.com/mcoughlin/kp84`
[2] `https://github.com/HiPERCAM`
[3] `https://github.com/trmrsh/cpp-ultracam`

5.3 Analysis and Results

Lightcurve Modelling

We used the LCURVE code (Copperwheat et al., 2010) to model and infer physical parameters from the lightcurves we obtained with high-speed photometers. For lightcurves with multiple bands, we simultaneously modelled all bands (measuring the relative surface brightnesses of objects at multiple wavelengths aids in determining the relative temperatures of the objects in the system). For all objects, we used the following set of free parameters: the mass ratio $q = \frac{M_B}{M_A}$, the inclination i, the radius of the primary component, R_A, the radius of the secondary component, R_B, the temperature of the secondary component, T_B, the mid-eclipse time, t_0, and an absorption coefficient α to account for effects in which the cooler component in the binary is irradiated and reprocesses flux originating from the hotter component. We fit for a different α for each band, as radiation reprocessing is wavelength dependent. Measuring the mass ratio, q, from lightcurve modelling arises primarily from fitting ellipsoidal modulation due to the tidal deformation of one or both components in the system. The fractional amplitude of ellipsoidal modulation, $\frac{\Delta F_{ellipsoidal}}{F}$, is given by:

$$\frac{\Delta F_{ellipsoidal}}{F} = 0.15 \frac{(15+u)(1+\tau)}{3-u} \left(\frac{R}{a}\right)^3 q \sin^2(i), \tag{5.1}$$

(Morris, 1985), where u is the passband-dependent linear limb darkening coefficient, and τ is the passband-dependent gravity darkening coefficient. We obtain all gravity and limb darkening coefficients from Claret, Cukanovaite, et al. (2020c), and Doppler beaming coefficients from Claret, Cukanovaite, et al. (2020a). For our full modelling, we use the 4-parameter Claret limb-darkening law described in Claret (2000). Previous work such as that presented in Bloemen et al. (2012) found tension between the mass ratio inferred from purely ellipsoidal modulation, and that determined by other less model-dependent measurements such as radial velocity semi-amplitudes, which they attributed to the possibility that some close binaries may not be entirely synchronized. At these short orbital periods, we expect some of our systems to be synchronized, but those at longer periods may not be (Fuller and Lai, 2012). In any case, we emphasize that mass ratios derived from ellipsoidal modulation come from model-dependent expressions, and thus there is value in obtaining more model-independent measurements in the form of a

radial velocity semi-amplitudes as well as orbital decay due to general relativity (Burdge, Coughlin, et al., 2019).

We estimated masses for five of the eclipsing systems (ZTF J0538+1953, ZTF J2029+1534, ZTF J0722−1839, ZTF J1749+0924, and ZTF J1901+5309) using temperatures derived from spectroscopy, and radii derived from lightcurve modelling. As discussed above, lightcurve modelling allows us to infer the radii of the two component objects with respect to the semi-major axis in these systems. We combined these measurements (as well as our spectroscopic temperature constraints) with the semi-empirical mass-radius relations described in Soares (2017) in order to estimate the masses of both components. We adopted a 10 percent model error in estimating our uncertainties based on the scatter of measured radii vs estimated radii reported in Soares (2017), because mass-radius relations (especially for low mass He WDs) are sensitive to additional degrees of freedom such as the mass of the hydrogen envelope on the surface of the WD and the evolutionary history of the object (in particular, the occurrence of hydrogen shell flashes; Istrate et al. (2016)). In the future, as we measure orbital decay rates for these systems, we will be able to constrain masses in a more model-independent manner.

Orbital Dynamics

We acquired phase-resolved spectra for all objects in the sample; however, at this time, we were only able to extract reliable radial velocity solutions for the single-lined systems. For these systems, we measured velocities by fitting Voigt profiles to the Balmer series of absorption lines and to helium absorption lines, when present. Single-lined spectroscopic binaries show a radial velocity from only one of their two components, whereas double-lined systems contain contributions from both. Double-lined systems are in principle more valuable, as one can precisely constrain the mass ratio of the system, and if combined with an inclination constraint from lightcurve modelling, solve for both of the dynamical masses in the system using the binary mass functions

$$\frac{M_A^3 \sin^3(i)}{(M_A + M_B)^2} = \frac{P_b K_B^3}{2\pi G} \ , \tag{5.2}$$

and

$$\frac{M_B^3 \sin^3(i)}{(M_B + M_A)^2} = \frac{P_b K_A^3}{2\pi G} \ . \tag{5.3}$$

where K_A and K_B are the radial velocity semi-amplitudes of the two components, i is the inclination of the system, and P_b is the orbital period. These expressions arise from Newtonian mechanics, and thus, the physics involved is straightforward, allowing for a more robust estimate of masses than those which invoke more complicated physical models, such as WD mass-radius relations, evolutionary tracks, and atmospheric models. However, in practice, fitting double-lined WDs is challenging when the components are both faint and in a short orbital period binary. One reason is that the absorption lines in WDs are intrinsically broad, such that their overlap is significant even at maximum radial velocity shift (the can be several hundred across, whereas the Doppler shifts correspond to on the order of 10). WDs do have non local thermodynamic equilibrium (NLTE) cores in their hydrogen absorption lines with a narrower full width half maximum (FWHM) allowing for more precise radial velocity measurements; however, resolving these line cores require moderate resolution spectra at good SNR. In binary systems with short orbital periods, exposures must be short to avoid significant orbital smearing, and this results in too few photons per exposure to reliably use medium resolution spectra without suffering from readout noise. Because of these technical challenges, the work to measure the dynamical masses of the double-lined systems of our sample (e.g. ZTF J0722−1839) is ongoing. See Figure 5.4 for an illustration of well-measured radial velocities in our sample (for the single-lined systems), and Table 5.3 for the measured radial velocity semi-amplitudes of objects in our sample.

Spectroscopic modelling

In addition to being used to measure radial velocities, spectra can be used to estimate the temperature, surface gravity, and atmospheric abundances of stars. For single-lined systems, we fit atmospheric models to the entire spectrum in order to estimate the temperature of the dominant component, and supply this temperature to our lightcurve modelling. We perform an iterative process for double-lined systems, due to the spectra being a blend of two WDs (one must account for this, because cool WDs often have deep absorption lines, and thus, even if they contribute only a small fraction of the overall luminosity, they can significantly impact line profiles). First, we fit a single WD model to the spectrum to estimate the temperature of the dominant component. We then

Table 5.3: Orbital Characteristics

Quantity:	K_A $(km\,s^{-1})$	K_B $(km\,s^{-1})$	i (deg)	T_0 $(MBJD_{TDB})$	P_b (s)
ZTF J1539+5027[1]	292^{+254}_{-583}	961^{+178}_{-139}	$84.15^{+0.64}_{-0.57}$	58305.1827886(12)	414.7915404(29)
ZTF J0538+1953			$85.43^{+0.07}_{-0.09}$	58734.23560684(49)	866.60331(16)
ZTF J1905+3134					1032.16441(62)
PTF J0533+0209[2]		$618.7^{+6.9}_{-6.9}$	$72.8^{+0.8}_{-1.4}$	58144.596848(46)	1233.9729(17)
ZTF J2029+1534			$86.64^{+0.70}_{-0.4}$	58757.255378(55)	1252.056499(41)
ZTF J0722−1839			$89.66^{+0.22}_{-0.22}$	58874.1823868(11)	1422.548655(71)
ZTF J1749+0924			$85.45^{+1.40}_{-1.15}$	58634.41086(2)	1586.03389(44)
ZTF J2228+4949					1713.58282(25)
ZTF J1946+3203		$284.8^{+4.8}_{-4.8}$	$77.08^{+1.6}_{-1.2}$	58836.38825(13)	2013.82141(75)
ZTF J0643+0318		$432.5^{+12.0}_{-12.0}$			2214.8058(11)
ZTF J0640+1738		$315.9^{+8.0}_{-8.0}$	$65.3^{+5.1}_{-5.1}$	58836.38825(13)	2236.0160(16)
ZTF J2130+4420[3]		$418.5^{+2.5}_{-2.5}$	$86.4^{+1.0}_{-1.0}$	58672.1808578(1)	2360.4062(14)
ZTF J1901+5309			$87.28^{+0.52}_{-0.50}$	58703.3738042(31)	2436.10817(93)
ZTF J2320+3750		$466.0^{+9.0}_{-9.0}$	$84.5^{+2.7}_{-3.2}$	58769.28488(28)	3314.7998(35)
ZTF J2055+4651[4]		$404.0^{+11.0}_{-11.0}$	$83.3^{+0.5}_{-0.5}$	58731.944425(1)	3380.8701(29)

Measured orbital parameters for all of our systems, including the radial velocity semi-amplitudes of the components, K_A and K_B, the orbital inclination, i, the time of superior conjunction, T_0, and the orbital period, P_b. All quantities were determined using the analyses described in Section 3, with the exception of ZTF J1539+5027, ZTF J0533+0209, ZTF J2130+4420 and ZTF J2055+4651, whose parameters were taken from previous publications. Burdge, Coughlin, et al. (2019)[1], Burdge, Fuller, et al. (2019)[2], Kupfer, Bauer, Marsh, et al. (2020)[3], Kupfer, Bauer, Burdge, van Roestel, et al. (2020)[4]

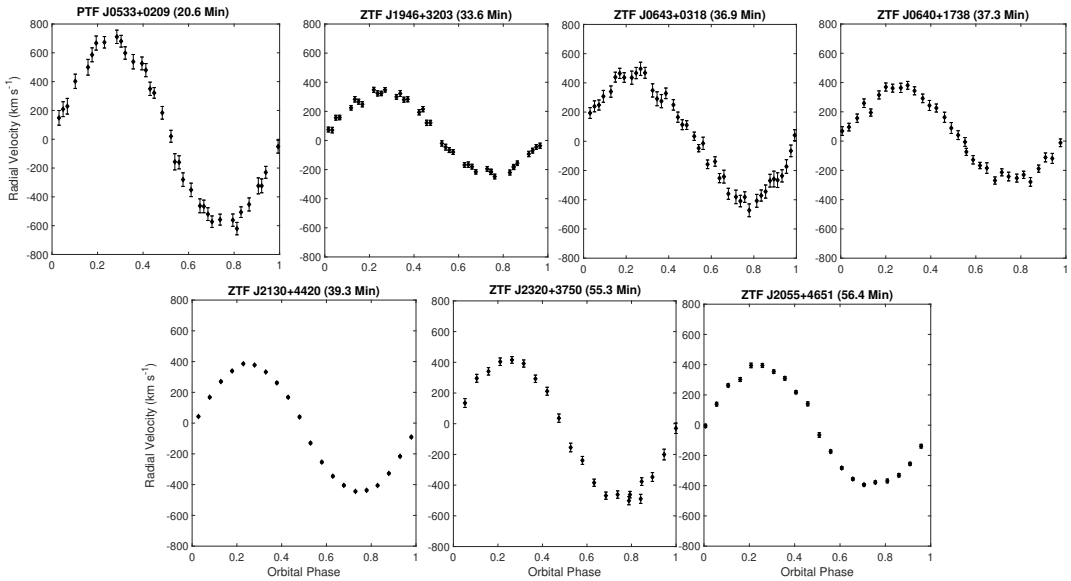

Figure 5.4: The phase-folded radial velocity measurements for a subset of the sample which is single-lined. All measurements shown are phase-folded according to the orbital period and ephemeris obtained from lightcurve modelling.

proceed to model the lightcurve while fixing the temperature of the hotter component to this value. Using this model, we can estimate both a surface brightness ratio, and ratio of component radii. We use this information to construct a composite model of two WD atmospheres, and we fit this composite model to the spectra to arrive at the final temperature estimates. For the DA WD systems we use the NLTE DA models described in Tremblay, Bergeron, and Gianninas (2011) with Stark broadening from Tremblay and Bergeron (2009). For the coolest and lowest surface gravity DA in our sample, ZTF J2320+3750, we use models described in Gianninas, Dufour, et al. (2014) and Tremblay, Gianninas, et al. (2015). For modelling lower surface gravity ($\log(g)$) mixed H/He atmosphere objects which could be either hot subdwarfs or young He WDs, we used the model spectra described in Stroeer et al. (2007). Please note, that when we refer to He WDs throughout this publication, it indicates helium core composition, not atmospheric composition. We did not factor spectroscopically measured surface gravity

into our final parameter estimation, except for in the case of ZTF J2320+3750, in which the He WD component was poorly constrained by mass-radius relations alone due to the significant temperature sensitivity of these relations at such low mass.

Orbital Evolution

The orbital evolution of short orbital period binary systems is dominated by energy loss due to the emission of gravitational radiation, but can also be strongly influenced by the presence of mass transfer in accreting systems, especially ones with large mass ratios such as AM CVns (Postnov and Yungelson, 2014). Measuring orbital evolution in detached systems is particularly valuable, as general relativity predicts that the orbital frequency derivative, $\dot{f}_{GW}$, is directly related to the gravitational-wave frequency $f_{GW} = \frac{2}{P_b}$ and the chirp mass of the system, $\mathcal{M} = \frac{(M_A M_B)^{\frac{3}{5}}}{(M_A+M_B)^{\frac{1}{5}}}$, as given by

$$\dot{f}_{GW} = \frac{96}{5}\pi^{\frac{8}{3}}\left(\frac{GM_c}{c^3}\right)^{\frac{5}{3}} f_{GW}^{\frac{11}{3}}, \tag{5.4}$$

(Taylor and Weisberg, 1989).

Conveniently, the strain of gravitational radiation emitted from such a binary depends only on the orbital frequency, chirp mass, and distance to the object, and thus the gravitational wave strain *LISA* will measure is given by

$$S = \frac{2(G\mathcal{M})^{5/3}(\pi f_{GW})^{2/3}}{c^4 D}, \tag{5.5}$$

Multiplying this quantity by $\sqrt{f_{GW}T_{obs}}$ gives the characteristic strain, where T_{obs} is the total time *LISA* has operated (Thorne, 1987; Moore et al., 2015). For the characteristic strains computed in this work, T_{obs} is taken to be 4 years.

By constraining the chirp mass and orbital frequency from optical data, a *LISA* gravitational-wave signal can be used to infer a distance to the system, which will be particularly useful since most of the objects being discovered are too faint for reliable Gaia astrometric solutions. For over-constrained systems where the distance is well determined via a measurement like the parallax, the gravitational-wave strain could be compared with that predicted based on an orbital decay rate due to purely general relativity, to estimate a

deviation in the decay rate from tidal dissipation. Thus far, orbital decay has been detected and reported for two objects in the sample: ZTF J1539+5027 (Burdge, Coughlin, et al., 2019), and PTF J0533+0209 (Burdge, Fuller, et al., 2019). The precisely measured decay rates in these two systems were enabled by regular photometric monitoring combined with well-sampled archival Palomar Transient Factory data collected a decade ago. We have not reached this threshold for any other systems, but continue to monitor all systems for orbital frequency evolution. The uncertainties of the ephemerides reported in Table 5.3 give a characteristic estimate of the precision with which each system can be timed, and this can be compared to the predicted phase-shift in timing residuals given the expected decay rate of the system (see Burdge, Coughlin, et al. (2019) for more details) in order to estimate how long it will take to measure the orbital evolution precisely. The period derivative should be easily detectable in all systems before *LISA* begins to operate if their orbital evolution is dominated by the emission of gravitational waves.

Distance Estimates

We report our estimated distances to the systems in Table 5.4. Estimating the distance to systems in our sample is an important element in this work as they are crucial in computing accurate gravitational wave amplitudes for the sources as measured from the solar system. Most of the systems in our sample have temperature estimates, as well as radius estimates; this allows us to compute distances directly based on these values, and synthetic spectra for WDs. We use system parameters inferred from a combination of lightcurve modelling and spectroscopic fitting to generate a composite synthetic spectrum for each system, and compute a synthetic apparent magnitude from these spectra. We chose to compute Pan-STARRS1 g-band apparent magnitudes, and comparing to the measured value. We use Pan-STARRS1 g due to its availability for all objects and its short wavelength compared to other available passbands, ensuring minimal potential contamination from blended background sources in dense fields (which on average, are likely to contribute more to redder bands). These spectroscopic distance estimates are used in computing the *LISA* SNR. We estimate uncertainties on these distance estimates by setting up a Monte Carlo simulation in which we sample over distance and the temperatures and radii of both WDs (with priors set by the lightcurve+spectroscopic

analysis). During each iteration, we use the two temperatures and radii to generate a synthetic spectrum, and automatically query the reddening catalog described in Green, Schlafly, et al. (2019) at the coordinates of the source using the distance sample from that iteration to estimate the reddening along the line of sight, and use this to apply a reddening correction to the synthetic photometry we generate. We then compare this synthetic flux to the measured Pan-STARRS1 g, and compute the likelihood function using the uncertainty reported by Pan-STARRS1. The spectroscopic distances reported in Table 5.4 were computed using the posterior distribution of this analysis.

It is worth noting that *Gaia* has revolutionized astronomy by providing the capability to estimate distances to a large number of stars in the Galaxy via the measurement of parallax. However, for faint populations of sources with uncertain parallaxes, there are subtleties to inferring distance from the parallax, $\bar{\omega}$. Nonetheless, we wish to emphasize that when available, a precisely measured *Gaia* parallax is incredibly valuable, as this method of estimating distances arises from a simple geometric effect, whereas other techniques of estimating distance invoke more complicated model dependence. Here, we compare two approaches for estimating distances the sample of ZTF short period binaries using *Gaia* parallaxes, though the technique we ultimately use in this paper is the spectroscopic distance estimate described above.

The two parallax-based distance estimates presented in Table 5.4 use an exponentially decreasing space density prior as described in Bailer-Jones et al. (2018). An important element of this prior is that it invokes a characteristic length scale (note, this is not a scale height). The distances reported by Bailer-Jones et al. (2018) couple this prior with length scales derived from a model of the galaxy. However, this model has its shortfalls when considering a specific population of objects such as WDs, as it is purely geometric and intended to be relatively independent of the properties of stars, and thus is not an optimal choice for characterizing a sub-population of stars where additional information is present. Notably, as illustrated in Table 5.4, the Bailer-Jones technique tends to yield large distances at low Galactic latitudes, where the characteristic length scale is significantly larger than at higher Galactic latitude. Because WDs are foreground objects and this length scale is estimated based on all the stars in a region of the sky, this method likely overestimates distances in the Galactic plane for WD populations.

The alternative method, adopted by Kupfer, Korol, et al. (2018), invokes the same exponentially decreasing space density prior, but assumes a 400 pc characteristic length scale for all sources based on WD population synthesis work, rather than a length scale dependent on sky position. We report estimates based on a modified version of this method, with the same maximum likelihood measurement, but instead use a 68 percent credible interval derived from the highest posterior density of our distribution to estimate the error bars.

Combined Analysis and Observed Characteristics

We conduct a combined analysis of the lightcurve modelling of each system and modelling of the phase-resolved spectroscopy in order to estimate the properties of the systems reported in Table 5.5. We conducted the combined analysis using the nested sampling package MULTINEST (Feroz et al., 2009). When sampling, we combined modelling the lightcurve with priors on the temperature of the hotter component in each binary based on a spectroscopic fit, and for the single-lined systems, an additional constraint based on the measured radial-velocity semi-amplitude. For single-lined systems, we used the velocity semi-amplitude constraint plus constraints on the mass ratio from ellipsoidal modulation to infer parameters for the system. For double-lined systems, we instead used the mass-radius relations described in Soares (2017) to constrain the system parameters, allowing us to infer masses from radii estimated using the lightcurve. The single-lined, eclipsing, and ellipsoidal variable ZTF J1946+3203 is an exception, as in this system we inferred masses from a combination of the radial velocity semi-amplitude, and well-constrained inclination and mass ratio inferred from the lightcurve, as well as radii measurable by the eclipses. Thus, this system serves as an example of one with parameters that can be used in testing mass-radius relations. Note, that we did not model the two AM CVn systems, ZTF J1905+3134 and ZTF J2228+4949, and that modelling of the mass transferring system ZTF J0643+0318 is still underway.

***LISA* Signal to Noise**

In order to estimate the *LISA* gravitational wave SNR, we adopt the same formalism as outlined Burdge, Coughlin, et al. (2019) and Burdge, Fuller, et al. (2019) (which was based on the formalism outlined in Korol, Rossi, Groot, et al. (2017)), correcting a factor

Table 5.4: Distance and Reddening Estimates

Technique:	Spectroscopic	Bailer-Jones	400 pc Length Scale	E(g-r)	*Gaia* $\bar{\omega}$	*Gaia* μ RA	*Gaia* μ Dec
	(kpc)	(kpc)	(kpc)	(m_{AB})	(mas)	$(mas\,yr^{-1})$	$(mas\,yr^{-1})$
ZTF J1539+5027	$2.34^{+0.14}_{-0.14}$	$1.39^{+0.87}_{-0.53}$	$1.25^{+0.72}_{-0.45}$		-0.11 ± 0.79	-3.41 ± 1.53	-3.82 ± 1.58
ZTF J0538+1953	$0.684^{+0.018}_{-0.014}$	$1.07^{+1.48}_{-0.45}$	$0.84^{+0.46}_{-0.26}$	$0.25^{+0.02}_{-0.02}$	1.15 ± 0.48	-2.22 ± 0.54	-5.67 ± 0.45
ZTF J1905+3134	$3.8 - 9.5$						
PTF J0533+0209	$1.74^{+0.14}_{-0.14}$	$1.54^{+1.06}_{-0.58}$	$1.23^{+0.63}_{-0.40}$	$0.11^{+0.02}_{-0.02}$	0.47 ± 0.48	1.43 ± 0.74	2.56 ± 0.91
ZTF J2029+1534	$2.02^{+0.15}_{-0.15}$	$2.39^{+1.89}_{-1.17}$	$1.17^{+0.74}_{-0.47}$	$0.08^{+0.03}_{-0.01}$	-1.43 ± 1.43	-5.94 ± 1.51	-9.92 ± 1.93
ZTF J0722−1839	$0.928^{+0.023}_{-0.031}$	$2.51^{+2.28}_{-1.10}$	$1.41^{+0.61}_{-0.42}$	$0.14^{+0.03}_{-0.01}$	0.41 ± 0.35	-5.83 ± 0.52	4.18 ± 0.65
ZTF J1749+0924	$1.55^{+0.20}_{-0.18}$	$3.34^{+2.55}_{-1.58}$	$1.34^{+0.76}_{-0.50}$	$0.13^{+0.03}_{-0.01}$	-2.68 ± 1.36	-6.50 ± 2.78	6.90 ± 3.74
ZTF J2228+4949	$0.72 - 1.77$	$1.79^{+1.48}_{-0.67}$	$1.31^{+0.54}_{-0.36}$	$0.14^{+0.02}_{-0.02}$	0.57 ± 0.31	-3.83 ± 0.56	-2.56 ± 0.53
ZTF J1946+3203	$2.38^{+0.18}_{-0.20}$	$2.18^{+4.12}_{-1.08}$	$1.15^{+0.51}_{-0.33}$	$0.14^{+0.02}_{-0.04}$	0.72 ± 0.35	-1.86 ± 0.46	-4.27 ± 0.49
ZTF J0643+0318		$2.13^{+1.59}_{-0.74}$	$1.55^{+0.51}_{-0.39}$	$0.45^{+0.02}_{-0.05}$	0.47 ± 0.22	0.71 ± 0.40	1.50 ± 0.41
ZTF J0640+1738	$5.9^{+1.3}_{-1.2}$	$1.90^{+1.61}_{-0.80}$	$1.24^{+0.61}_{-0.39}$	$0.12^{+0.02}_{-0.02}$	0.51 ± 0.44	-0.36 ± 1.16	1.10 ± 1.33
ZTF J2130+4420	$1.209^{+0.046}_{-0.047}$	$1.116^{+0.043}_{-0.040}$	$1.16^{+0.10}_{-0.08}$	$0.18^{+0.02}_{-0.02}$	0.833 ± 0.031	0.009 ± 0.031	-1.682 ± 0.0048
ZTF J1901+5309	$0.831^{+0.050}_{-0.047}$	$0.89^{+0.11}_{-0.09}$	$0.88^{+0.08}_{-0.10}$	$0.05^{+0.02}_{-0.02}$	1.11 ± 0.12	2.94 ± 0.25	4.75 ± 0.26
ZTF J2320+3750	$2.51^{+0.22}_{-0.22}$	$1.29^{+0.79}_{-0.42}$	$1.16^{+0.54}_{-0.35}$	$0.15^{+0.01}_{-0.01}$	0.68 ± 0.39	13.00 ± 0.49	11.74 ± 0.43
ZTF J2055+4651	$2.57^{+0.12}_{-0.13}$	$2.17^{+0.63}_{-0.41}$	$1.94^{+0.30}_{-0.36}$	$0.53^{+0.02}_{-0.01}$	0.432 ± 0.098	-3.33 ± 0.17	-5.16 ± 0.17

Comparison of three methods for estimating distances to the sample of binaries, including a spectroscopic distance, and two parallax based distances. Note that the Bailer-Jones (Bailer-Jones et al., 2018) and 400 pc length scale (Kupfer, Korol, et al., 2018) techniques depend on *Gaia* astrometry, while the spectroscopic distances are determined from the measured radii and temperatures of the objects. We also estimate the reddening, E(g-r), for each system (Green, Schlafly, et al., 2019), and present the measured *Gaia* parallax, $\bar{\omega}$, and proper motions , μ RA and μ Dec, for each system.

Table 5.5: Physical System Parameters

Quantity:	M_A	M_B	R_A	R_B	T_A	T_B
Units:	$(M_\odot)$	$(M_\odot)$	$(R_\odot)$	$(R_\odot)$	(kK)	(kK)
ZTF J1539+5027[1]	$0.610^{+0.017}_{-0.022}$	$0.210^{+0.015}_{-0.015}$	$0.01562^{+0.00038}_{-0.00038}$	$0.03140^{+0.00054}_{-0.00052}$	$48.9^{+0.9}_{-0.9}$	< 10
ZTF J0538+1953	$0.45^{+0.05}_{-0.05}$	$0.32^{+0.03}_{-0.03}$	$0.02069^{+0.00028}_{-0.00034}$	$0.02319^{+0.00032}_{-0.00026}$	$26.45^{+0.725}_{-0.725}$	$12.8^{+0.2}_{-0.2}$
PTF J0533+0209[2]	$0.652^{+0.037}_{-0.040}$	$0.167^{+0.030}_{-0.030}$		$0.057^{+0.004}_{-0.004}$		$20^{+0.8}_{-0.8}$
ZTF J2029+1534	$0.32^{+0.04}_{-0.04}$	$0.30^{+0.04}_{-0.04}$	$0.029^{+0.002}_{-0.003}$	$0.028^{+0.003}_{-0.003}$	$18.25^{+0.25}_{-0.25}$	$15.3^{+0.3}_{-0.3}$
ZTF J0722−1839	$0.38^{+0.04}_{-0.04}$	$0.33^{+0.03}_{-0.03}$	$0.0224^{+0.0004}_{-0.0002}$	$0.0249^{+0.0001}_{-0.0003}$	$19.9^{+0.15}_{-0.15}$	$16.8^{+0.15}_{-0.15}$
ZTF J1749+0924	$0.40^{+0.07}_{-0.05}$	$0.28^{+0.05}_{-0.04}$	$0.022^{+0.003}_{-0.004}$	$0.025^{+0.004}_{-0.004}$	$20.4^{+0.2}_{-0.2}$	$12.0^{+0.6}_{-0.6}$
ZTF J1946+3203	$0.272^{+0.046}_{-0.043}$	$0.307^{+0.097}_{-0.085}$	$0.0299^{+0.0049}_{-0.0045}$	$0.111^{+0.012}_{-0.013}$	$11.5^{+2.3}_{-4.6}$	$28.0^{+1.7}_{-1.7}$
ZTF J0640+1738	$0.39^{+0.12}_{-0.089}$	$0.325^{+0.30}_{-0.15}$		$0.152^{+0.040}_{-0.032}$	$10.2^{+8.3}_{-6.8}$	$31.5^{+5.0}_{-5.0}$
ZTF J2130+4420[3]	$0.545^{+0.020}_{-0.020}$	$0.337^{+0.015}_{-0.015}$		$0.125^{+0.005}_{-0.005}$		$42.4^{+3.0}_{-3.0}$
ZTF J1901+5309	$0.36^{+0.04}_{-0.04}$	$0.36^{+0.05}_{-0.05}$	$0.029^{+0.001}_{-0.002}$	$0.022^{+0.003}_{-0.002}$	$26.0^{+0.2}_{-0.2}$	$16.5^{+2.0}_{-2.0}$
ZTF J2320+3750	$0.69^{+0.03}_{-0.03}$	$0.20^{+0.01}_{-0.01}$		$0.152^{+0.015}_{-0.017}$		$9.2^{+0.2}_{-0.2}$
ZTF J2055+4651[4]	$0.68^{+0.05}_{-0.05}$	$0.41^{+0.04}_{-0.04}$	$0.0148^{+0.002}_{-0.002}$	$0.17^{+0.01}_{-0.01}$	$63.0^{+1.0}_{-1.0}$	$33.7^{+1.0}_{-1.0}$

Derived physical parameters for the components in our systems, including the masses of the two components, M_A and M_B, the radii of the components, R_A and R_B, and the effective surface temperatures of the components, T_A and T_B. We have excluded systems with significant mass transfer contributing to the luminosity: ZTF J0643+0318, ZTF J1905+3134, and ZTF J2228+4949. All were determined using the analyses described in section 3, with the exception of ZTF J1539+5027, PTF J0533+0209, ZTF J2130+4420 and ZTF J2055+4651, whose parameters were taken from previous publications.Burdge, Coughlin, et al. (2019)[1], Burdge, Fuller, et al. (2019)[2], Kupfer, Bauer, Marsh, et al. (2020)[3], Kupfer, Bauer, Burdge, van Roestel, et al. (2020)[4]

of 2 error which was present in the previous estimates, resulting in overall lower signal-to-noise (SNR) estimates. We use the updated sensitivity curve presented in Robson et al. (2019).

For a more detailed discussion of *LISA* SNR estimates, and their subtleties, please see the Appendix.

5.4 Discussion of individual systems

ZTF J1539+5027

ZTF J1539+5027 is a deeply eclipsing DWD binary system with an orbital period of just $\approx 6.91\,min$ (Burdge, Coughlin, et al., 2019) consisting of a cool He WD orbiting a heated CO WD. This is one of two systems in our sample with confirmed orbital decay, and thus, a precise measurement of its chirp mass (assuming the decay is due to energy loss to gravitational radiation). There is ongoing work to more precisely characterize this system using observations obtained with the high-speed photometer HiPERCAM (see the first panel in Figure 5.2) and the COS spectrograph on the Hubble Space Telescope. The system is among the highest SNR *LISA*-detectable gravitational-wave sources known, and presents a curious evolutionary puzzle, as the CO WD in the system has been heated to $\approx 50,000\,K$, but there are no observational indications of active mass transfer (see Burdge, Coughlin, et al. (2019) for further details).

ZTF J0538+1953

ZTF J0538+1953 is a 14.44-min orbital period eclipsing detached DWD system. The hotter WD is $\approx 26,000\,K$, and the cooler companion $\approx 13,000\,K$. The two components are of comparable radii (with the cooler being slightly larger than its hot companion, indicating that it is likely the less massive component). The lightcurve exhibits a moderate degree of flux reprocessed by the heated face of the cooler WD in the system (causing an 8 percent peak-to-peak amplitude photometric modulation on the orbital period), though this effect is much smaller than that observed in ZTF J1539+5027. After conducting lightcurve modelling, we found a best fit for the mass ratio $q = \frac{M_B}{M_A} = 5.01 \pm 0.55$, where M_B corresponds to the mass of the cooler, larger secondary. This is highly unlikely because this physically conflicts with WD mass-radius relations (which were used to

infer the final reported masses).

Upon further inspection of the residuals of the model, we see that even with the best-fit model, there is a residual signal with a few percent amplitude at twice the orbital frequency, phase-shifted with respect to the expected phase of ellipsoidal modulation. This signal could arise as a result of incomplete modelling of the reprocessed radiation on the heated face of the secondary, or potentially, be indicative of a dynamically excited tidal pulsation, as is expected to occur at twice the orbital frequency in circular orbit systems. Further follow-up should allow us to understand this signal, but for the purposes of this work we have omitted quoting a mass ratio of the object based on the lightcurve, as it is difficult to disentangle this signal from any weak ellipsoidal modulation that may be present.

ZTF J0538+1953 is perhaps best compared to SDSS J0651+2844, the 12.75-min orbital period detached binary discovered by Brown, Kilic, Hermes, et al. (2011) and further characterized in Hermes, Kilic, et al. (2012). ZTF J0538+1953's components have measured R/a values of ≈ 0.11 for the hot $\approx 26,000\,K$ and ≈ 0.13 for the cooler $\approx 13,000\,K$ component, whereas the components of SDSS J0651+2844 have R/a values of ≈ 0.12 for the hotter object and ≈ 0.045 for the cooler, more compact companion.

Invoking mass-radius relations in combination with the lightcurve modelling (which make use of the radii inferred from eclipses to determine masses), we find that the cooler component in ZTF J0538+1953 is consistent with a $0.32^{+0.03}_{-0.03}\,M_\odot$ object, suggesting it is a He WD. The hotter WD in the system has a mass consistent with a $0.45^{+0.05}_{-0.05}\,M_\odot$ object, which lies in a regime where the WD could be a He WD, CO WD, or hybrid WD (Perets et al., 2019).

ZTF J1905+3134

ZTF J1905+3134 is an AM CVn system exhibiting a photometric modulation at $\approx$ 17.2 minutes, and strong double-peaked He 2 emission, similar to that seen in SDSS J1351−0643 (Green, Hermes, et al., 2018). Shorter orbital period AM CVn systems like SDSS J1351−0643 and ZTF J1905+3134 do not normally undergo outbursts like their longer period counterparts, and instead remain in a constant high state (Ramsay, Green, et al., 2018), and ZTF J1905+3134's strong He 2 emission is characteristic of

shorter period systems in the high state. The photometric modulation in this system could either originate from the orbital period or the disk precession period (Green, Hermes, et al., 2018); however, the deep, sharp temporal feature in the lightcurve (see Figure 5.2) suggests the system is eclipsing (with a possible additional eclipse of a hot spot shortly after the deeper eclipse), which would make this the shortest orbital period eclipsing AM CVn known. Further photometric follow-up of this faint system could constrain these features more precisely, but current follow-up (which consists of just a few orbital cycles) lacks the SNR necessary for detailed modelling. ZTF J1905+3134 is the only object in our sample which completely lacks a *Gaia* astrometric solution, so we instead refer to Ramsay, Green, et al. (2018) in order to estimate the distance based on its luminosity and the period-luminosity relation for AM CVn systems. AM CVn systems around the period range of 17 minutes exhibit absolute luminosity values in the range of $M_G \approx 5 - 8$. Thus, using a uniform prior on the absolute luminosity reflecting this range, and comparing to the *Gaia* apparent magnitude of $G = 20.90 \pm 0.030$, we estimate that the object lies approximately $3.8 - 9.55\,kpc$ from the Sun.

PTF J0533+0209

PTF J0533+0209 is a $\approx$ 20.6-min orbital period detached binary system first described in Burdge, Fuller, et al. (2019). The system is unique due to its He-dominated DBA atmosphere, which exhibits only traces of hydrogen —a previously unseen characteristic among ELM WDs. The system's atmospheric composition raises question about formation channels because it requires fine-tuning of evolutionary models to produce an object with so little hydrogen (see Burdge, Fuller, et al. (2019) for further details). Like ZTF J1539+5027, orbital decay has been detected in this system, enabling the measurement of a chirp mass assuming orbital evolution primarily due to general relativity. The system houses an unseen compact object, likely a CO WD.

ZTF J2029+1534

ZTF J2029+1534 is a detached eclipsing DWD binary with an orbital period of $\approx$ 20.9 minutes. With relatively large R/a values of ≈ 0.15 and ≈ 0.12, and temperatures of $\approx 19,500\,K$ and $\approx 17,000\,K$, respectively, this system likely consists of two similar temperature He WDs, with mass-radius relations giving estimated masses of $0.32^{+0.04}_{-0.04}\,M_\odot$

and $0.30^{+0.04}_{-0.04}\,M_\odot$ for the two components, respectively. The system is among the faintest in the sample, with a Pan-STARRS g-band apparent magnitude of ≈ 20.4.

ZTF J0722−1839

ZTF J0722−1839 is a detached eclipsing DWD binary with an orbital period of ≈ 23.70 minutes. Remarkably, the primary and secondary eclipses in this system both result in an attenuation of nearly half of the system's flux (with the deeper eclipse attenuating by slightly over 50 percent of the flux, and the secondary eclipse over 40 percent of the flux). To exhibit two eclipses of this depth, the system must be fine-tuned. These eclipses indicate that the objects must be able to almost completely occult each other, indicating similar radii, and their nearly equal depths indicates nearly equal luminosity per unit surface area, implying similar temperatures for the two WDs. Finally, to achieve such deep eclipses, the system must be also be near edge on. Based on the system parameters reported in Table 5.3, we infer that this system is a double He WD system, with two He WDs of similar temperatures and radii. This may imply that the two objects have similar ages, requiring a formation mechanism capable of producing the two objects in rapid succession. The system is double-lined due to the comparable luminosity of both objects and similar line profiles due to the similarity in temperature and surface gravity (see Figure 5.5). Further work is underway to measure precise dynamical masses in this system.

ZTF J1749+0924

ZTF J1749+0924 was the final discovery in the sample described in this paper, identified using the BLS algorithm. The system likely consists of a pair of eclipsing He WDs with an orbital period of approximately 26.4 minutes. ZTF observed this system in a continuous cadence mode (taking exposures with an approximately 40 s cadence continuously for an hour and a half, on two separate occasions). On both occasions of continuously sampled observations by ZTF, the system exhibited multiple eclipses during the observation window (with each "eclipse" having only a single detection due to the short duty cycle of the feature). The system likely contains a pair of He WDs, with masses of $0.40^{+0.07}_{-0.05}\,M_\odot$ and $0.28^{+0.05}_{-0.04}\,M_\odot$.

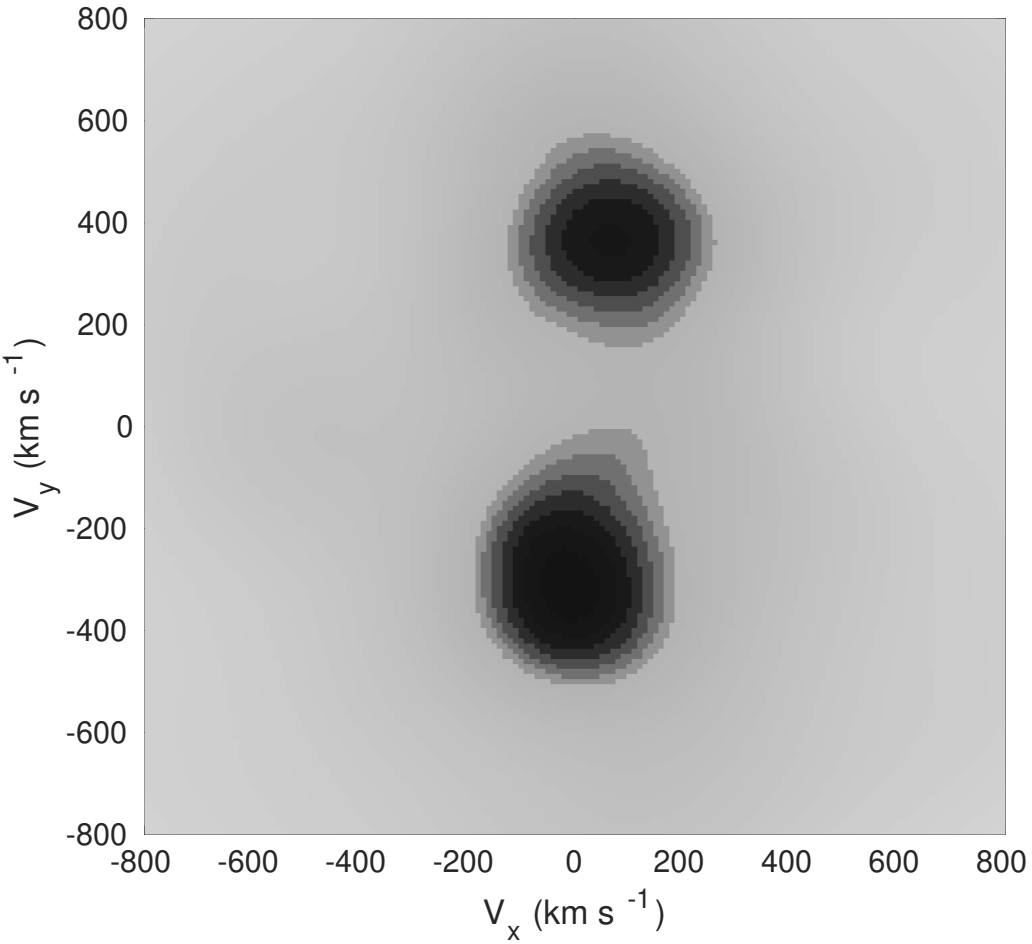

Figure 5.5: Doppler tomogram (Marsh, 2001) of the Balmer series of absorption lines in ZTF J0722−1839. The two dark features correspond to absorption line cores tracking each object, reflecting the system's double-lined nature. However, due to the shallow topographical nature of these features in the tomogram (as a result of overall low-SNR spectra in each phase bin), the velocities of the two components are poorly constrained with the current set of spectra; however, further spectroscopic follow-up of this system is underway, as it is clearly a promising candidate for measuring dynamical masses, which would serve as a test of WD mass-radius relations.

ZTF J2228+4949

ZTF J2228+4949 is an AM CVn system whose spectrum exhibits double-peaked He 2 emission characteristic of a hot accretion disk, much like that seen in ZTF J1905+3134. The system exhibits a photometric modulation at ≈ 28.56 minutes; compared to other high state AM CVn systems (Ramsay, Green, et al., 2018), ZTF J2228+4949 has an unusually long period. We propose that this system may be the longest-period high-state AM CVn system known, potentially due to an unusually high accretion rate at its orbital period. In any case, our survey, which targets systems displaying strong optical periodicity, is naturally biased towards systems in a persistent high state, as they are more likely to exhibit photometric modulation due to the presence of a superhump (Green, Hermes, et al., 2018), and also do not undergo outbursts, which can greatly impact the ability to search for periods. We estimate a spectroscopic distance of $0.72 - 1.77\,kpc$, based on the typical absolute magnitude of AM CVns at these periods falling between $M_G \approx 8 - 10$. Because ZTF J2228+4949 may have an unusually high accretion rate for its period, it is possible that the source is more distant than this spectroscopic estimate. A more precise distance estimate not based on the system's luminosity would be particularly valuable, as it would allow one to constrain whether the luminosity is indeed elevated compared to other sources at comparable orbital periods.

ZTF J1946+3203

ZTF J1946+3203 is a single-lined spectroscopic eclipsing binary which shows strong ellipsoidal variations (see Figure 5.6). The more luminous component in this system has a surface temperature of approximately $28,000 \pm 2,000\,K$ and a DAB atmosphere exhibiting both H and He 1 lines, with a spectroscopically measured surface gravity of $\log(g) = 5.74 \pm 0.2$. A combined analysis of the lightcurve and radial velocities yields mass estimates of $0.272^{+0.046}_{-0.043}\,M_\odot$ for the less luminous component (likely a He WD), and a mass of $0.307^{+0.097}_{-0.085}\,M_\odot$ for the more luminous component (which could be consistent with either a hot He WD, or an sdB). Systems like ZTF J1946+3203 are particularly valuable, as they exhibit eclipses, ellipsoidal variations, and an unambiguous radial velocity semi-amplitude, strongly constraining component masses, temperatures, and radii.

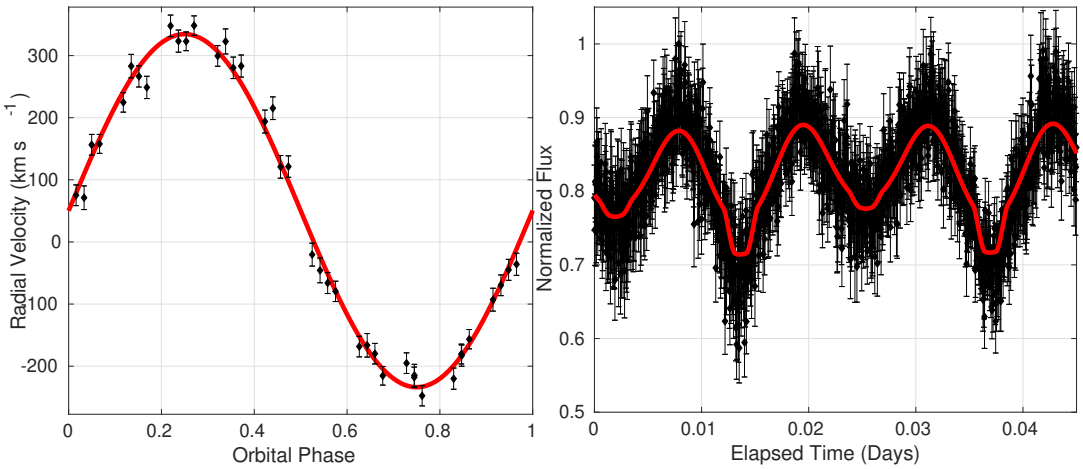

Figure 5.6: Left Panel: Radial velocities of ZTF J1946+3203 as measured from phase-resolved spectra obtained with LRIS (black points). The smearing-corrected measured semi-amplitude for this system is 284.8 ± 4.8 $km\,s^{-1}$, with the sinusoidal fit shown in red. Right panel: Best fit model (red) to the CHIMERA g-band lightcurve of the system (black points), which exhibits both strong ellipsoidal modulation, but also an eclipse. The presence of ellipsoidal modulation, eclipses, and a cleanly measured radial velocity semi-amplitude allowed us to measure both component masses and radii, which we have determined is likely a double He WD binary system. The data in this Figure is the same as shown in Figures 2 and 4, and is meant to illustrate an example model fit to the data used in parameter estimation.

ZTF J0643+0318

ZTF J0643+0318 is a single-lined spectroscopic eclipsing binary undergoing mass transfer, and consequently exhibiting a strong He 2 emission feature. Further work is underway to characterize this system.

ZTF J0640+1738

ZTF J0640+1738 is a single-lined spectroscopic binary exhibiting ellipsoidal modulation. The atmosphere of its more luminous component exhibits helium lines in addition to hydrogen, much like an sdB. Based on its large radius and high temperature, the system is likely a WD+sdB system. Because degenerate He WDs pass through the same location in color-luminosity space as sdBs, it is difficult to differentiate the two classes of objects.

The parameters for this system are poorly constrained, due to the absence of a high quality follow-up lightcurve. Further follow-up is underway to better constrain this system's characteristics.

ZTF J2130+4420

ZTF J2130+4420 is a mass transferring WD+sdB system described in Kupfer, Bauer, Marsh, et al. (2020). When the high-SNR HiPERCAM lightcurve of the system was modelled, the shape of the primary minimum in the lightcurve could only be reproduced with an accretion disk eclipsing the sdB in the system (which dominates the luminosity). The lightcurve of J2130+4420 and the similar system J2055+4651 are very distinctive, with minima of different depths, making them easy to identify as ellipsoidal/eclipsing variables and distinguish from other periodic variables in this period range.

ZTF J1901+5309

ZTF J1901+5309 is an eclipsing pair of He WDs described in detail in Coughlin, Dekany, et al. (2019). While the core composition of the WDs is ambiguous due to the system being a double-lined spectroscopic binary, we have determined masses using mass-radius relations for the two components, and identified both as consistent with He WDs.

ZTF J2320+3750

ZTF J2320+3750 consists of a CO WD orbiting a He WD. The He WD exhibits a spectrum similar to other ELMs, including a Mg II metal line (ELMs often show enhanced photospheric abundances of metals, which has been attributed to a combination of rotational mixing and radiative levitation–see Kaplan, Bhalerao, et al. (2013) and Hermes, Gänsicke, et al. (2014)). The spectrum of ZTF J2320+3750, with an example of the model used to fit it is illustrated in Figure 5.7. Notably, ZTF J2320+3750 has a large radial velocity semi-amplitude for its orbital period. Large-scale massively multiplexed spectroscopic surveys should be quite sensitive to detecting such systems with multiple observations.

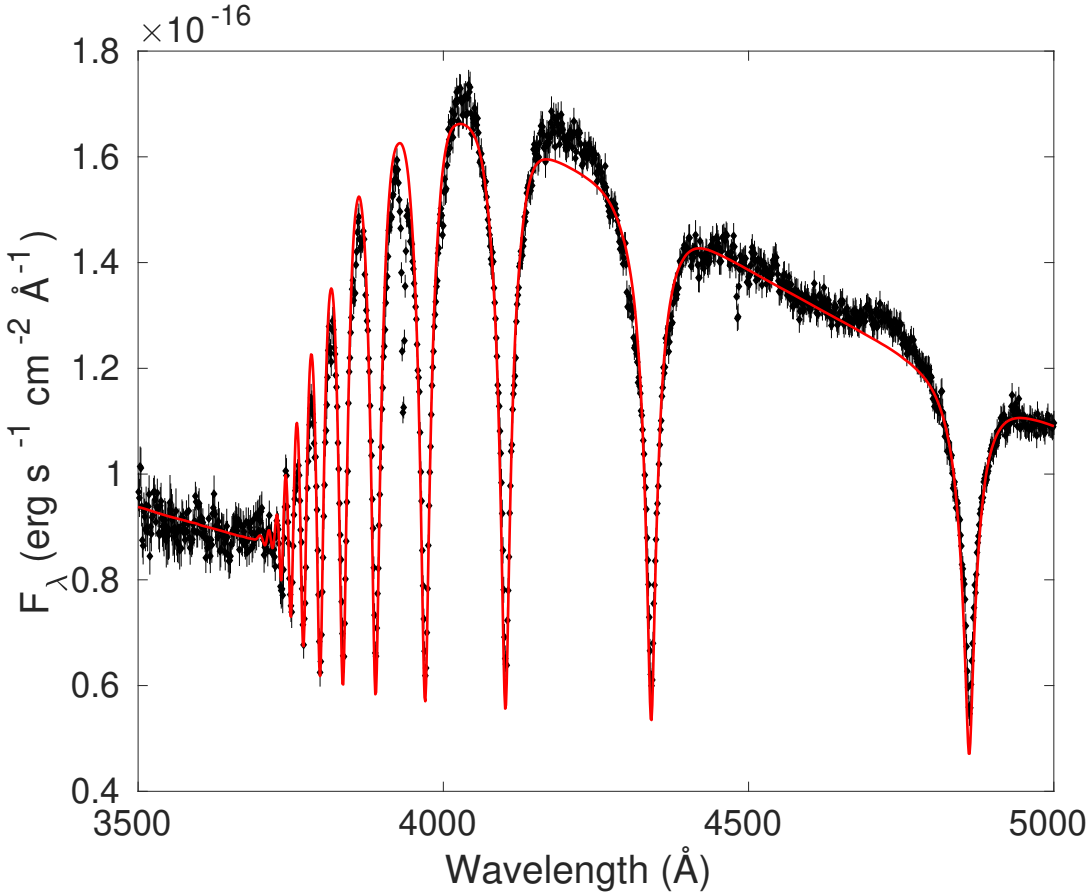

Figure 5.7: The coadded and de-redenned LRIS spectrum of ZTF J2320+3750 (black points), fit with a spectroscopic model (red) to determine the surface temperature and gravity of the white dwarf.

ZTF J2055+4651

ZTF J2055+4651 is a mass-transferring and eclipsing WD+sdB system described in Kupfer, Bauer, Burdge, van Roestel, et al. (2020). The system has a lightcurve which is incredibly similar to ZTF J2130+4420, with minima of very different depths, making it easily distinguishable from other variables such as δ Scuti pulsators. The high-SNR HiPERCAM lightcurve revealed a weak eclipse of the donating sdB star by a massive WD accretor, implying an accretor temperature of over $60,000\,K$ (see Kupfer, Bauer, Burdge, van Roestel, et al. (2020) for further details).

5.5 Discussion

Selection Biases

In order to determine what underlying population of objects our sample represents, we must consider selection biases introduced when identifying objects based on photometric periodicity and color. By selecting objects with the colors satisfying Pan-STARRS $(g - r) > 0.2$ and $(r - i) > 0.2$, our survey probes a large color space, effectively selecting all objects with $T > 6,700\,K$. Because our selection was a simple color cut, the objects in our sample span a large dynamic range in absolute luminosity, ranging from DWDs to systems containing helium stars. The selection does omit cool objects ($T < 6,700\,K$), and cool secondary of ZTF J1539+5027 suggests the possibility that tides may not efficiently heat all WDs at short orbital periods (Burdge, Coughlin, et al., 2019), suggesting that there may be value in extending the selection to encompass a cooler sample of objects as well.

Binary systems containing a high temperature component are prone to exhibiting pronounced eclipses, and are intrinsically more luminous than their cool counterparts, allowing us to probe a larger volume on average by targeting blue systems than if we simply selected objects at all colors. Less luminous cool WDs do outnumber hot WDs, meaning that the space density of short period DWDs could be substantially larger than that of the high temperature systems we are targeting if WDs in close binaries are not efficiently heated by tides. We believe our omission of cool WDs is unlikely to have significantly diminished the number of DWDs detectable in ZTF, because WDs are intrinsically faint due to their small size, and cool WDs fall below the ZTF's detection

threshold at much closer distances than their hot counterparts, greatly limiting the volume which can be probed in the cool temperature regime (consider a $0.3\,M_\odot$ He WD at $6,700\,K$–such an object would have an apparent magnitude of 21 in g at a distance of just $430\,pc$, and a $0.6\,M_\odot$ CO core WD at this temperature would reach this apparent magnitude at just $270\,pc$).

We also searched the entire catalog of WD candidates reported in Gentile Fusillo et al. (2019), which includes cooler WDs, and discovered no binary candidates which were not already encompassed by the Pan-STARRS color cut. Of the 15 systems described here, ZTF J0538+1953, PTF J0533+0209, ZTF J0722−1839, ZTF J2228+4949, ZTF J0640+1738, ZTF J1901+5309, and ZTF J2320+3750 are members of the Gentile Fusillo et al. (2019) WD catalog.

In contrast to optical surveys, gravitational wave surveys like *LISA* are agnostic to the temperatures of sources, and thus will probe this cooler population of binaries, which remain hidden to optical surveys. Sources with luminous non-degenerate helium star components such as ZTF J0643+0318, ZTF J2130+4420, and ZTF J2055+4651 are intrinsically luminous enough that they can exceed ZTF's detection threshold at several kpc, even when heavily extincted, as is the case for both ZTF J0643+0318 and ZTF J2055+4651. Thus, by targeting redder sources, one could potentially expect to find more such systems.

We did not employ any selection invoking the astrometric solutions of the *Gaia* survey (Gaia Collaboration, 2018) because ZTF's limiting apparent magnitude of ≈ 21 is beyond the threshold of *Gaia*'s ability to measure reliable parallaxes. Additionally, ZTF has acquired a significant amount of photometry in dense regions of the Galactic plane, where *Gaia* astrometric solutions are less reliable than in lower-density, higher galactic latitude fields.

Curiously, of the eclipsing systems in our sample, only one contains a clear $> 0.5\,M_\odot$ WD, even though the ELM survey found primarily pairs of He core+CO core WDs. However, this is easily understood as a selection effect. In general, CO WDs are less luminous than their He WD counterparts due to their smaller size. Thus, when such systems do undergo eclipses, it results in a shallow eclipse, as the CO WD subtends a

small cross section of the larger He WD companion when it occults it, and during the secondary eclipse when the CO WD is occulted, little luminosity is lost, as the CO WD only contributes a small fraction of the total luminosity of the system (unless the CO WD is significantly hotter than the He WD, as is the case in ZTF J1539+5027).

Objects discovered via ellipsoidal modulation carry a different selection effect. As discussed in Faulkner et al. (1972), there is a direct relation between the density of an object and the orbital period at which it overflows its Roche lobe, with only a weak dependence on mass ratio. In cases where the companion has a higher mass than the object overflowing its Roche lobe ($q < 1$, as is necessarily the case for most double degenerate objects exhibiting ellipsoidal modulation), one can relate the orbital period at which the object fills its Roche lobe, P_b, in days, and the density ρ of the Roche filling object in $g\ cm^{-3}$ with the useful approximation

$$P_b \approx \frac{0.43}{\rho^{1/2}}\ , \tag{5.6}$$

which does not deviate by more than three percent for $1 < q < 100$ (Eggleton, 1983). The selection effect introduced by this relation is quite apparent –photometric surveys like ZTF only detect ellipsoidal modulation in objects nearly filling their Roche lobes, and therefore can only detect such binaries in a narrow range of orbital periods, governed by the lower-density component in the system. Consequentially, high density objects such as CO WDs can only be discovered at extremely short orbital periods using ellipsoidal modulation, as these objects do not begin to fill their Roche lobes until $P_b \approx 1\,min$. At these orbital periods, gravitational radiation acts so quickly that the merger timescale of the systems is short (less than $500\,yr$ for a pair of $0.6\,M_\odot$ CO WDs at 60 s orbital period, which would exhibit ellipsoidal modulation on the order of a few percent at this period). However, selecting targets which exhibit ellipsoidal modulation does not introduce significant bias regarding the mass of the unseen companion, other than the basic requirement that it should be more dense/less luminous than the detected object (otherwise it would be the object dominating the signal). This has already manifested itself in our small sample of objects, as several of the systems exhibiting ellipsoidal modulation contain higher-mass presumably CO core WDs, such as ZTF J2320+3750

and ZTF J0533+0209, whereas the majority of the eclipsing systems containing pairs of He WDs.

In conclusion, it is unsurprising, based on selection biases, that our sample contains systems with at least one low-mass He WD, or a non-degenerate He star component, as detecting ellipsoidal modulation and/or eclipses is challenging for systems containing only CO WDs or more compact objects. Notably, the location of our sample when plotted on a Hertzsprung-Russell diagram (see Figure 5.8) reflects this, as all systems are clearly over-luminous relative to the WD cooling track. It is worth noting that detecting objects via photometry has important advantages over spectroscopic selection in that obtaining spectra requires dividing photons across many pixels, and thus requires integrating for much longer to exceed the signal per pixel necessary to avoid significant dilution of the SNR due to readout noise. This means that spectroscopic surveys must either target significantly brighter objects than a photometric survey, or sacrifice critical temporal resolution by acquiring longer exposures than a photometric survey of equivalent depth. Such considerations are important when comparing massively multiplexed spectroscopic surveys and photometric surveys like ZTF, and their discovery potential in the phase-space of short orbital period binaries.

LISA

Our survey targets binary systems with orbital periods under an hour because *LISA*'s gravitational wave sensitivity peaks in this regime. As illustrated in Figure 5.9, half of our sample falls above the *LISA* sensitivity curve after 4 years of observations, though the current uncertainty in *LISA* SNR for most sources originates from an uncertainty in the distance to the sources. It is also worth noting that the characteristic strains plotted in Figure 5.9 are a quantity which does not account for inclination, and as discussed earlier, a near edge-on inclination significantly diminishes the gravitational wave signal expected from a binary compared to a face-on system. Many of the ZTF sources consist of two He core WDs, whereas the ELM survey is dominated by He WDs orbiting higher mass CO core counterparts, with the notable exception of the system reported in Brown, Kilic, Bédard, et al. (2020), meaning that on average the chirp mass is lower in the ZTF sample of objects than in the ELM survey.

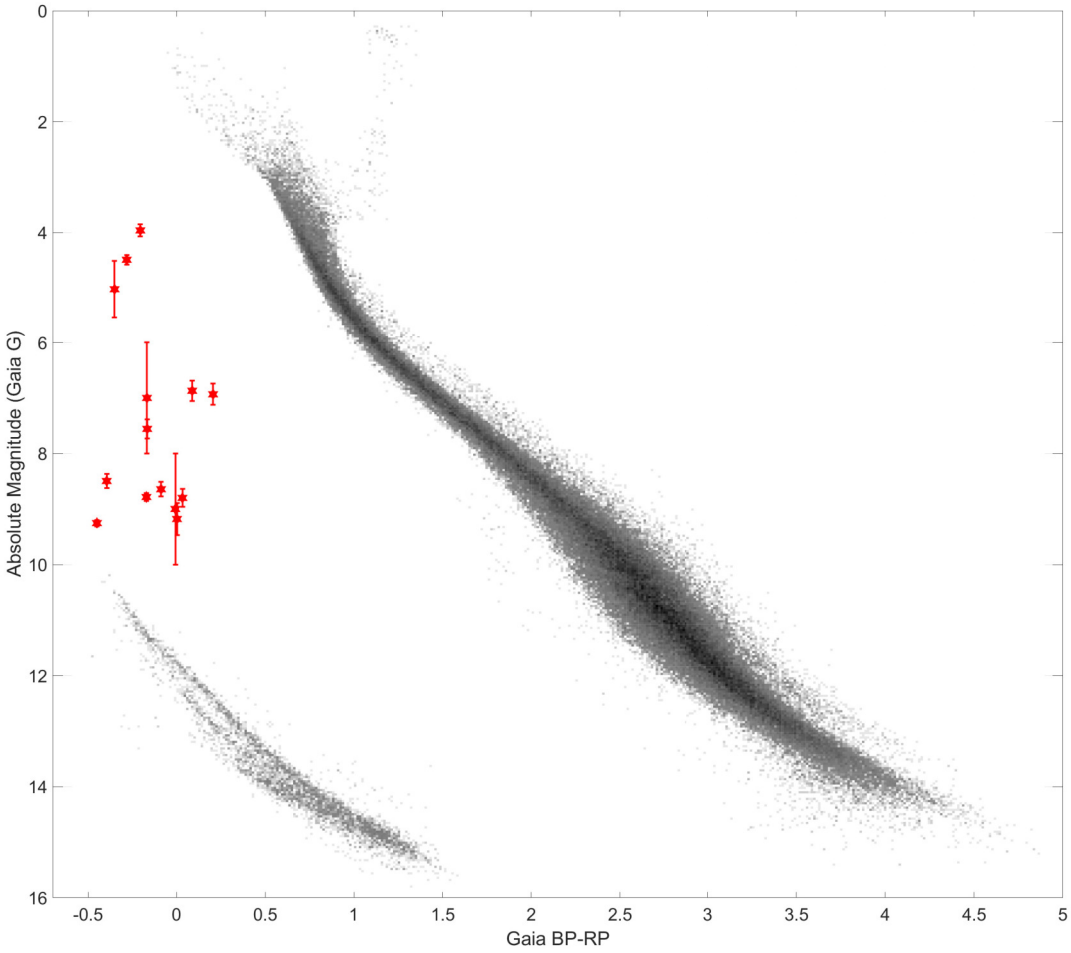

Figure 5.8: Hertzsprung-Russell diagram illustrating the de-reddened locations of 14 binaries in the sample with *Gaia* astrometric solutions (ZTF J0643+0318 is omitted, as its modelling is ongoing). The red stars represent objects which are in our sample, with absolute luminosities calculated based on their spectroscopic distances. Most objects cluster between absolute magnitudes of 6.5 and 10.0, with the exception of the systems containing either He burning stars or young and hot He WDs (which contribute significant additional luminosity, dwarfing both the luminosity of the companion WD and any accretion luminosity). The background color magnitude diagram (CMD) is the a sample of all stars in *Gaia* within 100 parsecs that have reliable astrometric solutions.

The average orbital period of the systems in the ZTF sample is significantly shorter than in the ELM sample, due both to selection criteria (this work did not pursue objects with $P_b > 60\,min$), and selection bias, as eclipses and ellipsoidal modulation become more difficult to detect at longer periods, though future work will characterize longer period systems. Shorter period objects like ZTF J1539+5027 have a small lifetime (see Table 5.6) and are thus rarer, and likely to be more distant if detected at all.

As illustrated in Figure 5.9, targeting objects at short periods compensates for the loss in characteristic strain due to such systems being rarer (and thus more distant), as *LISA*'s sensitivity increases by more than an order of magnitude over the period range of objects in our sample. The increase in sensitivity from *LISA* couples with the $f^{2/3}$ frequency dependence of the gravitational wave amplitude, and the boost in SNR due to $\sqrt{N_{cycle}}$ over 4 years of observations, meaning that the characteristic strain scales as $f^{7/6}$. Thus, a system like ZTF J1539+5027 has an enormous advantage in detectability by *LISA* over a higher chirp mass system such as J2055+4651.

The most significant contributions of our survey to the sample of *LISA*-detectable binary systems are ZTF J1539+5027 and ZTF 0538+1953, which along with SDSS J0651+2844 form a trio of high-SNR eclipsing *LISA*-detectable binaries. Due to their eclipses, we can precisely measure time these systems using optical data, and thus given a few months to years of monitoring, measure orbital decay with high confidence, and potentially even measure the acceleration of orbital decay.

Many of our binaries have precisely constrained inclinations as a result of features in their lightcurves (in particular those systems exhibiting eclipses). Eventually, these systems will serve as a test of *LISA*, which can also measure inclinations in systems through the ratio of the amplitudes of the two gravitational wave polarizations, which have differing inclination dependence. The cross polarization, $h_\times$, scales as $(1 + \cos^2(i))$, whereas the plus polarization, h_+, scales as $\cos(i)$, thus vanishing for the edge-on inclination which most eclipsing systems are near. Ellipsoidal variables like PTF J0533+0209 stand to benefit significantly from a *LISA* gravitational wave signal, which can be used to precisely constrain the inclination of these systems. When combined with the radial velocity semi-amplitude and photometric ellipsoidal modulation amplitude, this allows

for a robust estimate of the component masses.

When *LISA* begins to operate, we will gain new information on the sources. For a system like ZTF J1539+5027, which is already well constrained electromagnetically (but also a high SNR *LISA* source), the primary new constraint will be a precise distance estimate. Currently, this estimate is based on the measured radius and temperature of the object (known as a spectroscopic distance estimate), but such an estimate is quite model dependent, and assumes a reliable understanding of variables such as extinction along the line of sight. *LISA* will provide a precisely measured gravitational wave strain amplitude, and the chirp mass is already well estimated for this system based on electromagnetic constraints, and thus one can infer the distance to the source using this amplitude. For some sources, particularly those which are ellipsoidal variables with well measured temperatures, this precise distance measurement will help further constrain the properties of the system by placing tight constraints on the optical luminosity of the system.

Perhaps one of the most exciting classes of systems *LISA* will detect are those like ZTF J1539+5027, but also bright enough to have their distances measured precisely via parallax. With such sources, one could use the gravitational-wave strain amplitude to precisely measure the chirp mass of the system in a robust manner. Such a measurement would be extremely exciting, as these systems have precisely measurable orbital decay rates from eclipse timing (or even if they lack optical periodicity to measure this from, *LISA* could be used to measure the frequency evolution of the system). One could use such systems to directly measure the difference in measured $\dot{P}_b$ from that expected due to general relativity, probing the efficiency of tides in the system. Currently, the only system in our sample which has a distance measured precisely enough for such an exercise is ZTF J2130+4420, which unfortunately is a rather low-SNR *LISA* source. Additionally, this system is undergoing mass transfer, so any measured deviation of the orbital evolution from general relativity could be influenced by an exchange of angular momentum due to mass transfer.

Table 5.6: LISA SNR of systems

Name	yr *LISA* SNR	$\mathcal{A}$	$2\cos(i)$	$1+\cos^2(i)$	Decay Timescale (Myr)
ZTF J1539+5027	~ 96	$(9.96 \pm 0.93) \times 10^{-23}$	0.204 ± 0.022	1.0104 ± 0.0023	0.20753 ± 0.00043
ZTF J0538+1953	~ 96	$(2.38 \pm 0.30) \times 10^{-22}$	0.1593 ± 0.0031	1.00635 ± 0.00024	1.42 ± 0.17
PTF J0533+0209	~ 8	$(5.5 \pm 1.1) \times 10^{-23}$	0.591 ± 0.046	1.087 ± 0.014	3.89 ± 0.95
ZTF J2029+1534	~ 5	$(4.52 \pm 0.78) \times 10^{-23}$	0.117 ± 0.024	1.0034 ± 0.0014	5.35 ± 0.85
ZTF J0722−1839	~ 8	$(1.13 \pm 0.14) \times 10^{-22}$	0.0119 ± 0.0076	1.000036 ± 0.000050	5.95 ± 0.71
ZTF J1749+0924	~ 3	$(5.7 \pm 1.5) \times 10^{-23}$	0.158 ± 0.049	1.0062 ± 0.0039	9.1 ± 2.1
ZTF J1946+3203	< 1	$(2.46 \pm 0.80) \times 10^{-23}$	0.447 ± 0.055	1.050 ± 0.012	23 ± 11
ZTF J0640+1738	< 1	$(9.2 \pm 3.8) \times 10^{-24}$	0.83 ± 0.19	1.174 ± 0.079	
ZTF J2130+4420	~ 2	$(8.47 \pm 0.53) \times 10^{-23}$	0.127 ± 0.035	1.0040 ± 0.0022	16.6 ± 8.1
ZTF J1901+5309	~ 2	$(9.05 \pm 0.15) \times 10^{-23}$	0.095 ± 0.017	1.00226 ± 0.00083	24.5 ± 3.8
ZTF J2320+3750	< 1	$(1.58 \pm 0.18) \times 10^{-23}$	0.19 ± 0.11	1.009 ± 0.012	55.8 ± 3.1
ZTF J2055+4651	< 1	$(4.42 \pm 0.51) \times 10^{-23}$	0.233 ± 0.017	1.0136 ± 0.0020	30.9 ± 3.3

The sky and inclination dependent estimated *LISA* SNR of all systems in our sample (we marginalize over polarization angle), after 4 years of observations. All values are calculated using spectroscopic distances (see Table 5.4), and the characteristic decay timescale assuming gravitational wave decay, defined as $\frac{3}{8}\frac{P_b}{|\dot{P}_b|}$. As a point of comparison, we estimate SDSS J0651+2844 will reach an SNR of ~ 88 after four years (with $M_A = 0.49\,M_\odot$, $M_B = 0.247\,M_\odot$, and $d = 0.933\,kpc$). We have omitted estimates for the mass-transferring systems for which we do not have parameter estimates, and have ommitted a decay timescale estimate for ZTF J0640+1738 due to uncertainties larger than the estimate. The gravitational wave amplitude is defined as $\mathcal{A} = \frac{2(G\mathcal{M})^{5/3}}{c^4 d}(\pi f)^{2/3}$, and the $2\cos(i)$ and $1+\cos^2(i)$ give the inclination dependent coefficients of the two gravitational wave polarizations, h_+ and $h_\times$, respectively.

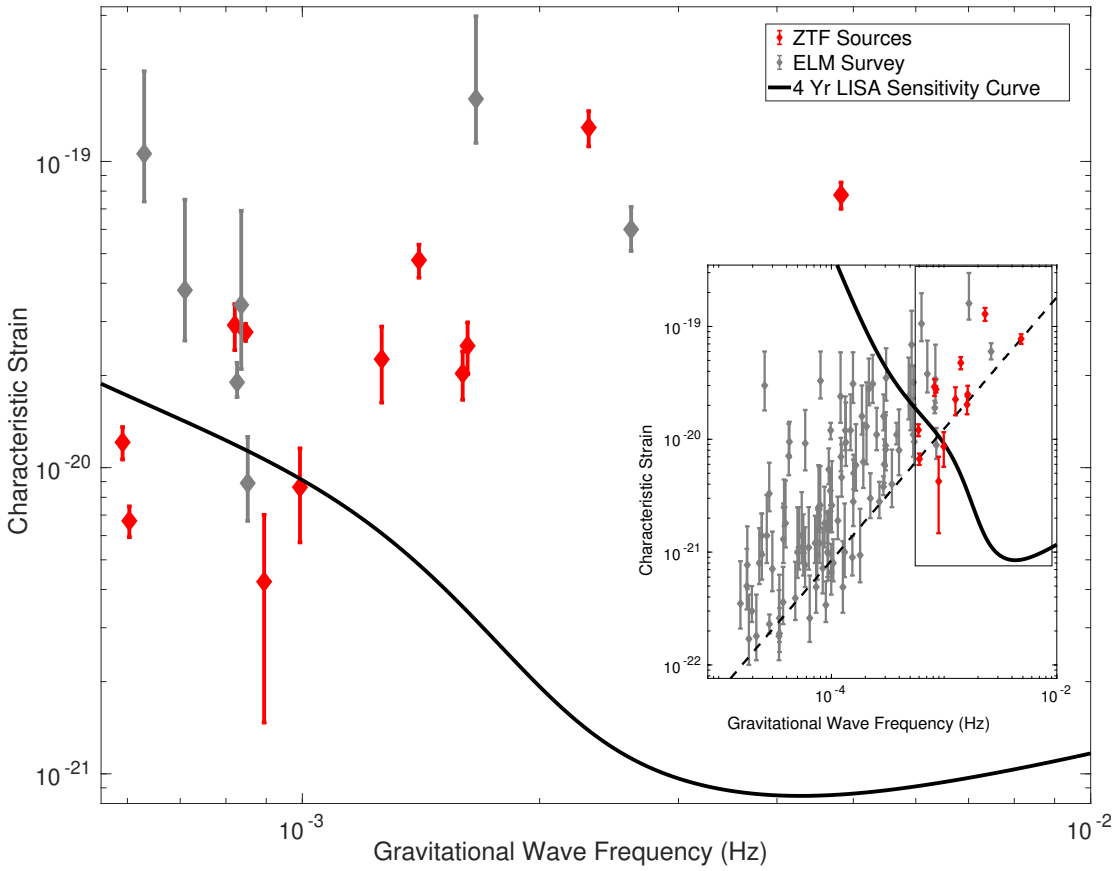

Figure 5.9: The characteristic gravitational wave strain of the sources described in this work (shown as red diamonds–note that the three mass-transferring sources for which we do not yet have parameter estimates have been omitted), compared with the sample of DWD binaries from the ELM survey (shown as grey diamonds), overplotted with the 4 year *LISA* sensitivity curve (solid black line). An inset compares the sample presented in this paper (which exclusively investigated systems with orbital periods under an hour), with the full sample of systems discovered by the ELM survey (Brown, Kilic, Kosakowski, Andrews, et al., 2020). The inset also presents the evolution of ZTF J1539+5027 with the dashed black line, illustrating what its characteristic strain would have been in the past at longer orbital periods. Overall, the ZTF sample contains two high SNR gravitational wave sources (ZTF J1539+5027 and ZTF J0538+1953, with 4-year SNRs of approximately 96). See Table 5.6 for further details. The 4 year *LISA* sensitivity curve was computed as described in Robson et al. (2019).

Evolutionary Fates

All of the binaries in our sample are either already interacting, or will interact in the near astronomical future (see Table 5.6). Thus, a significant question worth posing is what will occur when these systems interact. We illustrate possible outcomes should the systems merge in Figure 5.10, based on the work described in Shen (2015).

Most of the double He WD systems in our sample are close to a mass ratio of unity, and thus are likely to merge when they interact (Marsh, Nelemans, et al., 2004). As discussed in Shen (2015), these systems could evolve into two classes of objects: either a non-degenerate He-burning hot subdwarf star, which eventually cools into a CO WD, or alternatively, they could form an R CrB star, which would also eventually cool into a CO WD. In either case, these systems ultimately end up on the WD track, and thus serve as evidence that it is likely at least some low mass WDs merge and ultimately form a CO WD.

The other double degenerate systems in the sample, containing both a CO WD and a He WD, have larger mass ratios than double He WD systems. Thus, with the onset of mass transfer, it is possible that these systems could evolve into AM CVns (Ramsay, Green, et al., 2018). However, Shen (2015) proposes that these systems too could ultimately merge, and along the way potentially produce powerful helium detonations known as .Ia ("dot Ia") supernovae. Upon merger, they are expected to form an R CrB as the He WD is disrupted by its more dense CO companion, forming a helium atmosphere around this core. Ultimately, most of these R CrB stars would cool to form a CO WD on the WD cooling track.

Finally, the remaining systems in our sample contain a degenerate WD accreting from a non-degenerate He-burning star (ZTF J2130+4420 and ZTF J2055+4651). These systems will likely build up a layer of helium on the CO WD, which could eventually undergo a detonation, and if the CO WD is sufficiently massive, this could result in a "double-detonation" by igniting the degenerate carbon-oxygen core (Shen, Kasen, et al., 2018; Shen, Boubert, et al., 2018). However, in the case of ZTF J2130+4420, the CO WD is only $0.545^{+0.020}_{-0.020}\,M_\odot$, likely too low even to produce a sub-luminous Type Ia supernova, whereas ZTF J2055+4651, with its $0.68^{+0.05}_{-0.05}\,M_\odot$, is the more likely of the

two objects to produce such an event (Perets et al., 2019). Ultimately, the two objects could also exhaust helium shell burning, and simply cool into double degenerates. Upon merger, they would likely form a rapidly rotating CO WD, potentially preceded by an R CrB phase if substantial He remains as expected for hybrid WDs (Perets et al., 2019). For further details on these systems, please see Kupfer, Bauer, Marsh, et al. (2020) and Kupfer, Bauer, Burdge, van Roestel, et al. (2020).

5.6 Conclusion

Using data from the Zwicky Transient Facility, we have significantly increased the number of known binary systems with an orbital period of less than an hour. Using high-speed photometric follow-up in combination with spectroscopic follow-up we have characterized the physical parameters of the systems using model-dependent techniques invoking WD mass-radius relations. In future work, we hope to obtain more model-independent measurements such as orbital decay rates to more robustly characterize the physical parameters of these systems.

We will continue to analyze ZTF data as it accumulates more epochs and discover more such objects. At the current stage of the survey, the sample we have discovered exhibits a remarkably high fraction of pairs of He WDs, likely due to selection effects. As we continue the survey, we anticipate discovering more systems, and that our discoveries will begin to include other classes of sources, such as pairs of CO WDs. All of the detached systems in our sample should be undergoing rapid orbital decay due to general relativity, and we expect to detect this orbital decay in every detached system with high significance before *LISA* launches.

The algorithms and analysis techniques we are developing will be applicable to upcoming surveys such as the one which will be conducted by the Vera Rubin Observatory (LSST Science Collaboration et al., 2009). These data sets will be accompanied by their own challenges (in particular, lower cadence, split across many filters). Given the clear promise demonstrated by the discoveries emerging from ZTF, we are optimistic that optical time domain surveys will continue to revolutionize our understanding of binaries in the millihertz regime. These surveys will set the stage for *LISA*, having discovered dozens, if not hundreds of sources by the time the instrument begins to operate. In

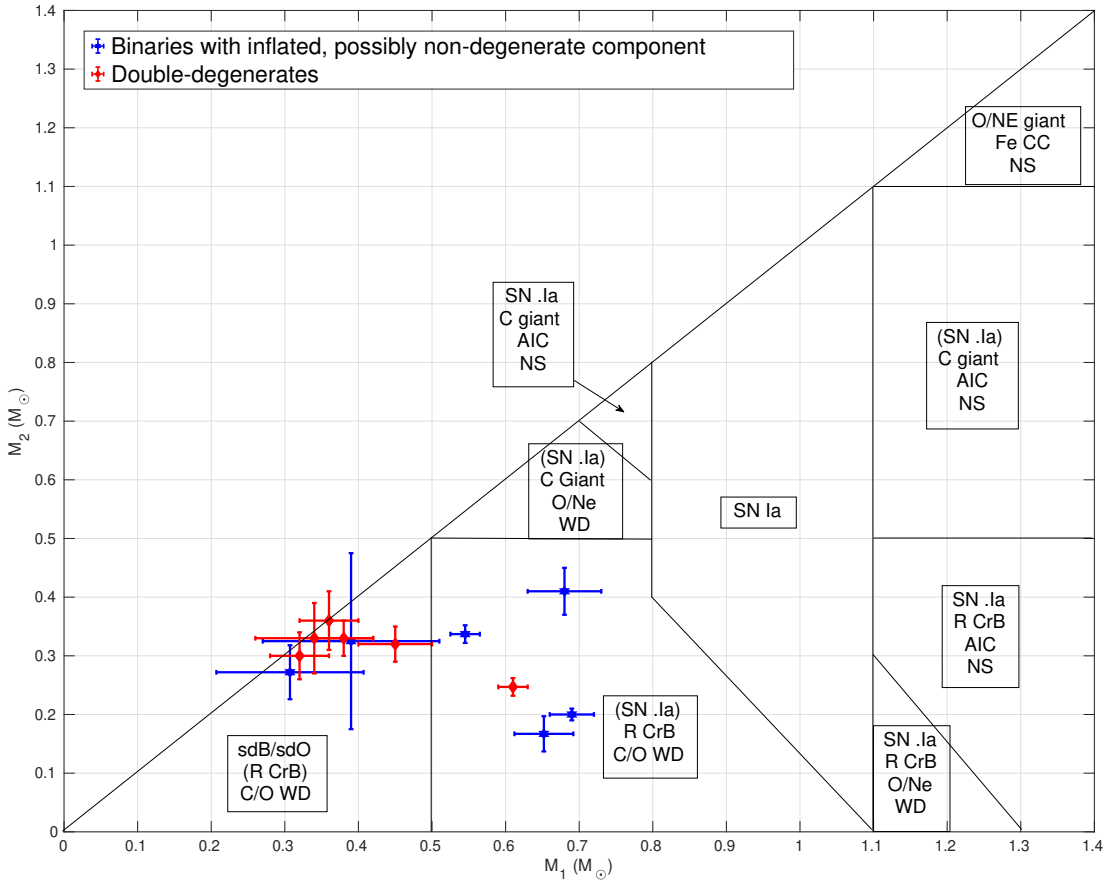

Figure 5.10: A reproduction of the diagram featured in Shen (2015), illustrating possible evolutionary fates of double degenerate pairs. In red, we plot the double degenerate objects discovered by our survey. Most of these are double He WDs that are expected to evolve into hot subdwarf stars (sdB/sdO) objects upon merger. Three other double degenerate systems (including ZTF J1539+5027) have CO cores and likely produce R CrB stars upon merger, though they could also turn into mass-transferring AM CVn systems that exhibit SN .Ia He-shell detonations. Systems containing non-degenerate objects (blue points) would only follow the scenarios described in Shen (2015) if the He-burning objects transitioned to a degenerate state prior to merger. They could produce other phenomena, including type Ia SNe, due to mass transfer/merger before becoming degenerate (see text).

future work, we will characterize our recovery efficiency in greater detail using synthetic lightcurves, in order to better characterize ZTF's sensitivity to detecting the population of DWDs in the galaxy. Efforts are currently underway to increase sensitivity to the shortest period binary systems by account for their orbital period evolution, which requires algorithms that can accommodate acceleration searches (Katz et al., 2020).

Binaries with compact object components are transitioning into a golden age, as we enter an era when time domain surveys such as ZTF enable detection via periodic features. Massively multiplexed spectroscopic surveys acquiring multiple epochs such as SDSS-V (Kollmeier et al., 2017) and LAMOST (Cui et al., 2012) will enable detection of these systems via large radial velocity shifts, with the feasibility of this technique having already been demonstrated on a smaller scale by the ELM survey. Deep all sky X-ray surveys such as that being conducted by the eROSITA instrument aboard the SRG mission (Merloni et al., 2012) will enable detection of ultracompact X-ray binaries and direct-impact accreting systems such as HM Cancri (Roelofs et al., 2010). Finally, *Gaia* (Gaia Collaboration, 2018) has completely revolutionized stellar astronomy by providing parallax measurements, which has enabled careful targeting of objects such as WDs. This era will culminate with the launch of *LISA*, which will enable detection of thousands of these systems in the form of gravitational waves, and revolutionize our understanding of compact binary systems.

K.B.B thanks the National Aeronautics and Space Administration and the Heising Simons Foundation for supporting his research.

M. W. C. acknowledges support from the National Science Foundation with grant number PHY-2010970.

P.R-G acknowledges support from the State Research Agency (AEI) of the Spanish Ministry of Science, Innovation and Universities (MCIU), and the European Regional Development Fund (FEDER) under grant AYA2017–83383–P.

V.S.D, ULTRACAM and HiPERCAM are supported by STFC.

The research leading to these results has received funding from the European Research Council under the European Union's Horizon 2020 research and innovation programme

numbers 677706 (WD3D) and 340040 (HiPERCAM).

Based on observations obtained with the Samuel Oschin Telescope 48-inch and the 60-inch Telescope at the Palomar Observatory as part of the Zwicky Transient Facility project. ZTF is supported by the National Science Foundation under Grant No. AST-1440341 and a collaboration including Caltech, IPAC, the Weizmann Institute for Science, the Oskar Klein Center at Stockholm University, the University of Maryland, the University of Washington, Deutsches Elektronen-Synchrotron and Humboldt University, Los Alamos National Laboratories, the TANGO Consortium of Taiwan, the University of Wisconsin at Milwaukee, and Lawrence Berkeley National Laboratories. Operations are conducted by COO, IPAC, and UW.

Based on observations made with the Gran Telescopio Canarias (GTC) installed in the Spanish Observatorio del Roque de los Muchachos of the Instituto de Astrofísica de Canarias, in the island of La Palma.

Based on observations made at the European Southern Observatory New Technology Telescope (NTT), La Silla.

The KPED team thanks the National Science Foundation and the National Optical Astronomical Observatory for making the Kitt Peak 2.1-m telescope available. The KPED team thanks the National Science Foundation, the National Optical Astronomical Observatory and the Murty family for support in the building and operation of KPED. In addition, they thank the CHIMERA project for use of the Electron Multiplying CCD (EMCCD).

Some of the data presented herein were obtained at the W.M. Keck Observatory, which is operated as a scientific partnership among the California Institute of Technology, the University of California, and the National Aeronautics and Space Administration. The Observatory was made possible by the generous financial support of the W.M. Keck Foundation. The authors wish to recognize and acknowledge the very significant cultural role and reverence that the summit of Mauna Kea has always had within the indigenous Hawaiian community. We are most fortunate to have the opportunity to conduct observations from this mountain.

This article is based on observations made in the Observatorios de Canarias del IAC with the William Herschel Telescope operated on the island of La Palma by the Isaac Newtoun Group of Telescopes in the Observatorio del Roque de los Muchachos.

This research benefited from interactions at the ZTF Theory Network Meeting that were funded by the Gordon and Betty Moore Foundation through Grant GBMF5076 and support from the National Science Foundation through PHY-1748958.

5.7 Appendix

Instrumental/Observational Information

LRIS

We obtained the majority of our spectroscopic follow-up using the Low Resolution Imaging Spectrometer (LRIS) (Oke, Cohen, et al., 1995) on the 10-m W. M. Keck I Telescope on Mauna Kea. We conducted most of our observations using the 600 grooves/mm grism with a blazing angle of 4000 , and the 1″ slit on the spectrograph, resulting in an effective FWHM resolution of 3.8-4.1 across the wavelength range of the blue arm (the approximate wavelength range is 3200–5800). The dispersion of this element results in approximately 0.63 of wavelength per pixel, meaning that we sample the PSF from this slit with more than 6 unbinned pixels, thus, we always bin along the dispersion axis when observing with this instrument, as it significantly reduces readout time and read noise, and comes with no cost in resolving power (at least in the case of 2x2 binning). For some observations which required particularly short exposures (such as ZTF J1539+5027), we binned 4x4, to further reduce readout time. Ultimately, the lower limit of exposure times during spectroscopic observations are set by the readout duty cycle and read noise floor (one splits photons across many pixels when obtaining spectra, resulting in a small number of counts per pixel, which can quickly become comparable to the readout noise in short exposures). Frame transfer CCDs offer an attractive solution to eliminating the readout duty cycle bottleneck (which, for observing ZTF J1539+5027 for example, was a prohibitive 34 percent, as the effective exposure time was 52 seconds, but even with 4x4 binning, the readout time was still 27 seconds). Electron Multiplying CCDs take this one step further by offering both the possibility of eliminating the issue of readout time, and also eliminating read noise, meaning that

observations can be obtained in photon-counting mode. The catch of such an instrument is a factor of $\sqrt{2}$ larger readout noise due to concidence losses (Tulloch and Dhillon, 2011); however, for faint targets which require high temporal resolution, these CCDs offer a solution that conventional CCDs do not. Coincidence losses can be avoided in the photon-counting limit where no more than one photon is incident on a pixel in any given image, making this technology particularly attractive for higher resolution CCDs where the dispersion is sufficiently high that this regime can be easily reached.

DBSP

We obtained the spectrum of ZTF J2228+4949 using the Double-Beam Spectrograph (DBSP) (Oke and Gunn, 1982) on the 200 $inch$ Hale telescope at Palomar observatory. The instrument provides a resolution comparable to LRIS, and has similar limitations in readout time overheads.

ISIS

Spectra for ZTF J2130+4420 were obtained using the ISIS spectrograph on the 4.2 m William Herschel Telescope. For further details on these observations, please see Kupfer, Bauer, Marsh, et al. (2020).

GMOS-N

Spectra for ZTF J2055+4651 were obtained using the GMOS-N spectrograph on the 8.1 m Gemini North Telescope. For further details on these observations, please see Kupfer, Bauer, Burdge, van Roestel, et al. (2020).

HiPERCAM

HiPERCAM is a high-speed photometer mounted on the 10.4-m Gran Telescopio Canarias (GTC) on the island of La Palma in the Canary Islands (Dhillon, Dixon, et al. 2018, Dhillon et al. in prep). The instrument is a frame transfer quintuple-beam imager, allowing for simultaneous imaging in u, g, r, i, and z band at frame rates of $> 1\,kHz$. The light-collecting power of a 10-meter class telescope, combined with the high frame

rate of this instrument, makes it optimal in obtaining the high SNR observations of the systems described in this work, particularly systems such as ZTF J1539+5027, whose eclipse ingress and egress last only a few seconds and spans an apparent magnitude range of approximately 21 in g at the start of the eclipse, and reaches > 27 in g at the base of the eclipse.

ULTRACAM

ULTRACAM is a three-channel high-speed photometer currently mounted on the 3.5 meter New Technology Telescope at La Silla observatory (Dhillon, Marsh, et al., 2007). All observations on this instrument were conducted using u and g filters on two of the channels, and the remaining channel either r or i band. Like the other high-speed photometers used in our observations, the instrument is operated in frame transfer mode, effectively eliminating the readout duty cycle.

CHIMERA

The Caltech HIgh-speed Multi-color camERA (CHIMERA) (Harding et al., 2016) is a dual-channel high-speed photometer mounted on the prime focus of the 200-inch Hale telescope at Palomar Observatory. CHIMERA consists of a pair of electron-multiplying CCDs capable of using either conventional amplifiers or those with electron-multiplying gain. We operated the detectors in the conventional amplifier mode with frame transfer enabled, as for all of our targets we obtained enough photons in several second exposures such that the $\sqrt{2}$ increase in shot noise from using the electron-multiplying gain would erase any gains from eliminating readout noise.

KPED

The Kitt Peak Electron Multiplying CCD Demonstrator (KPED) is a single-channel high-speed photometer mounted on the 2.1 meter telescope at Kitt Peak National observatory (Coughlin, Dekany, et al., 2019). The instrument uses the same electron-multiplying CCDs used by CHIMERA. The observations highlighted in this work were obtained using frame transfer mode and in g.

Table 5.7: Observations of systems used in analyses in this publication

Name	Instrument	Observation Dates (UTC)	Configuration	Frame Exptime
ZTF J1539+5027	LRIS	June 16, July 12, 13 2018	600 grooves/mm grism, 4x4 binning	52 *s*
	HiPERCAM	June 2, 4, 5 2019	u, g, r, i, z	6, 3, 3, 6, 9 *s*
ZTF J0538+1953	LRIS	Sept 3, 27 2019	600 grooves/mm grism, 4x4 binning	90 *s*
	HiPERCAM	Sept 4, 8 2019	u, g, r, i, z	3, 1, 1, 3, 4 *s*
ZTF J1905+3134	LRIS	July 5 2019	400 grooves/mm grism, 2x2 binning	300 *s*
	KPED	July 3 2019	g	10 *s*
PTF J0533+0209	LRIS	Nov 15 2017, Mar 19 2018	400 grooves/mm grism, 2x2 binning	120 *s*
	CHIMERA	Dec 14, 15 2017	g, i	10 *s*
PTF J2029+1534	LRIS	Mar 21 2020	600 grooves/mm grism, 2x2 binning	120 *s*
	CHIMERA	Oct 1 2019	g, r	3, 3 *s*
ZTF J0722−1839	LRIS	April 5, 6 2019, Feb 17 2020	600 grooves/mm grism, 2x2 binning	141 *s*
	ULTRACAM	Jan 26 2020	u, g, i	12, 6, 6 *s*
ZTF J1749+0924	LRIS	Mar 21 2020	600 grooves/mm grism, 2x2 binning	120 *s*
	CHIMERA	July 15 2020	g, r	5, 5 *s*
ZTF J2228+4949	DBSP	July 31, 2019	600 grooves/mm grating	200 *s*
ZTF J1946+3203	LRIS	Sept 27 2019	600 grooves/mm grism, 2x2 binning	168 *s*
	CHIMERA	August 6, 2019	g, i	3, 3 *s*
ZTF J0643+0318	LRIS	Jan 25, 2020	600 grooves/mm grism, 2x2 binning	170 *s*
	ULTRACAM	September 28, 2019	u, g, i	24, 8, 8 *s*
ZTF J0640+1738	LRIS	Feb 17 2019	600 grooves/mm grism, 2x2 binning	157 *s*
ZTF J2130+4420	ISIS	June 25, 26 2019	R300B grating	120 *s*
	HiPERCAM	July 8 2019	u, g, r, i, z	3.54, 1.77, 1.77, 1.77, 3.54 *s*
ZTF J1901+5309	LRIS	Sept 3 2019	600 grooves/mm grism, 2x2 binning	141 *s*
	CHIMERA	August 8 2019	g, i	3, 3 *s*
ZTF J2320+3750	LRIS	Sept 27 2019	600 grooves/mm grism, 2x2 binning	138 *s*
	CHIMERA	July 15 2020	g, r	5, 5 *s*
ZTF J2055+4651	GMOS-N	Sept 24, 25 2019	B600 grating	180 *s*
	HiPERCAM	July 8 2019	u, g, r, i, z	9, 3, 3, 3, 9 *s*

period-finding

In this section, we explore the sensitivity of the algorithms used to discover the systems described in this work using both a real example, as well as synthetic signals.

We typically search approximately 2 million trial frequencies per lightcurve. The highest frequency we search to is 720 times per day, and the lowest is defined as 2/baseline, where the baseline is the end date of the lightcurve, minus the start. Because the frequency grid depends on the baseline of the lightcurve, we compute it independently for each lightcurve. We used an oversampling factor of 4. To avoid aliases due to the sidereal day, we slice frequencies out of the frequency grid at 1.0 days, and its various harmonics.

One of the known systems we tested our technique on was the 12.75-min binary system, SDSS J0651+2844 (Brown, Kilic, Hermes, et al., 2011), whose phase-folded ZTF lightcurve is illustrated in Figure 5.11. This system did not become recoverable in the main ZTF survey until a substantial number of epochsover 600 epochs had been accumulated (see Figure 5.12 for further details), as its eclipses are quite shallow due to the more luminous component being the larger. We expect that as ZTF's sampling continues to increase, we should start to recover more eclipsing CO WD plus He WD white dwarf systems like SDSS J0651+2844, whereas our current discoveries in general exhibit larger photometric amplitudes than seen in SDSS J0651+2844 because they consist primarily of pairs of He WDs, or as in the case of ZTF J1539+5027, the more compact CO WD dominates the luminosity.

In Figure 5.12 we illustrate the sensitivity of the conditional entropy algorithm to both a sinusoidal signal and a square wave as a function of both the amplitude of the signal and the number of epochs. In addition to characterizing the sensitivity of the algorithm to a synthetic signal, we also present ZTF's median RMS scatter as a function of apparent magnitude, and the cumulative ZTF sampling of *Gaia* objects above a declination of -28° in Figure 5.12. Using this figure, one can for example, infer that at an apparent magnitude of 19, ZTF has an RMS scatter of $\approx 7\%$, and approximately two-thirds of all sources in *Gaia* above a declination of -28° have 500 or more detections in ZTF at this apparent magnitude. Using the top panels of the figure, one can then estimate that ZTF should have detected more than half of all sinusoidal sources at this apparent

magnitude with an amplitude of > 3.5%. These are crude estimates, and further work is underway to conduct careful simulations of ZTF data to better characterize detection efficiency by accounting for the cadence in each field, data artifacts, and other import elements that the simple treatment presented below cannot capture. The work presented in this publication is not intended to explore rates, and thus we leave the analysis at this.

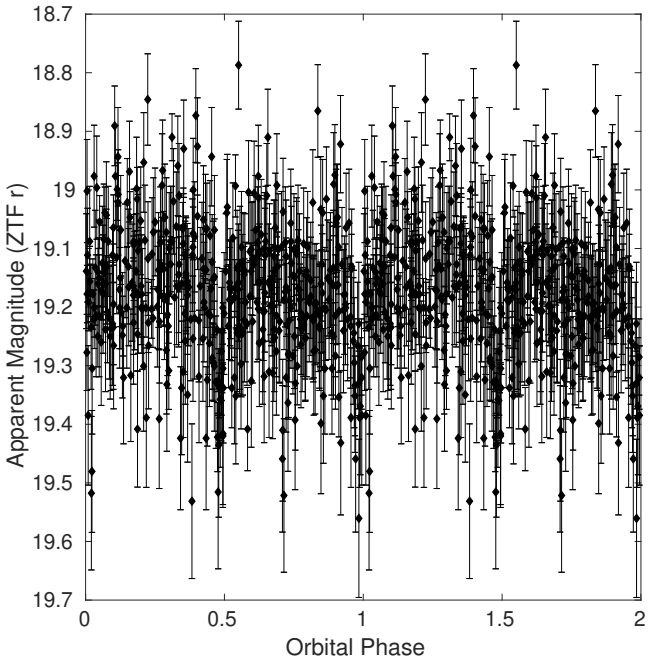

Figure 5.11: The phase-folded ZTF lightcurve of the 12.75-min orbital period binary, SDSS J0651+2844 (Brown, Kilic, Hermes, et al., 2011), which we blindly recover with our period-finding algorithms. An early dedicated observation of this system during ZTF's commissioning served as a proof of concept that a wide field optical time domain survey such as ZTF could function as a powerful tool for identifying members of this class of gravitational wave source.

LISA Signal to noise

Here, we walk through the basic formalism we used to estimate the signal-to-noise ratios of the binaries in this paper.

In order to estimate the *LISA* gravitational wave SNR, we adopt the same formalism as

outlined in Robson et al. (2019). In Burdge, Coughlin, et al. (2019) and Burdge, Fuller, et al. (2019), the chirp mass, M_c, was estimated from the rate of orbital decay due to gravitational wave emission. In this work, we do not yet have precise orbital decay measurements of any other systems, so we instead estimate the chirp mass from mass estimates based on lightcurve and spectroscopic modelling. We use the approximation for the orbit-averaged signal amplitude at the detector computed in Cornish and Larson (2003),

$$A^2 = \mathcal{A}^2((1+\cos^2(i))^2 \left\langle F_+^2 \right\rangle + 4\cos^2(i) \left\langle F_\times^2 \right\rangle), \tag{5.7}$$

where the intrinsic source amplitude is given by $\mathcal{A} = \frac{2(G\mathcal{M})^{5/3}}{c^4 d}(\pi f)^{2/3}$, and the orbit averaged detector responses are $\left\langle F_+^2 \right\rangle$ and $\left\langle F_\times^2 \right\rangle$ (see Cornish and Larson (2003) for the full expressions of these quantities). Note that Cornish and Larson (2003) includes a factor of $\frac{1}{2}$ in this expression which we have omitted. This factor of $\frac{1}{2}$ arises from time averaging over the $|\cos(\psi t)|^2$ in the signal; however, in order to find agreement with the sky, inclination, and polarization averaged SNR in Robson et al. (2019), we found we had to eliminate this $\frac{1}{2}$. We believe this is because in Robson et al. (2019), the phase of the gravitational wave is expressed as $e^{i\psi f}$, and when Robson et al. (2019) computes the inner product of the gravitational wave with itself, this term vanishes.

To estimate the signal-to-noise, we use the expression given in Korol, Rossi, Groot, et al. (2017),

$$SNR^2 = \frac{A^2 T_{obs}}{P_n(f_s)}, \tag{5.8}$$

where $P_n(f_s)$ is the power spectral density of the noise in a Michelson channel. We obtain the sky-averaged *LISA* noise curve from Robson et al. (2019) In order to estimate the power spectral density of the noise, we divide the sky-averaged sensitivity by the sky-averaged response function, $\sqrt{3/20}$ to obtain an effective non-sky-averaged curve (see Robson et al. (2019) for further details). Note that while the response function given in Robson et al. (2019) is $\sqrt{3/10}$, it is actually a composite of a response which arises from averaging over the sky (the $\sqrt{3/20}$) and an additional factor of $\sqrt{2}$ which arises from summing over two independent channels, which we want to preserve in our SNR estimate.

The signal to noise described in this work is simply an estimate which uses a time averaged approximation, and is not a substitute for a full time-dependent *LISA* simulation. Our estimates do account for sky location and inclination, as these parameters are well constrained for the sources in this work, and do have significant impacts on the estimated signal to noise. For the purposes of our SNR estimates, we marginalized over the polarization angle. We repeated our calculations using the waveforms given in Robson et al. (2019), and arrived at the same estimated signal to noise ratios using these combined with the orbit averaged signal (we compute the orbital-averaged response in Equation 5.8, using the waveforms given by Robson et al. (2019) Equation 15, with the amplitude given by Robson et al. (2019) Equation 20, and use this quantity as the expectation value of the numerator in Robson et al. (2019) Equation 36, and arrive at the same result as the formalism outlined above).

Combined with a distance and inclination estimate, knowing the chirp mass allows for a direct estimate of the gravitational wave strain of the source as measured from Earth. We report the estimated *LISA* SNR for the sources in the sample in Table 5.6.

It is worth noting that these SNRs are a factor of $\sqrt{2}$ different than those presented in Korol, Rossi, Groot, et al. (2017), Burdge, Coughlin, et al. (2019), and Burdge, Fuller, et al. (2019) due to an error which introduced a factor of two into the strain amplitude, in combination with a $\sqrt{\frac{1}{2}}$ from the prefactor of $\frac{1}{2}$ we omitted in Equation 5.7 in this work (which was not omitted in previous work). We also used the more up to date *LISA* sensitivity given in Robson et al. (2019), which changed results at the $\sim 10\%$ level compared to the sensitivity of Amaro-Seoane et al. (2017).

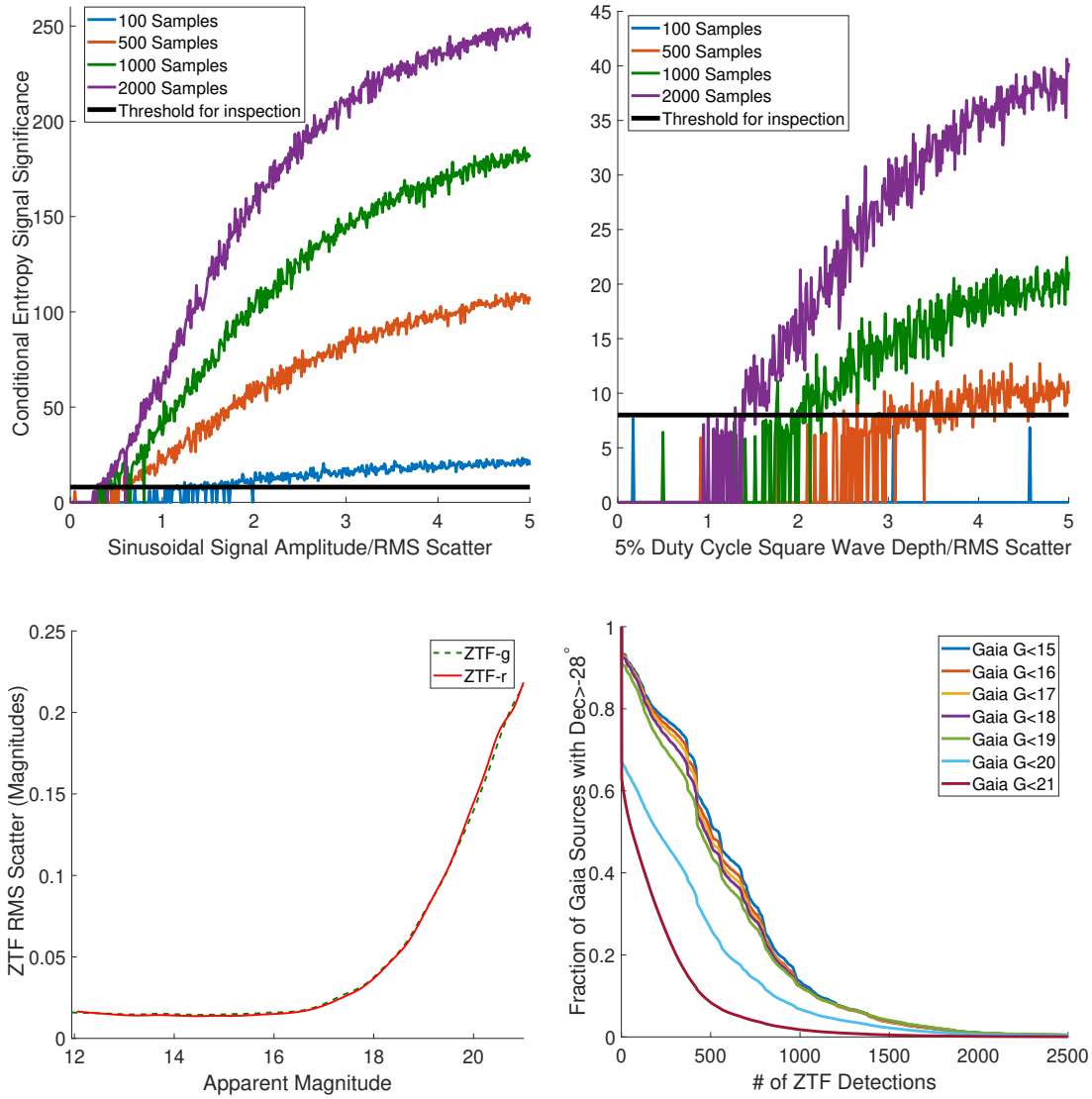

Figure 5.12: Upper left: The significance returned by the conditional entropy algorithm on a synthetic sinusoidal signal with a 10 minute period. On the x axis, we illustrate the semi-amplitude of the sinusoid compared to the RMS scatter injected into the signal. The horizontal black line illustrates the significance threshold we imposed for inspecting lightcurves visually for candidates. Upper Right: This panel is analogous to the upper left panel, but rather than a synthetic sinusoidal signal, the algorithm was instead run on a synthetic eclipsing signal in the form of a periodic square wave with a 10 minute period, and 5 percent duty cycle. Lower left: An empirical average of ZTF's RMS scatter for a sample of all *Gaia* sources with a color of $(BP - RP) < 0.5$. Lower right: An illustration of the fraction of *Gaia* sources with a declination of $> -28°$ and with a color of $(BP - RP) < 0.5$ vs the number of archival ZTF photometric detections of these sources. The large number of faint sources with no detections are dominated by sources which were not detected in the ZTF reference image used to seed the archival database (primarily located in dense regions of the Galactic plane). See Masci, Laher, Rusholme, et al. (2019) for further details.

Chapter 6

CONCLUSIONS AND FUTURE PROSPECTS

As highlighted in this thesis, ZTF has opened the floodgates to a new way of discovering the dominant population of gravitational wave sources detectable by *LISA* using wide field photometric surveys. The current rate of discovery using ZTF is approximately one new ultracomapct binary per month, meaning that a survey on a 48-inch telescope constructed in the 1940s has been single-handendly responsible for a tenfold increase in the average rate of discovery of sub-hour orbital period binaries when compared to the period between the recognition of AM CVn as an ultracompact binary in 1972 and the state of affairs when ZTF began operating in mid-2018.

Perhaps the most exciting prospect of the results of this thesis, is that ZTF represents just one of many time domain surveys which are currently operating or coming online. This rapidly maturing field will soon go deeper with the Vera Rubin Observatory (VRO), obtain densely sampled and high precision photometry for bright objects with missions like TESS, and will probe time domain phenomena in non-optical wavelengths with facilities such as the Spektr-RG and Roman space telescopes. Below, I discuss a few specific possibilities which may arise from these different facilities.

X-ray facilities such as Spektr-RG (SRG), with an order of magnitude greater depth than ROSAT, may finally be able to identify more direct impact accreting sources like HM Cancri and V407 Vul. The critical ingredient in distinguishing these sources from other X-ray sources in the sky will be to identify periodic X-ray flux modulation associated with an orbital period. These objects also exhibit optical periodicity, so a combination of optical and X-ray time domain datasets could be used synergistic-ally to narrow down on these candidates, though ultimately spectroscopic follow-up will be important in ruling out intermediate polar interlopers.

Facilities like the Roman observatory, operating in the IR, come with their own unique challenges and benefits. In general, the short orbital period binary systems we know

of consist of high temperature components, which emit the majority of their flux in the ultraviolet. For blackbodies where both the optical and IR are in the Rayleigh-Jeans tail, a filter such as K band will capture a factor of 10 less flux than an optical filter such as g. However, IR filters experience significantly less dust-extinction than optical or ultraviolet based passbands, making them powerful tools for probing dust obscured regions of the Galactic plane, assuming they have sufficient light collecting power to cope with the flux penalty associated with going to these wavelengths, and the angular resolution to cope with the enormous stellar density visible to them.

TESS presents a unique opportunity, because although it lacks the depth and angular resolution of a facility like ZTF, it has remarkable sampling, with 10 minute full frame images in recent sectors, and the possibility of saving 2-minute postage stamps for a selection of targets. This 2-minute cadence is particularly attractive for double-degenerates, as their eclipse durations are between 30 seconds and 2 minutes (assuming an edge on inclination) for orbital periods short enough that the objects would merge in a Hubble time (shorter than about 12 hours). Given the limited number of white dwarfs bright enough for TESS to identify, it may be feasible in the long run to obtain this form of data on every white dwarf brighter than an apparent magnitude of 18, allowing for a systematic exploration of this population of objects. No eclipsing pair of double carbon-oxygen core white dwarfs has ever been identified, likely because the duty cycle of these eclipses is very narrow, and TESS may be the optimal tool for identifying these objects due to its remarkably dense sampling.

Finally, the VRO, with a quarter of ZTF's field of view, but thirty-six times the light collecting power, will obtain useful photometry from white dwarfs at far greater distances than those accessible to ZTF. Unfortunately, the observatory will obtain far fewer epochs, and will divide these epochs among several filters, complicating extracting a useful signal from the data. Fortunately, the first binary system discovered with ZTF, ZTF J1539+5027, was discovered because its remarkably strong signal was so pronounced that it was only necessary to obtain a few dozen epochs to clearly recognize the nature of the object. I am hopeful that the VRO will be a powerful tool for finding more objects like ZTF J1539+5027, if they exist (note that ZTF was sufficient for discovery this object at 2.5 kpc, so the VRO should be able to identify such an object at about 15 kpc, assuming

no reddening). The VRO will not be a useful tool for identifying objects with very narrow temporal features such as narrow eclipses, as it will simply lack the sampling to blindly recover these objects. However, in the *LISA* era, VRO data on such objects will still be useful, because even if the sampling was not sufficient to blindly discover them in VRO data, it may still be adequate to measure their orbital period evolution over the decade that the survey operated.

In conclusion, I predict that the current discovery rate of sub-hour orbital period binaries, of about 1 per month, will increase over the next decade, yielding several hundred or even thousands of objects prior to the launch of the *LISA* mission.

BIBLIOGRAPHY

Alexakis, A. et al. (2004). "On Heavy Element Enrichment in Classical Novae". In: *ApJ* 602.2, pp. 931–937. DOI: 10.1086/381086. arXiv: astro-ph/0307126 [astro-ph].

Althaus, L. G., A. M. Serenelli, et al. (2005). "The formation and evolution of hydrogen-deficient post-AGB white dwarfs: The emerging chemical profile and the expectations for the PG 1159-DB-DQ evolutionary connection". In: *A&A* 435.2, pp. 631–648. DOI: 10.1051/0004-6361:20041965. arXiv: astro-ph/0502005 [astro-ph].

Althaus, L. G., M. E. Camisassa, et al. (2015). "White dwarf evolutionary sequences for low-metallicity progenitors: The impact of third dredge-up". In: *A&A* 576, A9. DOI: 10.1051/0004-6361/201424922. arXiv: 1502.03882 [astro-ph.SR].

Althaus, L. G., M. M. Miller Bertolami, and A. H. Córsico (2013). "New evolutionary sequences for extremely low-mass white dwarfs. Homogeneous mass and age determinations and asteroseismic prospects". In: *A&A* 557, A19. DOI: 10.1051/0004-6361/201321868. arXiv: 1307.1882 [astro-ph.SR].

Amaro-Seoane, P. et al. (2017). "Laser Interferometer Space Antenna". In: *arXiv e-prints*, arXiv:1702.00786. arXiv: 1702.00786 [astro-ph.IM].

Bailer-Jones, C. A. L. et al. (2018). "Estimating Distance from Parallaxes. IV. Distances to 1.33 Billion Stars in Gaia Data Release 2". In: *AJ* 156.2, p. 58. DOI: 10.3847/1538-3881/aacb21. arXiv: 1804.10121 [astro-ph.SR].

Bellm, E. C., S. R. Kulkarni, T. Barlow, et al. (2019). "The Zwicky Transient Facility: Surveys and Scheduler". In: *PASP* 131.1000, p. 068003. DOI: 10.1088/1538-3873/ab0c2a. arXiv: 1905.02209 [astro-ph.IM].

Bellm, E. C., S. R. Kulkarni, M. J. Graham, et al. (2019). "The Zwicky Transient Facility: System Overview, Performance, and First Results". In: *PASP* 131.995, p. 018002. DOI: 10.1088/1538-3873/aaecbe. arXiv: 1902.01932 [astro-ph.IM].

Bellm, E. C. and B. Sesar (2016). *pyraf-dbsp: Reduction pipeline for the Palomar Double Beam Spectrograph*. ascl: 1602.002.

Benacquista, M. J. (2011). "Tidal Perturbations to the Gravitational Inspiral of J0651+2844". In: *ApJL* 740.2, p. L54. DOI: 10.1088/2041-8205/740/2/L54. arXiv: 1109.2744 [astro-ph.SR].

Bergeron, P. et al. (2011). "A Comprehensive Spectroscopic Analysis of DB White Dwarfs". In: *ApJ* 737, p. 28. DOI: 10.1088/0004-637X/737/1/28. arXiv: 1105.5433 [astro-ph.SR].

Bildsten, L. et al. (2006). "The Thermal State of the Accreting White Dwarf in AM Canum Venaticorum Binaries". In: *ApJ* 640.1, pp. 466–473. DOI: 10.1086/500080. arXiv: astro-ph/0510652 [astro-ph].

Bloemen, S. et al. (2012). "Mass ratio from Doppler beaming and Rømer delay versus ellipsoidal modulation in the Kepler data of KOI-74". In: *MNRAS* 422.3, pp. 2600–2608. DOI: 10.1111/j.1365-2966.2012.20818.x. arXiv: 1202.5553 [astro-ph.SR].

Bovy, J. (2015). "galpy: A python Library for Galactic Dynamics". In: *ApJS* 216.2, p. 29. DOI: 10.1088/0067-0049/216/2/29. arXiv: 1412.3451 [astro-ph.GA].

Bovy, J. and H.-W. Rix (2013). "A Direct Dynamical Measurement of the Milky Way's Disk Surface Density Profile, Disk Scale Length, and Dark Matter Profile at 4 kpc $<_\sim R <_\sim 9$ kpc". In: *ApJ* 779.2, p. 115. DOI: 10.1088/0004-637X/779/2/115. arXiv: 1309.0809 [astro-ph.GA].

Bragaglia, A. et al. (1990). "Double Degenerates among DA White Dwarfs". In: *ApJL* 365, p. L13. DOI: 10.1086/185877.

Breger, M. (2000). "δ Scuti stars (Review)". In: *Delta Scuti and Related Stars*. Ed. by M. Breger and M. Montgomery. Vol. 210. Astronomical Society of the Pacific Conference Series, p. 3.

Brinkworth, C. S. et al. (2013). "Measuring the Rotational Periods of Isolated Magnetic White Dwarfs". In: *ApJ* 773.1, p. 47. DOI: 10.1088/0004-637X/773/1/47.

Brown, W. R., A. Gianninas, et al. (2016). "The ELM Survey. VII. Orbital Properties of Low-Mass White Dwarf Binaries". In: *ApJ* 818.2, p. 155. DOI: 10.3847/0004-637X/818/2/155. arXiv: 1604.04268 [astro-ph.SR].

Brown, W. R., M. Kilic, C. Allende Prieto, A. Gianninas, et al. (2013). "The ELM Survey. V. Merging Massive White Dwarf Binaries". In: *ApJ* 769.1, p. 66. DOI: 10.1088/0004-637X/769/1/66. arXiv: 1304.4248 [astro-ph.SR].

Brown, W. R., M. Kilic, C. Allende Prieto, and S. J. Kenyon (2010). "The ELM Survey. I. A Complete Sample of Extremely Low-mass White Dwarfs". In: *ApJ* 723.2, pp. 1072–1081. DOI: 10.1088/0004-637X/723/2/1072. arXiv: 1011.3050 [astro-ph.GA].

Brown, W. R., M. Kilic, C. Allende Prieto, and S. J. Kenyon (2012). "The ELM Survey. III. A Successful Targeted Survey for Extremely Low Mass White Dwarfs". In: *ApJ* 744.2, p. 142. DOI: 10.1088/0004-637X/744/2/142. arXiv: 1111.6588 [astro-ph.SR].

Brown, W. R., M. Kilic, A. Bédard, et al. (2020). "A 1201 s Orbital Period Detached Binary: The First Double Helium Core White Dwarf LISA Verification Binary". In: *ApJL* 892.2, p. L35. DOI: 10.3847/2041-8213/ab8228. arXiv: 2004.00641 [astro-ph.SR].

Brown, W. R., M. Kilic, J. J. Hermes, et al. (2011). "A 12 Minute Orbital Period Detached White Dwarf Eclipsing Binary". In: *ApJL* 737.1, p. L23. DOI: 10.1088/2041-8205/737/1/L23. arXiv: 1107.2389 [astro-ph.GA].

Brown, W. R., M. Kilic, S. J. Kenyon, et al. (2016). "Most Double Degenerate Low-mass White Dwarf Binaries Merge". In: *ApJ* 824.1, p. 46. DOI: 10.3847/0004-637X/824/1/46. arXiv: 1604.04269 [astro-ph.SR].

Brown, W. R., M. Kilic, A. Kosakowski, J. J. Andrews, et al. (2020). "The ELM Survey. VIII. Ninety-eight Double White Dwarf Binaries". In: *ApJ* 889.1, p. 49. DOI: 10.3847/1538-4357/ab63cd. arXiv: 2002.00064 [astro-ph.SR].

Brown, W. R., M. Kilic, A. Kosakowski, and A. Gianninas (2017). "Discovery of a Detached, Eclipsing 40 Minute Period Double White Dwarf Binary and a Friend: Implications for He+CO White Dwarf Mergers". In: *ApJ* 847.1, p. 10. DOI: 10.3847/1538-4357/aa8724. arXiv: 1708.05287 [astro-ph.SR].

Burdge, K. B., M. W. Coughlin, et al. (2019). "General relativistic orbital decay in a seven-minute-orbital-period eclipsing binary system". In: *Nature* 571.7766, pp. 528–531. DOI: 10.1038/s41586-019-1403-0. arXiv: 1907.11291 [astro-ph.SR].

Burdge, K. B., J. Fuller, et al. (2019). "Orbital Decay in a 20 Minute Orbital Period Detached Binary with a Hydrogen-poor Low-mass White Dwarf". In: *ApJL* 886.1, p. L12. DOI: 10.3847/2041-8213/ab53e5. arXiv: 1910.11389 [astro-ph.SR].

Burdge, K. B., T. A. Prince, et al. (2020). "A Systematic Search of Zwicky Transient Facility Data for Ultracompact Binary LISA-detectable Gravitational-wave Sources". In: *ApJ* 905.1, p. 32. DOI: 10.3847/1538-4357/abc261. arXiv: 2009.02567 [astro-ph.SR].

Burwitz, V. and K. Reinsch (1999). "The ROSAT discovered soft X-ray intermediate polars: UU Col and RX J0806+15". In: *Astronomische Gesellschaft Abstract Series*. Vol. 15. Astronomische Gesellschaft Abstract Series, p. 27.

Chambers, K. C. et al. (2016). “The Pan-STARRS1 Surveys”. In: *arXiv e-prints*, arXiv:1612.05560. arXiv: 1612.05560 [astro-ph.IM].

Charpinet, S. et al. (1996). “The Potential of Asteroseismology for Hot, Subdwarf B Stars: A New Class of Pulsating Stars?” In: *ApJL* 471, p. L103. DOI: 10.1086/310335. arXiv: astro-ph/9606069 [astro-ph].

Claret, A. (2000). “A new non-linear limb-darkening law for LTE stellar atmosphere models. Calculations for -5.0 <= log[M/H] <= +1, 2000 K <= T_{eff} <= 50000 K at several surface gravities”. In: *A&A* 363, pp. 1081–1190.

Claret, A. (2017). “Limb and gravity-darkening coefficients for the TESS satellite at several metallicities, surface gravities, and microturbulent velocities”. In: *A&A* 600, A30. DOI: 10.1051/0004-6361/201629705. arXiv: 1804.10295 [astro-ph.SR].

Claret, A. and S. Bloemen (2011). “Gravity and limb-darkening coefficients for the Kepler, CoRoT, Spitzer, uvby, UBVRIJHK, and Sloan photometric systems”. In: *A&A* 529, A75. DOI: 10.1051/0004-6361/201116451.

Claret, A., E. Cukanovaite, et al. (2020a). “Doppler beaming factors for white dwarfs, main sequence stars, and giant stars Limb-darkening coefficients for 3D (DA and DB) white dwarf models”. In: *arXiv e-prints*, arXiv:2007.15715. arXiv: 2007.15715 [astro-ph.SR].

Claret, A., E. Cukanovaite, et al. (2020b). “Gravity and limb-darkening coefficients for compact stars: DA, DB, and DBA eclipsing white dwarfs”. In: *A&A* 634, A93. DOI: 10.1051/0004-6361/201937326. arXiv: 2001.07129 [astro-ph.SR].

Claret, A., E. Cukanovaite, et al. (2020c). “Gravity and limb-darkening coefficients for compact stars: DA, DB, and DBA eclipsing white dwarfs”. In: *A&A* 634, A93. DOI: 10.1051/0004-6361/201937326. arXiv: 2001.07129 [astro-ph.SR].

Copperwheat, C. M. et al. (2010). “Physical properties of IP Pegasi: an eclipsing dwarf nova with an unusually cool white dwarf”. In: *MNRAS* 402.3, pp. 1824–1840. DOI: 10.1111/j.1365-2966.2009.16010.x. arXiv: 0911.1637 [astro-ph.SR].

Cornish, N. J. and S. L. Larson (2003). “LISA data analysis: Source identification and subtraction”. In: 67.10, p. 103001. DOI: 10.1103/PhysRevD.67.103001. arXiv: astro-ph/0301548 [astro-ph].

Coughlin, M. W., K. Burdge, et al. (2020). “ZTF J1901+5309: a 40.6-min orbital period eclipsing double white dwarf system”. In: *MNRAS* 494.1, pp. L91–L96. DOI: 10.1093/mnrasl/slaa044. arXiv: 2004.00456 [astro-ph.HE].

Coughlin, M. W., R. G. Dekany, et al. (2019). "The Kitt Peak Electron Multiplying CCD demonstrator". In: *MNRAS* 485.1, pp. 1412–1419. DOI: 10.1093/mnras/stz497. arXiv: 1901.04625 [astro-ph.IM].

Cropper, M. et al. (1998). "RX J1914.4+2456: the first double-degenerate polar?" In: *MNRAS* 293.2, pp. L57–L60. DOI: 10.1046/j.1365-8711.1998.01297.x.

Cui, X.-Q. et al. (2012). "The Large Sky Area Multi-Object Fiber Spectroscopic Telescope (LAMOST)". In: *Research in Astronomy and Astrophysics* 12.9, pp. 1197–1242. DOI: 10.1088/1674-4527/12/9/003.

Dekany, R. et al. (2020). "The Zwicky Transient Facility: Observing System". In: *PASP* 132.1009, p. 038001. DOI: 10.1088/1538-3873/ab4ca2.

Denissenkov, P. A. et al. (2013). "MESA Models of Classical Nova Outbursts: The Multicycle Evolution and Effects of Convective Boundary Mixing". In: *ApJ* 762.1, p. 8. DOI: 10.1088/0004-637X/762/1/8. arXiv: 1210.5209 [astro-ph.SR].

Dhillon, V. S., T. R. Marsh, et al. (2007). "ULTRACAM: an ultrafast, triple-beam CCD camera for high-speed astrophysics". In: *MNRAS* 378.3, pp. 825–840. DOI: 10.1111/j.1365-2966.2007.11881.x. arXiv: 0704.2557 [astro-ph].

Dhillon, V., S. Dixon, et al. (2018). "First light with HiPERCAM on the GTC". In: *Ground-based and Airborne Instrumentation for Astronomy VII*. Vol. 10702. Society of Photo-Optical Instrumentation Engineers (SPIE) Conference Series, p. 107020L. DOI: 10.1117/12.2312041. arXiv: 1807.00557 [astro-ph.IM].

Eggleton, P. P. (1983). "Aproximations to the radii of Roche lobes." In: *ApJ* 268, pp. 368–369. DOI: 10.1086/160960.

Einstein, A. (1905). "Zur Elektrodynamik bewegter Körper". In: *Annalen der Physik* 322.10, pp. 891–921. DOI: 10.1002/andp.19053221004.

Faulkner, J., B. P. Flannery, and B. Warner (1972). "Ultrashort-Period Binaries. II. HZ 29 (=AM CVn): a Double-White-Dwarf Semidetached Postcataclysmic Nova?" In: *ApJL* 175, pp. L79–L83. DOI: 10.1086/180989.

Feroz, F., M. P. Hobson, and M. Bridges (2009). "MULTINEST: an efficient and robust Bayesian inference tool for cosmology and particle physics". In: *MNRAS* 398.4, pp. 1601–1614. DOI: 10.1111/j.1365-2966.2009.14548.x. arXiv: 0809.3437 [astro-ph].

Fontaine, G. and P. Brassard (2008). "The Pulsating White Dwarf Stars". In: *PASP* 120.872, p. 1043. DOI: 10.1086/592788.

Fuller, J. and D. Lai (2012). "Dynamical tides in compact white dwarf binaries: tidal synchronization and dissipation". In: *MNRAS* 421.1, pp. 426–445. DOI: 10.1111/j.1365-2966.2011.20320.x. arXiv: 1108.4910 [astro-ph.SR].

Fuller, J. and D. Lai (2013). "Dynamical tides in compact white dwarf binaries: helium core white dwarfs, tidal heating and observational signatures". In: *MNRAS* 430.1, pp. 274–287. DOI: 10.1093/mnras/sts606. arXiv: 1211.0624 [astro-ph.SR].

Gaia Collaboration (2018). "Gaia Data Release 2. Summary of the contents and survey properties". In: *A&A* 616, A1. DOI: 10.1051/0004-6361/201833051. arXiv: 1804.09365 [astro-ph.GA].

Gehrels, N. et al. (2004). "The Swift Gamma-Ray Burst Mission". In: *ApJ* 611.2, pp. 1005–1020. DOI: 10.1086/422091. arXiv: astro-ph/0405233 [astro-ph].

Geier, S. et al. (2017). "The population of hot subdwarf stars studied with Gaia. I. The catalog of known hot subdwarf stars". In: *A&A* 600, A50. DOI: 10.1051/0004-6361/201630135. arXiv: 1612.02995 [astro-ph.SR].

Gentile Fusillo, N. P. et al. (2019). "A Gaia Data Release 2 catalogue of white dwarfs and a comparison with SDSS". In: *MNRAS* 482.4, pp. 4570–4591. DOI: 10.1093/mnras/sty3016. arXiv: 1807.03315 [astro-ph.SR].

Gianninas, A., B. Curd, et al. (2016). "Discovery of Three Pulsating, Mixed-atmosphere, Extremely Low-mass White Dwarf Precursors". In: *ApJL* 822.2, p. L27. DOI: 10.3847/2041-8205/822/2/L27. arXiv: 1604.04621 [astro-ph.SR].

Gianninas, A., P. Dufour, et al. (2014). "Precise Atmospheric Parameters for the Shortest-period Binary White Dwarfs: Gravitational Waves, Metals, and Pulsations". In: *ApJ* 794.1, p. 35. DOI: 10.1088/0004-637X/794/1/35. arXiv: 1408.3118 [astro-ph.SR].

Gianninas, A., M. Kilic, et al. (2015). "The ELM Survey. VI. Eleven New Double Degenerates". In: *ApJ* 812.2, p. 167. DOI: 10.1088/0004-637X/812/2/167. arXiv: 1509.07134 [astro-ph.SR].

Gianninas, A., B. D. Strickland, et al. (2013). "Limb-darkening Coefficients for Eclipsing White Dwarfs". In: *ApJ* 766.1, p. 3. DOI: 10.1088/0004-637X/766/1/3. arXiv: 1301.7091 [astro-ph.SR].

Graham, M. J., A. J. Drake, et al. (2013). "Using conditional entropy to identify periodicity". In: *MNRAS* 434.3, pp. 2629–2635. DOI: 10.1093/mnras/stt1206. arXiv: 1306.6664 [astro-ph.IM].

Graham, M. J., S. R. Kulkarni, et al. (2019). "The Zwicky Transient Facility: Science Objectives". In: *PASP* 131.1001, p. 078001. DOI: 10.1088/1538-3873/ab006c. arXiv: 1902.01945 [astro-ph.IM].

Green, G. M., E. Schlafly, et al. (2019). "A 3D Dust Map Based on Gaia, Pan-STARRS 1, and 2MASS". In: *ApJ* 887.1, p. 93. DOI: 10.3847/1538-4357/ab5362. arXiv: 1905.02734 [astro-ph.GA].

Green, M. J., J. J. Hermes, et al. (2018). "A 15.7-minAM CVn binary discovered in K2". In: *MNRAS* 477.4, pp. 5646–5656. DOI: 10.1093/mnras/sty1032. arXiv: 1804.07138 [astro-ph.SR].

Haberl, F. and C. Motch (1995). "New intermediate polars discovered in the ROSAT survey: two spectrally distinct classes." In: *A&A* 297, p. L37.

Harding, L. K. et al. (2016). "CHIMERA: a wide-field, multi-colour, high-speed photometer at the prime focus of the Hale telescope". In: *MNRAS* 457.3, pp. 3036–3049. DOI: 10.1093/mnras/stw094. arXiv: 1601.03104 [astro-ph.IM].

Hartman, J. D. and G. Á. Bakos (2016). "VARTOOLS: A program for analyzing astronomical time-series data". In: *Astronomy and Computing* 17, pp. 1–72. DOI: 10.1016/j.ascom.2016.05.006. arXiv: 1605.06811 [astro-ph.IM].

Heber, U. (2016). "Hot Subluminous Stars". In: *PASP* 128.966, p. 082001. DOI: 10.1088/1538-3873/128/966/082001. arXiv: 1604.07749 [astro-ph.SR].

Heger, A., N. Langer, and S. E. Woosley (2000). "Presupernova Evolution of Rotating Massive Stars. I. Numerical Method and Evolution of the Internal Stellar Structure". In: *ApJ* 528.1, pp. 368–396. DOI: 10.1086/308158. arXiv: astro-ph/9904132 [astro-ph].

Hermes, J. J., B. T. Gänsicke, et al. (2014). "Heavy metals in a light white dwarf: abundances of the metal-rich, extremely low-mass GALEX J1717+6757". In: *MNRAS* 444.2, pp. 1674–1682. DOI: 10.1093/mnras/stu1518. arXiv: 1407.7833 [astro-ph.SR].

Hermes, J. J., M. Kilic, et al. (2012). "Rapid Orbital Decay in the 12.75-minute Binary White Dwarf J0651+2844". In: *ApJL* 757.2, p. L21. DOI: 10.1088/2041-8205/757/2/L21. arXiv: 1208.5051 [astro-ph.SR].

Holberg, J. B. and P. Bergeron (2006). "Calibration of Synthetic Photometry Using DA White Dwarfs". In: *AJ* 132.3, pp. 1221–1233. DOI: 10.1086/505938.

Horne, K. and D. P. Schneider (1989). "Evidence for a High-Mass White Dwarf in Nova V1500 Cygni 1975". In: *ApJ* 343, p. 888. DOI: 10.1086/167758.

Israel, G. L. et al. (1999). "The discovery of 321 S pulsations in the ROSAT HRI light curves of 1BMW J080622.8+152732 = RX J0806.3+1527". In: *A&A* 349, pp. L1–L4.

Istrate, A. G. et al. (2016). "Models of low-mass helium white dwarfs including gravitational settling, thermal and chemical diffusion, and rotational mixing". In: *A&A* 595, A35. DOI: 10.1051/0004-6361/201628874. arXiv: 1606.04947 [astro-ph.SR].

Ivanova, N. et al. (2013). "Common envelope evolution: where we stand and how we can move forward". In: *Astronomy and Astrophysics Review* 21, p. 59. DOI: 10.1007/s00159-013-0059-2. arXiv: 1209.4302 [astro-ph.HE].

Ivezić, Ž. et al. (2019). "LSST: From Science Drivers to Reference Design and Anticipated Data Products". In: *ApJ* 873.2, p. 111. DOI: 10.3847/1538-4357/ab042c. arXiv: 0805.2366 [astro-ph].

Jansen, F. et al. (2001). "XMM-Newton observatory. I. The spacecraft and operations". In: *A&A* 365, pp. L1–L6. DOI: 10.1051/0004-6361:20000036.

Kalberla, P. M. W. et al. (2005). "The Leiden/Argentine/Bonn (LAB) Survey of Galactic HI. Final data release of the combined LDS and IAR surveys with improved stray-radiation corrections". In: *A&A* 440.2, pp. 775–782. DOI: 10.1051/0004-6361:20041864. arXiv: astro-ph/0504140 [astro-ph].

Kaplan, D. L., V. B. Bhalerao, et al. (2013). "A Metal-rich Low-gravity Companion to a Massive Millisecond Pulsar". In: *ApJ* 765.2, p. 158. DOI: 10.1088/0004-637X/765/2/158. arXiv: 1302.2492 [astro-ph.SR].

Kaplan, D. L., L. Bildsten, and J. D. R. Steinfadt (2012). "Orbital Evolution of Compact White Dwarf Binaries". In: *ApJ* 758.1, p. 64. DOI: 10.1088/0004-637X/758/1/64. arXiv: 1208.6320 [astro-ph.SR].

Katz, M. L. et al. (2020). "GPU-Accelerated Periodic Source Identification in Large-Scale Surveys: Measuring P and $\dot{P}$". In: *arXiv e-prints*, arXiv:2006.06866. arXiv: 2006.06866 [astro-ph.IM].

Kilic, M., W. R. Brown, A. Gianninas, et al. (2014). "A new gravitational wave verification source." In: *MNRAS* 444, pp. L1–L5. DOI: 10.1093/mnrasl/slu093. arXiv: 1406.3346 [astro-ph.SR].

Kilic, M., W. R. Brown, C. Allende Prieto, M. A. Agüeros, et al. (2011). "The ELM Survey. II. Twelve Binary White Dwarf Merger Systems". In: *ApJ* 727.1, p. 3. DOI: 10.1088/0004-637X/727/1/3. arXiv: 1011.4073 [astro-ph.GA].

Kilic, M., W. R. Brown, C. Allende Prieto, S. J. Kenyon, et al. (2012). "The ELM Survey. IV. 24 White Dwarf Merger Systems". In: *ApJ* 751.2, p. 141. DOI: 10.1088/0004-637X/751/2/141. arXiv: 1204.0028 [astro-ph.GA].

Kollmeier, J. A. et al. (2017). "SDSS-V: Pioneering Panoptic Spectroscopy". In: *arXiv e-prints*, arXiv:1711.03234. arXiv: 1711.03234 [astro-ph.GA].

Korol, V., E. M. Rossi, and E. Barausse (2019). "A multimessenger study of the Milky Way's stellar disc and bulge with LISA, Gaia, and LSST". In: *MNRAS* 483.4, pp. 5518–5533. DOI: 10.1093/mnras/sty3440. arXiv: 1806.03306 [astro-ph.GA].

Korol, V., E. M. Rossi, P. J. Groot, et al. (2017). "Prospects for detection of detached double white dwarf binaries with Gaia, LSST and LISA". In: *MNRAS* 470.2, pp. 1894–1910. DOI: 10.1093/mnras/stx1285. arXiv: 1703.02555 [astro-ph.HE].

Kovács, G., S. Zucker, and T. Mazeh (2002). "A box-fitting algorithm in the search for periodic transits". In: *A&A* 391, pp. 369–377. DOI: 10.1051/0004-6361:20020802. arXiv: astro-ph/0206099 [astro-ph].

Kupfer, T., V. Korol, et al. (2018). "LISA verification binaries with updated distances from Gaia Data Release 2". In: *MNRAS* 480.1, pp. 302–309. DOI: 10.1093/mnras/sty1545. arXiv: 1805.00482 [astro-ph.SR].

Kupfer, T., E. B. Bauer, K. B. Burdge, E. C. Bellm, et al. (2019). "A New Class of Large-amplitude Radial-mode Hot Subdwarf Pulsators". In: *ApJL* 878.2, p. L35. DOI: 10.3847/2041-8213/ab263c. arXiv: 1906.00979 [astro-ph.GA].

Kupfer, T., E. B. Bauer, K. B. Burdge, J. van Roestel, et al. (2020). "A new class of Roche lobe-filling hot subdwarf binaries". In: *arXiv e-prints*, arXiv:2007.05349. arXiv: 2007.05349 [astro-ph.SR].

Kupfer, T., E. B. Bauer, T. R. Marsh, et al. (2020). "The First Ultracompact Roche Lobe-Filling Hot Subdwarf Binary". In: *ApJ* 891.1, p. 45. DOI: 10.3847/1538-4357/ab72ff. arXiv: 2002.01485 [astro-ph.SR].

Law, N. M. et al. (2009). "The Palomar Transient Factory: System Overview, Performance, and First Results". In: *Publications of the Astronomical Society of the Pacific* 121.886, p. 1395. DOI: 10.1086/648598. arXiv: 0906.5350 [astro-ph.IM].

Levenhagen, R. S. et al. (2017). "A grid of synthetic spectra for hot DA white dwarfs and its application in stellar population synthesis". In: *The Astrophysical Journal Supplement Series* 231, p. 1. DOI: 10.3847/1538-4365/aa7681.

Levitan, D. et al. (2015). "Long-term photometric behaviour of outbursting AM CVn systems". In: *MNRAS* 446.1, pp. 391–410. DOI: 10.1093/mnras/stu2105. arXiv: 1410.6987 [astro-ph.SR].

Li, Z. et al. (2019). "Formation of Extremely Low-mass White Dwarfs in Double Degenerates". In: *ApJ* 871.2, p. 148. DOI: 10.3847/1538-4357/aaf9a1. arXiv: 1812.07226 [astro-ph.SR].

Littenberg, T. B. and N. J. Cornish (2019). "Prospects for Gravitational Wave Measurement of ZTF J1539+5027". In: *ApJL* 881.2, p. L43. DOI: 10.3847/2041-8213/ab385f. arXiv: 1908.00678 [astro-ph.IM].

Loeb, A. and B. S. Gaudi (2003). "Periodic Flux Variability of Stars due to the Reflex Doppler Effect Induced by Planetary Companions". In: *ApJ* 588.2, pp. L117–L120. DOI: 10.1086/375551. arXiv: astro-ph/0303212 [astro-ph].

Lomb, N. R. (1976). "Least-Squares Frequency Analysis of Unequally Spaced Data". In: *Ap&SS* 39.2, pp. 447–462. DOI: 10.1007/BF00648343.

Lorimer, D. R. and M. Kramer (2012). *Handbook of Pulsar Astronomy*.

LSST Science Collaboration et al. (2009). "LSST Science Book, Version 2.0". In: *arXiv e-prints*, arXiv:0912.0201. arXiv: 0912.0201 [astro-ph.IM].

Marsh, T. R. (1995). "The discovery of a short-period double-degenerate binary star". In: *MNRAS* 275.1, pp. L1–L5. DOI: 10.1093/mnras/275.1.L1. arXiv: astro-ph/9504088 [astro-ph].

Marsh, T. R. (2001). "Doppler Tomography". In: *Astrotomography, Indirect Imaging Methods in Observational Astronomy*. Ed. by H. M. J. Boffin, D. Steeghs, and J. Cuypers. Vol. 573, p. 1.

Marsh, T. R., V. S. Dhillon, and S. R. Duck (1995). "Low-Mass White Dwarfs Need Friends - Five New Double-Degenerate Close Binary Stars". In: *MNRAS* 275, p. 828. DOI: 10.1093/mnras/275.3.828.

Marsh, T. R., G. Nelemans, and D. Steeghs (2004). "Mass transfer between double white dwarfs". In: *MNRAS* 350.1, pp. 113–128. DOI: 10.1111/j.1365-2966.2004.07564.x. arXiv: astro-ph/0312577 [astro-ph].

Marsh, T. R. and D. Steeghs (2002). "V407 Vul: a direct impact accretor". In: *MNRAS* 331.1, pp. L7–L11. DOI: 10.1046/j.1365-8711.2002.05346.x. arXiv: astro-ph/0201309 [astro-ph].

Masci, F. J., R. R. Laher, U. D. Rebbapragada, et al. (2017). "The IPAC Image Subtraction and Discovery Pipeline for the Intermediate Palomar Transient Factory". In: *PASP* 129.971, p. 014002. DOI: 10.1088/1538-3873/129/971/014002. arXiv: 1608.01733 [astro-ph.IM].

Masci, F. J., R. R. Laher, B. Rusholme, et al. (2019). "The Zwicky Transient Facility: Data Processing, Products, and Archive". In: *PASP* 131.995, p. 018003. DOI: 10.1088/1538-3873/aae8ac. arXiv: 1902.01872 [astro-ph.IM].

Maxted, P. F. L. (2016). "ellc: A fast, flexible light curve model for detached eclipsing binary stars and transiting exoplanets". In: *A&A* 591, A111. DOI: 10.1051/0004-6361/201628579. arXiv: 1603.08484 [astro-ph.IM].

McCarthy, J. K. et al. (1998). "Blue channel of the Keck low-resolution imaging spectrometer". In: *Optical Astronomical Instrumentation*. Ed. by S. D'Odorico. Vol. 3355. Society of Photo-Optical Instrumentation Engineers (SPIE) Conference Series, pp. 81–92. DOI: 10.1117/12.316831.

Merloni, A. et al. (2012). "eROSITA Science Book: Mapping the Structure of the Energetic Universe". In: *arXiv e-prints*, arXiv:1209.3114. arXiv: 1209.3114 [astro-ph.HE].

Moore, C. J., R. H. Cole, and C. P. L. Berry (2015). "Gravitational-wave sensitivity curves". In: *Classical and Quantum Gravity* 32.1, p. 015014. DOI: 10.1088/0264-9381/32/1/015014. arXiv: 1408.0740 [gr-qc].

Morris, S. L. (1985). "The ellipsoidal variable stars." In: *ApJ* 295, pp. 143–152. DOI: 10.1086/163359.

Napiwotzki, R., N. Christlieb, et al. (2003). "SPY - the ESO Supernovae type Ia Progenitor survey". In: *The Messenger* 112, pp. 25–30.

Napiwotzki, R., C. A. Karl, et al. (2020). "The ESO supernovae type Ia progenitor survey (SPY). The radial velocities of 643 DA white dwarfs". In: *A&A* 638, A131. DOI: 10.1051/0004-6361/201629648. arXiv: 1906.10977 [astro-ph.SR].

Nelemans, G., L. R. Yungelson, and S. F. Portegies Zwart (2001). "The gravitational wave signal from the Galactic disk population of binaries containing two compact objects". In: *A&A* 375, pp. 890–898. DOI: 10.1051/0004-6361:20010683. arXiv: astro-ph/0105221 [astro-ph].

Nissanke, S. et al. (2012). "Gravitational-wave Emission from Compact Galactic Binaries". In: *ApJ* 758.2, p. 131. DOI: 10.1088/0004-637X/758/2/131. arXiv: 1201.4613 [astro-ph.GA].

Oke, J. B., J. G. Cohen, et al. (1995). "The Keck Low-Resolution Imaging Spectrometer". In: *PASP* 107, p. 375. DOI: 10.1086/133562.

Oke, J. B. and J. E. Gunn (1982). "An Efficient Low Resolution and Moderate Resolution Spectrograph for the Hale Telescope". In: *PASP* 94, p. 586. DOI: 10.1086/131027.

Paczyński, B. (1971). "Evolution of Single Stars. IV. Helium Stars". In: 21, p. 1.

Patterson, J. (1994). "The DQ Herculis Stars". In: *PASP* 106, p. 209. DOI: 10.1086/133375.

Paxton, B., L. Bildsten, et al. (2011). "Modules for Experiments in Stellar Astrophysics (MESA)". In: *ApJS* 192.1, p. 3. DOI: 10.1088/0067-0049/192/1/3. arXiv: 1009.1622 [astro-ph.SR].

Paxton, B., M. Cantiello, et al. (2013). "Modules for Experiments in Stellar Astrophysics (MESA): Planets, Oscillations, Rotation, and Massive Stars". In: *ApJS* 208.1, p. 4. DOI: 10.1088/0067-0049/208/1/4. arXiv: 1301.0319 [astro-ph.SR].

Paxton, B., P. Marchant, et al. (2015). "Modules for Experiments in Stellar Astrophysics (MESA): Binaries, Pulsations, and Explosions". In: *ApJS* 220.1, p. 15. DOI: 10.1088/0067-0049/220/1/15. arXiv: 1506.03146 [astro-ph.SR].

Perets, H. B. et al. (2019). "Normal type Ia supernovae from disruptions of hybrid He-CO white-dwarfs by CO white-dwarfs". In: *arXiv e-prints*, arXiv:1910.07532. arXiv: 1910.07532 [astro-ph.HE].

Perley, D. A. (2019). "Fully Automated Reduction of Longslit Spectroscopy with the Low Resolution Imaging Spectrometer at the Keck Observatory". In: *PASP* 131.1002, p. 084503. DOI: 10.1088/1538-3873/ab215d. arXiv: 1903.07629 [astro-ph.IM].

Pietrukowicz, P. et al. (2017). "Blue large-amplitude pulsators as a new class of variable stars". In: *Nature Astronomy* 1, p. 0166. DOI: 10.1038/s41550-017-0166. arXiv: 1706.07802 [astro-ph.SR].

Piro, A. L. (2019). "Inferring the Presence of Tides in Detached White Dwarf Binaries". In: *ApJL* 885.1, p. L2. DOI: 10.3847/2041-8213/ab44c4. arXiv: 1908.04896 [astro-ph.SR].

Podsiadlowski, P., Z. Han, and S. Rappaport (2003). "Cataclysmic variables with evolved secondaries and the progenitors of AM CVn stars". In: *MNRAS* 340.4, pp. 1214–1228. DOI: 10.1046/j.1365-8711.2003.06380.x.

Postnov, K. A. and L. R. Yungelson (2014). "The Evolution of Compact Binary Star Systems". In: *Living Reviews in Relativity* 17.1, p. 3. DOI: 10.12942/lrr-2014-3. arXiv: 1403.4754 [astro-ph.HE].

Ramsay, G., M. J. Green, et al. (2018). "Physical properties of AM CVn stars: New insights from Gaia DR2". In: *A&A* 620, A141. DOI: 10.1051/0004-6361/201834261. arXiv: 1810.06548 [astro-ph.SR].

Ramsay, G., M. Cropper, et al. (2000). "Detection of the optical counterpart of the proposed double degenerate polar RX J1914+24". In: *MNRAS* 311.1, pp. 75–84. DOI: 10.1046/j.1365-8711.2000.03065.x. arXiv: astro-ph/9908042 [astro-ph].

Ramsay, G., P. Hakala, and M. Cropper (2002). "RX J0806+15: the shortest period binary?" In: *MNRAS* 332.1, pp. L7–L10. DOI: 10.1046/j.1365-8711.2002.05471.x. arXiv: astro-ph/0203053 [astro-ph].

Ramsay, G., P. J. Wheatley, et al. (2008). "The defining characteristics of intermediate polars - the case of three-candidate systems". In: *MNRAS* 387.3, pp. 1157–1162. DOI: 10.1111/j.1365-2966.2008.13299.x. arXiv: 0804.1223 [astro-ph].

Rappaport, S. et al. (1995). "The relation between white dwarf mass and orbital period in wide binary radio pulsars". In: *MNRAS* 273.3, pp. 731–741. DOI: 10.1093/mnras/273.3.731.

Reding, J. S. et al. (2020). "An Isolated White Dwarf with 317-Second Rotation and Magnetic Emission". In: *arXiv e-prints*, arXiv:2003.10450. arXiv: 2003.10450 [astro-ph.SR].

Reinsch, K. et al. (2000). "Optical Spectroscopy of two Double-degenerate Polar Candidates". In: *Astronomische Gesellschaft Meeting Abstracts*. Vol. 17. Astronomische Gesellschaft Meeting Abstracts.

Robson, T., N. J. Cornish, and C. Liu (2019). "The construction and use of LISA sensitivity curves". In: *Classical and Quantum Gravity* 36.10, p. 105011. DOI: 10.1088/1361-6382/ab1101. arXiv: 1803.01944 [astro-ph.HE].

Roelofs, G. H. A. et al. (2010). "Spectroscopic Evidence for a 5.4 Minute Orbital Period in HM Cancri". In: *ApJL* 711.2, pp. L138–L142. DOI: 10.1088/2041-8205/711/2/L138. arXiv: 1003.0658 [astro-ph.SR].

Saffer, R. A., J. Liebert, and E. W. Olszewski (1988). "Discovery of a Close Detached Binary DA White Dwarf System". In: *ApJ* 334, p. 947. DOI: 10.1086/166888.

Scargle, J. D. (1982). "Studies in astronomical time series analysis. II. Statistical aspects of spectral analysis of unevenly spaced data." In: *ApJ* 263, pp. 835–853. DOI: 10.1086/160554.

Schwarzenberg-Czerny, A. (1996). "Fast and Statistically Optimal Period Search in Uneven Sampled Observations". In: *ApJL* 460, p. L107. DOI: 10.1086/309985.

Shah, S., G. Nelemans, and M. van der Sluys (2013). "Using electromagnetic observations to aid gravitational-wave parameter estimation of compact binaries observed with LISA. II. The effect of knowing the sky position". In: *A&A* 553, A82. DOI: 10.1051/0004-6361/201321123. arXiv: 1303.6116 [astro-ph.IM].

Shah, S., M. van der Sluys, and G. Nelemans (2012). "Using electromagnetic observations to aid gravitational-wave parameter estimation of compact binaries observed with LISA". In: *A&A* 544, A153. DOI: 10.1051/0004-6361/201219309. arXiv: 1207.6770 [astro-ph.IM].

Shen, K. J. (2015). "Every Interacting Double White Dwarf Binary May Merge". In: *ApJL* 805.1, p. L6. DOI: 10.1088/2041-8205/805/1/L6. arXiv: 1502.05052 [astro-ph.SR].

Shen, K. J., D. Boubert, et al. (2018). "Three Hypervelocity White Dwarfs in Gaia DR2: Evidence for Dynamically Driven Double-degenerate Double-detonation Type Ia Supernovae". In: *ApJ* 865.1, p. 15. DOI: 10.3847/1538-4357/aad55b. arXiv: 1804.11163 [astro-ph.SR].

Shen, K. J., D. Kasen, et al. (2018). "Sub-Chandrasekhar-mass White Dwarf Detonations Revisited". In: *ApJ* 854.1, p. 52. DOI: 10.3847/1538-4357/aaa8de. arXiv: 1706.01898 [astro-ph.HE].

Shklovskii, I. (1970). "Possible Causes of the Secular Increase in Pulsar Periods." In: *Soviet Astronomy* 13, p. 562.

Smak, J. (1967). "18-min. Light-Variations of HZ 29". In: *Information Bulletin on Variable Stars* 182, p. 1.

Soares, E. d. A. (2017). "Constraining Effective Temperature, Mass and Radius of Hot White Dwarfs". In: *arXiv e-prints*, arXiv:1701.02295. arXiv: 1701.02295 [astro-ph.SR].

Stroeer, A. et al. (2007). "Hot subdwarfs from the ESO supernova Ia progenitor survey. II. Atmospheric parameters of subdwarf O stars". In: *A&A* 462.1, pp. 269–280. DOI: 10.1051/0004-6361:20065564. arXiv: astro-ph/0609718 [astro-ph].

Strohmayer, T. E. (2005). "Precision X-Ray Timing of RX J0806.3+1527 with Chandra: Evidence for Gravitational Radiation from an Ultracompact Binary". In: *ApJ* 627.2, pp. 920–925. DOI: 10.1086/430439. arXiv: astro-ph/0504150 [astro-ph].

Sun, M. and P. Arras (2018). "Formation of Extremely Low-mass White Dwarf Binaries". In: *ApJ* 858.1, p. 14. DOI: 10.3847/1538-4357/aab9a4. arXiv: 1703.01648 [astro-ph.SR].

Tauris, T. M. (2018). "Disentangling Coalescing Neutron-Star-White-Dwarf Binaries for LISA". In: *Proc. SPIE* 121.13, p. 131105. DOI: 10.1103/PhysRevLett.121.131105. arXiv: 1809.03504 [astro-ph.SR].

Taylor, J. H., L. A. Fowler, and P. M. McCulloch (1979). "Measurements of general relativistic effects in the binary pulsar PSR1913 + 16". In: *Nature* 277.5696, pp. 437–440. DOI: 10.1038/277437a0.

Taylor, J. H. and J. M. Weisberg (1989). "Further Experimental Tests of Relativistic Gravity Using the Binary Pulsar PSR 1913+16". In: *ApJ* 345, p. 434. DOI: 10.1086/167917.

Thorne, K. S. (1987). "Gravitational radiation." In: *Three Hundred Years of Gravitation*, pp. 330–458.

Tremblay, P. .-E. and P. Bergeron (2009). "Spectroscopic Analysis of DA White Dwarfs: Stark Broadening of Hydrogen Lines Including Nonideal Effects". In: *ApJ* 696.2, pp. 1755–1770. DOI: 10.1088/0004-637X/696/2/1755. arXiv: 0902.4182 [astro-ph.SR].

Tremblay, P. .-E., P. Bergeron, and A. Gianninas (2011). "An Improved Spectroscopic Analysis of DA White Dwarfs from the Sloan Digital Sky Survey Data Release 4". In: *ApJ* 730.2, p. 128. DOI: 10.1088/0004-637X/730/2/128. arXiv: 1102.0056 [astro-ph.SR].

Tremblay, P. .-E., A. Gianninas, et al. (2015). "3D Model Atmospheres for Extremely Low-mass White Dwarfs". In: *ApJ* 809.2, p. 148. DOI: 10.1088/0004-637X/809/2/148. arXiv: 1507.01927 [astro-ph.SR].

Tulloch, S. M. and V. S. Dhillon (2011). "On the use of electron-multiplying CCDs for astronomical spectroscopy". In: *MNRAS* 411.1, pp. 211–225. DOI: 10.1111/j.1365-2966.2010.17675.x. arXiv: 1009.3403 [astro-ph.IM].

VanderPlas, J. T. (2018). "Understanding the Lomb-Scargle Periodogram". In: *ApJS* 236.1, p. 16. DOI: 10.3847/1538-4365/aab766. arXiv: 1703.09824 [astro-ph.IM].

von Zeipel, H. (1924). "The radiative equilibrium of a rotating system of gaseous masses". In: *MNRAS* 84, pp. 665–683. DOI: 10.1093/mnras/84.9.665.

Webbink, R. F. (1984). "Double white dwarfs as progenitors of R Coronae Borealis stars and type I supernovae." In: *ApJ* 277, pp. 355–360. DOI: 10.1086/161701.

Wolf, W. M. et al. (2013). "Hydrogen Burning on Accreting White Dwarfs: Stability, Recurrent Novae, and the Post-nova Supersoft Phase". In: *ApJ* 777.2, p. 136. DOI: 10.1088/0004-637X/777/2/136. arXiv: 1309.3375 [astro-ph.SR].

Yao, Y. et al. (2019). "ZTF Early Observations of Type Ia Supernovae. I. Properties of the 2018 Sample". In: *ApJ* 886.2, p. 152. DOI: 10.3847/1538-4357/ab4cf5. arXiv: 1910.02967 [astro-ph.HE].